FACULTY OF SCIENCE
UNIVERSITY OF COPENHAGEN

PhD Thesis

Fabian Czerwinski

Allan Variance Analysis and Fast Camera Detection Schemes for Optical Tweezers

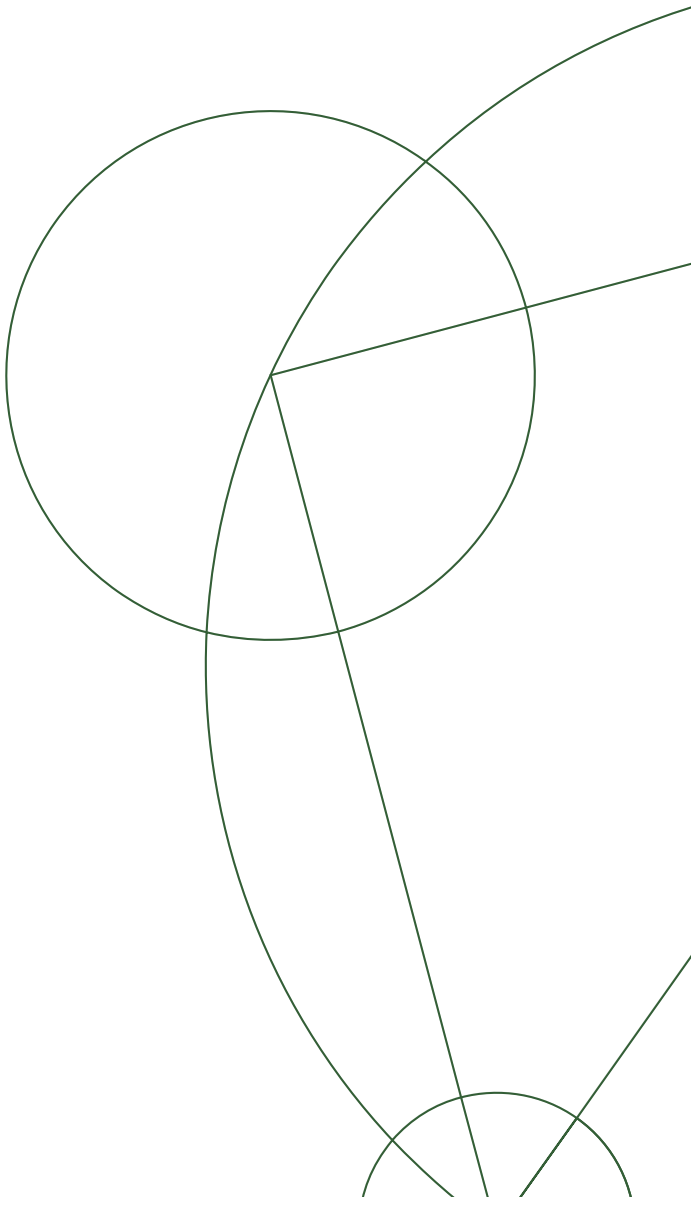

Academic Advisor: Lene B. Oddershede

Submitted: September 27, 2010

FACULTY OF SCIENCE
UNIVERSITY OF COPENHAGEN

PhD Thesis

Fabian Czerwinski

Allan Variance Analysis and Fast Camera Detection Schemes for Optical Tweezers

Academic Advisor: Lene B. Oddershede

Submitted: September 27, 2010

FACULTY OF SCIENCE
UNIVERSITY OF COPENHAGEN

Niels Bohr Institute
University of Copenhagen
Faculty of Science
Blegdamsvej 17
2100 Copenhagen
Denmark

PhD Thesis

PhD Thesis

Fabian Czerwinski

Allan Variance Analysis and Fast Camera Detection Schemes for Optical Tweezers

Allan Variance Analysis and
Fast Camera Detection Schemes
for Optical Tweezers

Fabian Czerwinski

September 27, 2010

Academic Advisor: Lene B. Oddershede

Academic Advisor: Lene B. Oddershede

Submitted: September 27, 2010

FACULTY OF SCIENCE
UNIVERSITY OF COPENHAGEN

submitted to the PhD School at the Faculty of Science,
University of Copenhagen, Denmark

PhD Thesis

Fabian Czerwinski

Allan Variance Analysis and Fast Camera Detection Schemes for Optical Tweezers

"The manifesto was the original manifesto."
EF, Swedish musicians, in song *två*

"Those are my principles, and if you don't like them... well, I have others." Grougho Marx, American comedian

Academic Advisor: Lene B. Oddershede

Submitted: September 27, 2010

FACULTY OF SCIENCE
UNIVERSITY OF COPENHAGEN

Summary

Optical tweezers are an ubiquitous tool in modern biophysics. By introducing Allan variance analysis complementary to power spectral analysis, we improved the most prominent calibration protocols by reducing the number of assumptions. We employed this method to find the optimal calibration interval, to optimize acquisition parameters, and to quantify low frequency noise. Going further, we developed a camera-based detection scheme that allowed for stable and reliable real-time acquisition of optical tweezers experiments. We present data and discuss how this scheme as well as Allan variance analysis hold potential for other single-molecule techniques. Both developments pave the road to establish optical tweezers as a diagnostic tool for the investigation of potentially harmful interactions of fullerenes and DNA. To understand this interaction, we applied different single-molecule approaches and put them into perspective to one another.

PhD Thesis

Fabian Czerwinski

Allan Variance Analysis and Fast Camera Detection Schemes for Optical Tweezers

Academic Advisor: Lene B. Oddershede

Submitted: September 27, 2010

Acknowledgement

My "Years at the NBI" began with Lene Oddershede's invitation to Copenhagen. She gave me the great opportunity to present my previous research in the BioComplexity Meeting. I enjoyed the stay, the intellectual challenge that came with it, and the supportive environment. This impression could never, not even remotely, be proven false for my time at one of the most stimulating places for modern physics in the world. I therefore highly acknowledge Lene's supervision throughout the years as well as the opportunity to participate in the great group she gathered.

In the course of my three years as PhD student, it was a pleasure to share lab space with Tabita Winther, Maria Christiansen, Ninna Rossen, Kamilla Nørregaard, Pernille Yde, Mette Eriksen, Natascha Witte, Haiyan Ma, Kirstine Berg-Sørensen, Nader Reihani, Richie Hanes, Magnus Andersson, Poul Martin Bendix, Lei Xi, Josep Mas, Anders Rosengren, Anders Kyrsting, and Shahid Mir. Special thanks to Mario Fischer, Peder Møller and Jesper Tholstrup for sharing the office and the white board. I thank Michael Sørensen and Jesper Tholstrup for their never-ending patience in teaching me biochemical procedures. Christine Selhuber-Unkel has been a great fellow scientist and friend throughout the years. Christian Stokholm and I shared a lot of fun and hard-working time in the laboratory. His amazing hands-on approaches and an attitude of "yeah, doesn't sound too bad, let's give it a shot" cannot be appreciated enough. It is hard to find words that capture my deepest thankful thoughts to my fellow PhD students: Marie Domange Jördö, Liselotte Jauffred, and Andrew Richardson. Inside and outside the lab, you three were a great inspiration of how to do science, how to work together, and how to relate personal to career goals.

On the daily basis, many more theoreticians and experimentalists have contributed to the life inside the BioComplexity Group. I simply loved the science and non-science related chats over lunch, at workshops and during a good game of foosball. Many thanks to the group members not mentioned above; especially to Benedicte Mengel, Silja Heilmann, Namiko Mitarai, Lykke Pedersen, Anne Alsing, Sandeep Krishna, Mogens Høgh Jensen, Alexander Hunziker, Simone Pigolotti, Philip Gerlee, Szabolcs Semsey, Ludvig Lizana, Andreas Blicher, and Thomas Heimburg.

The four months I spent in Cambridge at the Cavendish Laboratories were a very intense experience. The greatest pleasure were the discussions and teach-ins together with Sabrina Jahn, Franziska Lautenschläger, Joanne Gornall, Moritz Kreysing, Andreas Christ, Nick Thomson, Catalin Chimerel, and Lorenz Steinbock. And in particular to Oliver Otto: I am looking forward to more wicked LabVIEW sessions at some late hour and celebrating high5s over successful experiments. Ulrich Keyser has been an exceptional mentor throughout all these years; one sentence in some acknowledgement does not express the least of the need to thank for this guidance.

I acknowledge a stipend of the Faculty of Science, University of Copenhagen. It gave me ample freedom for my research that I returned in those hours where I communicated my excitement about biophysics in classes, seminars and lectures for young students. The Heinrich Boell Foundation awarded me with a non-monetary scholarship that supported my participation in stimulating seminars and symposia.

Appended Publications

These appended publications form the basis of my PhD thesis. Here, the chronological order according to the date of submission is listed. In addition to the introductions, results and discussions provided with these publications, this thesis puts them in perspective to the research on optical tweezers in biophysical experiments (sections 1–8). Furthermore, the publications' relevance for the usage of biophysical single-molecule techniques as diagnostic tools is discussed (section 9). The process of publishing these results in the context of my three years as PhD student at the Niels Bohr Institute under Lene Oddershede's supervision, is briefly outlined in **Appended Publications** on pages 79 et seq.

[Czerwinski et al., 2009a] Fabian Czerwinski, Andrew C. Richardson, and Lene B. Oddershede, "Quantifying Noise in Optical Tweezers by Allan Variance," Opt. Express 17, 13255-69 (2009), doi 10.1364/OE.17.013255

[Czerwinski et al., 2009b] Fabian Czerwinski, Andrew C. Richardson, Christine Selhuber-Unkel, and Lene B. Oddershede, "Allan Variance Analysis as Useful Tool to Determine Noise in Various Single-Molecule Setups," Proc. SPIE, 7400, 740004 (2009), doi 10.1117/12.827975

[Jauffred et al., 2010] Liselotte Jauffred, Marit Sletmoen, Fabian Czerwinski, and Lene B. Oddershede, "Quantum dots as handles for optical manipulation," Proc. SPIE, 7762, 77620Q (2010), doi 10.1117/12.860486

[Otto et al., 2011] Oliver Otto, Joanne L. Gornall, Gunter Stober, Fabian Czerwinski, Ralf Seidel, and Ulrich F. Keyser, "High-Speed Video-Based Tracking of Optically Trapped Colloids," accepted for publication in J. Opt.

[Czerwinski and Oddershede, 2010] Fabian Czerwinski and Lene B. Oddershede, "TimeSeriesStreaming.vi: LabVIEW program for reliable data streaming of large analog time series," accepted for publication in Comput. Phys. Commun.

[Czerwinski et al., 2011] Fabian Czerwinski, Magnus Andersson, and Lene B. Oddershede, "Optimizing active and passive optical tweezers calibration," under review for publication in J. Opt.

[Otto et al., 2010] Oliver Otto, Fabian Czerwinski, Joanne L. Gornall, Gunter Stober, Lene B. Oddershede, Ralf Seidel, Ulrich F. Keyser, "Real-time Particle Tracking at 10,000 fps using Optical Fiber Illumination," accepted for publication in Opt. Express

[Czerwinski and Otto, 2010] Fabian Czerwinski and Oliver Otto, "Observing and Controlling Biomolecules with Optical Tweezers and LabVIEW," National Instruments Case Studies, 13024 (2010)

FACULTY OF SCIENCE
UNIVERSITY OF COPENHAGEN

PhD Thesis

Fabian Czerwinski

Allan Variance Analysis and Fast Camera Detection Schemes for Optical Tweezers

Academic Advisor: Lene B. Oddershede

Submitted: September 27, 2010

Contents

PhD Thesis
Fabian Czerwinski
Allan Variance Analysis and Fast Camera Detection Schemes for Optical Tweezers
Academic Advisor: Lene B. Oddershede
Submitted: September 27, 2010

Introduction and Objectives

1 Optical Tweezers: A Fascinating Tool in Modern Biophysics

Biophysics rule the world. At least, they rule my world. The material composition of biology is a fact, the laws of physics must hold here just as much as they do when we describe our picture of gravity or atomic structure. From postulating a material world, either a need or a desire to understand its composition derives. Approaching an understanding of living matter from a physicist's point of view, means putting numbers on everything where it conceptionally makes sense. An in-depth understanding starts with static systems, and tries to comprehend the dynamics of these systems in a next step. Ultimately, we want to be able to test our understanding by manipulating the system of interest in a very controlled manner. This leads either to a revision of our picture or a more detailed description. To work towards a more comprehensive understanding is exciting in itself, and, in the case of biological systems, holds the potential to motivate or to intervene in a discourse about something that may be called biotechnology.

Biotechnology, the field of applied biology of living cells or bioprocesses for engineering, medicine, or technology, is maybe the vastest growing technology nowadays. Nanotechnology, as a field of ultimate miniaturization of technical components, by the same standards though has been changing the way we can communicate, produce, and shape our environment for the last 30 years. Although nanotechnological developments are certainly able to address some of the world's most pressing issues (climate change, worldwide communication, etc.), consumer-oriented products "using nanotechnology" often become outrageously absurd. How can one distinguish between useful and dangerous, futile and progressive?

Inspired and driven by biophysicists, many apparatuses have been invented and improved over the last decades. As the basic research branch of biotechnology, modern biophysicists resolve cristallographic structures of lipids, proteins, etc., and put them in relation to all-atom simulations and analytical reasoning [Nölting, 2004, Nelson, 2004]. Moreover, observations using a broad variety of microscopes, microfluidics, and fluorescence techniques allow, for instance, for a quantitative measurement of genetic drift [Hallatschek et al., 2007], or for the determination of the bandwidth of protein-associated signal cascades [Hersen et al., 2008]. These are just few examples of a large number of intelligent and inspiring pieces of work that contribute to our understanding of biology.

Light microscopy is the most versatile and successful observation technique yield-

Academic Advisor: Lene B. Oddershede

Submitted: September 27, 2010

ing precise spatial and temporal information of particle motion [Bacia et al., 2006]. A prominent example is the tracking of single fluorophores or whole organelles in living cells to clarify cellular processes in vivo [Manley et al., 2008, Betzig et al., 2006, Cheezum et al., 2001]. Single-molecule microscopy has evolved as one of the most important quantifying biophysical approaches. It covers a very broad range of techniques that push the limits of ultrahigh-resolution imaging techniques, single-molecule fluorescence microscopy, and force microscopy [Walter et al., 2008]. When the manipulation of a biological system by physical entities like force, torque, or free energy is the research focus, force-microscopy techniques become the methods of choice [Strick et al., 2003, Neuman and Nagy, 2008].

Optical tweezers are a prominent force-microscopy technique, and have come to be a widely used tool in physics and biology only a few decades after their invention [Ashkin, 1970]. Optical tweezers are created by a tightly focused laser beam [Neuman and Block, 2004]. If focused in all three dimensions, a single laser beam can stably trap and manipulate individual objects with accuracies ranging from tens of micrometers down to a few nanometers. Objects as diverse as living cells [Ashkin et al., 1987], metallic particles [Hansen et al., 2005, Seol et al., 2006], and quantum dots [Jauffred and Oddershede, 2010, Jauffred et al., 2008b] can be trapped individually. With appropriate detection schemes the trap can also be utilized to measure forces and distances, typically in the order of piconewtons and nanometers. Due to the fact that the technique is nearly non-destructive to biological specimen, it has been successfully used, for example, to measure forces exerted and distances travelled by individual motor molecules [Abbondanzieri et al., 2005], or to unravel structures created by DNA or RNA templates [Liphardt et al., 2001].

2 Ongoing Research about Optical Tweezers

The research on optical traps follows three major categories: a) optical atom traps, b) traps that change the materials' properties, and c) optical tweezers. Atom traps are not the scope of this thesis, though they are extremely fascinating tools. Specially arranged laser beams form potentials, in which atoms take discrete energy levels, until their kinetic energy drops below a certain threshold to form coherent wave packages and ultimately condensates. Due to their almost microscopic sizes, they allow for the investigation of fundamental consequences of quantum mechanical postulates. This thesis only partially touches the fundamental interaction of light and matter, but phenomena such as optical binding and light guiding will certainly find use in future applications. Understanding the fundamental interaction of light rays with matter was the motivation for Arthur Ashkin back in 1970 [Ashkin, 1970]. He and his coworkers designed the very first optical traps that trapped micrometer-sized transparent objects. In a first prototype they used a diverging laser beam to counterbalance the gravity of polystyrene microspheres. Later on, they used two diverging beams to trap spheres stably in the focal plane. As mentioned before, a tightly focused laser beam can also achieve this [Pralle et al., 1999]. The most

outreaching and interdisciplinary development of optical traps leads to the usage of optical tweezers to investigate soft matter phenomena. Here, the optical manipulation of trapped, biofunctionalized handles draws the most attention. These handles can be controlled with extremely high accuracy.

2.1 Detection Schemes and Low Frequency Noise

Two main routes are pursued to measure the position of objects and handles inside optical tweezers. They are monitored and recorded by a certain detection scheme, namely photodiodes and video-based particle tracking [Neuman and Block, 2004]. While photodiodes are suited for position detection of a single object, they are not ideal for applications like holographic optical tweezers. Monitoring of multiple tweezers at the same time is complicated. In contrast, video-based particle tracking is capable of following several objects in the field of view at the same time [van der Horst and Forde, 2010, Jesacher et al., 2008a]. Multiplex video-based tracking at high bandwidth in combination with fast hologram calculations would open an entirely new class of holographic optical tweezers [Jesacher et al., 2008b, Hanes et al., 2009]. The progress in the development of new cameras and illumination systems has made it possible to extend the acquisition speed of this method to the microsecond timescale.

For such delicate measurements, it is extremely important to eliminate as many noise sources as possible. Recently, an optical tweezers setup having sensitivity to steps of the length of one DNA basepair [Carter et al., 2009] compensated drift by subtracting the motility of a marker, which was followed by a beam parallel to the trapping laser beam. This solution thus necessitates the use of two parallel laser beams. Other solutions are that, for instance, air currents have been eliminated by covering the setup, measurements have been conducted in the middle of the night, or, in the case of biophysical optical tweezers assays, the molecule investigated has been moved away from any surface that might be subject to drift. But how useful and efficient are these efforts? And how does one laboratory compare to another in terms of noise? In order to answer these questions it is essential to be able to quantify noise. The dominant approach to quantify noise is to use power spectral analysis. The Fourier transformed integrated noise in a predefined bandwidth has been used to judge the impact of some experimental arrangements [Gittes and Schmidt, 1998, Klein et al., 2007]. However, for biophysical experiments, power spectral analysis lacks the resolution of accumulative noise with a typical band of frequencies smaller than 0.1 Hz. Therefore, it is not a very efficient method to pinpoint low-frequency noise and determine the optimal measurement time for calibration, e.g., for single-molecule assays. For this purpose, Allan variance has proven to be a better choice [Czerwinski et al., 2009a].

Calibration protocols are an essential topic for any quantitative approach. The importance to make as few assumptions as practicably is re-emphasized when optical tweezers probe mechanical and dynamic features close to or even inside cells [Sun et al., 2010, Fischer et al., 2010]. These improved calibration protocols usually

involve active driving that might disturb the system. An assumption-free quantification of noise in active calibration assays is therfore desireable.

2.2 Another Scope

In general, the two aspects described above are aiming to improve resolution either in time (faster visual detection schemes) or in space (calibration protocols). Another aspect of optical tweezing is the actual tweezed handle. Colloidal quantum dots are semiconducting crystals with sizes ranging from 6–80 nm. They are bright and photostable with a broad excitation spectrum and a narrow emission spectrum [Michalet et al., 2005]. Because of the high quantum yield and low bleaching, quantum dots have a broad range of applications with respect to the investigation of biological systems. They can be considered as a class of unconventional handles that can be trapped and manipulated by optical tweezers. In addition to the small size of quantum dots, tuned settings enable infrared lasers to be a light source for two-photon excitation and for optical tweezers at the same time [Jauffred and Oddershede, 2010]. This is just one example of how an innovative combination of different tools can lead to better experimental setups.

In principle, single-molecule techniques also combine tools from various disciplines to achieve experimental conditions that reveal the dynamics of a particular molecule of interest. The underlying ideas and dogmas for the usage of single-molecule techniques are nicely captured by [Walter et al., 2008]:

> Single-molecule approaches:
>
> (i) reveal heterogeneity and disorder in a sample, albeit in a finite observation window
>
> (ii) afford precise localization and counting of molecules in spatially distributed samples such as a living cell
>
> (iv) enable the quantitative measurement of kinetics or statistics of complex biological processes
>
> (v) reveal rare and/or transient species along a reaction pathway
>
> (vi) enable the ultimate miniaturization and multiplexing of biological assays
>
> (vii) facilitate the direct quantitative measurement of mechanical properties of single biopolymers and their assemblies
>
> (viii) provide a way to 'just look at the thing', as one can argue that seeing single-molecule behavior is believing.

A central dogma therein is the *ergodicity hypothesis*: sufficiently long time averages or a sufficient number of observations of a single molecule are equivalent to the behavior of the entire ensemble [Walter et al., 2008, Schwabl, 2004]. So, if the ergodicity hypothesis holds, all information of an ensemble can be observed following a

single molecule only. Nonetheless, for DNA assays that investigate binding proteins or molecular motors often a huge heterogenity is observed. In a few cases this is also true for the visualization of individual molecules by fluorescent tags. The following references are in strong favor to accept this behavior as intrinsic to the observed complex itself [Blanco and Walter, 2010, Ditzler et al., 2007, Davenport et al., 2000, Wen et al., 2008, Eid et al., 2009]. Opposing this statement, conditional changes like confinement, competing binding partners, or local charge gradients in single-molecule assays alter the systems' behavior. Therefore, these single-molecule observations only reflect biological process under those very conditions. References that rather argue along this path are [Fodeke and Minton, 2010, Tsao et al., 2010, Minton, 2005].

2.3 Complementary Techniques

Every single-molecule approach is only as strong as the complementary techniques that are probing the same system. Relevant research topics often draw a lot of attention from different disciplines. The enzyme topoisomerase IB is part of a complicated network which regulates the topological state of a DNA molecule. It is a good example of how single-molecule magnetic tweezers experiments, molecular dyamics simulations, biochemical assays, structures from nuclear magnetic resonance spectroscopy and many more approaches form a very comprehensive picture of our knowledge about this system [Koster et al., 2007, Pommier, 2009, Koster et al., 2008].

For a broad aim such as the characterization of the interactions of potentially toxic nanoparticles with biological matter (section 9), various different approaches are essential to gain and contribute to an understanding of the underlying mechanisms. It is absolutely crucial to work across disciplines and to approach important research topics by joined efforts. When challenging and improving very specific steps along this path, this thesis attempts to add a share to the emerging fields of biophysics, optics, bio- and nanotechnology, and toxicology.

3 Thesis Objectives

This thesis outlines the, mostly experimental, work I performed during my three years as a PhD student in the Optical Tweezers Group at the Niels Bohr Institute, University of Copenhagen. I participated in the group activities to push the limits of optical tweezers research with a focus on the instrumental as well as on the experimental-analytical side. This led to the five peer-reviewed publications and the three proceedings that form the basis of this thesis.

The main objective of this thesis is to put those publications into a common context. Furthermore, the thesis supplies more motivational and basic thoughts for each of publications, and clarifies the links between them. It also contains more experimental details and yet unpublished results. Finally, it provides a distinct perspective with respect to the new methods and on future experiments.

The groups of sections embed the specific objectives of the thesis. I worked a lot on the optimization of experimental conditions, with centers of interest on protocols for calibrations, hard- and software aspects of optical tweezers instrumentation, and the implementation of a real-time tracking system for visual sampling beyond 10 kHz (sections 4 and 5). Already interlinked with those but more specific with respect to the Allan variance method, sections 6, 7 and 8 describe our efforts in pioneering an idea of low frequency noise analysis for single-molecule techniques. Allan variance analysis is more thoroughly introduced than possible in journal publications. Starting out from mathematically very general descriptions, the method's specific usage and implications for optical tweezers assays and other single-molecule are outlined and reviewed. All these efforts accumulated in the adaptation of optical tweezers assays as a diagnostic tool for research that is lacking proper standardization. Therefore, in section 9, I give an overview of our efforts to use complementary single-molecule techniques to take on the challenges of modern toxicology. This should also serve the purpose to discuss the potential of bottom-up single-molecule approaches for a detailed understanding of the mechanisms that may cause carbon nanoparticles to be harmful for biological organisms. We utilized fullerenes and fullerols as model systems for carbon nanoparticles.

Within the sections, the reader may find references to equations, figures, and other sections or subsections. Equations and figures are numbered continuously throughout the thesis which articulates the intertwined relation of the various sections. The duty of teaching students in form of exercises, courses and seminars during my period as a PhD student, easily turned into a very educational experience for myself as well. I must have learnt at least as much from the students than they could potentially have learnt from me. On that account, I am eager to provide an educational tone to the thesis, pointing out derivations and assumptions clearly, and being as transparent and open-minded as possible in my scientific writing.

Optical Tweezers: Calibration, Implementation, and Usage

Firstly, we introduce a minimal setup of optical tweezers. In section 4, this is used to exemplify calibrations and measurements of positions and forces. An overview of an active and a passive calibration protocol is given. Furthermore, we introduce an optimized calibration protocol that has been developed in the course of this thesis. Briefly, simulations for typical optical tweezers experiments are explained for further usage.

Section 5 explains experimental improvements that we implemented with respect to the minimal setup described before. They have been made on three different setups. This includes idea, implementation and discussion of the additional features. Emphasize is put on software implementation and on the limitations that experiments are exposed to.

Optical tweezers as a tool themselves are fascinating. The momentum transfer of a laser beam exerts forces on a micronsized object. The forces will trap the object stably in three dimensions if the object's refractive index is larger than the one of the surrounding medium and the laser beam is Gaussian shaped and focused in three dimensions. Parameters like laser power, beam shape, etc., need to be carefully controlled. For most biophysical applications of optical tweezers, it is advisable to minimize the effect of local heating as the power flux at the focal point can easily reach up to $1\,\mathrm{W}/\mu\mathrm{m}^2$. Because experiments are performed in measurement chambers filled with aqueous solutions, the absorption of light by water must be kept to a minimum. This is the case for infrared light at the wavelength of $\lambda = 1064\,\mathrm{nm}$ that all three optical-tweezers setups displayed in this thesis are built upon.

In the minimal setup shown in Fig. 1 the optical trap is static with respect to the microscope. The position of the measurement chamber though is carefully controlled by a piezo-electric stage with nominal precision of 0.1 nm. The trap forms at the focal point of an objective with high numerical aperture. Small adjustments of the trap position in the direction of beam propagation are done by a telescope (not shown in Fig. 1). The forward scattered light is collected onto a photodiode. The amplified output of the diode can be converted into the position of the trapped object. Custom written LabVIEW programs handle data acquisition and processing. A camera is used to retain visual information. Microscope and optical compartments are based on an air-suspended table.

This minimal setup has been implemented in a number of laboratories worldwide [Hansen et al., 2005, Bormuth et al., 2008, Lang et al., 2002, Keen et al., 2007]. Es-

pecially for the implementation and integration of novel technical components, it provides a very good reference to previous systems. Good examples are, for instance, the compensation of spherical abberations [Reihani and Oddershede, 2007], the implementation of a force feedback [Visscher and Block, 1998], applying torque on trapped objects [Rodriguez-Otazo et al., 2009], and the development of alternative detection schemes [Curran et al., 2010].

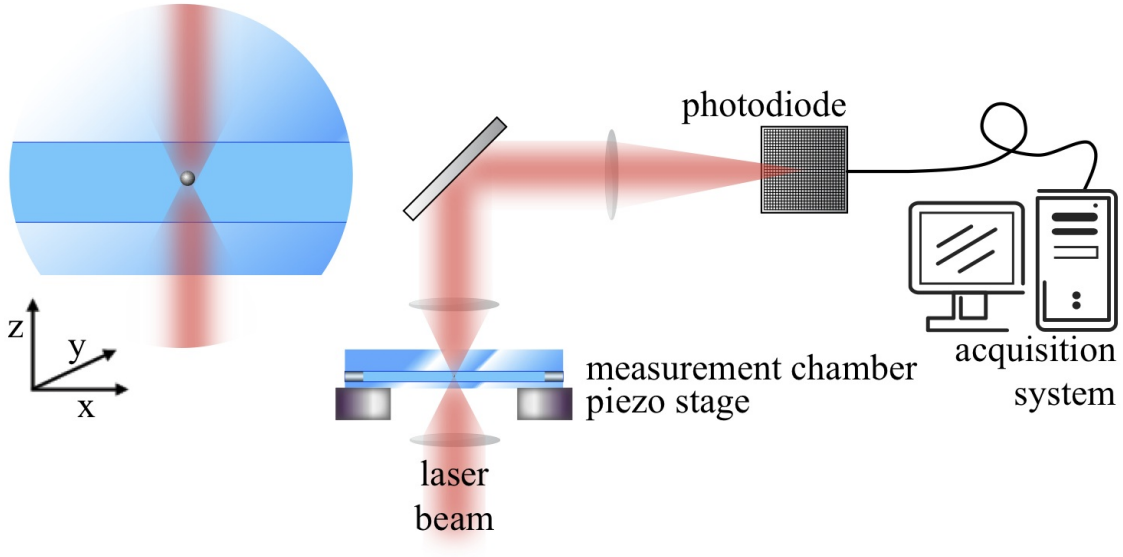

Figure 1: Schematic drawing of a minimal single laser beam optical tweezers [Czerwinski et al., 2009a]. An infrared laser beam is focused into a sealed measurement chamber. The chamber is mounted on a piezo stage. An object is trapped in the middle of the chamber which is filled with aqueous solution. The forward scattered light is collected onto a photodiode. The positional signal (x, y, z) of the object inside the trap is processed by an acquisition system.

Although this minimal setup has only a few user-controlled degrees of freedom, it provides very good stability and acceptable coupling efficiencies of about 10–20 % of the initial laser power. Even though being very minimalistic, still all ambient and setup-associated compartments can induce noise contributions to an experiment. These noise sources cover a wide range from water molecules bombarding the trapped object to acoustics present in the laboratory. A more detailed discussion is given in sections 6, 7 and 8. Noise sets the absolute, stochastic, and statistcal limitations to experiments. Theoretical treatment is possible in some cases, and can even be employed to calibrate the potential of the optical trap (section 4). In the vast majority of cases though, in particular for noise at low and very-low frequencies, a purely empirical quantification is the only way to challenge unwanted noise contributions.

4 Optical Tweezers Calibration (Theoretical) Framework

In a minimal optical tweezers setup (Fig. 1) the position of a trapped object is acquired as an output signal of a photodiode, typically in measures of volts. To convert this signal into positions in meters and to characterize the confinement the trap creates, one needs to calibrate the system. Here, we solve the equation of motion for an object in a confining potential. Then the harmonic assumption is made to derive fitting functions for calibration protocols. That and further assumptions are discussed for their validity.

Equation of Motion An object (mass m, acceleration $\ddot{x}$, friction coefficient γ, velocity $\dot{x}$) moves through a viscous medium. The collisions with smaller particles result in a stochastic force F_ξ on the object [Ming and Uhlenbeck, 1945]. The autocorrelation time τ_c can be seen as the average time an object can 'remember' its position. We assume that the average of the stochastic force vanishes for integration times $\tau > \tau_c$:

$$\langle F_\xi(t) \rangle_{\tau > \tau_c} = 0 \,. \tag{1}$$

The object interacts only in a narrow time window, so the autocorrelation function Φ is only notable for $\tau \leq t_1 - t_2 \leq \tau_c$:

$$\langle F_\xi(t_1) F_\xi(t_2) \rangle_\tau = \Phi_\tau (t_1 - t_2) \,. \tag{2}$$

Superimposed to the stochastic motion, the object can move in an external potential V. Using the deterministic force field $F_{\text{ext}} = -\nabla V$, the equation of motion becomes

$$m\ddot{x}(t) + \gamma \dot{x}(t) + \nabla V|_{x(t)} = F_\xi(t) \,. \tag{3}$$

It is a Langevin equation because of the purely stochastic nature of F_ξ.

In orthogonal coordinates the motions of an object in different dimensions are decoupled, i.e., the covariance matrices $\text{cov}(x, y) = \text{cov}(y, z) = \text{cov}(z, x) = 0$, Eq. (3) correspondingly holds for all three coordinates.

There are also three rotational degrees of freedom. These can be superimposed to Eq. (3) to deduct a *complete* equation of motion [Volpe and Petrov, 2006]:

$$m\ddot{\mathbf{x}}(t) + \left(\gamma \frac{\mathbf{x}(t)}{|\mathbf{x}(t)|} \times \dot{\mathbf{x}}(t) \right) + \nabla V|_{\mathbf{x}(t)} + \nabla_\rho \frac{1}{|\mathbf{x}(t)|} \Gamma|_{\mathbf{x}(t)} = F_{\xi,\rho}(t) \,. \tag{4}$$

For a spherical object with homogeneous optical density, we assume the torque Γ to be much smaller than the translational forces, and further expecting most of the thermal energy $k_B T = 4.1\,\text{pN nm}$ resulting in a translational stochastic force. Hence, we simplify again to the vectorial analog of Eq. (3):

$$m\ddot{\mathbf{x}}(t) + \gamma \dot{\mathbf{x}}(t) + \nabla V|_{\mathbf{x}(t)} = F_\xi(t) \,. \tag{5}$$

In the regime of low Reynolds numbers $m\ddot{\mathbf{x}} = 0$, i.e., the inert term can be neglected [Purcell, 1977, Berg-Sørensen and Flyvbjerg, 2004]. We assume the confinement by an external potential V to be harmonic $V = kx^2 + \text{const.}$, and the stochastic force for Gaussian distributed white noise to be [Ming and Uhlenbeck, 1945]:

$$F_\xi(t) = \sqrt{2\gamma k_\mathrm{B} T}\ \xi(t)\,. \tag{6}$$

These assumptions simplify Eq. (3) immensely:

$$\gamma\dot{x}(t) + kx(t) = \sqrt{2\gamma k_\mathrm{B} T}\ \xi(t)\,. \tag{7}$$

Before describing the exact procedure and handling to calibrate optical tweezers alongside Eq. (7) in the following subsections 4.1 and 4.2, we briefly want to comment on the assumptions made so far.

The assumptions made to arrive at Eq. (4) are only the choise of an orthogonal set of eigenvectors as coordinate system. In all physically relevant cases, this can be achieved [Korsch, 2002]. However, in an experiment it is essential to minimize the crosstalk between channels as this might result in incorrect recording. Good calibration procedures account for this problem [Hansen et al., 2006]. The assumptions that estimate the actual amplitude of the stochastic force (Eq. (6)) has been experimentally validated. A self-consistent tool for this purpose is described in [Bernacchia and Pigolotti, 2009]. Neglecting the rotational degrees of freedom, and thus implying that the torque does not influence the measurement, is the weakest assumption made so far. The heterogeneity of the material as well as the spherical shape should not always be taken for granted. In fact, more and more publications have addressed the incidental and intentional steering of optically trapped objects in recent years [Valentine et al., 2008, Deufel et al., 2007].

4.1 Passive and Active Calibration

Calibrating optical tweezers has been a debated issue. In principle, one could simply monitor the fluctuations of a trapped object in real space, assume those objects to be spherical and the potential to be harmonic. Fitting the observed histogram with a Gaussian and compare the outcome with the analytical handling of Brownian motion would lead to a calibration. Still, the assumptions put strong restrictions to the actual measurement. For instance, hydrodynamic interactions with nearby surfaces, aspherical object shapes, and thermal drift, all these effect would not be accounted for. Although for very precise measurements they are not accurate enough, simple real space or phase shift calibration, and constant-flow Stokes drag calibration are easily implemented, and certainly valid in some experimental ranges, see for example [Richardson et al., 2008, Hanes et al., 2009, Otto et al., 2011]. However, they will not be discussed in this thesis.

There is an ongoing development of precise calibration protocols for optical tweezers. Mostly, newly proposed methods finetune previous ones, adapt to certain experimental conditions, or reduce the number of assumptions. Essentially, there

are passive and active methods. We speak about passive calibration when the thermal force F_ξ is the only driving force the trapped object experiences. Thermally driven away from the optical axis, the object experiences a restoring gradient force [Oddershede, 2009]. For active calibrations, there are usually active signals put into the systems with the aim to replace assumptions, e.g., of the width of the thermal fluctuations by active parameters that can be monitored [Neuman and Block, 2004, Tolic-Nørrelykke et al., 2006]. The motion of the object is then a superposition of the active driving and the thermal motion.

Still, in any case a calibration measurement is simply a long time series of the visited positions of the trapped object. The acquisition frequency must be large enough to monitor the objects positions at the thermal limit. A rigorous treatment of the thermal limit argument is given in section 6. If this criterion is not met, there are alternative considerations [Wong and Halvorsen, 2006]. However, these do not overcome the limitation of seriously improper signal analysis when, e.g., transformed to frequency space. A rule of thumb should be an order of magnitude oversampling with respect to the object's thermal limitations.

Using a Fourier transform, the acquired time series is transformed into a power spectral density (PSD) in frequency space [Berg-Sørensen and Flyvbjerg, 2004]. For Eq. (7), the PSD reveals the Lorentzian profile for the frequency spectrum of an object in a harmonic potential:

$$S(f) = \frac{\beta^2 k_\mathrm{B} T}{\gamma \pi^2 (f_\mathrm{c}^2 + f^2)} \tag{8}$$

with the conversion factor $\beta^2 = D_{[m]}/D_{[V]}$ [Berg-Sørensen and Flyvbjerg, 2004].

When an active sinusoidal driving $x_\mathrm{driving}(t) = A \sin(f_\mathrm{driving} t)$ of the piezo stage is superimposed to the Brownian fluctuations, Eq. (7) becomes:

$$\gamma \left(\dot{x}(t) - \dot{x}_\mathrm{driving}(t) \right) + kx(t) = F_\xi(t) \ . \tag{9}$$

The PSD evolves to [Fischer and Berg-Sørensen, 2007]:

$$P(f) = S(f) + P_\mathrm{response}(f) \xrightarrow[t_\mathrm{acq} \to \infty]{} \frac{\beta^2 k_\mathrm{B} T}{\gamma \pi^2 (f_\mathrm{c}^2 + f^2)} + \left(\frac{A}{2} \right)^2 \frac{f_\mathrm{drive}^2 \delta(f - f_\mathrm{drive})}{\pi^2 (f_\mathrm{drive}^2 - f^2)} \ . \tag{10}$$

The second term in Eq. (10) is nonzero for $f \to f_\mathrm{drive}$. The height of the peak at f_drive in the PSD is independent of phase differences of the actual driving and the response of the object.

For simulated active and passive time series of 20 consecutive intervals the averaged power spectral densities are plotted in Fig. 2. The Lorentzian fit (Eq. (8) and filter corrections [Berg-Sørensen and Flyvbjerg, 2004]) are also shown.

The Lorentzian fit yields the corner frequency f_c that marks the transition of the non-confined high frequency spectrum and the confined low frequency spectrum. It

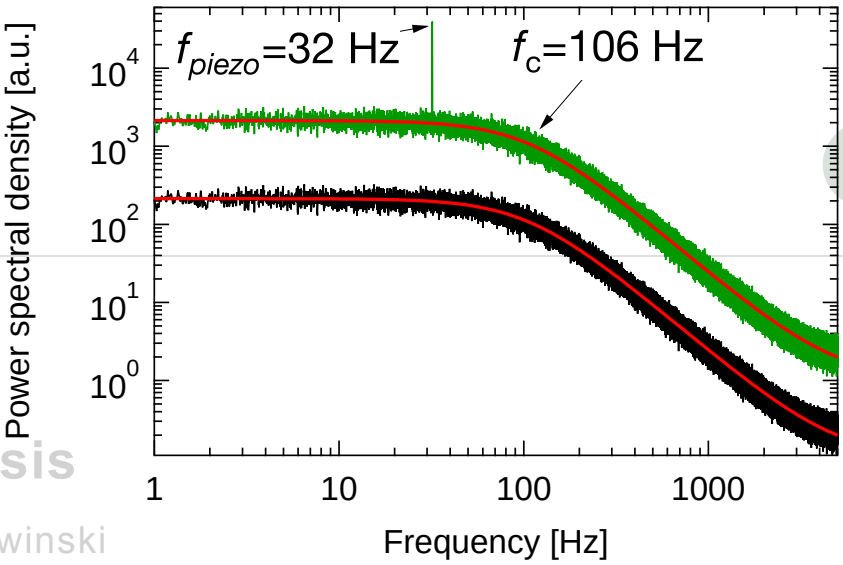

Figure 2: Power spectral density of simulations of a passive (black) and an active (green) calibration measurement. The Lorentzian fit (red) accounts for filtering effects.

is inversely proportional to the characteristic time τ_c, and so inversely proportional to the drag coefficient γ and proportional to the harmonic trap stiffness k:

$$f_c = \frac{1}{2\pi\tau_c} = \frac{k}{2\pi\gamma} \,. \tag{11}$$

Equation (10) allows for measurements of f_c and γ in distinct frequency bands. β is either known as in camera schemes due to a priori calibration, e.g., using measure grids, or must be determined in a passive real space measurement in advance. Hence, one passive measurement is necessary. Integrating Eq. (8) gives [Bronstein et al., 2001, p. 1053]:

$$\int S(f) = \frac{\beta^2 k_B T}{\gamma\pi^2} \int \frac{df}{f_c^2 + f^2} = \frac{\beta^2 k_B T}{\gamma\pi^2} \frac{1}{f_c} \arctan\frac{f}{f_c} + \text{const.} \,. \tag{12}$$

The arctangent arctan $\frac{f}{f_c}$ provides a 'three line fit' that is considerably more accurate than a 'two line fit' by Eq. (8).

4.2 Optimized Calibration Protocol

The calibration protocols discussed in section 4.1 are the most prominent and powerful ones. These protocols allow for a precise calibration with uncertainties as small

as 3 %. However, all of them have to make an assumptions about the sampling frequency f_{acq}, sampling time t_{acq}, and optimal measurement time τ_{opt} that is used for an individual calibration.

Typically, power spectrum analysis is used to test the high frequency band, accounting for effects like aliasing, etc., and to calibrate an object inside the harmonic potential [Gittes and Schmidt, 1998]. This approach in frequency space re-assembles a standard variance analysis in real space. In comparison, Allan variance analysis probes the deviation of directly neighbored intervals, and calculates half the squared mean. The (positional) deviation of the setup becomes a function of the measurement time. Because of the convergence of Allan variance for purely stochastic fluctuations, it is possible to make an assumption-free analysis about the absolutely smallest deviation of the system which is achieved at the optimal measurement time for an individual calibration. A very detailed introduction, verification and discussion of Allan variance analysis is provided in sections 6, 7, and 8, and with a focus on acquisition parameters in subsection 7.1. Since we have been extensively using this approach, we have also suggested an optimized calibration protocol that was used throughout this thesis [Czerwinski et al., 2011].

Optimized protocol for calibration of optical tweezers setups We suggest an optimized protocol for optical trapping calibration which also includes the advantages of Allan variance analysis. It includes six steps.

1. Acquire data of positional output in a passive calibration experiment for long time series (in the order of minutes) with a sufficiently high acquisition frequency (typically larger than 10 kHz).

2. Calculate Allan variance of adjacent time series for a set of measurement times.

3. Determine the optimal measurement time where the Allan deviation is minimal. Use this optimal measurement time for all individual calibrations.

4. Calibrate over statistically independent measurement intervals of length of the optimal measurement time using the power spectral density method.

5. If desirable, use an active calibration method in the same manner. This is particularly useful if, for instance, the drag on the trapped object, the viscosity, or the shape are unknown.

6. Average the fitting parameters (corner frequency f_c and conversion factor β) of consecutive, statistically independent intervals.

The sampling frequency has to be set in advance, but oversampling is not a problem at all, so it is advisable to use the maximal detector bandwidth. A smaller rate might be chosen to save disk space. The sampling should be stored in one long time series, since the determination of the optimal calibration time happens posterior to the acquisition. Here, we determine the optimal calibration time as the measurement

interval with the (absolute) minimum of the Allan deviation (section 6). Other ways of determining the optimal calibration time have been suggested, such as the shortest measurement time that significantly deviates from the thermal limit. One might leave pauses in between statistically independent intervals of twice the correlation time, to ensure statistical independence. For stable setups, active calibration can be done with the same accuracy as passive calibration [Czerwinski et al., 2011]. This protocol is not limited to optically trapped spherical particles, but is applicable to any kind of object in the optical trap. For example, we demonstrated its usage on gold nanorods [Czerwinski et al., 2009b].

4.3 Monte-Carlo Simulations

To compare the experimentally measured time series to values expected for systems that are not exposed to drift, we programmed a Monte-Carlo simulation in Matlab (Mathworks, Natick)[Czerwinski, 2009].

Basically, it was a straight-forward coding exercise from [Lemons, 2002, p. 46]. Therein, the author gives a step-by-step elaboration of a Monte Carlo simulation of a Brownian object. The output of the simulation was a time series of a micron-sized sphere in an optical trap in meters. This was generated by drawing random numbers from a Gaussian distribution. Those numbers are scaled to the step size for the time interval over which numbers are drawn. Of course, the autocorrelation for intervals smaller than τ_c was taken into account. The cumulative sum was the actual time series. It was assumed, that the object was spherical, and therefore, the drag coefficient was given by the Stoke's equation:

$$\gamma = 6\pi\eta r \ , \tag{13}$$

with the sphere's radius r and the viscosity of the surrounding medium η that was chosen to be the one of water $\eta = 8.9 \cdot 10^{-4}$ sPa which was the second assumption. The quality of the Gaussian distribution was checked using a self-consistent method for density estimation [Bernacchia and Pigolotti, 2009]. The nearest spacing of neighboring numbers in the Gaussian distribution was $2.22 \cdot 10^{-16}$. The radius of the sphere r, the corner frequency f_c, the acquisition frequency f_{acq}, and the number of sampled points could be varied. Adjacent time series gained by simulations were treated as regular data and compared to experimental results. A typical simulated time series consisted of 2^{23} individual data points.

5 Implementation: Setup, Hardware and Software

This section provides a detailed description of all three optical tweezers setups used in the course of this thesis. Two tables sum up the technical specifications and the publications these setups contributed to. We developed a CMOS camera detection scheme that reached long-term stability for hours at acquisition rates of tens of kHz. Hardware and software implementation are described and compared to photodiode

detection and CCD camera recording. Fast real-time analysis comes with a need of new software design that we explain here.

5.1 Optical Tweezers Setups

The experimental work presented in this thesis was measured on three different optical tweezers setups. Table 1 provides a listing of these setups that contributed measurements to the appended publications. The technical specifications of the key features are summarized in Table 2.

The three setups are in principle all just extended versions of a core that we referred to as *minimal setup* (Fig. 1).

	NBItweezers1	NBItweezers2	CambridgeTrap
[Czerwinski et al., 2009a]	x		
[Czerwinski et al., 2009b]	x		
[Jauffred et al., 2010]		x	
[Otto et al., 2011]			x
[Czerwinski and Oddershede, 2010]	x	x	x
[Czerwinski et al., 2011]	x	x	
[Otto et al., 2010]		x	x
[Czerwinski and Otto, 2010]	x		x

Table 1: Three optical tweezers setups contributed measurements to the appended publications.

Lasers Trapping lasers are the core of every optical tweezers setup. Their stability, coherence and beam profile are essential. These parameters were supplied by the manufacturers and were tested prior to installation. Fluctuations or alterations are strong indicators for weakened laser systems. The output power of the laser systems used ranged from 50 mW to 1 W, respectively 10 W. Regular use never exceeded 3 W though. The typical life time of laser is about 5–10 yrs.

The laser units are usually fixed in their position. Their coupling into the microscope is controlled by two-mirrors gating, or by adjustment of the optical fiber output. The exact height of the infrared focal point with respect to the visual focal point of the objective can be adjusted by a telescope in the infrared path. This telescope is formed by two lenses.

Objectives To actually form a single-beam optical trap the laser beam must be focused with an high numerical aperture (NA) objective into the sample. Only

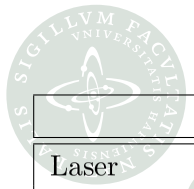

	NBItweezers1	**NBItweezers2**	**CambridgeTrap**
Laser	Spectra Physics Millennia Nd:YVO_4	Spectra Physics J20I-BL-106C Nd:YVO_4	IPG Laser YLM-5-LP Ytterbium
Wavelength	1064 nm		
Microscope	Leica DMRIBE	Leica DMI 6000 B	custom-built
Objectives	Leica, water, HCX 63x NA=1.2 Leica, oil, HCX PL APO 100x NA=1.4		Olympus, water, UPlanSApo/IR 60x NA=1.2
Coupling efficiency	20 %	18 %	12 %
Illumination	120 W halogen lamp, Köhler	excitation lasers (HeNe 594 nm, 633 nm Ar 458 nm, 476 nm, 488 nm, 496 nm, 514 nm)	100 W mercury lamp, Köhler, fiber (NA=0.39) detection laser (634 nm)
Detection	Hamamatsu S5981 Si-PIN QPD, Pacific Silicon Sensor DL100-7PCBA3 PSD, Allied Vision Technologies Pike-100B CCD, Andor Ixon cooled electron-multiplying CCD		custom-built J129 QPD, Mikrotron MC1362 CMOS, Imagingsource DMK31AF03 CCD
Trapped objects	polystyrene spheres (diameters ranging from 500 nm – 5 μm) gold nanorods, gold and silver nanoparticles	quantum dots	
National Instruments hardware	PCI-M6251, PCI-GPIB	PCI-6040E, PCI-GPIB	PCIe-1429, PCI-6521, PCI-GPIB
piezo stage	P-517.2	P-517.3i	P-517.3
Microfluidics	custom-made low volume flow chambers,[a] Havard Apparatus PicoPlus 11 syringe pump		PMMA block, PDMS spacer

Table 2: Technical specifications of the three optical tweezers setups used for measurements presented in this thesis.

[a]Detailed description provided in subsection 5.1.

immersion media allow for objectives with sufficiently high NA. There is a conceptual difference between so called water immersion and oil immersion objectives. Whereas water immersion media, i.e., simply water or oil with a refractive index of water, match the refractive index of the aqueous medium inside the measurement chamber, oil immersion media match the refractive index of the glass coverslide. Therefore, the objectives also follow different principal designs: prior to experiments, one matches the tube length of the water immersion objectives to the anticipated thickness of the glass slide by tuning the collar. This task is tricky, as the glass coverslides come slightly non-uniform in their thickness which severely effects the measured trap stiffness [Reihani et al., 2010]. For oil immersion objectives, the NA is directly controlled by an adjustable aperture. Again, this adjustment is essential as it defines the achievable trapping strength. Changing the immersion oil to NA$\approx$ 1.54 for infrared laser beams compensates spherical aberrations that eventually destabilize the optical trap [Reihani and Oddershede, 2007].

The choice of one objective type or the other depends on the actual design of the experiment. When particularly strong traps with less laser power are needed and trapping is supposed to be done about 10–20 μm into the sample, oil immersion objectives are the better choice. The option to compensate and to tune the trapping location close to the surface is important, too. On the other hand, water immersion objectives have a trapping location that ranges through entire measurement chambers of thickness up to 220 μm. That is simply perfect for experiments performed in the center of the chamber. For DNA-pulling assays that involve one of the handles to be positioned at the tip of a glass capillary (section 9), water immersion objectives are the better and more flexible choice. At the same time, roughly 3–5 times as much power must be used to achieve trap stiffnesses of the same strength as in the case of oil immersion objectives [Reihani and Oddershede, 2007, Reihani et al., 2010].

Microscope, Optical Table, Piezo Stages and Temperature All three setups were located on optical tables that could be actively damped by air.

Both setups at the Niels Bohr Institute are built into a microscope, whereas the CambridgeTrap was custom built from the bottom up. Building a custom setup could be inspired by the idea of minimized drift because of the minimized number of components. The advantages of a design embedded into a microscope are the plug-and-play alignment of additional filters, and the stability of the microscope core.

Measurement chambers were mounted on a piezo stage (P-517.3CL, Physics Instrument) operated in closed loop (see subsection 7.2). The nanopositioning piezo stages allowed multi-axis motion with a resolution of 1 nm, a nominal accuracy of 0.1 nm, and a range of 100 μm in the x- and y-directions and 20 μm in the z-direction. For active calibration measurements the piezo stage was driven in a sinusoidal motion, typically with driving frequencies up to 128 Hz and peak-to-peak distances of up to 300 nm.

All experiments described here were carried out at room temperature. The laboratories were in the basement of the Niels Bohr Institute or at the ground floor of the

Physics of Medicine Building at the Cavendish Laboratories. Both labs were temperature controlled, but the ambient temperature might have fluctuated by $\pm 1\,\mathrm{K}$. During explicit experiments, the temperature was recorded.

Microfluidics In optical tweezers applications, a lot of the experiments are performed in simple custom-made measurement chambers. By melting single or double layers of parafilm between two glass slides, chambers of just a few tens of microliters are built. Double-sticky tape seals just as good and thus provides the quickest way to produce chambers. Sealing by vacuum grease or by nail polish avoids evaporation at the outlets of the chambers.

However, for more elaborated experiments, it is desirable to be able to exchange the medium inside the measurement chamber (see section 9). For that purpose we developed a slightly advanced design of our chambers. Metallic long syringe needles of $120\,\mu\mathrm{m}$ outer diameter are embedded into a double layer of parafilm whilst heating to $80\,^{\circ}\mathrm{C}$, i.e., fluid phase. Connected to a syringe mounted on a LabVIEW-controlled pump with flow rates down to $100\,\mathrm{nL/min}$, this design allowed for very gentle media replacement. We placed the pump just next to the setup, so there was no additional flange, etc., needed. In this way, we replaced the medium in flow chambers of $20\,\mu\mathrm{L}$ volume in times ranging from 30 s to 30 min. For high flow rates the lag time of flow rate changes was at most 10 s, as measured by the displacement of polystyrene sphere inside the optical trap that was positioned in the middle of the chamber.

Handles Trapping an object makes this object a handle in the tweezing light beam. There are a number of concerns that should be kept in mind during experiments. For instance, the experienced drag of a handle in the proximity of a surface increases due to additional confinement. When handles are polarizable like metallic particles, the polarizability dominates the forces on the handle. There are many more of these kind of effects, some of which solutions have been developed for. The diversity of handles inside a sample should be kept to a minimum, otherwise the results tend not to be comparable. What sounds like a triviality here, turns out to be quite substantial when working with polystyrene spheres whose diameters vary by 10 % within one batch.

Illumination and Detection Every detection system needs illumination of some sort. In the case of the minimal setup, the forward scattered light of the actual trapping laser forms an image of the trapped object in the back focal plain. Photodiodes are very, very fast (up to MHz) and sufficient to map out the object's positions as actual voltage signals. The two most prominent designs for photodiodes are quadrant photodiodes (QPD) and position-sensitive diodes. In general, a QPD provides a finer resolution, whereas a position-sensitive diode has a wider linear regime, i.e., the displacement of the object from the center of the trap will be recorded still correctly even for large displacements [Huisstede et al., 2005]. Also, a position-sensitive diode shows slightly smaller noise than a QPD [Czerwinski et al., 2009a]. In any case it is essen-

tial to use optimized photodiodes for the detected wavelength to minimize filtering or electron-diffusive effects [Berg-Sørensen et al., 2003]. It is also possible to use the backward scattered laser light for detection [Huisstede et al., 2005, Otto et al., 2010], but in the case for polystyrene spheres, the amount of available photons is substantially smaller.

Instead of using the trapping laser to record positions, an additional detection laser could be installed [Otto et al., 2011, Otto et al., 2010]. It is focused through onto the object inside the trap by a separate telescope and usually an additional filter for the trapping wavelength in the detection path is installed.

To achieve visual detection with CMOS cameras at short shutter times, an external light source must be installed. For longer shutter times though, often the quantum yield of modern CCD cameras (Pike-100 B, Allied Vision Technologies), and CMOS cameras (MC1362, Mikrotron) is good enough to use scattered light [Otto et al., 2010].

For fiber illuminating, we integrated a mercury arc lamp (100 W, LSH102, LOT-Oriel) and an optical fiber (600 μm core diameter multimode silica fiber, Thorlabs) into a modular and powerful light source. It had some major advantages. The lamp housing was passively cooled, so it did not contribute any noise. With an arc size of only 250 μm the 100 W lamp produced very intense collimated illumination. The region of interest was illuminated in transmission mode with an effective distance between light source and the focal point of less than 2 mm. Light diffracted by an object in the region of interest was imaged onto a camera by a tube lens. In contrast to fiber illumination, light microscopes are usually equipped with a light source that is focused onto the sample by Köhler illumination through a well-aligned condensor lens.

5.2 Advantages and Implementation of CMOS Detection

Apart from trapping, detection is the other second crucial point in optical tweezers setups. CMOS cameras hold great potential for tracking, recording, and tracing of objects that are typical handles for experiments. Sub-pixel accuracy can be easily achieved. Position tracking in real time with very low error rates provides a memory-efficient way to make CMOS detection stable for long measurement times. Video recording can therefore be tuned to demand, e.g., by thresholds or distinct position patterns. All this can also easily be motivated by the dogma *seeing is believing*. CMOS detection also holds great potential for the tracking of multiple objects at a time [Czerwinski and Otto, 2010].

Either for experiments of purely passive rheology, or as active rheology, e.g., with optical tweezers as force inducer, the high bandwidth that CMOS cameras offer for pre-defined regions of interest exceeds the needs for most biophysical experiments. Care must be taken when setting up the CMOS detection scheme because not all software drivers allow for multiple regions of interest. Not just rheology techniques rely on high bandwidth detection, but also time-shared optical tweezers, or holographical optical tweezers would benefit from larger acquisition frequencies for long mea-

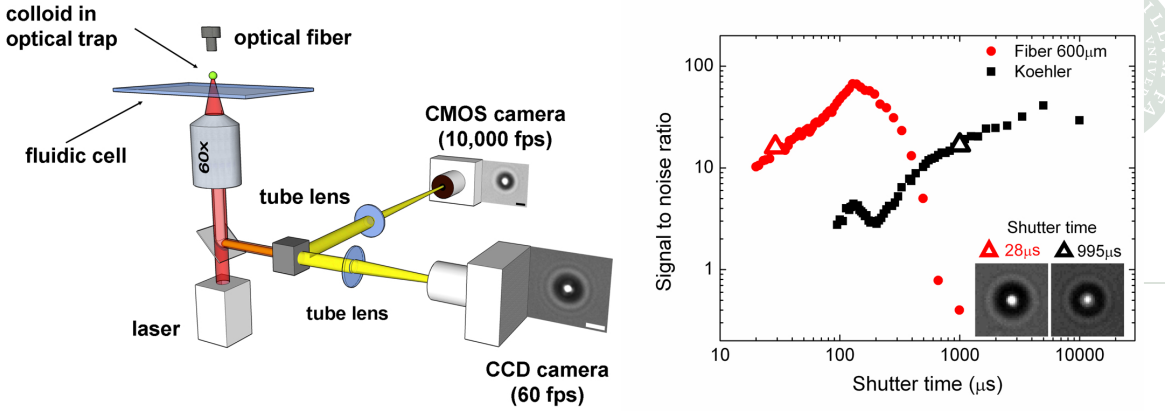

Figure 3: Schematic drawing of the optical tweezers setup with implemented fiber illumination [Otto et al., 2010]. A laser with wavelength 1064 nm is focused into a measurement chamber by a 60x water immersion objective. Collimated light of a mercury light arc lamp illuminates the region of interest through an optical fiber. A high-speed CMOS camera captures 10,000 fps and is used for position determination. A slower CCD with up to 300 fps is used to provide a full field of view. The length of the scale bars in the images of trapped polystyrene spheres are 2 μm.

surement times [Hanes et al., 2009, Curtis and Grier, 2003, Jesacher et al., 2008a]. Thinking one step ahead, the opportunity to create adapted optical energy landscapes to investigate, e.g., confined diffusive transport inside cells or through membranes, would also be assisted by a fast camera detection.

The development of the best possible CMOS cameras for scientific research has been recognized also by commercial manufactures.[1] With further advances in CMOS technology it will be straight forward to use the purely software-based algorithm that we have implemented to beat even results that we could achieve.

Recently, several groups have investigated and improved the speed and illumination techniques for tracking of single objects in optical tweezers. Gibson et al. demonstrated video-based position determination of polystyrene spheres in optical tweezers using a CMOS camera and standard desktop PC. They recorded particle positions at 1,000 fps in real-time and were limited by the brightness of their tungsten-halogen lamp and because they used the camera memory [Gibson et al., 2008]. Replacing the lamp by a 100 W halogen light source Keen et al. showed image acquisition at 2,000 fps, but, again, were restricted by the buffer size of their camera to measurement times of 4 s [Keen et al., 2007]. Van der Horst et al. increased the threshold in

[1] *The online home of Scientific CMOS technology* (`http://www.scmos.com/`) may be the most outspoken project of this kind at the moment. Three major manufacturers have joined forces here to develop a 'no compromise' solution.

video-based position determination to 2,500 fps but were ultimately limited by the light intensity [van der Horst and Forde, 2010]. Otto et al. carried out experiments on single polystyrene spheres in optical tweezers with a CMOS camera and a LabVIEW software environment [Otto et al., 2008]. The size of the pre-allocated memory limited the measurement time at acquisition frequencies larger than 5,000 fps. By combining a novel pixel sensor with data analysis based on field programmable gate array (FPGA) circuits Towrie et al. determined the position of 6 colloidal spheres simultaneously [Towrie et al., 2009]. Their system allowed for frame rates up to 15,000 fps but is ultimately restricted by the brightness of their standard light source. Biancaniello et al. overcame these limitations by introducing laser illumination into an optical tweezers setup allowing for video-based off-line position tracking with 10 kHz bandwidth [Biancaniello and Crocker, 2006]. Although lasers are the ultimate high brightness light source, the alignment of the optical setup is accompanied by effects like coherence and collimation.

We characterized and checked our optical tweezers with the new detection scheme by calibrating for different detection schemes and at varied acquisition frequencies. As an example, we trapped a polystyrene sphere with 3.27 μm diameter at different laser powers. The results are shown in Fig. 4. We used the calibration protocol described in subsection 4.2. In addition we performed Stokes drag calibration. These results can be found in Ref. [Otto et al., 2011, Fig. 5]. The trap stiffness linearly depended on the trap stiffness k, as expected. Figure 4 now shows the calibration results for the corner frequency f_c as a function of acquisition frequency or the temporal bandwidth respectively. For small acquisition frequencies $f_{acq} < 1,000$ fps blurring affects the calibration procedure. Accounting for this effect has been suggested [Halvorsen and Wong, 2010], but is only possible for large datasets. For more than 6,000 fps, the signal-to-noise ratio we achieved with Köhler illumination only was not sufficient anymore. With the improved fiber illumination, the position of the trapped polystyrene sphere could be tracked at up to 10 kHz for hours. In fact, for a single sphere we could achieve real-time tracking at sampling rates of 40 kHz, only interrupted by the Windows-operating system (subsection 5.3). The obtained values for f_c agreed with the ones obtained from QPD measurements within the error bars. Still, photodiodes provide the highest temporal resolution possible. So, they are the best choice when very fast position recording is necessary, for instance, to measure the non-conservative contribution of the force field of an optical tweezers [Huang et al., 2009].

The implementation that we describe here is only valid for tracking in the focal plane. Since the outcome of used cross-correlation algorithm (subsection 5.3) for fluctuations in in axial direction would respond quite non-linear [Dreyer et al., 2004], we only implemented a look-up table approach for axial position determination. These tend to be very slow and calculation-time intense. We are looking into more appropriate implementations at the moment.

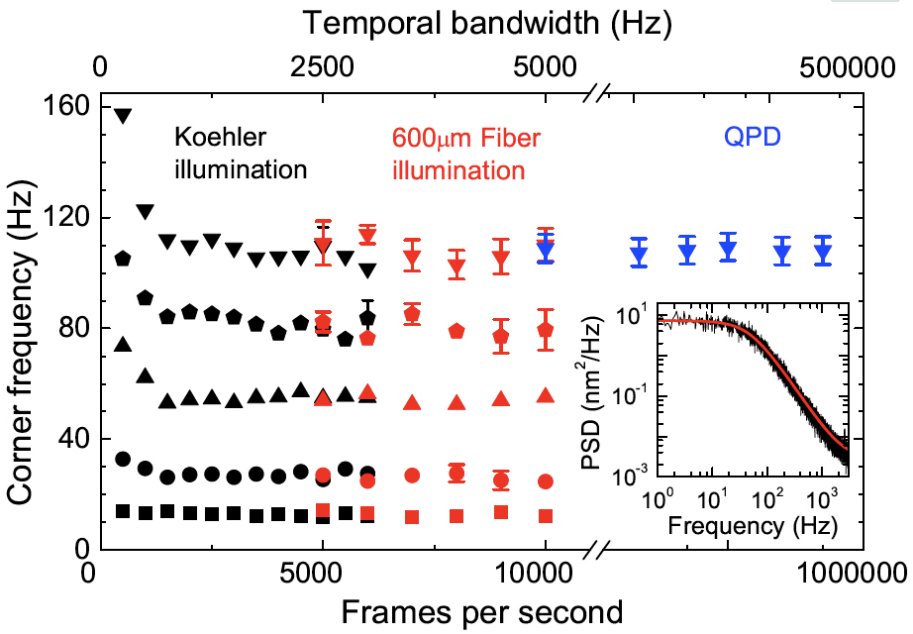

Figure 4: Calibration of optical tweezers at different acquisition frequencies [Otto et al., 2010]. Determination of corner frequencies was done at five different laser powers (bottom to top: 25 mW, 50 mW, 100 mW, 150 mW, and 200 mW). The results compare Köhler (black) and 600 μm fiber illumination respectively. At a separate setup an additional calibration with a quadrant photodiode (blue) was performed. Here, the laser power was adjusted to the CMOS-based measurement. The error is calculated from a series of calibration intervals and is given by the symbol size if not explicitly indicated. At set laser power, the corner frequency remains constant with increasing camera frame rate. The deviations at low frame rates are attributes to aliasing and blurring effects of the recording. The shutter time of the CMOS camera was 162 μs for Köhler and 95 μs for fiber illumination. The inset shows averaged Lorentzian fits to averaged power spectral densities of consecutive calibration intervals.

5.3 Tracking Algorithm and Software Implementation

We aim to perform video-based position tracking of particles at temporal bandwidths previously only accessible to photodiode detector systems or FPGA controlled cameras [Berg-Sørensen and Flyvbjerg, 2004, Towrie et al., 2009]. Therefore, our scheme must be capable of simultaneous high-speed image acquisition and position tracking, in real time. The CMOS camera used had a resolution of 1280 px×1024 px on a CMOS chip with 14 μm pixel size. Our image system had a resolution of 214 nm/pixel. By defining a region of interest of smaller sizes like 100 px × 100 px, image acquisition faster than a few thousands frames per second could be easily achieved. This left as limiting step the number of photons arriving within the shutter time. The smallest shutter times used in this study were 20 μs.

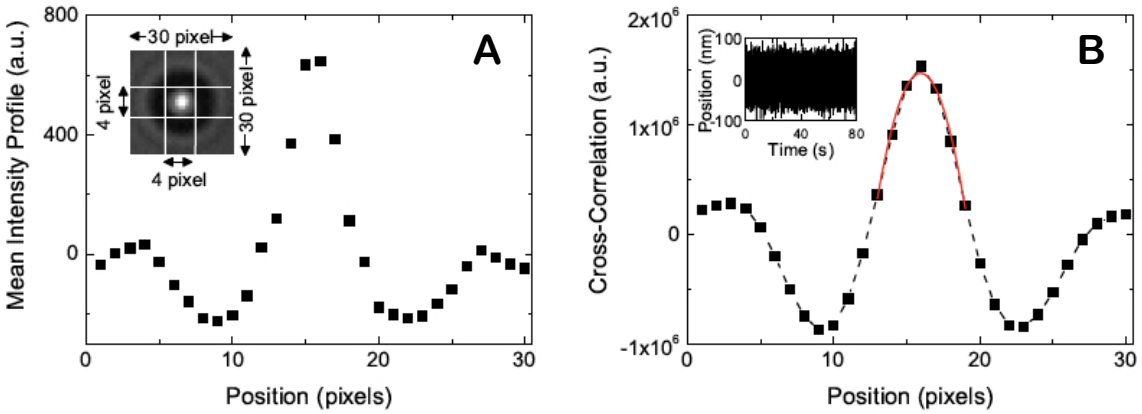

Figure 5: Implementation of the position tracking algorithm [Otto et al., 2010]. **A** The graph shows the mean intensity profile along a $4 \times 30\,\mathrm{px}^2$ rectangular array of the $30 \times 30\,\mathrm{px}^2$ region of interest (inset). The profile is calculated in x- and y-direction independently. **B** 1-dimensional cross-correlation transformation and a second order polynomial fit of seven pixels around the maximum. Time trace of tracked polystyrene sphere (inset).

Since the typical amplitude of the motion of an optically trapped object is of the order of tens of nanometers, position determination needs to be done for one or more objects with sub-pixel accuracy. Our position tracking algorithm uses cross-correlation analysis initially described in [Gosse and Croquette, 2002]. The initial position is user-defined within a sub-region of interest of, e.g., 30 px×30 px. The inset in Fig. 5 and in Ref. [Otto et al., 2011, Fig. 2a)], the CMOS image was plotted. For position calculation the transformation was performed independently in x- and y-direction. A rectangular array of pixels, $4\times30\,\mathrm{px}^2$ in size, passing through the center of the sub-ROI, is binned and then normalized to give the mean intensity profiles for the x- and y-axes. To obtain sub-pixel accuracy, the cross-correlation of the mean intensity distribution with its reverse was calculated by applying the convolution

theorem. A typical result is shown in the grey dashed line in Fig. 5 B. The peak in the cross-correlation is fit with a second-order polynomial using seven points around the maximum value to determine the particle position (red fit in Fig. 5 B). The inset in Fig. 5 B shows the positions of an optically trapped polystyrene sphere with diameter 3.27 μm for a 80 s time trace tracked at 10,000 fps in real time. The only really time consuming step was the Fourier transformation at the very beginning of the algorithm. Calculating the one-dimensional cross-correlation and the polynomial fit took less than 1 μs.

Following the strategy of a fully software implemented tracking algorithm leaves us 20 μs to perform camera memory readout, image processing, position determination, and position streaming. We programmed our acquisition software in LabVIEW and C++. Image recording, tracking and streaming are done in a highly parallelized manner to give individual modules the maximum time when assigned directly to a CPU core. A detailed description of the programming strategy is provided in [Czerwinski and Oddershede, 2010].

The main program is designed in a modular fashion to offer independent as well as interconnected control of different sources of signals. Further, it contains support for data-streaming protocols. The programming architecture combines horizontal modules (acquisition, queuing, image processing, streaming) with vertical programming patterns (sequential structure, parallel while loops, multicore processing) in order to assure negligible error rates and optional customization. For the example of a downscaled graphical program code, the different modules of the program are highlighted each by their background color in Fig. 6. The modules dealt with elements that concern computer specifications, acquisition and image processing, queuing, and position streaming. The streamed data could be screened for assigned triggers providing a image recording on demand option. Each of the modules functioned independently from the others as it communicates through well-defined programming patterns. Communication between timed loops was achieved by queues. Streaming of the tracked positions was done into the RAM and subsequently onto the hard disk. We tested continuous acquisition for 20 min at 40,000 fps. There was virtually no limitation but disk space. We also benchmarked our software implemented tracking algorithm by monitoring the lost frames in a time trace. A frame is considered to be lost if the colloid position had not been calculated before the subsequent frame was acquired. In long-term measurements at 10,000 fps we found to loose less than 5 frames in every 100,000 frames recorded by the camera. This corresponds to a relative value of 0.005 %.

Due to the fast cross-correlation algorithm written in C++ by Gunter Stober, the time critical step is not the calculation of the cross-correlation, but the transformation of the image to an array which is a LabVIEW internal function. Since the CMOS data in principle becomes available as array rather than as image, there may be a possibility for further software improvement. That is impossible though, as long as the source codes of the image coding and the driver of the Mikrotron camera are not freely available. All further improvements might make sense, when dedicated real-time ma-

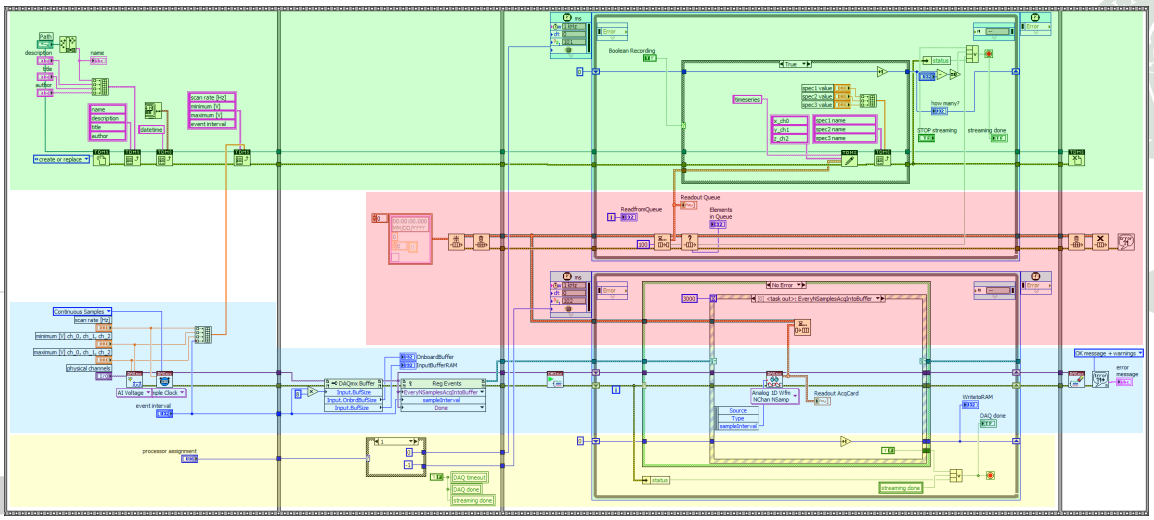

Figure 6: LabVIEW block diagram of program TimeSeriesStreaming.vi [Czerwinski and Oddershede, 2010]. Programming modules are highlighted by background color. The diagram illustrates the modular architecture of the program. Horizontal modules (acquisition, queuing, streaming) are combined with vertical programming patterns (sequential structure, parallel while loops). A high resolution version of Fig. 6 is available through the program URL `http://www.nbi.dk/~czerwin/TimeSeriesStreaming.html`.

chines are used. Otherwise the operating system Windows —and its calls of running programs— is the weakest link. At the moment "Windows calling LabVIEW" limits the performance of our LabVIEW programs at real-time tracking beyond 40 kHz. Our fully software-implemented solutions use the frame grabber card PCIe-1429 (National Instruments, Austin) as hardware interface [Czerwinski and Otto, 2010]. This strategy allows for every compatible CMOS camera to be implemented this way. Moreover, our software can simply adapt to future CMOS camera technologies.

FACULTY OF SCIENCE
UNIVERSITY OF COPENHAGEN

PhD Thesis

Fabian Czerwinski

Allan Variance Analysis and Fast Camera Detection Schemes for Optical Tweezers

Academic Advisor: Lene B. Oddershede

Submitted: September 27, 2010

Allan Variance for Optical Tweezers and Single-Molecule Techniques

In section 6, we motivate the need for an assumption-free method to determine low frequency noise in experiments that investigate biologically relevant length and force scales. We then introduce Allan variance analysis as a method with a lot of advantages. We compare Allan variance to typically used methods, such as normal variance and power spectral density analysis. We introduce a good way of presenting and fitting the outcomings of Allan variance analysis for single-molecule techniques.

Section 7 describes experimental findings on the basis of this methodic framework. These deal with optical tweezers firstly. Since the method is totally assumption free, it can be used as a standardizing method to compare every single-molecule assay. Together with yet unpublished data, propositions for the usage of Allan variance analysis in the DNA-tethered assays of force microscopy are given in section 8.

6 Allan Variance: Motivation, Definition, Mathematical Elaboration

Every physical experiment is exposed to noise. Often, the main sources of noise are known or can be tested for. Consequently, these can be accounted for, e.g., by appropriate filtering, active feedbacks, etc. A good example for the understanding of internal noise is the passive calibration protocol described above. Here, Brownian fluctuations caused by the bombardment of the observed object by surrounding molecules can be interpreted as white noise of the object itself, and used to provide a relation to calibrate with. Other classical examples are electric peaks in sensitive noise spectra. Distinct 50 Hz noise usually relates to improper shielding from the electric circuit, or peaks in the kHz range to higher-order crosstalk between electronic channels. Either shielding of the noise source, amplification of the signal or mathematical treatment are good strategies to overcome these problems. The best methods are those that do not require any a priori knowledge of the system itself.

6.1 Motivation

In biophysical experiments we operate at the thermal energy. The investigated sample itself becomes a source of noise, again, referring to the Brownian fluctuations of objects in confined potentials. Furthermore, the experimentalist must account

for low frequency noise —called *drift* by experimentalists' jargon. Since the sources of low frequency noise are of very different origins (temperature gradients, feedbacked oscillations of stages, etc.), those drift phenomena are usually accounted for by simple offest correction. Most common are the observation of the interferometric image of a marker located just in the vicinity of the actual measurement [Neuman et al., 2007, Carter et al., 2009].

Even with these very good techniques at hand, a quantification of low frequency noise on a day-to-day basis is desirable, as this seems to depend on a not clearly defined number of parameters that are either impossible or very hard to measure or even to control (temperature gradients, acoustic noise, etc.). A quantification (in real time) shall thus enable to pinpoint some of the low-frequency noise sources. However, it is by itself desirable to extrapolate the behavior of a system in infinity from a finite measurement. This would offer the chance of a standardizing comparison of drift-exposed experiments among different setups, different experiments, and even different laboratories.

Allan variance analysis was developed by David Allan in the 1960s. It found a broad usage in the refinement of engineering standards in the development of atomic clocks. When we read about inaccuracies of 10^{-9}s per day for atomic clocks,[2] the potential of Allan variance analysis to extrapolate the accumulated effect of all noise sources becomes obvious. In addition, like every variance, it is totally free of any assumption, and can in principle be used for every kind of time series.

6.2 Definition

Given a time series of total acquisition time t_{acq}, individual measurement times τ and a series of mean positions x_i during those measurement intervals, Allan variance is defined as:

$$\sigma^2_{\mathrm{Allan},\,x}(\tau) = \frac{1}{2}\left\langle (x_{i+1} - x_i)^2 \right\rangle_\tau \,, \tag{14}$$

or in words, the Allan variance is half the mean of the squared displacement of the difference of the means of consecutive intervals of length τ. The Allan deviation is the square root of the Allan Variance $\sqrt{\sigma^2_{\mathrm{Allan},\,x}(\tau)}$.

This definition is not limited by the type or style of data acquisition. For the remainder of this thesis, it is assumed to be equidistant with an acquisition rate f_{acq}, but all claims shall hold for non-equidistant acquisition as well.[3]

A measurement of the Allan variance of any experimental system would look like this: The positional time series of an object is acquired at highest possible technical

[2] This corresponds to a nominal uncertainty of 10^{-14}. Value taken from `http://en.wikipedia.org/wiki/Atomic_clock` on September 8, 2010.

[3] Programs and fitting routines developed in the course of this thesis are able to handle equidistant as well as non-equidistant cases. Calculation times are typically a factor 15 larger for non-equidistant data, because vectorization of routines and algorithms is either difficult or impossible. Hence, when designing tests of the Allan variance of an experiment, it is advisable to choose equidistant acquisition.

precision and at acquisition rates f_{acq} oversampling the necessary frequency by factor 10. The length of the time series should be as long as possible, since $\tau < t_{\mathrm{acq}}/2$. For example, the highest technical precision could be given by the acquisition card or the fluctuation of an electronic signal. In optical tweezers, the necessary frequency might be a rough estimate of the corner frequency as it sets the thermal limit of positional acquisition (compare to Eq. (30)). This is by no means different than data acquisition as it routinely happens for, e.g., a calibration measurement. Therefore, it is straight forward to implement Allan variance beside, say, real-time power spectral analysis. Furthermore, also the Allan variance of electronic signals and fluorescence intensities, i.e., any kind of time series measured with the necessary precision, quantifies useful parameters.

Allan variance is a homogeneous function with respect to the time series data:

$$\begin{aligned}\sigma^2_{\mathrm{Allan},\,\beta x}(\tau) &= \frac{1}{2}\left\langle(\beta x_{i+1}-\beta x_i)^2\right\rangle_\tau = \frac{1}{2}\left\langle\beta^2\left(x_{i+1}-x_i\right)^2\right\rangle_\tau \\ &= \frac{\beta^2}{2}\left\langle\left(x_{i+1}-x_i\right)^2\right\rangle_\tau = \beta^2\sigma^2_{\mathrm{Allan},\,x}(\tau)\ .\end{aligned} \tag{15}$$

This has an important implication. Often, when data is acquired the exact conversion into SI units is not known, but depends on a calibration that is done later on. This calibration gives a conversion factor β (section 4). Allan variance can be calculated at any point in time and then scaled to the correct units using the linear conversion factor β. Practically, this means that linear functions, e.g., the conversion from one unit to another, do not affect the qualitative behavior.

With respect to the time domain, Allan variance is not necessarily an homogeneous function. In the specific case that the time series data is independent of time, i.e., for purely stochastic white noise, it is independent of linear transformations of the measurement time:

$$\begin{aligned}\sigma^2_{\mathrm{Allan},\,x}(\beta'\tau) &= \frac{1}{2}\left\langle\left(x_{i+1}-x_i\right)^2\right\rangle_{\beta'\tau} \\ &= \frac{1}{2}\left\langle\left(\frac{1}{\beta'\tau}\int_{\beta'\,(i-1)\tau}^{\beta'\,i\tau}x(t)\;dt-\frac{1}{\beta'\tau}\int_{\beta'\,i\tau}^{\beta'\,(i+1)\tau}x(t)\;dt\right)^2\right\rangle \\ !&= \frac{1}{2}\left\langle\left(\frac{1}{\beta'\tau}\int_{\beta'\,(i-1)\tau}^{\beta'\,i\tau}\xi(t)\;dt-\frac{1}{\beta'\tau}\int_{\beta'\,i\tau}^{\beta'\,(i+1)\tau}\xi(t)\;dt\right)^2\right\rangle \\ &= \frac{1}{2}\left\langle\left(\int_{i-1}^{i}\xi'(t')\;dt'-\int_{i}^{i+1}\xi'(t')\;dt'\right)^2\right\rangle \\ &= \frac{1}{2}\left\langle\left(\int_{i-1}^{i}x'(t')\;dt'-\int_{i}^{i+1}x'(t')\;dt'\right)^2\right\rangle \\ &= \frac{1}{2}\left\langle\left(x'_{i+1}-x'_i\right)^2\right\rangle_\tau = \sigma^2_{\mathrm{Allan},\,x'}(\tau)\ .\end{aligned} \tag{16}$$

For a purely stochastic motion the Allan variance is invariant with respect to the measurement time. This is only true if each acquired point contains enough in-

formation, i.e., the acquisition happens faster than the measurement time at least needed to observe motion at the thermal limit. This observation has an experimental correspondent shown in Figure 12 B.

Allan variance is only additive for two samples x and y that are orthogonal to each other, i.e., they are not correlated, or in the trivial case when one of the signals is constant:

$$\begin{aligned}\sigma^2_{\text{Allan},\,x+y}(\tau) &= \frac{1}{2}\left\langle((x_{i+1}+y_{i+1})-(x_i+y_i))^2\right\rangle_\tau = \frac{1}{2}\left\langle((x_{i+1}-x_i)+(y_{i+1}-y_i))^2\right\rangle_\tau \\ &= \frac{1}{2}\left\langle(x_{i+1}-x_i)^2+2(x_{i+1}-x_i)(y_{i+1}-y_i)+(y_{i+1}-y_i)^2\right\rangle_\tau \\ &= \frac{1}{2}\left\langle(x_{i+1}-x_i)^2\right\rangle_\tau + \langle(x_{i+1}-x_i)(y_{i+1}-y_i)\rangle_\tau + \frac{1}{2}\left\langle(y_{i+1}-y_i)^2\right\rangle_\tau \\ &= \sigma^2_{\text{Allan},\,x}(\tau) + \langle(x_{i+1}-x_i)(y_{i+1}-y_i)\rangle_\tau + \sigma^2_{\text{Allan},\,y}(\tau)\ .\end{aligned} \tag{17}$$

The crossterm $\langle(x_{i+1}-x_i)(y_{i+1}-y_i)\rangle_\tau$ is equal to zero for the trivial solutions that at least one of the signals is constant, or when the covariance matrix of samples of x and y is zero, i.e., in the orthogonal case. The latter is fulfilled for the Brownian motion of an object inside a harmonic potential, not necessarily though for the Brownian motion of an object flexibly tethered to a surface (see subsections 8.1 and 8.2). If data is acquired for an experiment that, e.g., shows crosstalk between electric channels, the crossterm is different from zero, at least in the bandwidth of the crosstalk.

Allan variances can be constructed for any kind of measured quantity. For example, when the force transducing object in an optical tweezers is operated in the center of the harmonic potential, and no anharmonic contribution has to be accounted for [Richardson et al., 2008], it gives a direct force response $F = kx$. The Allan variance of the force measurement is linear to the positional Allan variance:

$$\sigma^2_{\text{Allan},\,F}(\tau) = \frac{1}{2}\left\langle(F_{i+1}-F_i)^2\right\rangle_\tau = \frac{1}{2}\left\langle k^2\,(x_{i+1}-x_i)^2\right\rangle_\tau = k^2\sigma^2_{\text{Allan},\,x}(\tau)\ . \tag{18}$$

using the linearity of Eq. (15). This is particularly important to investigate the potential trade off of force sensitivity and positional accuracy (section 7).

6.3 Regular and Overlapping Allan Variance

The error of a calculated value of the Allan variance for a measurement time τ is:

$$SE_{\sigma 2\text{Allan},x} = \frac{\sigma^2_{\text{Allan},\,x}(\tau)}{n}\,, \tag{19}$$

with n being the number of measurement intervals used for averaging.

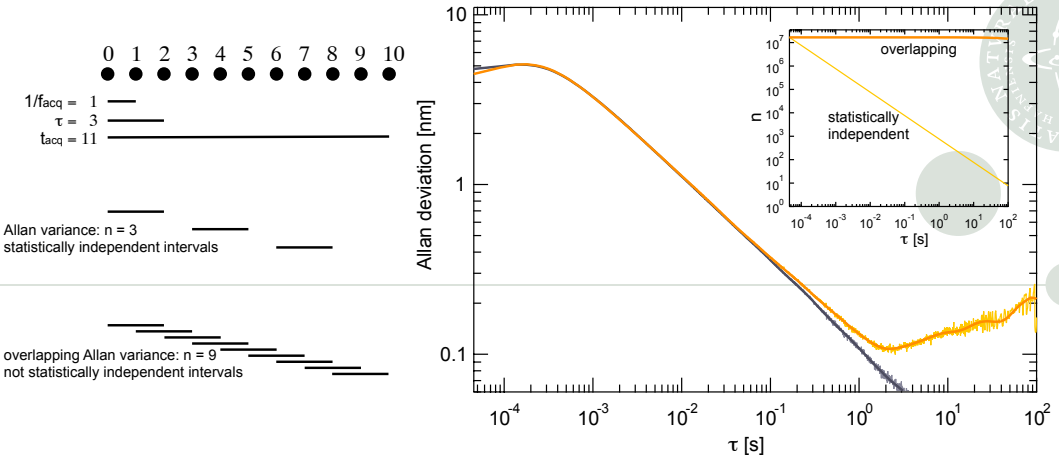

Figure 7: **left** Schematic equidistant time series $(f_{\mathrm{acq}}, t_{\mathrm{acq}})$ with 11 data points. For measurement times $\tau = 3$, the Allan variance yields the average of two distances of three statistically independent measurement intervals; the overlapping Allan variance instead averages over eight distances from 9 possible combinations of neighboring intervals. **right** Allan deviation (light yellow) and overlapping Allan deviation (orange) of the positions of polystyrene sphere inside an optical trap. The absolute minimum of the overlapping Allan deviation at $\tau = 2\,\mathrm{s}$ is the optimal time for calibration, because the deviation is absolutely lowest. For a simulated experiment using the same parameters but no external drift, the Allan deviation (light grey) and overlapping Allan deviation (dark grey) are plotted. The inset illustrates the number of combinations n of neighboring intervals given the requirements.

If the measurement intervals should be statistically independent for a measurement time τ in a total acquisition time t_{acq}, n is at least:

$$n = \left\lfloor \frac{t_{\mathrm{acq}}}{\tau} \right\rfloor = \left\lfloor \frac{f_{\mathrm{acq}} t_{\mathrm{acq}}}{f_{\mathrm{acq}} \tau} \right\rfloor . \tag{20}$$

The floor function $\lfloor ... \rfloor$ applies for cases where $t_{\mathrm{acq}} \neq m\tau$ with m being the number of statistically independent measurement intervals.

Giving up the statistical independence and taking all available neighboring intervals into account, the number of available differences n increases to:

$$n = \lfloor f_{\mathrm{acq}} t_{\mathrm{acq}} - (f_{\mathrm{acq}} \tau - 1) \rfloor = \left\lfloor f_{\mathrm{acq}} \left(t_{\mathrm{acq}} - \tau + \frac{1}{f_{\mathrm{acq}}} \right) \right\rfloor . \tag{21}$$

This is basically the number of all measurement points minus the length of one interval that is 'just too short' to contribute. When this approach is used, it should be referred to as the overlapping Allan variance. In Fig. 7, a schematic comparison of the statistical independent and the overlapping case is given. Also, Allan deviations obtained from experiments and from simulations illustrate the differences. For

$1/f_{\mathrm{acq}} \lessapprox \tau \ll t_{\mathrm{acq}}/2$, Allan variance and overlapping Allan variance are virtually the same, whereas for $1/f_{\mathrm{acq}} \ll \tau \lessapprox t_{\mathrm{acq}}/2$, n decreases by orders of magnitude (Fig. 7 right inset). However, the regular Allan variance can be vectorized, the overlapping only in a complicated highly parallelized fashion. Therefore, the computational cost of the overlapping Allan variance for longer time series is higher.

6.4 Functional Form of Allan Variance

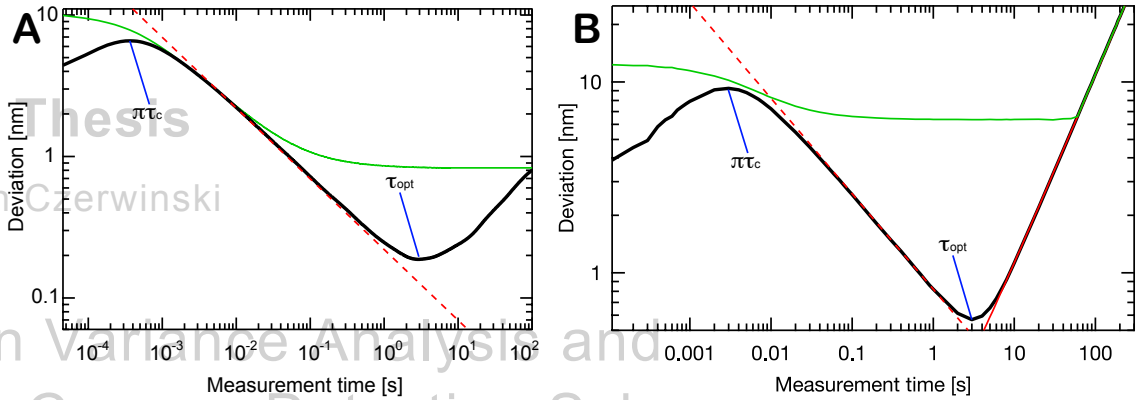

Figure 8: Standard (green) and Allan (black) deviation of a polystyrene sphere in a harmonic potential under positional drift derived from an experiment (**A**) and from simulated data with $1/f$-noise (10 nm/s, **B**). Thermal limits for both cases are plotted (red). The purple pointer highlight the local maxima at $\pi\tau_{\mathrm{c}}$ and minima at τ_{opt}.

The graph of a typical Allan deviation in comparison to a standard deviation for experimental and simulated data is shown in Fig. 8. Data is obtained for an micronsized object trapped in a harmonic potential. The functional form of an Allan deviation can be divided into regimes:

$\tau < \pi\tau_{\mathrm{c}} = (2f_{\mathrm{c}})^{-1}$**:** Allan deviation described by mean squared displacement Eq. (23)

$\tau = \pi\tau_{\mathrm{c}} = (2f_{\mathrm{c}})^{-1}$**:** Local maxima of Allan deviation

$2\pi^2\tau_{\mathrm{c}} = 2\pi/(2f_{\mathrm{c}}) < \tau < \tau_{\mathrm{opt}}$**:** Thermal limit Eq. (30), slope $-1/2$

$\tau = \tau_{\mathrm{opt}}$**:** Absolute minimum of Allan deviation

$\tau > \tau_{\mathrm{opt}}$**:** Drift exposure, characteristic slope less than 1.

The deviation from the thermal limit (in Fig. 8 for $\tau > 3\,\mathrm{s}$) is due to drift, as the comparison between simulated and experimental data illustrates. The Allan derivations reaches an absolute minimum for measurement times in the range of

seconds. This is the timespan which denotes the optimal measurement time for calibrations. Here one finds a balance between a time long enough allowing for the Gaussian distributed parameters to be accurately determined and a time short enough that drift does not yet play the dominant role. This optimal measurement time depends on the trap stiffness (subsection 7.1).

Standard variance A classically used measure of noise is the standard variance with the definition:

$$\sigma^2_{\text{std},\,x}(\tau) = \frac{1}{2}\left\langle (x_i - \bar{x})^2 \right\rangle_\tau \text{ with } \bar{x} = \frac{1}{n}\sum_1^n x_i\,. \tag{22}$$

In comparison to the Allan variance that compares neighboring intervals, the standard variance puts a measurement interval x_i always in relation to the mean of the entire time series $\bar{x}$. Therefore, the standard deviation does not always converge to finite value, especially not for purely stochastic white noise [Allan, 1966]. The power spectral density in frequency space is the equivalent to the standard variance in real space. To show how power spectral density and Allan variance can even be presented in the same plot, we used the data from a trapped polystyrene sphere (diameter 792 nm) and sampled its position for 12 min [Czerwinski et al., 2011]. In Fig. 9, the corresponding power spectrum, averaged 4, 32, and 8192 times, respectively, is plotted together with the Allan variance of the same time sequence. To get the same physical values plotted on the ordinate axis, the Allan variance was plotted as $2\tau\sigma^2_{\text{Allan},\,x}$ and the time domain as $\pi\tau$. The reason for the ordinate rescaling is the particular form of the Fourier transformation used [Berg-Sørensen and Flyvbjerg, 2004]. Interestingly, the Allan variance reconstructs the power spectrum and yields a high resolution analysis of the data, particularly at low frequencies. Considerable averaging is needed to make the power spectral density equally precise to the Allan variance of the same dataset. The power spectrum yields noisier information regarding the low frequencies, hence, details regarding noise and drifts are lost. For high frequencies, the product of Allan variance and measurement time is slightly smaller than the real power spectral density. This corresponds to the difference between standard and Allan deviation for $\tau < 2\pi^2\tau_c$, as illustrated in Fig. 8.

Mean squared displacement In analyzing time series data of experiments from tethered-particle motion, diffusion studies from experimental observations, or in rheology, the most prominent method is to look at the mean squared displacement. It is advantageous because it discriminates for offset problems and is also assumption free. The definition of the time averaged mean squared displacement in a plane used in this thesis is [Tejedor et al., 2010]:

$$\rho^2(t,\tau) = MSD_r(\tau) = \left\langle (x(t+\tau) - x(t))^2 + (y(t+\tau) - y(t))^2 \right\rangle_\tau\,. \tag{23}$$

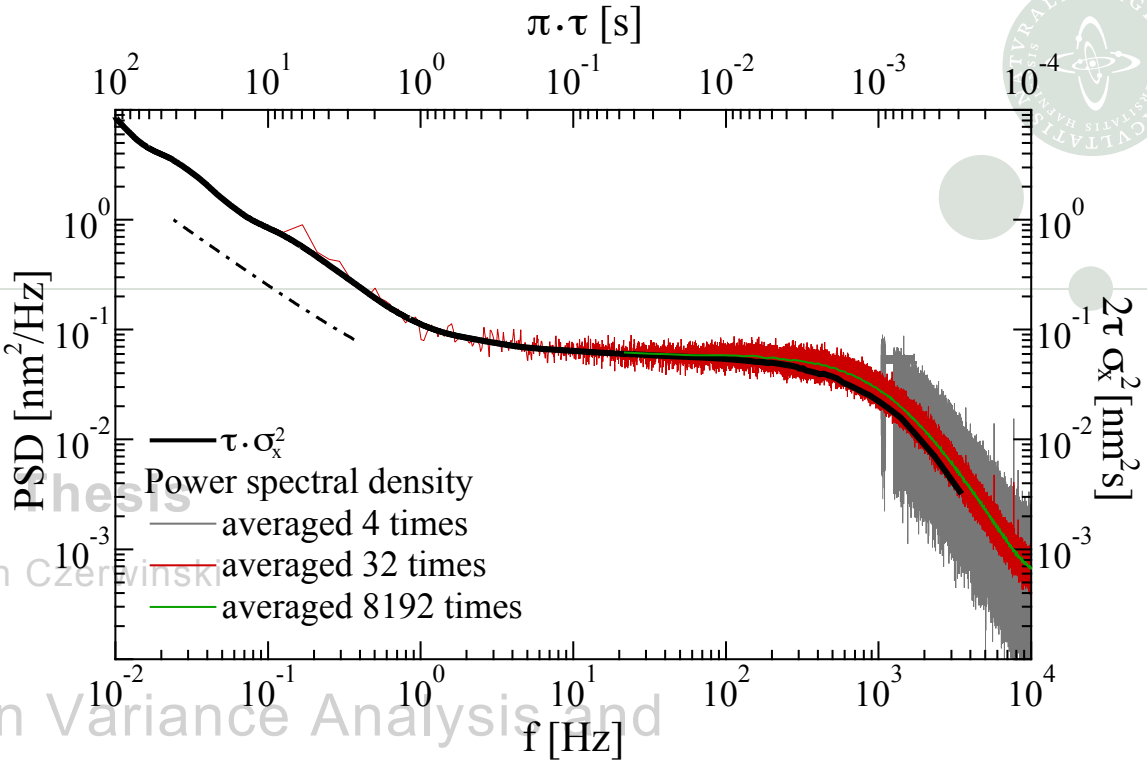

Figure 9: Power spectral density and Allan variance of a trapped sphere [Czerwinski et al., 2011]. Power spectral density plots are averaged over 4, 32 and 8192 timeseries with respective loss of resolution for low frequency band. The corresponding product of Allan variance and measurement time is overlaid. The dashed-dotted line shows the $1/f$-slope for very low frequencies.

and for an individual coordinate:

$$\rho^2(t,\tau) = \left\langle (\rho(t+\tau) - \rho(t))^2 \right\rangle_\tau \ . \tag{24}$$

If the coordinates x and y are orthogonal, and the measurement time is $\tau \approx \tau_c$, so that drift is considerably smaller than the fluctuations of x and y, then the mean squared displacement is basically an just as good of a discription as the sum of two conditionally independent Allan variances. This would allow to simplify Eq. (23) to [Han et al., 2008, Jauffred et al., 2010]:

$$\rho^2(\tau) = \left\langle (x(t) - \bar{x})^2 + (y(t) - \bar{y})^2 \right\rangle_\tau \ . \tag{25}$$

However, this simplification is not always quite correct, particularly in the band of measurement times that show a considerable difference between standard variance and Allan variance, or in cases where the standard variance is large even at short measurement times. This case applies to gold nanorods [Czerwinski et al., 2009b, Fig. 6].

Thermal limit of a Brownian object in a harmonic potential The mean squared displacement of a Brownian object is given by the diffusion equation:

$$\left\langle x^2 \right\rangle = 2D\tau_{\mathrm{c}}\,. \tag{26}$$

In relation to the thermal energy $k_{\mathrm{B}}T$, the Einstein relation for the diffusion coefficient D is:

$$\gamma D = k_{\mathrm{B}}T\,. \tag{27}$$

The limit to what the position of a Brownian object is known is set by the root of the mean squared displacement of the object:

$$SE_{\langle x\rangle} = \frac{1}{\sqrt{n}}\sqrt{\langle x^2\rangle} = \frac{1}{\sqrt{n}}\sqrt{2D\tau_{\mathrm{c}}} = \sqrt{\frac{\tau_{\mathrm{c}}}{n}}\sqrt{\frac{2k_{\mathrm{B}}T}{\gamma}}\,. \tag{28}$$

A harmonic potential $V(x) = kx^2 = \frac{\gamma}{\tau_c}x^2$ confines the object. This sets the limit to the accessible squared displacement.

The number n of measurements of length τ can be approximated by the ratio that measures how often the correlation time τ_c has been sampled, or equivalently, how often the corner frequency f_c is oversampled by the the acquisition frequency f:

$$n \approx \frac{\tau}{\tau_c} = \frac{f_c}{f}\,. \tag{29}$$

Therefore, the position of a Brownian object confined by a harmonic potential for measurement time τ is approximated by:

$$SE_{\langle x\rangle} \approx \sqrt{\frac{2k_{\mathrm{B}}T\gamma}{k^2\tau}} = \frac{1}{\pi f_{\mathrm{c}}}\sqrt{\frac{k_{\mathrm{B}}T}{2\gamma\tau}}\,. \tag{30}$$

The last equality derives by using Eq. (11): $k = 2\pi\gamma f_{\mathrm{c}}$.

In an experiment, all parameters are only known to a certain extend. The relative error to the analytical thermal limit Eq. (30) is thus:

$$\frac{\Delta SE_{\langle x\rangle}}{SE_{\langle x\rangle}} = \sqrt{\frac{1}{2}\left(\frac{\Delta T}{T}\right)^2 + \frac{1}{2}\left(\frac{\Delta\gamma}{\gamma}\right)^2 + \left(\frac{\Delta f_{\mathrm{c}}}{f_{\mathrm{c}}}\right)^2 + \frac{1}{2}\left(\frac{\Delta\tau}{\tau}\right)^2}\,. \tag{31}$$

Microscope and sample holder are passively temperature controlled through the temperature in the room. It is known to $\pm 1\,\mathrm{K}$. However, the exact temperature at the trapped object is not known. As mentioned above, the absorption coefficient for water is $1.5\,\mathrm{K/W}$. It should be slightly higher for polystyrene spheres [Hansen, 2006]. In the experiments in the remainder of the thesis, the error due to the estimation of the temperature is estimated not to exceed approximately $3\,\mathrm{K}/300\,\mathrm{K}{=}1\,\%$. However, for metallic particles the absorption coefficient can exceed $100\,\mathrm{K/W}$ with a very strong dependence on particle size and trapping in two or three dimensions [Hansen, 2006, Bendix et al., 2010]. Furthermore, our objectives are also not

temperature controlled. This effect however might affect only the measured trap stiffness [Mahamdeh and Schäffer, 2009]

The main contributions to the error of the drag coefficient arise from the assumptions that have to be made, e.g., in order to find a value for the drag coefficient from Stoke's equation $\gamma = 6\pi\eta r$. The viscosity of the surrounding medium η is usually known in bulk, but might have some local heterogenity around the trapped object. The objects radius r strongly depends on the quality the monodispersity of the tested sample. For polystyrene spheres, r varies in the order of 1–10 % (subsection 5.1). Using the above discussed *active protocol*, assumption become obsolete and γ is determined to 3 % [Tolic-Nørrelykke et al., 2006]. Then, a change in γ due to the possible vicinity to a surface is also corrected for.

Determining the corner frequency, or the trap stiffness, respectively, is the most important part of the calibration protocol. For the above discussed calibration protocols, the assumption of the harmonic potential must hold. If tested and ensured prior to experiments [Richardson, 2009, Richardson et al., 2008], k can be determined accurately down to 3 % [Tolic-Nørrelykke et al., 2006, Czerwinski et al., 2011]. In addition, uncertainties in the trap stiffness contribute twice as much to the relative error in position with respect to the thermal limit, so they should be minimized by all costs by simply averaging over as many calibration intervals as necessary.

The precision of the measurement time is set by the choice of the acquisition frequency. At sampling times of 100 ms already acquisition frequencies larger than 10 kHz ensure relative uncertainties smaller than 0.1 %. Therefore, this effect is totally neglectful and does not need to be taken into account. In standard experiments with nicely monodispersible polystyrene spheres, at room temperature and 22 kHz acquisition rate, using active driving, the error is about:

$$\frac{\Delta SE_{\langle x\rangle,\,\mathrm{OT}}}{SE_{\langle x\rangle,\,\mathrm{OT}}} \approx \sqrt{\frac{1}{2}\left(\frac{\Delta T}{T}|_{0.01}\right)^2 + \frac{1}{2}\left(\frac{\Delta\gamma}{\gamma}|_{0.023}\right)^2 + \left(\frac{\Delta f_\mathrm{c}}{f_\mathrm{c}}|_{0.03}\right)^2} = 3.48\,\%. \quad (32)$$

In a very difficult case of trapping, e.g., quantum dots, with estimated local heating and a passive calibration protocol, this value should be estimated rather like:

$$\frac{\Delta SE_{\langle x\rangle,\,\mathrm{QD}}}{SE_{\langle x\rangle,\,\mathrm{QD}}} \approx \sqrt{\frac{1}{2}\left(\frac{\Delta T}{T}|_{0.05}\right)^2 + \frac{1}{2}\left(\frac{\Delta\gamma}{\gamma}|_{0.30}\right)^2 + \left(\frac{\Delta f_\mathrm{c}}{f_\mathrm{c}}|_{0.30}\right)^2} = 36.91\,\%. \quad (33)$$

Comparing to experimental data, the fluctuations of the Allan deviation around the thermal limit for quantum dots are smaller than 37 %, as shown in Fig. 10 B where the plotted errors are 23 %.

Representation of Allan variance results Three pieces of information are the most important when employing Allan variance analysis for biophysical experiments. The bandwidth over which the thermal limit of the reporting object is met, the optimal measurement time τ_opt for calibrations, and the slope of the loss in accuracy when

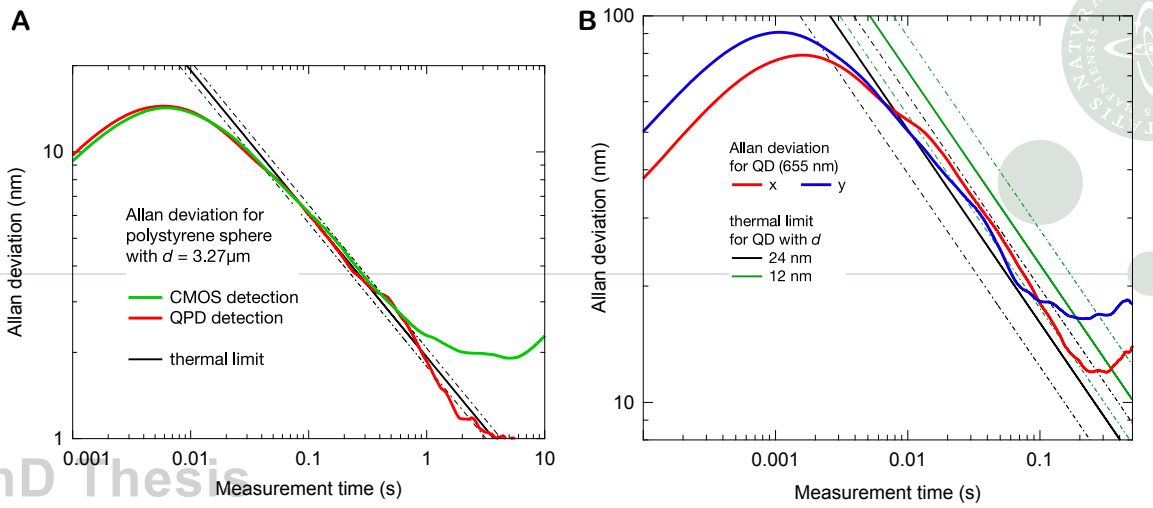

Figure 10: Comparison of polystyrene sphere and spherical quantum dot to thermal limits of detection. **A** Allan deviation of polystyrene spheres using different detection schemes. Both are equal within the errors of the thermal limit Eq. (32) for measurement times $< 1\,\mathrm{s}$. The CMOS detection deviates from the thermal limit for longer measurement times. **B** Allan deviation of quantum dot with emission wave length of 655 nm. x- and y-direction are determined accurate within errors of the thermal limit estimating a diameter $d = 24\,\mathrm{nm}$, rather than 12 nm. Compare to representation in [Jauffred et al., 2010].

drift becomes dominant. We find that double-logarithmic plots provide the best illustration of that. In a loglog plot, the exponent of the drift appears as straight line with a slope that represents the exponent. Furthermore, the ranging of orders of magnitudes of measurement time and exact quantification of the deviation is also well captured in this representation.

7 Allan Variance in Optical Tweezers

Inspired by the usage of Allan variance by Gibson and coworkers [Gibson et al., 2008], we started out to systematically employ Allan variance analysis to optical tweezers experiments. Undoubtably, we had the great pleasure of walking into this field with good expertise, but various unknowns. We could fill these with empirical procedures and numbers, replacing crude estimates.

We can only speculate why the powerful method of Allan variance has not found a broader use in the scientific community of optical tweezers, or more general single-molecule biophysics, before we among others had become kind of advocates of this method. In principle, the data acquisition that is routinely done to calibrate the

setup prior to experiments, is suitable for an Allan style treatment. However, long measurement times are necessary to access the effect of low frequency noise, but at the same time data needs to be recorded with high acquisition frequencies. Our implementation of a powerful data streaming program [Czerwinski and Oddershede, 2010] allowed us to stream time series for hours with virtually no limitation. In addition, we vectorized certain Matlab scripts, literally to boost the performance of those into real time. At the same time, the Padgett Group at the University of Glasgow integrated a LabVIEW solution to calculate Allan variance into their very successful particle tracking software suite. The same attempts are part of the latest version of the St Andrews Tracker (StAT). Therefore, the complementarity of power spectral and Allan variance analysis more and more manifests itself in a parallel output of both whenever people do single-molecule experiments. So, the new availability of reliable, long term stable acquisition together with improved data analysis were simply not given when we had started our work. Anyways, by September 2010, we knew more than 20 research groups in the field of single-molecule biophysics that routinely integrated Allan style analysis into their daily experimental procedures. This number will increase in the near future due to the availability through software hubs and the simplicity of this method.

The framework for the representation of Allan deviations in this section has been introduced in section 6. If not stated or parameterized otherwise, Allan variance analysis was conducted on adjacent time series consisting of 2^{24} consecutive points. For an acquisition rate $f_{\mathrm{acq}} = 22$ kHz, this corresponds to time series of about 13 min. Apart from filters inherently present in the detection diodes and electronics [Berg-Sørensen et al., 2003, Berg-Sørensen and Flyvbjerg, 2004, Hansen et al., 2006, Huisstede et al., 2006b], all additional filtering was applied during data analysis after acquisition [Huisstede et al., 2006a, Berg-Sørensen et al., 2006]. After each measurement, for both active and passive, the data was scrutinized to calibrate along the calibration protocol introduced in subsection 4.2. The Allan deviation of each data set was calculated by customized Matlab programs that are available for download [Czerwinski, 2008, Czerwinski, 2010]. For comparison, we eventually simulated time series using the procedure described in subsection 4.3.

Optical tweezers, when operated properly at the harmonic potential and inside the linear region of the detection scheme [Richardson et al., 2008, Huisstede et al., 2005, Otto et al., 2011], are extraordinarily sensitive for force measurements. Routinely, a good apparatus applies forces ranging from 0.1–140 pN [Neuman and Nagy, 2008, Neuman and Block, 2004]. There is a good understanding of optical tweezers force sensitivity, although it often accumulates in totally qualitative statements, such as weaker traps were generally more sensitive because a wider travel range corresponds to the same force. This argument is correct in itself, but quantitative proof is needed to allow for an optimized experimental design. A simple linear transformation with the trap stiffness k transforms positional data into an actual force measurement, and using the linearity of Allan variance, Eq. (18) gives the Allan deviation of a

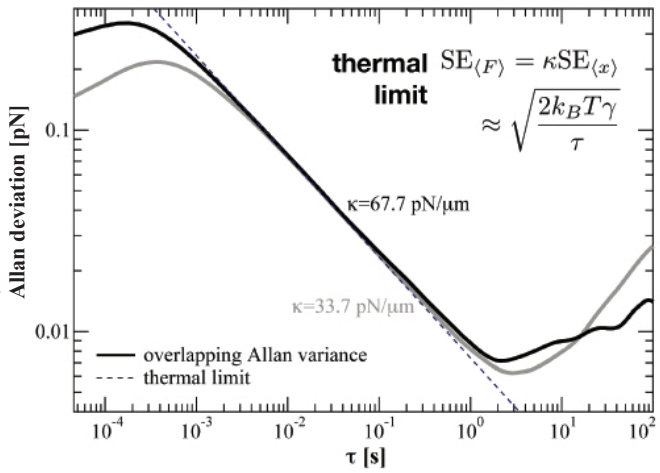

Figure 11: Quantifying test of the influence of trap stiffness k on the measurable force. A polystyrene sphere with radius $r = 400\,\mathrm{nm}$ was hold in an optical trap at two different trap stiffnesses. The Allan deviations of the measured fluctuating forces are plotted. To be determined with an accuracy of $0.1\,\mathrm{pN}$, the forces must be averaged over $\tau = 5\,\mathrm{ms}$, for $0.01\,\mathrm{pN}$ about a second. Remarkably, the influence of trap stiffness is rather minor for relevant measurement times.

time series of force measurements. An example is plotted in Fig. 11. Firstly, it turns out, that the thermal limit for force measurements becomes independent of the trap stiffness k (dashed line). Secondly, in this example, the tested polystyrene spheres ($r = 400\,\mathrm{nm}$) fluctuate at their thermal limit in almost the same band of measurement times. Thirdly, the better sensitivity for small measurement times is physically meaningless, since it is buried in the Brownian motion of the spheres, and the better force accuracy in the seconds regime is fairly small. We plot this example to show how Allan variance analysis can actually quantify purely qualitative statements in real experiments. Furthermore, figures like Fig. 11 based on empirical measurements on a certain setup could be used to probe, if and to what extend certain loading rates might be accessible for force-microscopy experiments.

7.1 Optimize Acquisition Parameters

The exact value of the Allan deviation depended on the used trap stiffness, as sketched by Fig. 12 A. As expected, a stronger trap ensured a smaller Allan deviation than a weaker trap, which implied a higher positional accuracy. The conceptional qualitative behavior was not altered though and has been outlined in subsection 6.4. Stronger traps experience drift earlier than weaker ones, as the shift to shorter optimal measurement times for stronger traps shows. This is caused by

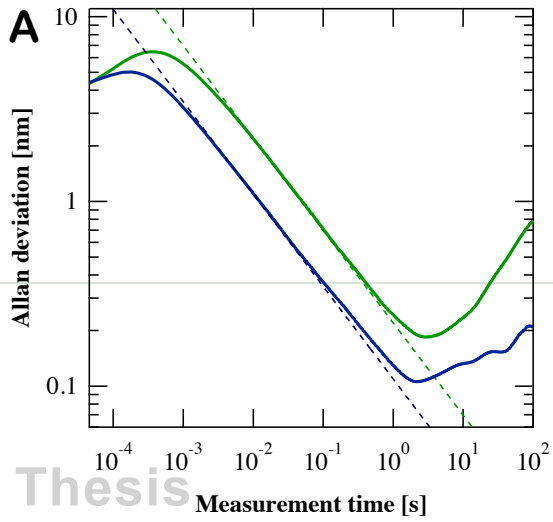

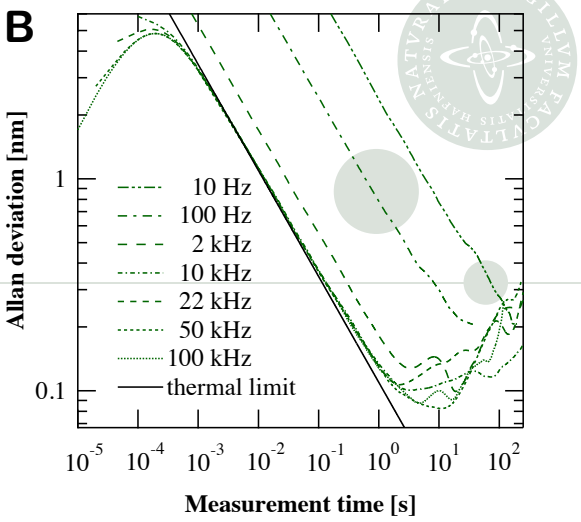

Figure 12: Allan variance analysis to optimize acquisition parameters [Czerwinski et al., 2009a]. **A** Allan deviation for the same polystyrene sphere trapped with $k = 67.7\,\mathrm{pN}/\mu\mathrm{m}$ (blue) and $k = 33.6\,\mathrm{pN}/\mu\mathrm{m}$ (green). The optimal calibration time is a function of trap stiffness. Compare to Fig. 11. **B** Allan deviation parameterized for various acquisition frequencies at trap stiffness $k = 67.7\,\mathrm{pN}/\mu\mathrm{m}$. For $f_{\mathrm{acq}} > 1/\tau_{\mathrm{c}}$, the Allan deviations collapse onto the thermal limit. For smaller acquisition frequencies, the data are undersampled, and thus lack information. They appear to be off the thermal limit.

the smaller absolute deviation given the thermal limit. Drift is thus more observable and becomes observable earlier, i.e., at shorter measurement times (compare to [Czerwinski and Otto, 2010, Fig. 2]). The rescaling of the deviations in Fig. 12 A to forces is shown in Fig. 11.

In Fig. 12 B, the graphs have the same characteristic trajectories as those shown in Fig. 12 A, but it is apparent that the Allan deviation decreases with increasing acquisition frequency up to a certain threshold. This threshold is the inverse correlation time τ_c^{-1} and thus linearly depends on the trap stiffness. It can be found in the plotted data set at $\tau_c^{-1} = 2\pi f_c \approx 10\,\mathrm{kHz}$. Above this threshold, an increase in frequency does not change the Allan variance for the majority of the measurement times. Only beyond the optimal interval, around 10 s, in this specific case, it seems beneficial to improve the acquisition frequency above 10 kHz. However, the bandwidth of the used position-sensitive photodiode was found to lie in between 43 and 47 kHz. Aliasing is the reason for the decreasing slope at high frequencies, i.e., very short measurement times, that however is not of any physical meaning.

Internal noise are Brownian fluctuations or deviations from the center of the trap, i.e., everything that directly affects the trapped object itself. External noise is then

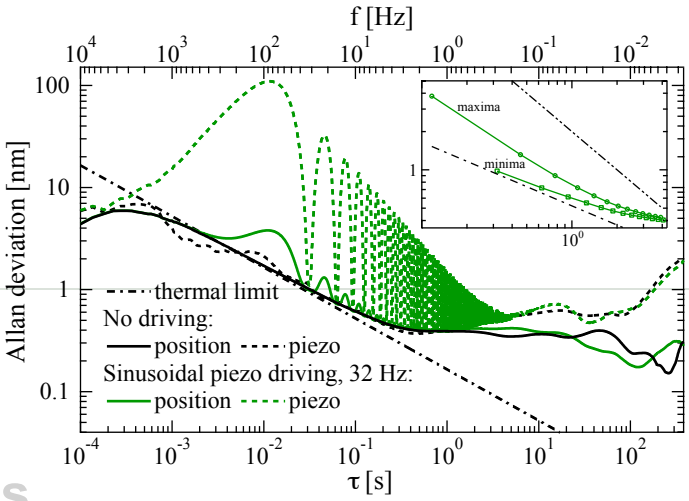

Figure 13: Active and passive calibration protocols achieve the same accuracy [Czerwinski et al., 2011]. Allan deviation is plotted for passive and active calibrations. Allan deviation for sphere positions (radius $r = 396\,\mathrm{nm}$, solid) as well as piezo positions (dashed) show almost identical patterns for measurement times larger than a second. Minima and maxima position converge to the same values (inset).

the dispositioning due to acoustics, temperature gradients, etc., basically all parameters that influence the entire setup and result ultimately in drift. The distinction of internal to external noise is important, when the optimized calibration protocol is used. The accuracy of the active calibration protocol is just as good as the passive one for $\tau \approx \tau_{\mathrm{opt}}$. This is, of course, a function of the piezo stage driving frequency (compare to [Czerwinski et al., 2011, Fig. 4]).

In particular for the trapping of small objects, such as nanometer-sized quantum dots, often even fundamental parameters like diameter are only known to a certain extend [Jauffred et al., 2008a]. These objects are also more sensitive to internal noise sources like laser instabilities or variations in the number of incidenting photons due to the relatively small cross-section. Still, Allan variance can be used to quantify essential parameters as the optimal calibration time, or the accuracy of the position determination. An example is shown in Fig. 10.

7.2 Pinpointing Low-Frequency Noise Sources

Allan variance analysis provides a high resolution in comparison to power spectra at low frequencies. We employed this feature to identify and eliminate low-frequency noise sources. These sources might be of unexpected origin, such as the feedback control of the piezo in Fig. 14 B or potentially the airflow in the optical path of one of the detection schemes, shown in Fig. 14 A.

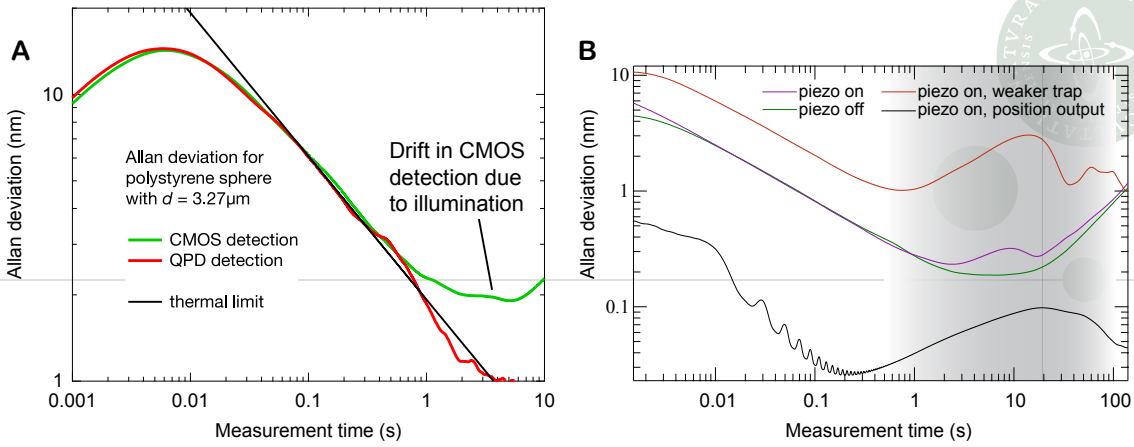

Figure 14: Identifying low frequency noise induced by optical detection path and piezo controller. **A** Allan deviation of two different spheres of the same kind [Otto et al., 2010]. Positions were monitored with a quadrant photodiode and a CMOS camera. Whereas the QPD uses forward scattered light, the CMOS camera uses a fiber-illuminated image of the region of interest around the sphere. For measurement times longer than a second, this optical path is exposed to drift which becomes dominant over the positional signal. A graph with the same data exemplified the deviation from the thermal limit in Fig. 10 A. **B** Impact of piezo stage on position of a trapped sphere [Czerwinski et al., 2009a]. When the piezo is switched on a hill in the Allan deviation within the interval $0.5\,\mathrm{s} < \tau < 110\,\mathrm{s}$ is observed (grey shading). It is more pronounced for a weaker trapped sphere, $\kappa = 15.3\,\mathrm{pN}/\mu\mathrm{m}$ (red), than for a strongly trapped sphere, $\kappa = 33.6\,\mathrm{pN}/\mu\mathrm{m}$ (violet). The Allan variance of the piezo itself is plotted in black. When the piezo is switched off (green), the piezo stage does not disposition the sphere.

Not just the optical path of an optical trap, but also the optical path of the detection must be carefully investigated for potential drift. Using the same trapping geometry, but different detection schemes, we could pinpoint the influence of drift of an external light source that eventually limited the setup's achievable accuracy.

Many optical tweezers experiments involve the usage of piezo stages. The manufacturers' provided noise tests are the power spectral densities of an actively driven stage. The spectra are the expected driving peak over a background noise level. However, they do not address the low frequencies less than 0.01 Hz.[4] To investigate if these piezo stages and their electronic controllers would anyways induce noise, we performed experiments where a sphere was optically trapped and its Allan variance was calculated for the situations where the piezo stage was on or off, or in controller

[4]Documentation of piezos and piezo controller units on manufacturers' websites in August 2010.

feedback. Figure 14 B shows the Allan deviation of a trapped sphere, with the piezo on, run in controller feedback. When decreasing the trap stiffness, the loss in accuracy over measurement intervals of $0.5\,\mathrm{s} < \tau < 110\,\mathrm{s}$ became even more pronounced; whereas switching off the piezo stage and the controller while keeping the trap constant eliminated the effect. Hence, the feedback-controlled piezo stage does add noise to the system, over a system-specific measurement time interval. Those low-frequency phenomena would be challenging to identify using standard noise-detection methods.

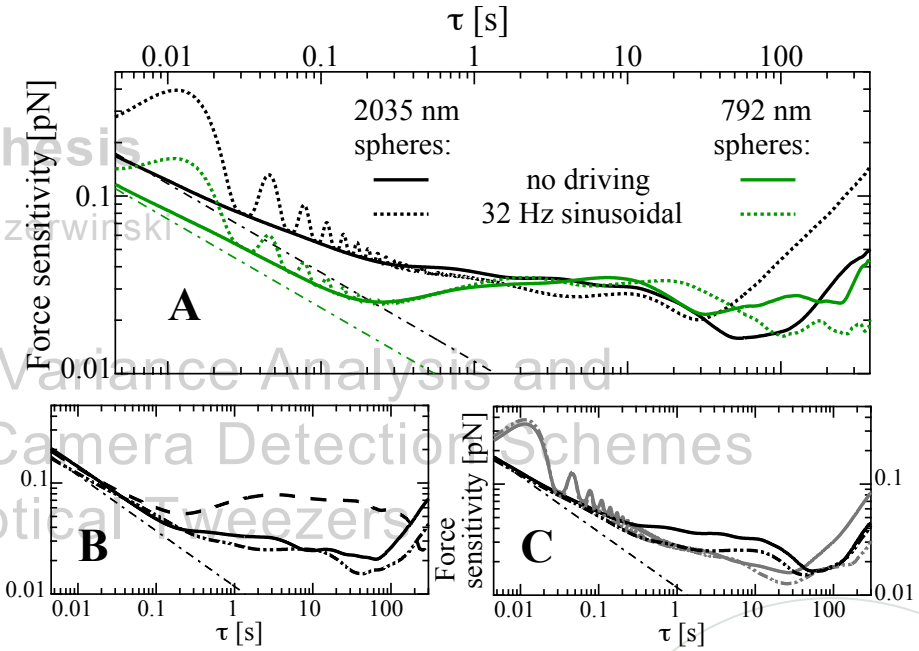

Figure 15: Application of Allan variance to quantify noise contributions in experimental settings [Czerwinski et al., 2011]. **A** Comparison of force sensitivity for different polystyrene spheres for active and passive calibration protocols. **B** Force sensitivity in rectangular (solid), quadratic (dashed-double-dotted), and open (dashed) chamber. **C** Force sensitivity in chambers with volume $10\,\mu\mathrm{L}$ (solid) and $20\,\mu\mathrm{L}$ (dashed-double-dotted), for driven (grey) and perpendicular (black) direction.

To improve the accuracy of calibrations, one useful focus can be put on increasing the optimal measurement time for individual calibrations. The noise picked up in measurement intervals between 0.1 s and 60 s is rooted in external noise close to the sample [Czerwinski et al., 2009a, Czerwinski et al., 2009b]. Therefore, we systematically altered parameters such as the geometry of the measurement chamber, the chambers volume, the cover slides used for assembly, etc., to get grip on a general trend (see Fig. 15). The strong point for this strategy was that the Allan deviation gave a direct measure of the achievable accuracy that directly provided a quantifi-

cation of the comparison of distinct settings. Despite this, often the number of possibly influencing parameters is just huge, and their interplay not always fully known. Regularly, it breaks down to a solely empirical approach comparing one setting directly to another, but with little information about one accurate parameter or source. Nevertheless, the consequently quantitative method is capable of comparing also the same settings on different setups of the same design due to is assumption-free application. The idea of a "Allan variance of the day" or an "Allan variance of the XYZ Lab" would certainly help standardizing the instrumental parameters with the goal of improving optical tweezers standards in general. This is also an opportunity with respect to other supersensitive measurements of force-microscopy assays or fluorescent single-molecule detection.

8 Allan Variance: Implications for Other Single-Molecule Techniques

In this section, we present Allan variance for other single-molecule techniques and emphasize the strength of this analysis method. Tethered-particle motion experiments were conducted by Liselotte Jauffred and Lin Han and kindly provided for this novel type of analysis. The analyzed data from magnetic-tweezers setups has been published previously [Czerwinski, 2007], or was kindly provided by Daniel Klaue and Ralf Seidel. The use of Allan variance for single-molecule fluorescence techniques is outlined and briefly discussed.

8.1 Tethered Particle Motion

For laboratories that already have a pronounced knowledge in surface-associated optical or magnetic tweezers assays, tethered particle motion (TPM) provides a straight forward implementation of a slighty distinctive experimental method. The Meisner Lab and the Philips Lab are contributing good experimental examples [Chen et al., 2010b, Han et al., 2008], and the Nelson Lab has been developing the state-of-the-art analysis [Nelson et al., 2006]. A typical DNA-based assay would be a double-stranded DNA molecule tethered between a sub-micron polystyrene sphere and a surface. The specific binding is achieved by specific protein-protein interactions, e.g., digoxygenin–anti-digoxygenin, or biotin–streptavidin. Dynamics that are slower than the fluctuations of the reporter object can be monitored by sufficiently high acquisition frequencies. The latest CCD cameras with 300 Hz acquisition are usually sufficient since the confinement of the reporter object by the tether is fairly weak. However, the shorter the DNA tether the stronger the confinement, and consequently the higher the necessary sampling rate. So, for very short tethers and smaller reporter objects it is beneficial to implement a fast routine based on real-time tracking of image stacks from a CMOS camera as reported in section 5.

The observed time traces in the x, y-plane are typically traced posterior to experiments, see, for example, the St Andrews tracker. The mean squared displacement

(Eq. (23)) is calculated, and further analyzed. In this way, for instance, the DNA looping rates induced by DNA-protein interactions can be found. Problems arise from hydrodynamic and non-specific interactions of the DNA with the nearby surface. The height of the reporter object above the surface is typically only up to 100 nm which renders a simple Faxen's law correction inadequate.

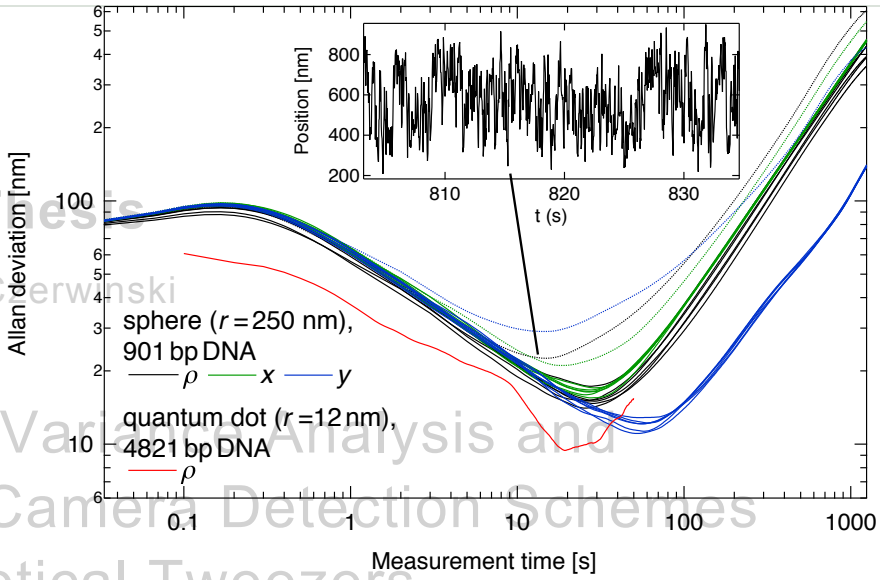

Figure 16: Allan deviation of TPM data of double-stranded DNA from Philips Lab (polystyrene spheres, radius 250 nm, x green, y blue, ρ black, data kindly provided) and Optical Tweezers Group at the Niels Bohr Institute (quantum dot, radius 12 nm, ρ red) [Jauffred et al., 2010]. The slope of all deviations for measurement times $0.5\,\mathrm{s} < \tau < 10\,\mathrm{s}$ is approximately -0.3 which is significantly different than -0.5 as expected for Gaussian distributed fluctuations. The dotted deviations are from a trace that shows transient sticking events (inset, [Han et al., 2008]). These relatively short events influence the overlapping Allan deviation.

We wanted to understand if Allan variance analysis could improve a basic understanding of TPM as an experimental setup. Especially, since the dynamics usually investigated by TPM focuses on transition rates over seconds, where Allan variance has been shown to be superior to simple Fourier analysis. In Fig. 16 we plot the Allan deviation for seven TPM time traces recorded with 30 Hz for about 20 min. The reporter was a polystyrene sphere with a radius $r = 250\,\mathrm{nm}$ tethered by a double-stranded DNA molecule with a contour length of $L_\mathrm{c} = 901\,\mathrm{bp}\cdot 0.34\,\mathrm{nm/bp} = 307\,\mathrm{nm}$. No active drift correction was done during experiments. The data was kindly provided by Lin Han and Martin Linden, members of the Philips Lab at Caltech.

Firstly, the deviation of the individual deviation with respect to each other is within

the error of the mean, if the time series that shows distinct sicking events is omitted. This emphasizes the reliability of the method for TPM data. Secondly, sticking events show up as increased deviation, i.e., as inaccuracies when Allan variance analysis is employed. Thirdly, the y-coordinate is significantly less exposed to drift than the x-coordinate. This is true for other time series taken on this setup with different settings and parameters. Hence, it is a feature that is inherent to this setup. As a consequence, efforts in optimizing spacial accuracy and pinpointing noise sources should address mainly potential sources that effect the x-direction. Fourthly, the optimal observation time is with 30 s longer than for comparable handles in optical tweezers, a result of the weaker confinement. Fifthly, the confinement does not enforce a Gaussian position distribution. The exponential scaling $\tau^{-0.3}$ for all deviations in the interval $0.5\,\mathrm{s} < \tau < 10\,\mathrm{s}$ is significantly different from $\tau^{-0.5}$ for Gaussian distributed positions. It has been speculated that this distribution is caused by the reduction of the partition function of the DNA polymer by torsional constraints, steric hinderance (object hits surface), and surface charge effects. The comparison of these Allan variance analysis data with those obtained by another surface-tethered technique, namely magnetic tweezers, distributes most of the change in slope to a gradient in force, i.e., to charge surface effects, and a mild contribution to torsional constraint, but none to steric hinderance. A detailed discussion is given in subsection 8.2.

Allan variance analysis as explained here, is a good method to learn more about TPM setups and settings, in particular since it probes the relevant time scales of this technique better than other variance methods. A more systematic application with respect to sphere diameters, acquisition parameters, and tether lengths is an ongoing project in cooperation with the authors of Ref. [Han et al., 2008]. This is very important as apparently the actual choice of the reporter sphere effects the measured rates [Milstein et al., 2010, Chen et al., 2010b]. A construction of a thermal limit as done for optical tweezers in subsection 6.4 is desirable, but non-trivial because of the many unknowns.

In state-of-the-art TPM setups, the fundamental limitation to resolve dynamics of the tether arises from the size of the reporter object. For that reason, Liselotte Jauffred developed a tethered-particle assay with quantum dots that had diameters ranging from 10–40 nm. This approach reduces the drag coefficient about 10- to 20-fold in comparison to polystyrene spheres. For quantum dots though, an excitation laser, and a CCD or CMOS camera with very high quantum efficiency are needed. And the temporal resolution is limited by the number of emitted photons that arrive per pixel. The assays that Jauffred et al. tested used a long double-stranded DNA molecule with $L_\mathrm{c} = 4821\,\mathrm{bp} \cdot 0.34\,\mathrm{nm/bp} = 1639\,\mathrm{nm}$. Data was recorded with $f_\mathrm{acq} = 10\,\mathrm{Hz}$. The shutter time was 8 ms, so sampling with 100 Hz should in principle be possible.

The Allan deviation of a tethered quantum dot is plotted in Fig. 16. Remarkably, the optimal observation time is found to be 20 s, about two orders of magnitude larger than for optically trapped quantum dots. This might be due to the different kind of confinement, and the non-accounting of blurring by the used tracking routine.

However, the spacial accuracy was just as good as for optically trapped quantum dots, and about a factor 2 better than for the TPM assays discussed before, even though the DNA molecule was more than 5 times longer. The slope for confinement-sensing measurement times is -0.36, so slightly larger, but due to the low acquisition frequencies based on too few points.

The use of quantum dots as reporter beads is a promising direction to improve TPM experiments. As shown, the accuracies that can be achieved are better than for polystyrene spheres. The implementation in terms of alignment is very challenging though. Also, blinking and other features inherent to quantum dots put a limitation to maximal observation times.

8.2 Magnetic Tweezers

Even though they are sometimes used for cellular studies [Walter et al., 2006], typically magnetic tweezers are the method of choice for single-molecule studies on DNA or RNA that require a controlled torque, an intrinsic force clamp, or a good force control in the regime from 50 fN–10 pN [Klaue and Seidel, 2009, Seidel et al., 2005, Ramanathan et al., 2009]. The polystyrene sphere as used in TPM experiments, is replaced by one that has a magnetic core. In the gradient of the magnetic field of two external rare-earth permanent magnets,[5] the magnetic bead is pulled upwards by a force F_{mag}. The DNA tether is put under tension, and the bead height corresponds to the end-to-end distance of the DNA. A schematic view is given in Fig. 17a. By varying the distance between the magnets and the sample, F_{mag} can be controlled. Since the magnetic moment of the bead relaxes quickly within the external magnetic field, by rotating the permanent magnets, torque can be applied to the bead. If a torsionally constraint molecule is used as tether, e.g., by having multiple specific DNA-surface and DNA-bead bonds, the torque on the bead acts directly on the molecule. If the torque is small enough, plectonems an be induced [Czerwinski, 2007, Brutzer et al., 2010]. An overview of the common calibration technique has been published recently [Velthuis et al., 2010]. In principle, it uses the real-time tracking of the tethered bead's position, and a slightly adapted power spectrum method that accounts for nearby surface (compare to section 4). The challenging off-center attachments of DNA molecules were topic of an earlier work that used the same calibration protocol but accounted for the torsional stiffness as well [Klaue and Seidel, 2009]. Maybe the most prominent experiments, involving the extensive use of magnetic tweezers, are measurements of the single-enzymatic activity of topoisomerases that control the topological shape of DNA molecules [Taneja et al., 2007, Koster et al., 2005, Dekker et al., 2002].

Allan variance analysis can be employed to magnetic tweezers data and helps to pinpoint the main sources of low frequency noise. The tracked positions of the

[5] Sometimes, electromagnets are used, but usually with drawbacks on the stability of the magnetic field.

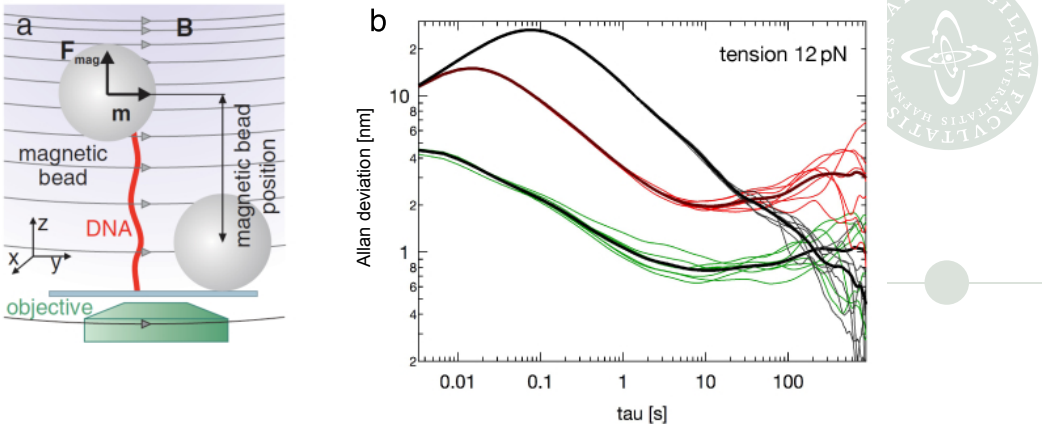

Figure 17: **a** Schematic view of magnetic tweezers setup [Klaue and Seidel, 2009]. The DNA tether is extended by the force F_{mag} that the magnetic bead experiences by the gradient of the magnetic field B. The bead's magnetic moment m is parallel to B. The coordinate system is defined here as follows: x is perpendicular to the magnetic field, y parallel to the field, and z perpendicular to x and y. In a good aligned system, z coincides with the direction of the strongest gradient. **b** Allan deviation calculated from bead positions for x (black), y (red) and z (green). A single-stranded DNA molecule was kept under 12 pN tension. The mean of six consecutive time series of $t_{\mathrm{acq}} = 3000\,\mathrm{s}$ is plotted as thick black graph on top of the individual Allan deviations.

reporter bead and of a reference bead in the vicinity were sampled as an adjacent time series with 300 Hz for the deviations plotted in Fig. 17 b and 60 Hz for those in Fig. 18. In Fig. 17 b a single-stranded DNA molecule (contour length $L_{\mathrm{c}} \approx 1.4\,\mu\mathrm{m}$) under 12 pN tension confined the fluctuations of the superparamagnetic bead. The deviations in x, y and z showed qualitative different behavior. Allan deviations of the individual coordinates of six consecutive measurements t_{acq} show only little difference for up to 5 min, emphasizing the reproducibility and reliability of the analysis. For long measurement times, the axis perpendicular to the magnetic field and to its gradient is the least exposed to drift. The other two axis start picking up drift for measurement times beyond 10 s. Therefore, we conclude the movement of the magnets with respect to the sample being the origin of this drift phenomena. A good strategy to improve the instrumental setup would thus start stabilizing the planar movement, as the axial change seems not to be more pronounced. The confinement due to the force field was different in z than it is in the x, y-plane. Therefore, for measurement intervals $0.1\,\mathrm{s} < \tau < 2\,\mathrm{s}$ the slope was smaller than -0.5 as we would expect for a harmonic confinement. In fact, for z it was -0.39, whereas for x and y -0.48 held, all fit in 97 % confidence intervals. Good magnetic tweezers calibrations account for this slightly anharmonic behavior in the plane, by a surface corrected drag

coefficient. It is noteworthy that these 'planar slopes of the Allan deviation' were different than for the TPM experiments (Fig. 16). The rotational motion of the bead is limited by the alignment of the magnetic moment m. This should be in the same order of magnitude as the torsional rigidity of a double-stranded DNA molecule for TPM experiments. Still, holding the bead away from the surface changes the slope significantly. For that reason, the non-Gaussian position distributions in tethered-particle assays are rather caused by gradients in the confining force (magnetic field gradients, surface charges, etc.) than by torsional constraints.

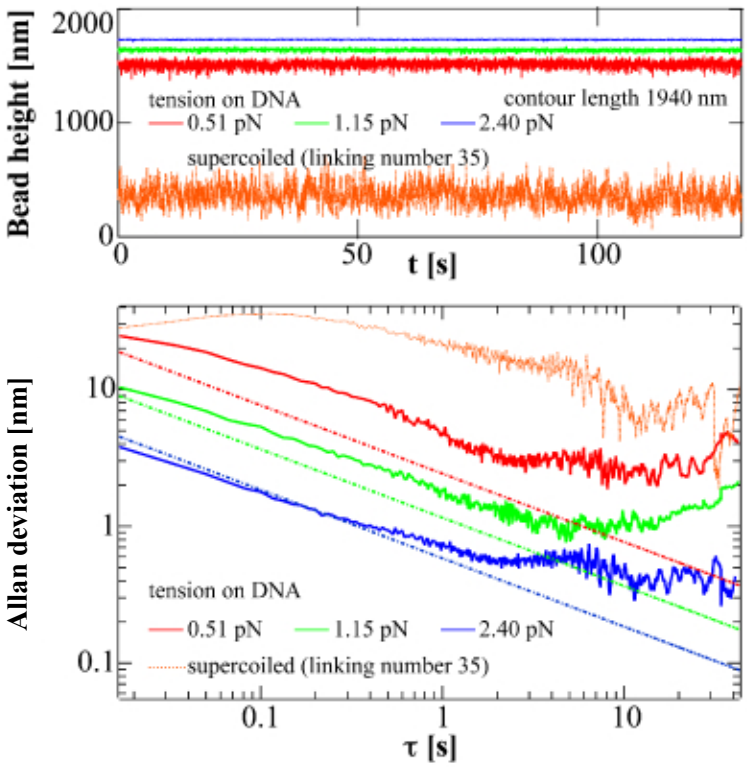

Figure 18: **top** Time series of bead for different tension on tethering DNA (contour length 1940 nm) and for the same supercoiled DNA tether (tension 0.51 pN). **bottom** Allan deviation of plotted time series. The dashed-dotted lines are guides-to-the-eye for thermal limits if assumptions would be made as for harmonic confinement. Introducing plectonemic supercoils increased the intrinsic noise.

We systematically varied the pretension on a double-stranded DNA tether that was torsionally constraint until plectonemic supercoils could be introduced. By turning the external magnets 35 times, the fluctuations of the reporter bead increased, indicating a weaker confinement due to the mobility of the plectonemic structures

(Fig. 18 top). As expected, the deviation and therewith the accuracy is a function of the tension on the DNA. Allan variance is beneficial here, since it quantifies these effect directly. The double-stranded DNA tethered suppresses fluctuations in comparison to the single-stranded one, as a simple comparison of the values in Fig. 18 bottom and Fig. 17 b convinces us. In case the tether length would be exactly the same, this kind of analysis could relate to the different torsional constraints or the different solutions to the partition function. More important though, Allan variance analysis quantifies the inaccuracy that arises from the additional internal dynamics of the plectonemic structures on the DNA. If in a certain experimental setting the activity of a plectonem-removing enzyme like topoisomerase IB could be resolved, is directly shown in a plot like Fig. 18 bottom. Thus, Allan deviation plots hold the potential to serve as a map to dissect good experimental conditions such as DNA tether length, number of present supercoils, tension on tether, etc., from those that potentially bury information within internal noise.

8.3 Fluorescence Single-Molecule Techniques

There are a number of advantages of low and single-molecule fluorescence experiments. With constantly improving cameras for detection, artificial enhancement to boost fluorescence signals is not necessary anymore. The quality of single-molecule fluorescence data also keeps improving, so even rather subtle effects as the influence of fluorescence markers on the diffusion of an object can be addressed. This is particularly important for the interpretation of experiments like RNA diffusion/transport in cells [Golding et al., 2005].

Here, we just want to endorse Allan variance analysis once more, as an assumption-free method that puts it in line to other analysis. It is common to argue that, for a distribution of photons form a single source, the center position of the distribution function can be determined with an accuracy of [Bobroff, 1986, Walter et al., 2008]:

$$SE_{<x>,\,\mathrm{Bobroff}} = \sqrt{\frac{\sigma_x^2}{N_{\mathrm{ph}}} + \frac{a^2}{12N_{\mathrm{ph}}} + \frac{8\pi\sigma_x^4 b^2}{a^2 N_{\mathrm{ph}}^2}} \tag{34}$$

with the number of collected photons N_{ph}, the effective pixel size a, and the noise from signal and detector background b. Following this argument, usually the number of photons is estimated correctly to a factor 2, the effective pixel size is fairly well measured, whereas the noise from detector and background must be determined in a leading-up experiment. The measurement accuracy (Eq. (34)) assumes a normal distribution, and uses the standard variance. Most observations of fluorescence are taken for minutes with shutter times of a few milliseconds. A mixture of highpass filters and "smoothing-by-eye" very often tries to account for drift. We have uttered our critizism to these approaches in section 6, and are excited to become part of a discussion on findings deriving from Allan variance analysis of single-molecule fluorescence data.

By the same token, the setting-up and interpretation of various assays of fluorescence energy transfer (FRET) data, improves by the same standards, and seems to become one of the main or maybe the domineering sources for rate constants of very complex enzymatic machineries [Wu et al., 2010, Stone et al., 2007]. Going a step further, FRET experiments are investigated for, e.g., lag times of enzymatic initiation and measurements of rare intermediates. Allan variance applied to the two recorded fluorescent intensities and to the effective FRET value could underscore and potentially emphasize the stability of the actual measurements, and also serve as a map for observable rates as suggested in subsections 8.1 and 8.2.

PhD Thesis

Fabian Czerwinski

Allan Variance Analysis and Fast Camera Detection Schemes for Optical Tweezers

Academic Advisor: Lene B. Oddershede

Submitted: September 27, 2010

FACULTY OF SCIENCE
UNIVERSITY OF COPENHAGEN

PhD Thesis

Fabian Czerwinski

Allan Variance Analysis and Fast Camera Detection Schemes for Optical Tweezers

Academic Advisor: Lene B. Oddershede

Submitted: September 27, 2010

Optical Tweezers as Diagnostic Tool

A lot of optical applications and setups have shaped our understanding of biological systems, and investigated their kinetics and dynamics. Two other major technological developments are boosting coherent, standardized, and directed investigations of biosystems: biotechnology and nanotechnology. Biotechnological approaches typically cover the synthesis of proteins and biological products in small cellular units. This allows for very sensitive engineering of test systems to understand the basic mechanisms that trigger and control processes in biological systems. Nanotechnology on the other hand covers the extreme miniaturization of material. When materials whose properties in bulk are quite well-established are sized down to compositions of countable atoms or molecules, their optical, chemical and physical properties change dramatically. A handwaving, simple argument is the ratio of surface to ensemble molecules. In reality, the story is more complex, since, e.g., also local modifications (semiconductor doping, local surface modifications), sorting and surface-coatings must be conceptualized as property alterations at the nanoscale.

In our studies, we focused on materials that form stable structures at the nanoscale. But not everything that is smaller than some arbitrary 100 nm is necessarily a *nanoparticle*. We are working with Auffan's published "definition of inorganic nanoparticles for an environmental health and safety perspective" [Auffan et al., 2010]. Therein, the authors argue towards a more elaborated definition that includes thermodynamical and size-dependent interfacial properties with an emphasize of the impact on biological effects by, e.g., oxidative stress or the release of toxic ions. This definition holds for the gold and silver particles [Hansen et al., 2005, Bosanac et al., 2008, Selhuber-Unkel et al., 2008] and for the cadminum selenide quantum dots mentioned in this thesis [Jauffred et al., 2008b, Jauffred et al., 2010]. Most carbon nanostructures also form stable nanoparticles. Here, fullerenes form a model subgroup. Fullerenes are very condensed carbon structures, of at least 60 carbon atoms in the densest packing.[6] Their packing at the atomic scale reassembles a soccer ball (C_{60}) or variations of rugby balls (C_{70}, C_{84}). The outer diameter is about 1 nm and the average atom-atom distance approximately 0.14 nm. Since their discovery in 1985, probably because of the well-defined structure, they became "physicists' darling" through an uncountable number of conducted studies with various techniques.

Fullerenes also draw a lot of attention with respect to commercial solutions. The successful synthesis of fullerene derivatives, for instance, oxidized $C_{60}O$ or hydroxylated $C_{60}(OH)_{22}$, broadened the potential use in products. Examples are fullerenes

[6] Sometimes, carbon nanotubes are considered part of the fullerene family, too. We only call fullerenes those carbon nanostructures that form stable minimal crystals and have more than four symmetry axes.

as doping in solar cells, or as UV-absorbent in closed applications, not exposed to the consumer. Where they become directly exposed to consumers, international legislation in the EU and the USA forces the manufacturer to label the product. The strangest example might be the C_{60}-coating a Japanese manufacturer offers for their bowling balls [Hood, 2004]. As properties change at the nanoscale, and risks become very difficult to evaluate and to assess, the potentially toxic impact of fullerenes, just as for many other nanoparticles, must be investigated. Politically, it is a discourse between consumer rights and safety on the one and commercial promises on the other side. Scientifically, it is the necessity to establish standards when assessing the risk of nanoparticles. Nanotoxicology is the branch of scientific research that standardizes the impact of nanoparticles on human health [Oberdörster et al., 2005]. Because fullerenes are not biodegradable, but at the same time they are nowadays produced in quantities that exceed the natural occurring ones by orders of magnitude, environmental toxicologists have been starting to address also questions about fullerenes in an environmental context. The impact of nanoparticles on ecosystems, geo-, and biophysical formations at large scale inspires the discipline of nanoecotoxicology [Behra and Krug, 2008]. Here, arguing from the basis of a concerted approach that modern technologies enable us to, scientists take up the cudgels for a design of safer materials for the future.

Nanotoxicology lacks standardized methods to label certain nanoparticles as toxic. An anecdote that draw a lot of attention exemplifies this. In 2004, Eva Oberdörster published a study where she had exposed juvenile largemouth bass to fullerenes by adding C_{60} in solvent to the aquarium [Oberdörster, 2004]. Then, a disorientation of the fish was observed and they eventually died. The researcher related these observations to the measured uptake of fullerenes into the brain tissue. Two years later at a conference, Henry et al. presented data about the mortality rate of zebrafish when exposed to C_{60} and when exposed to the solvent THF only [Henry et al., 2007]. The control showed that the increased mortality was caused by the solvent only, with no impact of the C_{60} molecules.

In another perspective, toxicology provides an advantage of knowledge and tools from surface chemistry, analytical chemistry, material sciences and toxicology itself [Behra and Krug, 2008]. Our goal was therefore, to emphasize the capability of modern single-molecule techniques as supportive tools to address questions in nanotoxicology. Specifically, we focused on the interaction of fullerenes and fullerene derivatives with nucleic acids. We propose a quasi bottom-up approach with the general idea to investigate the interaction that might trigger potentially harmful consequences for biological processes.

Scenario of nanotoxic interferences of fullerenes for regular cellular processes. We needed to embed our single-molecule approach into a scenario that would frame the potential danger of fullerenes to biological processes. In this scenario, individual fullerene derivatives or agglomerates of fullerenes in aqueous solution diffuse

and eventually penetrate into or through cells or membranes [Monticelli et al., 2009, Chen et al., 2010a, Wong-Ekkabut et al., 2008]. Once they are inside a cellular environment, they can form specific or non-specific complexes with nucleic acids. Affinity and binding strength might be so high that regular enzymatic function becomes impossible. For instance, the transcription of a DNA site with a strongly bound fullerene might be impossible, resulting in inaccessible genetic code. The dose assessment during all steps of the scenario must be kept controlled. On the single-molecule scale this is reflected by monitoring the concentration of fullerenes at any time.

At the beginning of section 9, we introduce a simulation study about the interaction of a single fullerene with a nucleic acids. From the limitations and shortcomings of this study, we derive an experimental strategy to capture the mechanical behavior of fullerene-DNA interactions. Divided in subsections, we mainly used three different single-molecule techniques to establish proof-of-principle experiments for their usage as diagnostic tools in nanotoxicology. For the preliminary experiments presented, we used commercially available fullerenes C_{60} and fullerols $C_{60}(OH)_{22}$ purchased from BuckyUSA, Houston.

9 Binding of Fullerenes and Fullerols to DNA

A particular scenario that one could imagine has been captured by a molecular-dynamics simulation [Zhao et al., 2005]. In a cubic box with 7 nm edges in aqueous solution with monovalent sodium ions (approximately 3 M), one single C_{60} and a 12 bp long double-stranded DNA interacted as depicted in Fig. 19 A. For all atoms in the systems, the AMBER force field was used. The 60 C-atoms of the fullerene though were modeled as so-called Lennard-Jones particles with certain parameters. Because of this choice of parameters, the C_{60} fullerene interacted with the environment through a 0.9 nm shell around it. The shell was cut off to prevent long range interactions. Initial configurations for the surfaces of the DNA and the fullerene were chosen to be as close as 0.7 nm. Then the entire molecular system fluctuates to simulate the first 15 ns of the actual reaction. In these very specific circumstances, not surprisingly, the fullerene bound to the DNA backbone, establishing tight bonds with the phosphor atoms. For the one simulation rendered in Fig. 19A, the binding energy was found to be 35.7 kcal/mol, i.e., $59.5\,k_{\mathrm{B}}T$ at $T = 300\,\mathrm{K}$.

There are a few problems with this kind of all-atoms/molecular-dynamics simulations in general and with that simulation in particular. Generally, molecular-dynamics simulations only probe very short reaction times because of the high computational costs that the positional updates of those systems with circa 6,000 molecules. Furthermore, the choice of a particular force field is at least challenging. Often, a certain research group simulates with the force fields that they are most experienced with. These are most often specialized towards different anticipated properties. Since we are not at all experts for molecular-dynamics simulations, we are not able to judge

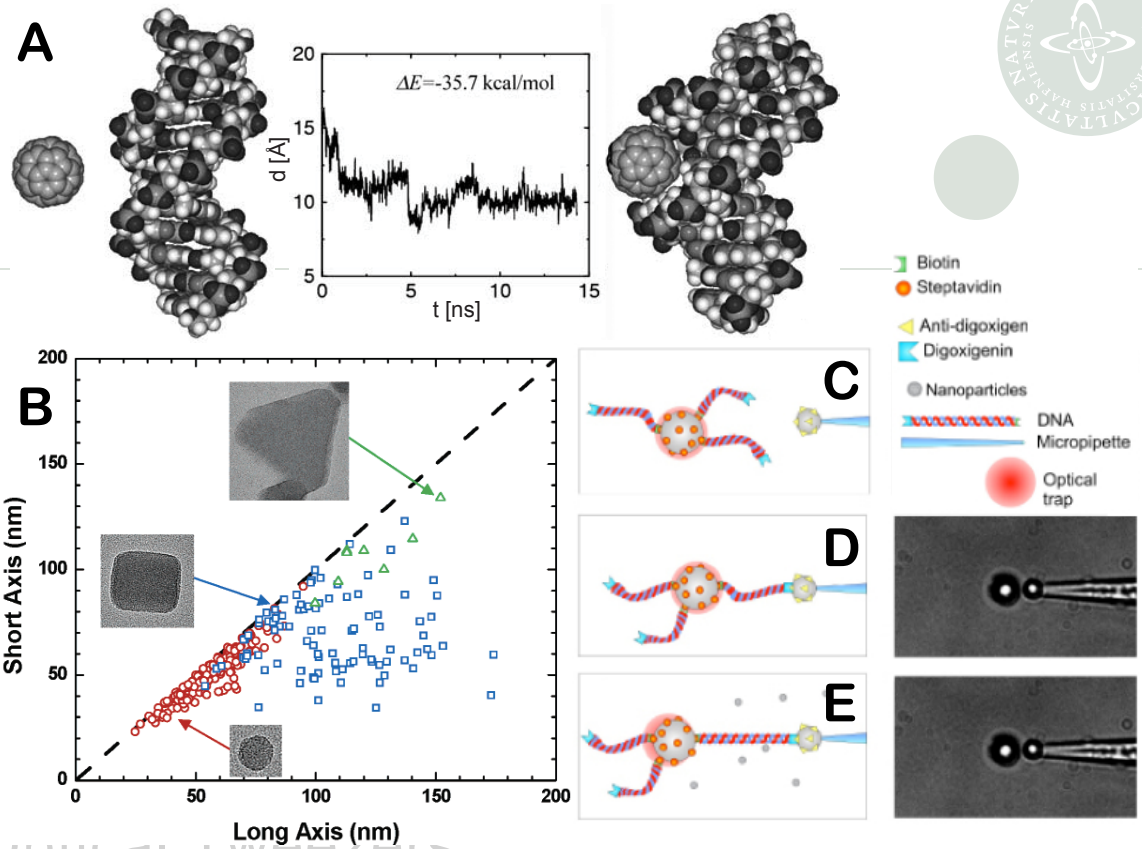

Figure 19: **A** Molecular dynamics simulation of an individual fullerene C_{60} in the vicinity of a 12 bp double-strand DNA [Zhao et al., 2005]. From the typical starting configuration (left snapshot) the fullerene binds into he minor groove of the DNA (right snapshot) with binding energy of 35.7 kcal/mol, i.e., $59.5\,k_{\mathrm{B}}T$ at $T = 300\,\mathrm{K}$. For the remainder of the simulation, the fullerene does not leave the "docking site". The distance between the C_{60}'s center of mass and that of the DNA minor groove site is plotted. **B** Fullerenes aggregate in water to nC_{60} [Fortner et al., 2005]. nC_{60} size and shape distribution. Small aggregates are typically circular in cross-section, intermediate and large ones tending to be rectangular, and with a small fraction of triangular larger particles. **C-E** Experimental strategy in single-molecule optical tweezers experiment. An anti-digoxygenin coated polystyrene sphere is mounted on a pipette, and a DNA-coated sphere is calibrated in the vicinity. Once a DNA tether has formed, the DNA is put under tension and the displacement of the trapped sphere is recorded. Repetitive stretching and relaxing ensures the probing of a single DNA. Nanoparticles, e.g., fullerenes, are flushed in. If the DNA's elasticity changes, a change in the force extension relation shall be observed. Drawings by Dejan Trpcevski.

the use of the AMBER force field in this context. More particularly, the modeling of the C_{60} fullerene by Lennard-Jones potentials with a sharp cut-off at 0.9 nm but placing it 0.7 nm close to the DNA surface, already suggested the binding to happen at a certain position along the DNA. We speculate that this happened to be the minor groove simply because of the chosen initial conditions. The concentration of monovalent sodium was very high. Potassium rather than sodium is usually more relevant for biological processes related to DNA. And multivalent ions were not even considered although they play an important role in a biological context. Also, picking an individual C_{60} fullerene was not the best choice, since they are hydrophobic, and hence form agglomerates in aqueous solutions.

Fullerenes that are an organized structure of carbon atoms are essentially not charged, so they appear hydrophobic. In charged solvents like water, they from aggregates called nC_{60} [Fortner et al., 2005]. In a careful study, Fortner et al. analyzed the size and shape distribution of these nC_{60} aggregates, replotted in Fig 19 B. The smallest nC_{60} that they found were spherical with a diameter of 26 nm, the largest more than 150 nm.

9.1 Optical Tweezers

We wanted to understand the interaction of single fullerene derivatives or agglomerates of fullerenes with nucleic acids on the single-molecule level. For this purpose we designed an optical tweezers experiment that would probe the change in the elastic response of a single DNA molecule upon binding of carbon nanoparticles. Figure 19 C-E illustrates our experimental strategy. An anti-digoxigenin-coated polystyrene sphere is mounted on a pipette, and a biotin-coated sphere grafted with DNA inside an optical trap is calibrated in the vicinity. After suspension of a DNA molecule between the two spheres, the DNA is stretched. The displacement of the trapped sphere is recorded and proportional to the actual force on the DNA. Repetitive stretching and fitting to the worm-like chain model for forces up to 12 pN ensures the probing of a single DNA if a persistence length $L_p \approx 50\,nm$ is found [Wang et al., 1997, Husale et al., 2008]. The buffer (10 mM Tris, 10 mM Mg^{2+}, 100 mM Na^{+}) is gently replaced by one that contains carbon nanoparticles, e.g., fullerene agglomerates or derivatives, using the microfluidic system described in subsection 5.1. If we observe a change in the force-extension relation, we can interpret the response upon the binding of the particles to the DNA. We started with nC_{60}, and continued with the hydroxyl fullerene derivatives ($C_{60}(OH)_{22}$) that are dissolvable as individual particles in aqueous solution. Using the derivatives allowed for a study at controlled particle concentration rather than the crude filtering approach we applied to solutions containing nC_{60} where we could only estimate the final concentration of aggregates.

We applied the experimental strategy explained above using double-stranded, 3,256 bp long DNA molecules. These molecules had a biotin label at one end, and digoxygenin label on the other. The protocol to produce these DNA molecules from

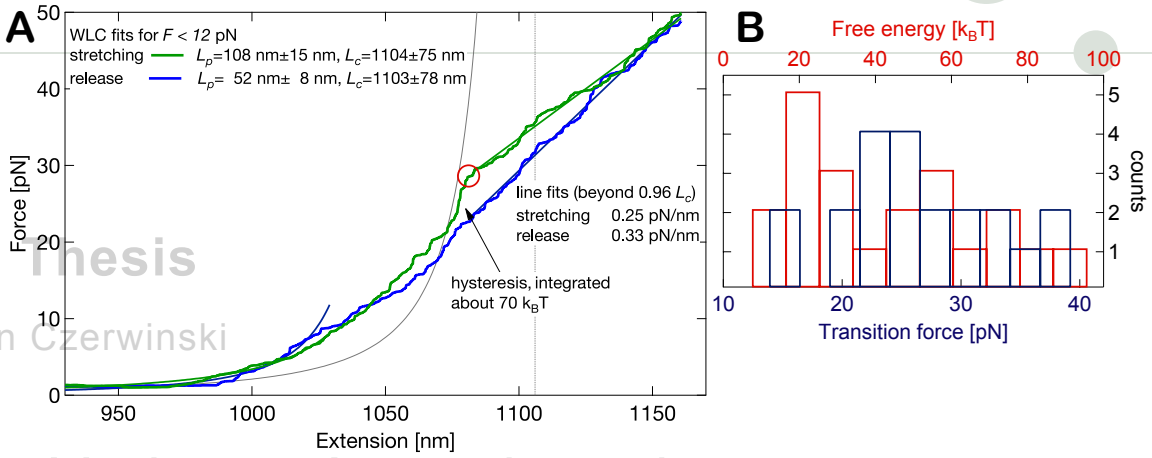

Figure 20: Stretching of single DNA molecules in the presence of nC_{60} using optical tweezers. **A** Upon the formation of the specific bonds, we tested for a single DNA tether between two polystyrene spheres by fitting force-extension measurements by the worm-like chain model (grey graph, persistence length $L_p = 53\,nm$, data not plotted). The contour length $L_c = 1107\,nm$ is indicated by the dotted line. The solution was substituted for nC_{60}-containing buffer. The tension was gradually increased up to 50 pN and released in the same manner. The total measurement time here is 9 s, data is acquired with 22 kHz, and median-smoothed of 1 ms time intervals. A stark difference of the force-extension curve prior to nC_{60} exposure is observed. The stretching happened in a worm-like chain behavior with significantly increased persistence length until at some transition force (red circle) a linear relation dominates. When the tension is released, we observe a hysteresis between stretching and release with free energies from 12–80 k_BT. **B** The distribution of transition forces and free energies of 21 force-extension curves. Transition forces mark the beginning of distinct harmonic spring behavior. The free energy is the area between stretching and release curve. Table 3 provide the numerical values.

PCR and the exact sequence have been described in [Hansen, 2008, p. 30]. The calibration was done prior to tethering (Fig 19 C) using the protocol introduced in subsection 4.2. We filtered the nC_{60}-containing buffer three times by using Millipore 50 nm pore size filters. Because most of the fullerenes agglomerated in larger clusters (Fig. 19 B), we estimated to recover only 10 % of the amount of initial fullerenes in suspension and considered this as upper limit of fullerene concentration.[7] We measured 12 individual DNA molecules, and obtained 21 pairs of stretching and tension releasing force-extension curves. Substituting the buffer with the nC_{60}-containing one was the most difficult step as often dirt or other particles were captured inside the trap. Not trapping the sphere for a while would result in sticking of the spheres to each other which was pretty irreversible. The development of the very low volume flow chambers was crucial. Prior to experiments isopropanol cleaned the chambers, then we re-used them.

A typical result for a pair of force-extension curves is plotted in Fig. 20 A. Qualitatively, all observed pairs behave the same. The DNA molecule is stretched and follows for low forces more or less a worm-like chain behavior until at a curve specific transition force a distinct harmonic spring behavior is observed. When the tension is released, and we observed a hysteresis between stretching and release with free energies in the order of 12–80 k_BT. Table 3 provides the numerical value for transition forces and free energies. The transition force was taken to be the value where the measured force was 10 % different than expected for purely harmonic behavior (fits for extensions larger than $0.96L_c$). Therefore, the error for the transition force could be as high as ±5 pN. The free energy is the area between stretching and release curve. There is no distinct distribution noticeable, and the mean of the transition force is 23.5 ± 7.9 pN and the mean of the free energy $51 \pm 22\, k_BT$.

From these kind of pairs of force-extension relations, we conclude a severe impact of the binding of nC_{60} agglomerates to DNA molecules. Even strong tensions were not sufficient to permanently unbind agglomerates nor washing, since the force-extension behavior never reassembled the one of DNA in the absence of nC_{60}. Two tethers could have been stretched four and five times, respectively, before they ruptured. The history of these tethers did not reassemble any trend (see events 4–8 and 17–20 in Table 3). We also varied the stretching speed for event pairs (11,12) and (13,14) by a factor of 3. Here the amount of data is not adequate to draw any conclusions, but it might indicate that loading rate did not change the observed behavior. This was also not expected because DNA dynamics are much faster, and thus always in equilibrium under these experimental conditions. Here, we do not necessarily claim to see worm-like chain behavior for low forces. But, when treating the DNA molecule as extrapolated, 'exact' worm-like chains [Crut et al., 2007], we found for 80 % of the pairs a significantly higher persistence length than 50 nm for stretching and approximately 50 nm for release. This set of experiments could also not rule out one scenario: Maybe nC_{60} could form 'bridges' between different DNA

[7] Buffers containing water-soluble hydroxyl fullerene derivatives $C_{60}(OH)_{22}$ were not filtered.

event number	1	2	3	4	5	6	7	8	9	10
transition force (pN)	28.1	32.4	33.2	28.0	26.8	12.4	25.8	23.1	15.9	16.1
free energy (k_BT)	70	67	89	65	34	12	45	48	52	49

11	12	13	14	15	16	17	18	19	20	21
19.0	18.2	18.1	17.9	40.5	17.3	25	14.9	29.8	36.2	15.3
80	28	49	36	91	37	36	15	52	74	42

Table 3: Transition forces and free energies of force-extension relations for double-stranded, 3,256 bp long DNA molecules in the presence of nC_{60} agglomerates with smaller diameters than 50 nm and estimated concentrations smaller than 40 nM.

molecules on the trapped sphere rather than solely affecting the initial tether. From the number of streptavidin binding sites we estimated about 20 DNA molecules per sphere. Lower concentrations did not allow for acceptable rates of initial tether formation. It is also in the same order of magnitude as studies with comparable DNA constructs [Husale et al., 2008]. Still, we could not rule out this scenario.

With these single-molecule experiments, we found the severe impact that nC_{60} agglomerates have on individual DNA molecules. They bind already for low concentrations of 40 nM. This estimate is very conservative as likely less than 10 % are recovered after multiple filtering procedures. The agglomerates smaller than 50 nm are formed of up to 80 C_{60}. So, a single agglomerate in 1 μL can bind to DNA and severely affect the genetic function as our incapability of pulling off or washing off the agglomerate indicates. A follow-up single-molecule study must address these findings with an emphasize on the concentration dependence of the binding affinity. Future studies should include answers to questions if there is a critical concentration and what are the kinematics of this binding. To address these questions it is crucial to control the concentrations more carefully. This is almost impossible for hydrophobic particles such as C_{60}. A promising way, however, is provided by water-soluble hydroxyl fullerene derivatives such as $C_{60}(OH)_{22}$, even though their surface properties are different due to the 22 hydroxyl groups on their surfaces.

We used a single-beam optical tweezers successfully as a tool to show the interaction of fullerene agglomerates with individual DNA molecules. Furthermore, we were able to address quantitative questions such as an upper limit for minimal concentrations of binding, and the incapability to unbind DNA-nC_{60} clusters by piconewton forces. We also described the qualitative behavior of the force-extension response of these clusters that might allow for speculating on binding mechanisms.

9.2 Atomic Force Microscopy

In the previous subsection 9.1 we showed how we monitored the interaction of fullerene agglomerates indirectly, i.e., without *seeing* the actual binding. The scientific approach was to use complementary techniques to address the system of interest with focus on a different quantity, aspect, or length scale. For biophysical systems that can be confined to a surface without dramatically changing their interaction with the environment, atomic force microscopy (AFM) is a very good possibility to resolve and localize static structures. Very good examples have been published [Moreno-Herrero et al., 2005a, Moreno-Herrero et al., 2005b]. DNA molecules can be deposited to a surface in different ways [Rivetti et al., 1996]. We used Mg^{2+} ions to project the 3d-arrangement of DNA molecules in solution onto a freshly cleaved mica surface, as shown for 48 kb long λDNA in Fig. 21 after 30 s incubation time (10 mM Tris, 100 mM K^+, 5 mM Mg^{2+}) and gentle washing with deionized water. For these kind of experiments, a number of prerequisites must be fulfilled, in particular when local structures like kinks or localized bending are observed [Moreno-Herrero et al., 2006, Wiggins et al., 2006]. The most important prerequisite is the ultrasharp AFM tip at the extremity of the cantilever whose bending reports the probing of the surface. It ultimately sets the resolution limit in the x, y-plane, there is virtually no resolution limit in z-direction. We used PPP-NCLR-10 tips (Nanosensors, NanoWorld AG) with < 10 nm nominal radius on a Nanosurf Atomic Force Microscope that operated in tapping mode.

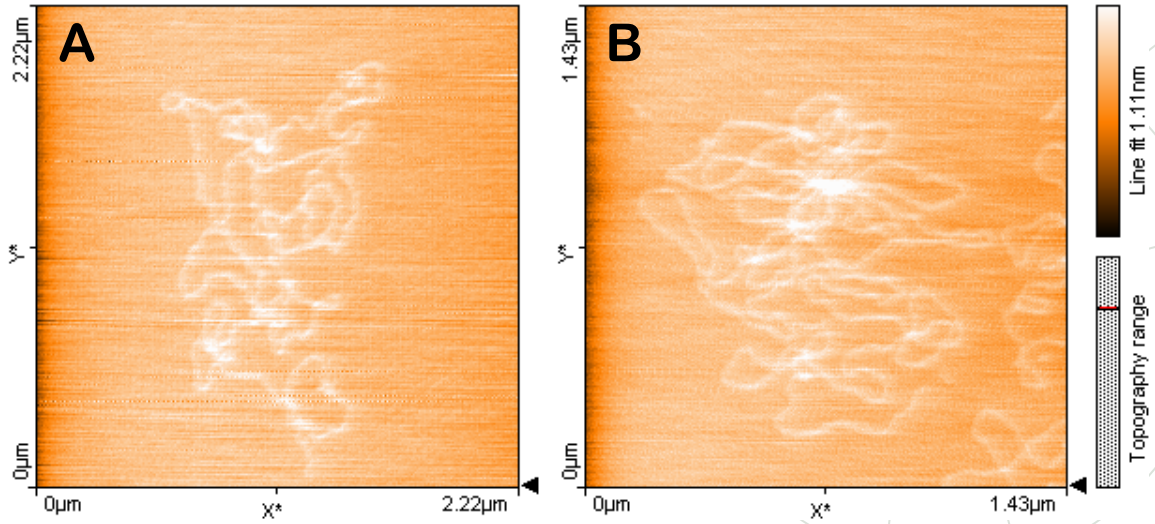

Figure 21: λDNA ($L_c = 16.7\,\mu$m) deposited on mica **A** without and **B** with 40 nM $C_{60}(OH)_{22}$. Prior to deposition, 50 ng λDNA were kept in 100 μL buffer (10 mM Tris, 100 mM K^+, 5 mM Mg^{2+}). Incubation and imaging were performed at room temperature. An image was recorded every 10 s in tapping mode on a Nanosurf AFM using 10 nm radius tips.

Besteman et al. employed AFM to investigate DNA condensation by multivalent ions [Besteman et al., 2007]. As speculated above fullerenes might condense DNA in a comparable manner. We mixed 50 ng λDNA in 100 μL buffer (10 mM Tris, 100 mM K^+, 5 mM Mg^{2+}) with fullerol-containing buffer (final concentration: 10 mM Tris, 100 mM K^+, 5 mM Mg^{2+}, 40 nM $C_{60}(OH)_{22}$), and let it incubate for 30 min before a 10 μL drop was put on freshly cleaved mica and gently washed with deionized water, just as the control. The AFM pictures showed an interesting feature.

Quite distinct from the control, we found for the fullerol-incubated DNA samples (Fig. 21 B) hubs of crossing DNA strands, just like Besteman et al. reported for condensed DNA [Besteman et al., 2007]. We tested three different batches with 40 nM $C_{60}(OH)_{22}$, and two with 20 nM $C_{60}(OH)_{22}$. We visualized 4×6 molecules for each batch of which approximately half showed hub-like structures. The AFM images though did not look great for a number of reasons. The Nanosurf AFM drifted quite a bit, so the line scan rate was kept high causing a loss in achievable resolution. The tips were to large to really resolve accurately local DNA structures, e.g., of potential condensation sites. This is also the reason why the data was not of adequate quality to apply DNA tracing algorithms [Wiggins et al., 2006].

If the hypothesis of DNA condensation by fullerenes and/or fullerols holds, AFM is the perfect tool to visualize it. We found good indication for DNA condensation by fullerols at moderate concentrations already, although a comprehensive AFM study must be performed with better equipment, i.e., a stabler atomic force microscope and sharper tips that are slightly stiffer than the ones used here. However, as a complementary technique to the optical-tweezers study in subsection 9.1, again, we observed fullerenes interacting directly with DNA, even though for experimental reasons we only investigated the hydroxylated fullerene derivative. Even though our technical equipment was not perfectly adjusted to our purposes, we are careful and thoughtful in drawing preliminary conclusions. We only know of one other example of AFM investigations of potentially toxic carbon nanostructures and DNA [An et al., 2010]. There, the conclusion was drawn upon very few samples and a postulated correlation to electron microscope pictures. This is once more an example for the importance of standardizing protocols in nanotoxicology.

9.3 Translocation through Glass Capillaries

In recent years, nanopores of different kinds have drawn a lot of attention as high throughput devices for biological material such as DNA, DNA-protein complexes, or colloid graftings [Dekker, 2007, Stein, 2007, Steinbock et al., 2009]. Glass capillaries provide a good alternative to very labor-intense solid-state nanopores. By laser-assisted pipet pulling, quartz glass nanocapillaries as small as 45 nm can routinely be produced [Steinbock et al., 2010]. The electron microscope picture of such a glass capillary is shown in Fig. 22(a). Steinbock et al. embedded this capillary into a custom-designed PDMS holder, leaving it the only possibility to passage from one reservoir to another (Fig. 22(b) and (c)). When an electric potential is applied over

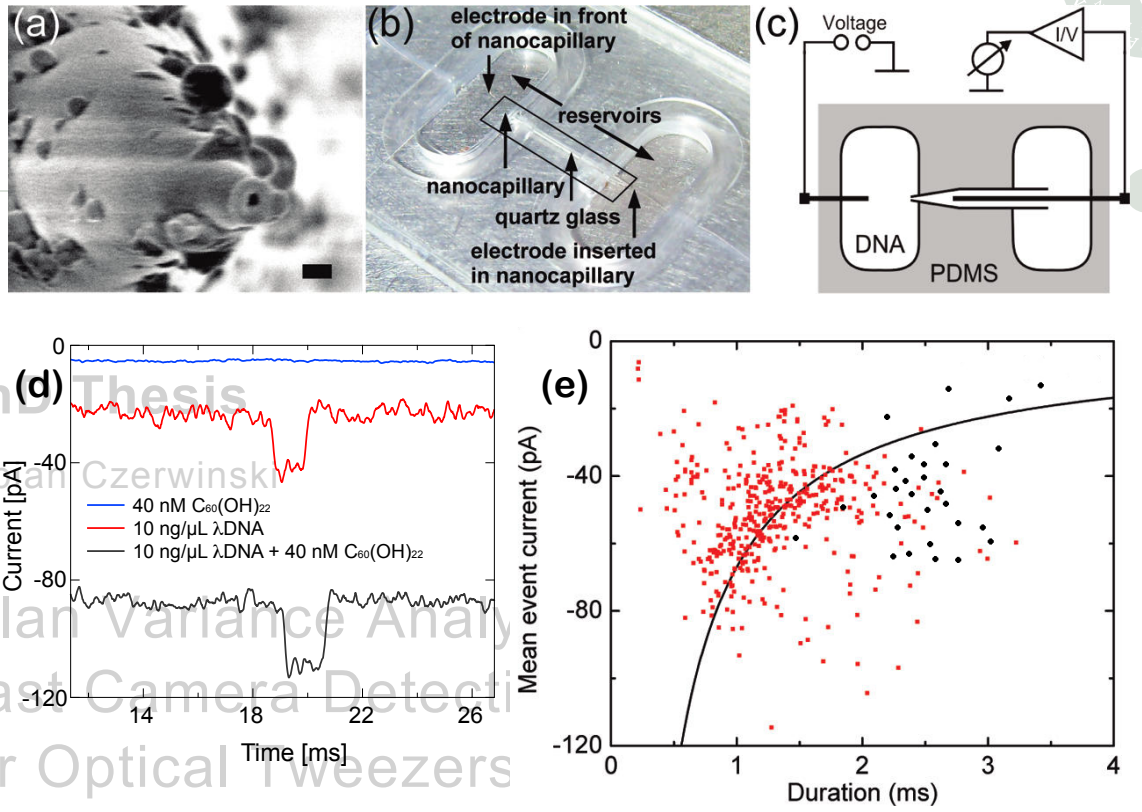

Figure 22: **(a)** Electron microscope of glass capillary with 45 nm inner diameter at the tip [Steinbock et al., 2010]. The scale bar is 100 nm. **(b)** Photograph of the PDMS cell with two reservoirs which were connected by the nanocapillary [Steinbock et al., 2010]. One electrode was placed in the reservoir, facing the nanocapillary. The second electrode was inserted into the capillary from the opposite reservoir. **(c)** Schematic of the experimental setup with sample cell, nanocapillary and measuring circuits [Steinbock et al., 2010]. **(d)** Translocation experiments with 10 ng/μL λDNA in 40 nM $C_{60}(OH)_{22}$, 10 mM Tris, 100 mM K^+, and with controls of only 40 nM $C_{60}(OH)_{22}$ and 10 ng/μL λDNA in 10 mM Tris, 500 mM K^+. The buffer had pH 8.0. The applied potential was -500 mV, and the baseline current was -12 nA. The graphs are offset. **(e)** Scatter plot illustrating the duration and mean event current of 431 events for λDNA [Steinbock et al., 2010] and of 29 events for λDNA+40 nM $C_{60}(OH)_{22}$. The black line is calculated with Eq. 35 using the values $t_0 = 1.56$ ms and $\langle I_0 \rangle = -43$ pA to calculate the expected current $\langle I_d \rangle$.

the two reservoirs, an ionic current flows through the capillary. Due to the small cross-section at the tip of the pipet, a translocating molecule can partially block the current. These blockage events are recorded in a change in the current. Li et al. introduced a simple equation for the average current blockade $\langle \Delta I_\mathrm{b} \rangle$ for an event with translocation time t_d [Li et al., 2003]:

$$\langle \Delta I_\mathrm{b} \rangle = \langle \Delta I_\mathrm{o} \rangle \frac{t_0}{t_\mathrm{d}} \quad , \tag{35}$$

where a simple event would show mean current blockage $\langle \Delta I_\mathrm{o} \rangle$ and translocation time t_0. It is a very simple model that assumes two parameters for an exemplary *simple event*, and hence, serves as an estimate for translocation experiments through glass capillaries.

At well-chosen ionic conditions, the current detection during translocation is so sensitive that even the folding of λDNA is detectable [Steinbock et al., 2010].

We decided to investigate, if and to what extend DNA condensation by fullerols would be distinguishable from DNA translocation. We tested dilutions of up to 40 nM $C_{60}(OH)_{22}$ in 10 mM Tris, 100 mM K^+ at pH 8.0 for potentials from −500 mV to 800 mV. No blockage events occurred (Fig. 22(d)). For samples with λDNA we observed translocations events that occurred as dips in the baseline current of 12 nA. We only tested one sample where 40 nM $C_{60}(OH)_{22}$ in 10 mM Tris, 100 mM K^+ at pH 8.0 had been incubated with λDNA for 30 min before we started to apply potential differences. Then we observed 29 events within 14 min. The events were analyzed by a custom-written LabVIEW software and their mean current and their duration plotted in a scatter plot. The plot allowed for comparison to plain λDNA. By eye it seems as if translocation events of DNA that were preincubated with fullerols took slightly longer and had on average larger absolute mean current values than a simple event. A Student's t-test found the chance of the distribution of 29 fullerol/DNA events to be drawn from the bare DNA distribution to be 12.4 %. Hence, we only interpret our findings as indication for the detection of condensed DNA, not as significant proof.

We suggest that DNA-translocation experiments through glass capillaries showed indications of direct interactions of DNA and hydroxylated fullerene derivatives. We consider this single-molecule approach just as optical tweezers and atomic force microscopy a useful complement to other tools in nanotoxicology.

As much as the scenario for potentially toxic implications might be debatable, we think that we showed a direct interaction of the model carbon nanostructure fullerene with nucleic acids that could be a cause of serious danger. We conducted a series of proof-of-principle single-molecule experiments that showed the possibility to examine this question in a very biophysical manner. We stress that the path of the fullerenes towards the nucleic acids goes beyond the scope of this thesis.

Conclusion and Perspective

Our research investigated the application of optical tweezers as a versatile tool in modern biophysics. We locate biophysics as the physicists' contribution to a quantitative understanding of biology and nanotechnological approaches towards biotechnology. Therein, we pointed out the relevance and implications of modern single-molecule techniques. We outlined the ongoing research surrounding optical tweezers and highlighted the importance of detection schemes, choices of biofunctionalized handles, and noise determination for further experimental advancements. We expressed our belief that a comprehensive understanding of biological systems can only emerge from interdisciplinary efforts that manifest themselves in the usage of various quantifying approaches towards answers of scientifically relevant questions. We see this thesis as an attempt to add our improvements of optical tweezers technology to that effort.

We put forward a minimal optical tweezers setup and explained two prominent calibration protocols to be applied. We optimized these calibration protocols by utilizing Allan variance analysis to calculate the optimal calibration intervals from time series. This assumption-free method does reduce the number of assumptions during the calibration procedure. We explained our Monte-Carlo simulations that we used to verify these findings.

We described in detail extensions to the minimal optical tweezers setup and commented on various hardware aspects that need to be carefully considered. The optical components, laser, objective, and illumination, are crucial. Moreover, precise control of microfluidics, handles, and stage, facilitate cutting-edge experiments with advanced options and specific accuracies. Herein, the detection is critical. In addition to high bandwidth photodiode detection schemes, we also implemented a fast CMOS camera scheme. This enabled real-time tracking of optical handles at acquisition frequencies of tens of kilohertz over periods of hours. It also allows for tracking of multiple handles at the same time. This lays the foundation for sophisticated detection and calibration of holographical optical tweezers. The core of this implementation is software based and hence provides a straight forward customization for future camera developments.

We advocated Allan variance analysis as a powerful tool complementary to the power spectral analysis that is classically used for noise characterization in single-molecule biophysics. For this reason we motivated and defined it carefully. Then we elaborated on the mathematical properties and gave explanations of the most essential functional form of Allan variance in biophysical experiments. We put an emphasize on how to construct Allan variance analysis for any measured quantity and exemplified this for active and passive force measurements.

In addition, to determine the optimal calibration interval, we used this method to systematically quantify positional accuracy and force sensitivity of optical tweezers setups. The computation of Allan deviation allows for a direct comparison to the thermal limit over more than six orders of magnitude of measurement times. For a broad collection of trapped handles, it can be used as a measure to distinguish the capability of specific experiments. It clearly differentiates the optimal measurement times for active and passive calibration protocols. Furthermore, it provides a procedure to optimize the acquisition parameters. We also showed its strength at pinpointing the low-frequency noise that is only measured insufficiently by other methods. We identified and quantified the impact of the drift caused by the piezo feedback systems, by illumination paths, and by the specific fluidics in use. In conclusion, we recommend Allan variance analysis as a method to standardize instrumental and experimental parameters for optical tweezers setups.

Our research investigated the implication of Allan variance analysis for other single-molecule techniques. In tethered particle motion experiments, it determines the impact of drift, discriminates the quality of data, compares different handles directly, and probes the precise confinement. In combination with magnetic tweezers, we identified the main contribution of the confinement to be the surface potential and the torsional constraint. For magnetic tweezers, we identified the dominant drift to originate from the relative position of sample and magnets, and could also distinguish its directionality. We also brought a representation forward that would serve as a rate map for observable enzymatic functions. We discussed the potential of this novel method for fluorescence single-molecule techniques with a stress on FRET data. In general, Allan variance analysis holds an opportunity to set standards for comparison among a vast group of supersensitive measurements.

The interactions of nanoparticles with biological matter are the pressing question in the field of nanotoxicology which examines the potential impact upon human health. We designed a single-molecule assay to address a risk scenario which may arise from fullerenes entering cells. Fullerenes and their derivatives serve as model systems of carbon nanostructures. By observing the force-extension relation of single DNA molecules in the presence of fullerene agglomerates, we found strong indications for a direct, non-specific, and irreversible binding to the DNA.

We approached this issue with two additional techniques. Firstly, λDNA was incubated with fullerols, the resulting products were then visualized utilizing atomic force microscopy. We found indication for DNA condensate-like structures, but were limited by the resolution of the setup. Secondly, we monitored λDNA-fullerol products while translocating then through a nanoglasscapillary driven by an electrophoretic force. Initial experiments gesture toward a compacted translocation product, but statistics are not significant at this point.

Coming from the technical-experimental side of optical tweezers application, our research improved setup standards. We applied this to address the potentially toxic impact of carbon nanostructures. In addition, we conducted the above proof-of-principle experiments with other single-molecule techniques. Our approach could be seen as a contribution to the interdisciplinary efforts in nanotoxicology.

Bibliography

[Abbondanzieri et al., 2005] Abbondanzieri, E., Greenleaf, W., Shaevitz, J., Landick, R. and Block, S. (2005). Direct observation of base-pair stepping by RNA polymerase. Nature *438*, 460–465.

[Allan, 1966] Allan, D. (1966). Statistics of atomic frequency standards. Proc. IEEE *54*, 221–230.

[An et al., 2010] An, H., Liu, Q., Ji, Q. and Jin, B. (2010). DNA binding and aggregation by carbon nanoparticles. Biochem. Biophys. Res. Commun. *393*, 571–576.

[Ashkin, 1970] Ashkin, A. (1970). Acceleration and trapping of particles by radiation pressure. Phys. Rev. Lett. *24*, 156–159.

[Ashkin et al., 1987] Ashkin, A., Dziedzic, J. and Yamane, T. (1987). Optical trapping and manipulation of single cells using infrared laser beams. Nature *330*, 769–771.

[Auffan et al., 2010] Auffan, M., Rose, J., Bottero, J.-Y., Lowry, G., Jolivet, J.-P. and Wiesner, M. (2010). Towards a definition of inorganic nanoparticles from an environmental, health and safety perspective. Nat. Nanotechnol. *4*, 634–641.

[Bacia et al., 2006] Bacia, K., Kim, S. and Schwille, P. (2006). Fluorescence cross-correlation spectroscopy in living cells. Nat. Methods *3*, 83–89.

[Behra and Krug, 2008] Behra, R. and Krug, H. (2008). Nanoecotoxicology: Nanoparticles at large. Nat. Nanotechnol. *3*, 253–254.

[Bendix et al., 2010] Bendix, P., Reihani, S. and Oddershede, L. (2010). Direct Measurements of Heating by Electromagnetically Trapped Gold Nanoparticles on Supported Lipid Bilayers. ACS nano *4*, 2256–2262.

[Berg-Sørensen and Flyvbjerg, 2004] Berg-Sørensen, K. and Flyvbjerg, H. (2004). Power spectrum analysis for optical tweezers. Rev. Sci. Instrum. *75*, 594–612.

[Berg-Sørensen et al., 2003] Berg-Sørensen, K., Oddershede, L., Florin, E. and Flyvbjerg, H. (2003). Unintended filtering in a typical photodiode detection system for optical tweezers. J. Appl. Phys. *93*, 3167–3176.

[Berg-Sørensen et al., 2006] Berg-Sørensen, K., Peterman, E. and Weber, T. (2006). Power spectrum analysis for optical tweezers II: Laser wavelength dependence of parasitic filtering. Rev. Sci. Instrum. *77*, 63106.

[Bernacchia and Pigolotti, 2009] Bernacchia, A. and Pigolotti, S. (2009). Self-consistent method for density estimation. arXiv *stat.ME*, 0908.3856v5.

[Besteman et al., 2007] Besteman, K., van Eijk, K., Vilfan, I., Ziese, U. and Lemay, S. (2007). Influence of charged surfaces on the morphology of DNA condensed with multivalent ions. Biopolymers *87*, 141–148.

[Betzig et al., 2006] Betzig, E., Patterson, G., Sougrat, R., Lindwasser, O., Olenych, S., Bonifacino, J., Davidson, M., Lippincott-Schwartz, J. and Hess, H. (2006). Imaging intracellular fluorescent proteins at nanometer resolution. Science *313*, 1642–1645.

[Biancaniello and Crocker, 2006] Biancaniello, P. and Crocker, J. (2006). Line optical tweezers instrument for measuring nanoscale interactions and kinetics. Rev. Sci. Instrum. *77*, 113702.

[Blanco and Walter, 2010] Blanco, M. and Walter, N. (2010). Analysis of complex single-molecule FRET time trajectories. Methods Enzymol. *472*, 153–178.

[Bobroff, 1986] Bobroff, N. (1986). Position measurement with a resolution and noise-limited instrument. Rev. Sci. Instrum. *57*, 1152–1157.

[Bormuth et al., 2008] Bormuth, V., Jannasch, A., Ander, M., van Kats, C., van Blaaderen, A., Howard, J. and Schäffer, E. (2008). Optical trapping of coated microspheres. Opt. Express *16*, 13831–13844.

[Bosanac et al., 2008] Bosanac, L., Aabo, T., Bendix, P. and Oddershede, L. (2008). Efficient Optical Trapping and Visualization of Silver Nanoparticles. Nano Lett. *8*, 1486–1491.

[Bronstein et al., 2001] Bronstein, I., Semendjajew, K., Musiol, G. and Mühlig, H. (2001). Taschenbuch der Mathematik. Harri Deutsch, Thun and Frankfurt am Main.

[Brutzer et al., 2010] Brutzer, H., Luzzietti, N., Klaue, D. and Seidel, R. (2010). Energetics at the DNA supercoiling transition. Biophys. J. *98*, 1267–1276.

[Carter et al., 2009] Carter, A., Seol, Y. and Perkins, T. (2009). Precision surface-coupled optical-trapping assay with one-basepair resolution. Biophys. J. *96*, 2926–2934.

[Cheezum et al., 2001] Cheezum, M., Walker, W. and Guilford, W. (2001). Quantitative comparison of algorithms for tracking single fluorescent particles. Biophys. J. *81*, 2378–2388.

[Chen et al., 2010a] Chen, R., Ratnikova, T., Stone, M., Lin, S., Lard, M., Huang, G., Hudson, J. and Ke, P. (2010a). Differential uptake of carbon nanoparticles by plant and Mammalian cells. Small *6*, 612–617.

[Chen et al., 2010b] Chen, Y.-F., Milstein, J. and Meiners, J.-C. (2010b). Protein-Mediated DNA Loop Formation and Breakdown in a Fluctuating Environment. Phys. Rev. Lett. *104*, 258103.

[Crut et al., 2007] Crut, A., Koster, D., Seidel, R., Wiggins, C. and Dekker, N. (2007). Fast dynamics of supercoiled DNA revealed by single-molecule experiments. Proc. Natl. Acad. Sci. USA *104*, 11957–11962.

[Curran et al., 2010] Curran, A., Yao, A., Gibson, G., Bowman, R., Cooper, J. and Padgett, M. (2010). Real time characterization of hydrodynamics in optically trapped networks of micro-particles. J. Biophotonics *3*, 244–251.

[Curtis and Grier, 2003] Curtis, J. and Grier, D. (2003). Structure of optical vortices. Phys. Rev. Lett. *90*, 133901.

[Czerwinski et al., 2011] Czerwinski, F., Andersson, M. and Oddershede, L. (2011). Optimizing active and passive optical tweezers calibration. J. Opt., under review for publication.

[Czerwinski and Oddershede, 2010] Czerwinski, F. and Oddershede, L. (2010). TimeSeriesStreaming.vi: LabVIEW program for reliable data streaming of large analog time series. Comput. Phys. Commun., accepted for publication.

[Czerwinski and Otto, 2010] Czerwinski, F. and Otto, O. (2010). Observing and Controlling Biomolecules with Optical Tweezers and LabVIEW. National Instruments Case Studies, 13024.

[Czerwinski, 2010] Czerwinski, F. (2010). allan v3.0. MatlabCentral, 26659.

[Czerwinski et al., 2009a] Czerwinski, F., Richardson, A. and Oddershede, L. (2009). Quantifying Noise in Optical Tweezers by Allan Variance. Opt. Express *17*, 13255–13269.

[Czerwinski et al., 2009b] Czerwinski, F., Richardson, A., Selhuber-Unkel, C. and Oddershede, L. (2009). Quantifying and pinpointing sources of noise in optical tweezers experiments. Proc. SPIE *7400*, 740004.

[Czerwinski, 2009] Czerwinski, F. (2009). BeadFluct v1.0. MatlabCentral, 24196.

[Czerwinski, 2008] Czerwinski, F. (2008). allan v1.71. MatlabCentral, 21727.

[Czerwinski, 2007] Czerwinski, F. (2007). Topological Changes of DNA Investigated by Magnetic Tweezers. PhD thesis, Delft University of Technology.

[Davenport et al., 2000] Davenport, R., Wuite, G., Landick, R. and Bustamante, C. (2000). Single-molecule study of transcriptional pausing and arrest by E-coli RNA polymerase. Science *287*, 2497–2500.

[Dekker, 2007] Dekker, C. (2007). Solid-state nanopores. Nat. Nanotechnol. *2*, 209–215.

[Dekker et al., 2002] Dekker, N., Rybenkov, V., Duguet, M., Crisona, N., Cozzarelli, N., Bensimon, D. and Croquette, V. (2002). The mechanism of type IA topoisomerases. Proc. Natl. Acad. Sci. USA *99*, 12126–12131.

[Deufel et al., 2007] Deufel, C., Forth, S., Simmons, C., Dejgosha, S. and Wang, M. (2007). Nanofabricated quartz cylinders for angular trapping: DNA supercoiling torque detection. Nat. Methods *4*, 223–225.

[Ditzler et al., 2007] Ditzler, M., Alemán, E., Rueda, D. and Walter, N. (2007). Focus on function: single molecule RNA enzymology. Biopolymers *87*, 302–316.

[Dreyer et al., 2004] Dreyer, J., Berg-Sørensen, K. and Oddershede, L. (2004). Improved axial position detection in optical tweezers measurements. Appl. Opt. *43*, 1991–1995.

[Eid et al., 2009] Eid, J., Fehr, A., Gray, J., Luong, K., Lyle, J., Otto, G., et al. (2009). Real-time DNA sequencing from single polymerase molecules. Science *323*, 133–138.

[Fischer and Berg-Sørensen, 2007] Fischer, M. and Berg-Sørensen, K. (2007). Calibration of trapping force and response function of optical tweezers in viscoelastic media. J. Opt. A–Pure Appl. Opt. *9*, S239–S250.

[Fischer et al., 2010] Fischer, M., Richardson, A., Reihani, S., Oddershede, L. and Berg-Sørensen, K. (2010). Active-passive calibration of optical tweezers in viscoelastic media. Rev. Sci. Instrum. *81*, 015103.

[Fodeke and Minton, 2010] Fodeke, A. and Minton, A. (2010). Quantitative characterization of polymer-polymer, protein-protein, and polymer-protein interaction via tracer sedimentation equilibrium. J. Phys. Chem. B *114*, 10876–10880.

[Fortner et al., 2005] Fortner, J., Lyon, D., Sayes, C., Boyd, A., Falkner, J., Hotze, E., et al. (2005). C60 in water: nanocrystal formation and microbial response. Environ. Sci. Technol. *39*, 4307–4316.

[Gibson et al., 2008] Gibson, G., Leach, J., Keen, S., Wright, A. and Padgett, M. (2008). Measuring the accuracy of particle position and force in optical tweezers using high-speed video microscopy. Opt. Express *16*, 14561–14570.

[Gittes and Schmidt, 1998] Gittes, F. and Schmidt, C. (1998). Signals and noise in micromechanical measurements. Methods Cell Biol. *55*, 129–156.

[Golding et al., 2005] Golding, I., Paulsson, J., Zawilski, S. and Cox, E. (2005). Real-Time Kinetics of Gene Activity in Individual Bacteria. Cell *123*, 1025–1036.

[Gosse and Croquette, 2002] Gosse, C. and Croquette, V. (2002). Magnetic tweezers: micromanipulation and force measurement at the molecular level. Biophys. J. *82*, 3314–3329.

[Hallatschek et al., 2007] Hallatschek, O., Hersen, P., Ramanathan, S. and Nelson, D. (2007). Genetic drift at expanding frontiers promotes gene segregation. Proc. Natl. Acad. Sci. USA *104*, 19926–19930.

[Halvorsen and Wong, 2010] Halvorsen, K. and Wong, W. (2010). Massively Parallel Single-Molecule Manipulation Using Centrifugal Force. Biophys. J. *98*, L53–L55.

[Han et al., 2008] Han, L., Lui, B., Blumberg, S., Beausang, J., Nelson, P. and Phillips, R. (2008). Calibration of tethered particle motion experiments. Mathemat. DNA Struct. Funct. Interact. *150*, 123–138.

[Hanes et al., 2009] Hanes, R., Jenkins, M. and Egelhaaf, S. (2009). Combined holographic-mechanical optical tweezers: Construction, optimisation and calibration. arXiv *physics.optics*, 0903.3679v2.

[Hansen et al., 2005] Hansen, P., Bhatia, V., Harrit, N. and Oddershede, L. (2005). Expanding the optical trapping range of gold nanoparticles. Nano Lett. *5*, 1937–1942.

[Hansen et al., 2006] Hansen, P., Tolic-Nørrelykke, I., Flyvbjerg, H. and Berg-Sørensen, K. (2006). tweezercalib 2.1: Faster version of MatLab package for precise calibration of optical tweezers. Comput. Phys. Commun. *175*, 572–573.

[Hansen, 2006] Hansen, P. (2006). Cellular mechanics studied by novel nano-tools and reconstituted model systems. PhD thesis, University of Copenhagen.

[Hansen et al., 2005] Hansen, P., Dreyer, J., Ferkinghoff-Borg, J. and Oddershede, L. (2005). Novel optical and statistical methods reveal colloid-wall interactions inconsistent with DLVO and Lifshitz theories. J. Colloid Interface Sci. *287*, 561–571.

[Hansen, 2008] Hansen, T. (2008). Studies of translation, on the ensemble level using in vivo techniques and on the single molecule level using optical tweezers. PhD thesis, University of Copenhagen.

[Henry et al., 2007] Henry, T., Menn, F.-M., Fleming, J., Wilgus, J., Compton, R. and Sayler, G. (2007). Attributing effects of aqueous C60 nano-aggregates to tetrahydrofuran decomposition products in larval zebrafish by assessment of gene expression. Environ. Health Perspect. *115*, 1059–1065.

[Hersen et al., 2008] Hersen, P., McClean, M., Mahadevan, L. and Ramanathan, S. (2008). Signal processing by the HOG MAP kinase pathway. Proc. Natl. Acad. Sci. USA *105*, 7165–7170.

[Hood, 2004] Hood, E. (2004). Nanotechnology: looking as we leap. Environ. Health Perspect. *112*, A740–A749.

[Huang et al., 2009] Huang, R., Wu, P., Tischer, C., Jonas, A. and Florin, E.-L. (2009). Direct Measurement of the Nonconservative Force Field Generated by Optical Tweezers. Phys. Rev. Lett. *103*, 108101.

[Huisstede et al., 2005] Huisstede, J., van der Werf, K., Bennink, M. and Subramaniam, V. (2005). Force detection in optical tweezers using backscattered light. Opt. Express *13*, 1113–1123.

[Huisstede et al., 2006a] Huisstede, J., van Rooijen, B., van der Werf, K., Bennink, M. and Subramaniam, V. (2006a). Dependence of silicon position-detector bandwidth on wavelength, power, and bias. Opt. Lett. *31*, 610–612.

[Huisstede et al., 2006b] Huisstede, J., van der Werf, K., Bennink, M. and Subramaniam, V. (2006b). Force constant calibration corrections for silicon position detectors in the near-infrared. Opt. Express *14*, 8476–8481.

[Husale et al., 2008] Husale, S., Grange, W., Karle, M., Bürgi, S. and Hegner, M. (2008). Interaction of cationic surfactants with DNA: a single-molecule study. Nucleic Acids Res. *36*, 1443–1449.

[Jauffred and Oddershede, 2010] Jauffred, L. and Oddershede, L. (2010). Two-photon quantum dot excitation during optical trapping. Nano Lett. *10*, 1927–1930.

[Jauffred et al., 2008a] Jauffred, L., Richardson, A. and Oddershede, L. (2008a). Three-dimensional optical control of individual quantum dots. Nano Lett. *8*, 3376–3380.

[Jauffred et al., 2008b] Jauffred, L., Richardson, A. and Oddershede, L. (2008b). Three-Dimensional Optical Control of Individual Quantum Dots. Nano Lett. *8*, 3376–3380.

[Jauffred et al., 2010] Jauffred, L., Sletmoen, M., Czerwinski, F. and Oddershede, L. (2010). Quantum dots as handles for optical manipulation. Proc. SPIE *7762*, 77620Q.

[Jesacher et al., 2008a] Jesacher, A., Maurer, C., Schwaighofer, A., Bernet, S. and Ritsch-Marte, M. (2008a). Near-perfect hologram reconstruction with a spatial light modulator. Opt. Express *16*, 2597–2603.

[Jesacher et al., 2008b] Jesacher, A., Maurer, C., Schwaighofer, A., Bernet, S. and Ritsch-Marte, M. (2008b). Full phase and amplitude control of holographic optical tweezers with high efficiency. Opt. Express *16*, 4479–4486.

[Keen et al., 2007] Keen, S., Leach, J., Gibson, G. and Padgett, M. (2007). Comparison of a high-speed camera and a quadrant detector for measuring displacements in optical tweezers. J. Opt. A–Pure Appl. Opt. *9*, S264–S266.

[Klaue and Seidel, 2009] Klaue, D. and Seidel, R. (2009). Torsional Stiffness of Single Superparamagnetic Microspheres in an External Magnetic Field. Phys. Rev. Lett. *102*, 028302.

[Klein et al., 2007] Klein, M., Andersson, M., Axner, O. and Fällman, E. (2007). Dual-trap technique for reduction of low-frequency noise in force measuring optical tweezers. Appl. Opt. *46*, 405–412.

[Korsch, 2002] Korsch, H. J. (2002). Mathematische Ergänzungen zur Einführung in die Physik. Binomi, Springe.

[Koster et al., 2008] Koster, D., Czerwinski, F., Halby, L., Crut, A., Vekhoff, P., Palle, K., Arimondo, P. and Dekker, N. (2008). Single-molecule observations of topotecan-mediated TopIB activity at a unique DNA sequence. Nucleic Acids Res. *36*, 2301–2310.

[Koster et al., 2005] Koster, D., Croquette, V., Dekker, C., Shuman, S. and Dekker, N. (2005). Friction and torque govern the relaxation of DNA supercoils by eukaryotic topoisomerase IB. Nature *434*, 671–674.

[Koster et al., 2007] Koster, D., Palle, K., Bot, E., Bjornsti, M.-A. and Dekker, N. (2007). Antitumour drugs impede DNA uncoiling by topoisomerase IB. Nature *448*, 213–217.

[Lang et al., 2002] Lang, M., Asbury, C., Shaevitz, J. and Block, S. (2002). An automated two-dimensional optical force clamp for single molecule studies. Biophys. J. *83*, 491–501.

[Lemons, 2002] Lemons, D. S. (2002). An Introduction to Stochastic Processes in Physics. The Johns Hopkins University Press, Baltimore and London.

[Li et al., 2003] Li, J., Gershow, M., Stein, D., Brandin, E. and Golovchenko, J. (2003). DNA molecules and configurations in a solid-state nanopore microscope. Nat. Mater. *2*, 611–615.

[Liphardt et al., 2001] Liphardt, J., Onoa, B., Smith, S., Tinoco, I. and Bustamante, C. (2001). Reversible unfolding of single RNA molecules by mechanical force. Science *292*, 733–737.

[Mahamdeh and Schäffer, 2009] Mahamdeh, M. and Schäffer, E. (2009). Optical tweezers with millikelvin precision of temperature-controlled objectives and base-pair resolution. Opt. Express *17*, 17190–17199.

[Manley et al., 2008] Manley, S., Gillette, J., Patterson, G., Shroff, H., Hess, H., Betzig, E. and Lippincott-Schwartz, J. (2008). High-density mapping of single-molecule trajectories with photoactivated localization microscopy. Nat. Methods *5*, 155–157.

[Michalet et al., 2005] Michalet, X., Pinaud, F., Bentolila, L., Tsay, J., Doose, S., Li, J., Sundaresan, G., Wu, A., Gambhir, S. and Weiss, S. (2005). Quantum dots for live cells, in vivo imaging, and diagnostics. Science *307*, 538–544.

[Milstein et al., 2010] Milstein, J., Chen, Y. and Meiners, J. (2010). Bead size effects on protein-mediated DNA looping in tethered-particle microscopy. submitted.

[Ming and Uhlenbeck, 1945] Ming, C. and Uhlenbeck, G. (1945). On the Theory of the Brownian Motion II. Rev. Mod. Phys. *17*, 323–342.

[Minton, 2005] Minton, A. (2005). Influence of macromolecular crowding upon the stability and state of association of proteins: predictions and observations. J. Pharm. Sci. *94*, 1668–1675.

[Monticelli et al., 2009] Monticelli, L., Salonen, E., Ke, P. and Vattulainen, I. (2009). Effects of carbon nanoparticles on lipid membranes: a molecular simulation perspective. Soft Matter *5*, 4433–4445.

[Moreno-Herrero et al., 2005a] Moreno-Herrero, F., Holtzer, L., Koster, D., Shuman, S., Dekker, C. and Dekker, N. (2005a). Atomic force microscopy shows that vaccinia topoisomerase IB generates filaments on DNA in a cooperative fashion. Nucleic Acids Res. *33*, 5945–5953.

[Moreno-Herrero et al., 2005b] Moreno-Herrero, F., Jager, M., Dekker, N., Kanaar, R., Wyman, C. and Dekker, C. (2005b). Mesoscale conformational changes in the DNA-repair complex Rad50/Mre11/Nbs1 upon binding DNA. Nature *437*, 440–443.

[Moreno-Herrero et al., 2006] Moreno-Herrero, F., Seidel, R., Johnson, S., Fire, A. and Dekker, N. (2006). Structural analysis of hyperperiodic DNA from Caenorhabditis elegans. Nucleic Acids Res. *34*, 3057–3066.

[Nelson, 2004] Nelson, P. (2004). Biological Physics. W. H. Freeman, New York.

[Nelson et al., 2006] Nelson, P., Zurla, C., Brogioli, D., Beausang, J., Finzi, L. and Dunlap, D. (2006). Tethered particle motion as a diagnostic of DNA tether length. J. Phys. Chem. B *110*, 17260–17267.

[Neuman and Block, 2004] Neuman, K. and Block, S. (2004). Optical trapping. Rev. Sci. Instrum. *75*, 2787–2809.

[Neuman et al., 2007] Neuman, K., Lionnet, T. and Allemand, J.-F. (2007). Single-molecule micromanipulation techniques. Annu. Rev. Mater. Res. *37*, 33–67.

[Neuman and Nagy, 2008] Neuman, K. and Nagy, A. (2008). Single-molecule force spectroscopy: optical tweezers, magnetic tweezers and atomic force microscopy. Nat. Methods *5*, 491–505.

[Nölting, 2004] Nölting, B. (2004). Methods in Modern Biophysics. Springer, Heidelberg.

[Oberdörster, 2004] Oberdörster, E. (2004). Manufactured nanomaterials (fullerenes, C60) induce oxidative stress in the brain of juvenile largemouth bass. Environ. Health Perspect . *112*, 1058–1062.

[Oberdörster et al., 2005] Oberdörster, G., Oberdörster, E. and Oberdörster, J. (2005). Nanotoxicology: an emerging discipline evolving from studies of ultrafine particles. Environ. Health Perspect. *113*, 823–839.

[Oddershede, 2009] Oddershede, L. (2009). Optical Tweezers Techniques. Handbook of Molecular Biophysics, 24–32.

[Otto et al., 2010] Otto, O., Czerwinski, F., Gornall, J., Stober, G., Oddershede, L., Seidel, R. and Keyser, U. (2010). Real-time Particle Tracking at 10,000 fps using Optical Fiber Illumination. Opt. Express, accepted for publication.

[Otto et al., 2011] Otto, O., Gornall, J., Stober, G., Czerwinski, F., Seidel, R. and Keyser, U. (2011). High-Speed Video-Based Tracking of Optically Trapped Colloids. J. Opt., accepted for publication.

[Otto et al., 2008] Otto, O., Gutsche, C., Kremer, F. and Keyser, U. (2008). Optical tweezers with 2.5 kHz bandwidth video detection for single-colloid electrophoresis. Rev. Sci. Instrum. *79*, 023710.

[Pommier, 2009] Pommier, Y. (2009). DNA topoisomerase I inhibitors: chemistry, biology, and interfacial inhibition. Chem. Rev. *109*, 2894–2902.

[Pralle et al., 1999] Pralle, A., Prummer, M., Florin, E., Stelzer, E. and Horber, J. (1999). Three-dimensional high-resolution particle tracking for optical tweezers by forward scattered light. Microsc. Res. Techniq. *44*, 378–386.

[Purcell, 1977] Purcell, E. (1977). Life at low Reynolds number. Am. J. Phys. *45*, 3–11.

[Ramanathan et al., 2009] Ramanathan, S., van Aelst, K., Sears, A., Peakman, L., Diffin, F., Szczelkun, M. and Seidel, R. (2009). Type III restriction enzymes communicate in 1D without looping between their target sites. Proc. Natl. Acad. Sci. USA *106*, 1748–1753.

[Reihani and Oddershede, 2007] Reihani, S. and Oddershede, L. (2007). Optimizing immersion media refractive index improves optical trapping by compensating spherical aberrations. Opt. Lett. *32*, 1998–2000.

[Reihani et al., 2010] Reihani, S., Mir, S., Richardson, A. and Oddershede, L. (2010). Cancellation of spherical aberrations induced by water immersion objectives during optical trapping. submitted.

[Richardson, 2009] Richardson, A. (2009). Development of optical trapping techniques for in vivo investigations. PhD thesis, University of Copenhagen.

[Richardson et al., 2008] Richardson, A., Reihani, S. and Oddershede, L. (2008). Non-harmonic potential of a single beam optical trap. Opt. Express *16*, 15709–15717.

[Rivetti et al., 1996] Rivetti, C., Guthold, M. and Bustamante, C. (1996). Scanning force microscopy of DNA deposited onto mica: equilibration versus kinetic trapping studied by statistical polymer chain analysis. J. Mol. Biol. *264*, 919–932.

[Rodriguez-Otazo et al., 2009] Rodriguez-Otazo, M., Augier-Calderin, A., Galaup, J.-P., Lamere, J.-F. and Fery-Forgues, S. (2009). High rotation speed of single molecular microcrystals in an optical trap with elliptically polarized light. Appl. Opt. *48*, 2720–2730.

[Schwabl, 2004] Schwabl, F. (2004). Statistische Mechanik. Springer, Heidelberg.

[Seidel et al., 2005] Seidel, R., Bloom, J., Noort, J., Dutta, C., Dekker, N., Firman, K., Szczelkun, M. and Dekker, C. (2005). Dynamics of initiation, termination and reinitiation of DNA translocation by the motor protein EcoR124I. EMBO J. *24*, 4188–4197.

[Selhuber-Unkel et al., 2008] Selhuber-Unkel, C., Zins, I., Schubert, O., Sönnichsen, C. and Oddershede, L. (2008). Quantitative optical trapping of single gold nanorods. Nano Lett. *8*, 2998–3003.

[Seol et al., 2006] Seol, Y., Carpenter, A. and Perkins, T. (2006). Gold nanoparticles: enhanced optical trapping and sensitivity coupled with significant heating. Opt. Lett. *31*, 2429–2431.

[Stein, 2007] Stein, D. (2007). Nanopores: molecular ping-pong. Nat. Nanotechnol. *2*, 741–742.

[Steinbock et al., 2010] Steinbock, L., Otto, O., Chimerel, C., Gornall, J. and Keyser, U. (2010). Detecting DNA folding with nanocapillaries. Nano Lett. *10*, 2493–2497.

[Steinbock et al., 2009] Steinbock, L., Stober, G. and Keyser, U. (2009). Sensing DNA-coatings of microparticles using micropipettes. Biosensors & Bioelectronics *24*, 2423–2427.

[Stone et al., 2007] Stone, M., Mihalusova, M., O'Connor, C., Prathapam, R., Collins, K. and Zhuang, X. (2007). Stepwise protein-mediated RNA folding directs assembly of telomerase ribonucleoprotein. Nature *446*, 458–461.

[Strick et al., 2003] Strick, T., Dessinges, M., Charvin, G., Dekker, N., Allemand, J., Bensimon, D. and Croquette, V. (2003). Stretching of macromolecules and proteins. Rep. Prog. Phys. *66*, 1–45.

[Sun et al., 2010] Sun, M., Wartel, M., Cascales, E., Shaevitz, J. and Mignot, T. (2010). Motor-driven Intracellular Transport Powers Bacterial Gliding Motility. submitted.

[Taneja et al., 2007] Taneja, B., Schnurr, B., Slesarev, A., Marko, J. and Mondragon, A. (2007). Topoisomerase V relaxes supercoiled DNA by a constrained swiveling mechanism. Proc. Natl. Acad. Sci. USA *104*, 14670–14675.

[Tejedor et al., 2010] Tejedor, V., Bénichou, O., Voituriez, R., Jungmann, R., Simmel, F., Selhuber-Unkel, C., Oddershede, L. and Metzler, R. (2010). Quantitative analysis of single particle trajectories: mean maximal excursion method. Biophys. J. *98*, 1364–1372.

[Tolic-Nørrelykke et al., 2006] Tolic-Nørrelykke, S., Schäffer, E., Howard, J., Pavone, F., Jülicher, F. and Flyvbjerg, H. (2006). Calibration of optical tweezers with positional detection in the back focal plane. Rev. Sci. Instrum. *77*, 103101.

[Towrie et al., 2009] Towrie, M., Botchway, S., Clark, A., Freeman, E., Halsall, R., Parker, A., et al. (2009). Dynamic position and force measurement for multiple optically trapped particles using a high-speed active pixel sensor. Rev. Sci. Instrum. *80*, 103704.

[Tsao et al., 2010] Tsao, D., Minton, A. and Dokholyan, N. (2010). A didactic model of macromolecular crowding effects on protein folding. PLoS ONE *5*, e11936.

[Valentine et al., 2008] Valentine, M., Guydosh, N., Gutierrez-Medina, B., Fehr, A., Andreasson, J. and Block, S. (2008). Precision steering of an optical trap by electro-optic deflection. Opt. Lett . *33*, 599–601.

[van der Horst and Forde, 2010] van der Horst, A. and Forde, N. (2010). Power spectral analysis for optical trap stiffness calibration from high-speed camera position detection with limited bandwidth. Opt. Express *18*, 7670–7677.

[Velthuis et al., 2010] te Velthuis, A., Kerssemakers, J., Lipfert, J. and Dekker, N. (2010). Quantitative Guidelines for Force Calibration through Spectral Analysis of Magnetic Tweezers Data. Biophys. J. *99*, 1292–1302.

[Visscher and Block, 1998] Visscher, K. and Block, S. (1998). Versatile optical traps with feedback control. Methods Enzymol. *298*, 460–489.

[Volpe and Petrov, 2006] Volpe, G. and Petrov, D. (2006). Torque detection using Brownian fluctuations. Phys. Rev. Lett. *97*, 210603.

[Walter et al., 2006] Walter, N., Selhuber, C., Kessler, H. and Spatz, J. (2006). Cellular unbinding forces of initial adhesion processes on nanopatterned surfaces probed with magnetic tweezers. Nano Lett. *6*, 398–402.

[Walter et al., 2008] Walter, N., Huang, C.-Y., Manzo, A. and Sobhy, M. (2008). Do-it-yourself guide: how to use the modern single-molecule toolkit. Nat. Methods *5*, 475–489.

[Wang et al., 1997] Wang, M., Yin, H., Landick, R., Gelles, J. and Block, S. (1997). Stretching DNA with optical tweezers. Biophys. J. *72*, 1335–1346.

[Wen et al., 2008] Wen, J.-D., Lancaster, L., Hodges, C., Zeri, A.-C., Yoshimura, S., Noller, H., Bustamante, C. and Tinoco, I. (2008). Following translation by single ribosomes one codon at a time. Nature *452*, 598–603.

[Wiggins et al., 2006] Wiggins, P., van der Heijden, T., Moreno-Herrero, F., Spakowitz, A., Phillips, R., Widom, J., Dekker, C. and Nelson, P. (2006). High flexibility of DNA on short length scales probed by atomic force microscopy. Nat. Nanotechnol. *1*, 137–141.

[Wong and Halvorsen, 2006] Wong, W. and Halvorsen, K. (2006). The effect of integration time on fluctuation measurements: calibrating an optical trap in the presence of motion blur. Opt. Express *14*, 12517–12531.

[Wong-Ekkabut et al., 2008] Wong-Ekkabut, J., Baoukina, S., Triampo, W., Tang, I.-M., Tieleman, D. and Monticelli, L. (2008). Computer simulation study of fullerene translocation through lipid membranes. Nat. Nanotechnol. *3*, 363–368.

[Wu et al., 2010] Wu, J., Stone, M. and Zhuang, X. (2010). A single-molecule assay for telomerase structure-function analysis. Nucleic Acids Res. *38*, e16.

[Zhao et al., 2005] Zhao, X., Striolo, A. and Cummings, P. (2005). C60 binds to and deforms nucleotides. Biophys. J. *89*, 3856–3862.

Appended Publications Summaries and My Contributions

In October 2007, I joined the Optical Tweezers Group at the Niels Bohr Institute, University of Copenhagen, to start my PhD projects under Lene Oddershede's supervision. Our laboratory was equipped with two optical tweezers setups, and had developed an in-depth knowledge of optical tweezers calibration. Furthermore, here I found world experts in the routine of optical trapping of metal objects that were only a few nanometers in size.

I started out to modify and improve the setups to match specific requirements for the planned DNA-associated assays. This encountered the experimental setup itself, the microfluidic system, and hardware as well as software modifications. In addition, I implemented various detection schemes. During these efforts, Andrew Richardson and I introduced to our laboratory a very simple, assumption-free and powerful method to quantify noise in biophysical single-molecule experiments . Allan variance had reportedly only been used by the Padgett Lab, University of Glasgow [Gibson et al., 2008]. We firstly tested and verified this method on optical tweezers with polystyrene spheres as they are used in our DNA-associated experiments [Czerwinski et al., 2009a]. Here, we could also show how Allan variance analysis could be used to optimize acquisition parameters and how to pinpoint and quantify common noise sources. Then we extended the low-frequency drift analysis to unusual handles [Czerwinski et al., 2009b, Jauffred et al., 2010]. For instance, these findings answered questions of optimal measurement times as well as the variation of drift exposure for different geometric constraints and optical axes. Extending our understanding of intrinsic noise and drift phenomena in optical tweezers, we proposed and verified an optimized calibration protocol [Czerwinski et al., 2011]. On the side of biophysical experiments, Allan variance analysis showed its strength for a lot of different types of single-molecule force-microscopy techniques that are state of the art to investigate the structural behavior of DNA (section 8). Here, I collected data for DNA-associated setups not just from our own experiments, but from the Seidel Lab (TU Dresden), Keyser Lab (Cambridge University), Stein Lab (Brown University), Philips Lab (Caltech), and Dekker Lab (TU Delft). This work has partially been discussed at the Biophysical Society Meeting 2010, but has not been submitted yet. A manuscript is in preparation. It was a very exciting point in discussions with scientific collaborators, broadening our knowledge on absolute, stochastic, statistic, and experimental limits that different DNA-associated assay are exposed to.

I had the great opportunity to join Ulrich Keyser's laboratory at the Cavendish Laboratories, Cambridge University, from September 2009 until January 2010. Here,

I took part in the development of another setup that was dedicated to measure at high temporal resolution, but based on a CMOS camera detection scheme. Our resulting setup outpaces almost all other visual detection schemes used in biophysical research these days [Otto et al., 2011, Otto et al., 2010], and will continue to adapt to new developments in camera technology.

The development of software solutions over the years are made available to the public via different ways (GitHub, MatlabCentral, personal website). Two of the software solutions are highlighted in this thesis, as accepted for publication in the peer-reviewed Computer Physics Communication [Czerwinski and Oddershede, 2010], and as proceeding to the conference NI Week 2011 [Czerwinski and Otto, 2010].

The following is a chronological listing of the scientific publications I contributed in the course of my PhD projects. They form the basis of this thesis. Firstly, the citation is given in the standard suggested by the Optical Society of America. Secondly, the abstract is used as a short summary, and thirdly, I provide a detailed description of my contributions to each of the publications.

Quantifying Noise in Optical Tweezers by Allan Variance

Citation [Czerwinski et al., 2009a] Fabian Czerwinski, Andrew C. Richardson, and Lene B. Oddershede, "Quantifying Noise in Optical Tweezers by Allan Variance," Opt. Express 17, 13255-69 (2009), doi 10.1364/OE.17.013255

Summary Much effort is put into minimizing noise in optical tweezers experiments because noise and drift can mask fundamental behaviours of, e.g., single molecule assays. Various initiatives have been taken to reduce or eliminate noise but it has been difficult to quantify their effect. We propose to use Allan variance as a simple and efficient method to quantify noise in optical tweezers setups.We apply the method to determine the optimal measurement time, frequency, and detection scheme, and quantify the effect of acoustic noise in the lab. The method can also be used on-the-fly for determining optimal parameters of running experiments.

My Contribution I participated in designing the experiment. I wrote the software to acquire and analyze the data. I participated in conducting the measurements. I developed the theoretical background and made the Figures. I wrote a first draft of the publication. I answered the referees' questions. I submitted all versions of the publication.

Allan Variance Analysis as Useful Tool to Determine Noise in Various Single-Molecule Setups

Citation [Czerwinski et al., 2009b] Fabian Czerwinski, Andrew C. Richardson, Christine Selhuber-Unkel, and Lene B. Oddershede, "Allan Variance Analysis as Useful Tool to Determine Noise in Various Single-Molecule Setups," Proc. SPIE, 7400, 740004 (2009), doi 10.1117/12.827975

Summary One limitation on the performance of optical traps is the noise inherently present in every setup. Therefore, it is the desire of most experimentalists to minimize and possibly eliminate noise from their optical trapping experiments. A step in this direction is to quantify the actual noise in the system and to evaluate how much each particular component contributes to the overall noise. For this purpose we present Allan variance analysis as a straightforward method. In particular, it allows for judging the impact of drift which gives rise to low-frequency noise, which is extremely difficult to pinpoint by other methods. We show how to determine the optimal sampling time for calibration, the optimal number of data points for a desired experiment, and we provide measurements of how much accuracy is gained by acquiring additional data points. Allan variances of both micrometer-sized spheres and asymmetric nanometer-sized rods are considered.

My contribution I did all major contributions to the proceeding. I participated in conducting the measurements for the polystyrene spheres. I added the various ways of presenting the data. I made all the Figures. I worte the first draft of the proceeding, edited and submitted the final version. I presented this work at the SPIE Conference 2009 in San Diego, CA, USA.

Quantum dots as handles for optical manipulation

Citation [Jauffred et al., 2010] Liselotte Jauffred, Marit Sletmoen, Fabian Czerwinski, and Lene B. Oddershede, "Quantum dots as handles for optical manipulation," Proc. SPIE, 7762, 77620Q (2010), doi 10.1117/12.860486

Summary Individual colloidal quantum dots can be optically trapped and manipulated by a single infrared laser beam operated at low laser powers. If the absorption spectrum and the emission wavelength of the trapping laser are appropriately chosen, the trapping laser light can act as a source for two-photon excitation of the trapped quantum dot. This eliminates the need for an additional excitation laser in experiments where individual quantum dots are used both as force transducers and for visualization of the system. To use quantum dots as handles for quantitative optical force transduction, it is crucial to perform a precise force calibration. Here, we present an Allan variance analysis of individual optically trapped quantum dots

and show that the optimal measurement time for experiments involving individual quantum dots is on the order of 0.3 seconds. Due to their small size and strong illumination, quantum dots are optimal for single molecule assays where, optimally, the presence of the tracer particle should not dominate the dynamics of the system. As an example, we investigated the thermal fluctuations of a DNA tether using an individual colloidal quantum dot as a marker, this being the smallest tracer for tethered particle method reported.

My contribution I analyzed the data with respect to their dynamic behavior in the trap. I contributed to Figures 3 and 5, and to writing section 3 and parts of section 4.

High-Speed Video-Based Tracking of Optically Trapped Colloids

Citation [Otto et al., 2011] Oliver Otto, Joanne L. Gornall, Gunter Stober, Fabian Czerwinski, Ralf Seidel, and Ulrich F. Keyser, "High-Speed Video-Based Tracking of Optically Trapped Colloids," accepted for publication in J. Opt.
The publication will be published in a special issue of Journal of Optics on optical tweezers in early 2011.

Summary We have developed an optical tweezers setup, with high-speed and real-time position tracking, based on a CMOS camera technology. Our software encoded algorithm is cross-correlation based and implemented on a standard computer. By measuring the fluctuations of a confined colloid at 6,000 frames per second, continuously for an hour, we show our technique is a viable alternative to quadrant photodiodes. The optical trap is calibrated by using power spectrum analysis and Stokes method. The trap stiffness is independent of the camera frame rate and scales linearly with the applied laser power. Analysis of our data by Allan variance demonstrates single nanometer accuracy in position detection.

My contribution I contributed to all parts of the work, except the early software implementation. I helped designing the LabVIEW core. I contributed in measuring the data, and in making the Figures. I added parts to a first draft of the publication.

TimeSeriesStreaming.vi: LabVIEW program for reliable data streaming of large analog time series

Citation [Czerwinski and Oddershede, 2010] Fabian Czerwinski and Lene B. Oddershede, "TimeSeriesStreaming.vi: LabVIEW program for reliable data streaming of large analog time series," accepted for publication in Comput. Phys. Commun.

Summary With modern data acquisition devices that work fastly and very precisely, scientists often face the task of dealing with huge amounts of data. These need to be rapidly processed and stored onto a hard disk. We present a LabVIEW program which reliably streams analog time series of MHz sampling. Its run time has virtually no limitation. We explicitly show how to use the program to extract time series from two experiments: For a photodiode detection system that tracks the position of an optically trapped particle and for a measurement of ionic current through a glass capillary. The program is easy to use and versatile as the input can be any type of analog signal. Also, the data streaming software is simple, highly reliable, and can be easily customized to include, e.g., real-time power spectral analysis and Allan variance noise quantification.

My contribution I designed the LabVIEW program, made it user-friendly and open for customization. I tested the program, developed a benchmarking strategy, and provided a program URL. I took the data. I made all the Figures. I wrote a first draft of the publication, edited the final version and submitted all versions.

Optimizing active and passive optical tweezers calibration

Citation [Czerwinski et al., 2011] Fabian Czerwinski, Magnus Andersson, and Lene B. Oddershede, "Allan variance for optimizing optical tweezers calibration," under review for publication in J. Opt.
If accepted the publication will also be published in the special issue of Journal of Optics on optical tweezers in early 2011.

Summary To obtain quantitative information from optical trapping experiments it is essential to perform a precise force calibration. Therefore, sources of noise should be pinpointed and eliminated. Fourier analysis is routinely used to calibrate optical trapping assays, this being excellent for pinpointing high frequency noise. In addition, Allan variance analysis is particularly useful for quantifying low-frequency noise and for predicting the optimal measurement time. We show how to use Allan variance in combination with Fourier analysis for optimal calibration and noise reduction in optical trapping assays. The methods are applied to passive assays, utilizing the thermal motion of a trapped particle, and to active assays where the bead is harmonically driven. The active method must be applied in assays where, e.g., the viscoelastic properties of the medium or the size or shape of the trapped object are unknown. For measurement times shorter than the optimal calibration time the noise is larger in active than in the passive assays. For times equal to or longer than the optimal measurement time though, the noise on passive and active assays are identical. As an example, we show how to quantify the influence on measurement noise of bead size and chamber geometry in active and passive assays.

My contribution I contributed to the design of the experiment, and I helped conducting all the experiments. Magnus and I developed the optimized calibration protocol. I analyzed the data and made all the Figures. I coontributed to a first draft of the publication and helped answering the editor's request.

Real-time Particle Tracking at 10,000 fps using Optical Fiber Illumination

Citation [Otto et al., 2010] Oliver Otto, Fabian Czerwinski, Joanne L. Gornall, Gunter Stober, Lene B. Oddershede, Ralf Seidel, Ulrich F. Keyser, "Real-time Particle Tracking at 10,000 fps using Optical Fiber Illumination," accepted for publication in Opt. Express

Summary We introduce optical fiber illumination for real-time tracking of optically trapped particles with microseconds time resolution. Our light source is based on a high-radiance mercury arc lamp and a 600 mm optical fiber for short-distance illumination of the sample cell. Particle tracking is carried out with a software implemented cross-correlation algorithm following image acquisition from a CMOS camera. Our image data reveals that fiber illumination results in a signal-to-noise ratio usually one order of magnitude higher compared to standard Köhler illumination. We demonstrate position determination of a single optically trapped colloid with up to 10,000 frames per second over hours. We calibrate our optical tweezers and compare the results with quadrant photo diode measurements. Finally, we determine the positional accuracy of our setup to 2 nm by calculating the Allan variance. Our results show that neither illumination nor software algorithms limit the speed of real-time particle tracking with CMOS technology.

My contribution I helped building the setup. I contributed parts to the software. I conducted experiments on the complementary setup with CCD and photodiode, and contributed the optimized calibration protocol. I also contributed to analyze the measurements. I supported the making of the Figures. I conributed parts to a first draft of the publication and helped editing the final version.

Observing and Controlling Biomolecules with Optical Tweezers and LabVIEW

Citation [Czerwinski and Otto, 2010] Fabian Czerwinski and Oliver Otto, "Observing and Controlling Biomolecules with Optical Tweezers and LabVIEW," National Instruments Case Studies, 13024 (2010)

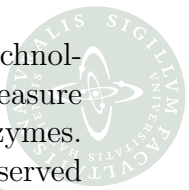

Summary Optical tweezers are an immensely versatile tool in modern biotechnology. By a highly focused laser beam only, they operate inside human cells, measure the elasticity of single DNA molecules, and probe the kinetics of various enzymes. Diverse handles such as gold nanorods or biofunctionalized microspheres are observed with sub-nanometer accuracy typically by photodiodes. Although offering high bandwidth photodiodes have major drawbacks: no long-term stability and the inability to follow more than one object at a time. Consequently, we combined LabVIEW, NI hardware, and a CMOS camera to record optical tweezers data for hours and to track multiple particles - simultaneously and in real-time! For the first time, we overcome the temporal limitation of video-based position tracking as we reach microsecond resolution. Still, the algorithm purely remains within the LabVIEW code. Taking advantage of multicore programming, multithreading, and pipelining, our VIs analyze 10,000 frames per second. They stream particle positions onto a hard disk in the TDMS format. By applying time series analyses in real-time, the VIs enable feedback implementation and direct responses even during measurements. In summary, innovative programming concepts and reliable hardware enhance optical tweezers to maintain sensitive control of the challenging world between biology and nanotechnology.

PhD Thesis

Fabian Czerwinski

Allan Variance Analysis and Fast Camera Detection Schemes for Optical Tweezers

My contribution I had some part of the main ideas and designed the experiments. I contributed to conducting the experiments, and to analyze the data. I made all the Figures and wrote a first draft of the proceeding to the conference NI Week 2011. I answered the editor's requests.

Academic Advisor: Lene B. Oddershede

Submitted: September 27, 2010

FACULTY OF SCIENCE
UNIVERSITY OF COPENHAGEN

PhD Thesis

Fabian Czerwinski

Allan Variance Analysis and Fast Camera Detection Schemes for Optical Tweezers

Academic Advisor: Lene B. Oddershede

Submitted: September 27, 2010

Quantifying Noise in Optical Tweezers by Allan Variance

Fabian Czerwinski, Andrew C. Richardson, and Lene B. Oddershede

Niels Bohr Institute, University of Copenhagen
Blegdamsvej 17, 2100 København Ø, Denmark

czerwinski@nbi.dk

http://www.nbi.dk/tweezer

Abstract: Much effort is put into minimizing noise in optical tweezers experiments because noise and drift can mask fundamental behaviours of, e.g., single molecule assays. Various initiatives have been taken to reduce or eliminate noise but it has been difficult to quantify their effect. We propose to use Allan variance as a simple and efficient method to quantify noise in optical tweezers setups. We apply the method to determine the optimal measurement time, frequency, and detection scheme, and quantify the effect of acoustic noise in the lab. The method can also be used on-the-fly for determining optimal parameters of running experiments.

OCIS codes: (000.3110) Instruments, apparatus, and components common to the sciences; (000.5490) Probability theory, stochastic processes, and statistics; (030.4280, 110.4280) Noise in imaging systems; (140.7010) Laser trapping; (230.5170) Photodiodes; (120.4800, 350.4800) Optical standards and testing; (350.4855) Optical tweezers or optical manipulation.

References and links

1. K. C. Neuman, and S. M. Block, "Optical trapping," Rev. Sci. Instrum. **75**, 2787–2809 (2004).
2. A. Ashkin, J. M. Dziedzic, and T. Yamane, "Optical trapping and manipulation of single cells using infrared laser beams," Nature **330**, 769–771 (1987).
3. P. Hansen, V. Bhatia, N. Harrit, and L. B. Oddershede, "Expanding the optical trapping range of gold nanoparticles," Nano Lett. **5**, 1937–1942 (2005).
4. L. Bosanac, T. Aabo, P. M. Bendix, and L. B. Oddershede, "Efficient Optical Trapping and Visualization of Silver Nanoparticles," Nano Lett. **8**, 1486–1491 (2008).
5. C. Selhuber-Unkel, I. Zins, O. Schubert, C. Sönnichsen, and L. B. Oddershede, "Quantitative optical trapping of single gold nanorods," Nano Lett. **8**, 2998–3003 (2008).
6. L. Jauffred, A. C. Richardson, and L. B. Oddershede, "Three-Dimensional Optical Control of Individual Quantum Dots," Nano Lett. **8**, 3376–3380 (2008).
7. E. A. Abbondanzieri, W. J. Greenleaf, J. W. Shaevitz, R. Landick, and S. M. Block, "Direct observation of base-pair stepping by RNA polymerase," Nature **438**, 460–465 (2005).
8. J. Liphardt, B. Onoa, S. B. Smith, I. Tinoco, and C. Bustamante, "Reversible unfolding of single RNA molecules by mechanical force," Science **292**, 733–737 (2001).
9. A. R. Carter, Y. Seol, and T. T. Perkins, "Precision surface-coupled optical-trapping assay with one-basepair resolution," Biophys. J. **96**, 2926–2934 (2009).
10. F. Gittes and C. F. Schmidt, "Signals and noise in micromechanical measurements," Methods Cell. Biol. **55**, 129–156 (1998).
11. M. Klein, M. Andersson, O. Axner, and E. Fallman, "Dual-trap technique for reduction of low-frequency noise in force measuring optical tweezers," Appl. Opt. **46**, 405–412 (2007).
12. D. W. Allan, "Statistics of atomic frequency standards," Proc. IEEE **54**, 221–230 (1966).
13. P. Banerjee, A. Chatterjee, and A. Suman, "Determination of Allan deviation of Cesium atomic clock for lower averaging time," Indian J. Pure Appl. Phys. **45**, 945–949 (2007).

#113667 - $15.00 USD Received 1 Jul 2009; revised 15 Jul 2009; accepted 15 Jul 2009; published 17 Jul 2009

14. G. M. Gibson, J. Leach, S. Keen, A. J. Wright, and M. J. Padgett, "Measuring the accuracy of particle position and force in optical tweezers using high-speed video microscopy," Opt. Express **16**, 14561–14570 (2008).
15. F. Czerwinski and L. B. Oddershede, "Reliable Data-Streaming Software for Photodiode Readout in LABVIEW," in. prep. (2009).
16. K. Berg-Sørensen, L. B. Oddershede, E. L. Florin, and H. Flyvbjerg, "Unintended filtering in a typical photodiode detection system for optical tweezers," J. Appl. Phys. **93**, 3167–3176 (2003).
17. L. B. Oddershede, S. Grego, S. Nørrelykke, and K. Berg-Sørensen, "Optical tweezers: probing biological surfaces," Probe Microsc **2**, 129–137 (2001).
18. K. Berg-Sørensen and H. Flyvbjerg, "Power spectrum analysis for optical tweezers," Rev. Sci. Instrum. **75**, 594–612 (2004).
19. P. M. Hansen, I. Toliç-Nørrelykke, H. Flyvbjerg, and K. Berg-Sørensen, "*tweezercalib 2.1*: Faster version of MATLAB package for precise calibration of optical tweezers," Comput. Phys. Commun. **175**, 572–573 (2006).
20. F. Czerwinski, "BeadFluct v1.0," MatlabCentral **24196** (2009), http://www.mathworks.com/matlabcentral/fileexchange/24196.
21. P. Kartaschoff, *Frequency and Time* (Academic Press, 1978).
22. F. Czerwinski, "allan v1.71," MatlabCentral **21727** (2008), http://www.mathworks.com/matlabcentral/fileexchange/21727.

1. Introduction

Optical tweezers are created by tightly focusing a laser beam [1], and if focused in all three dimensions a single laser beam can stably trap and manipulate individual objects with sizes ranging from tens of micrometers down to a few nanometers. Objects as diverse as living cells [2], metallic nanoparticles [3, 4, 5], and even quantum dots have been individually trapped [6]. With correct detection schemes the trap can also be utilized to measure forces and distances, typically in the pico-Newton and nanometer regimes. As the technique is nearly non-destructive to biological specimen, it has been successfully used for example to measure forces exerted and distances travelled by individual motor molecules [7], or to unravel structures created by DNA or RNA templates [8]. For such delicate measurements it is extremely important to eliminate as many noise sources as possible. Recently, an optical tweezers setup was reported to have a sensitivity to steps of a length of one DNA basepair (0.34 nm) [9]. Here, drift was compensated by subtracting the motility of a feducial marker, which was followed by a beam parallel to the trapping laser beam. This solution thus necessitates the use of two parallel laser beams.

Other imaginative solutions to eliminate noise have been invoked, not just in optical tweezers setups but also for other nano-scopic measurement techniques such as atomic force microscopes. For instance air currents have been eliminated by covering the setup, the entire setup has been mounted on a separate foundation, measurements have been conducted in the middle of the night, or, in case of optical trapping, the molecule investigated has been moved away from any surface that might be subject to drift. But how useful and efficient are these efforts? And how does one lab compare to another in terms of noise? In order to answer these questions it is essential to be able to quantify noise.

The dominant approach to quantify noise is typically with a Fourier analysis. The Fourier transformed integrated noise in a predefined bandwidth has been used to judge the impact of some experimental arrangements [10, 11]. However, Fourier analysis lacks the resolution of accumulative noise with a typical band of frequencies smaller than 0.1 Hz. Simply looking at the spectrum of integrated noise can neither be used as a measure of resolution nor of accuracy.

Allan variance has been put forward as a method to quantify noise and it is developed to extrapolate the impact of tiny aberrations at infinity from a finite measurement. It has mostly found use in engineering communities but also in quantification of noise in atomic clocks [12, 13]. In this letter, we show how to use Allan variance analysis as a reliable method to quantify noise stemming from various sources in optical trapping setups. Allan variance was previously used to quantify noise in an optical tweezers setup with the goal of showing that CMOS cameras have sufficient time resolution to be used as particle tracking devices [14].

#113667 - $15.00 USD Received 1 Jul 2009; revised 15 Jul 2009; accepted 15 Jul 2009; published 17 Jul 2009

Here, we significantly extend the use of Allan variance to much larger time scales and by using this method we answer the following questions: What is the optimal time interval to calibrate to achieve the highest accuracy? Which sampling frequency suits the desired experiment best? What is the noise spectrum of commonly used detection systems such as a quadrant photodiode or a position sensitive diode? In which intervals is one type of detector more accurate than the other? What noise does a piezo stage induce? Which effect does the geometry and stability of the measurement chamber have? Can one leave the radio on during measurements? Lastly, should one work during nights, which kind of virtual silence is silent enough?

We provide the tools to apply Allan variance analysis to any possible noise factor in an optical tweezers setup. Furthermore, the method can equally well be used for other types of equipment where it is custom to analyze long time series, e.g. magnetic tweezers or atomic force microscopy.

2. Materials and Methods

The experiment simply consisted of trapping a polystyrene sphere in an aqueous environment. The optical trap was implemented in an inverted microscope (Leica DMIRBE) where the laser beam (Spectra Physics, Nd:YVO4, 1064 nm) was tightly focused by a water immersion objective (Leica, HCX, 63x, NA=1.20). To eliminate spherical aberrations of the infrared light, the collar of the objective was set to its lowest setting (0.13 mm). The laser was switched on at least an hour prior to experiment to have an optimal pointing stability. The trapping takes place inside a measurement chamber consisting of two glass cover slips (lower one: thickness 0.13–0.16 mm; upper one: 1 mm) separated by one layer of double-sticky tape. The chamber was filled with a dilute solution of polystyrene spheres (Bangs Labs diameter (800 ± 10) nm) in millipore water. The chambers were sealed by vacuum grease to prevent evaporation of liquid during the experiment. The chamber height was measured by laser deflection for all used chambers to be (95 ± 5) μm. Spheres were trapped 40 μm above the lower glass slip to avoid significant interaction with adjacent surfaces [10]. Experiments were carried out at room temperature.

Figure 1 shows the components which were essential for the present study. After the sample, the scattered laser light was focused through a lens onto a photodiode. Data was collected either by a position-sensitive diode (Pacific Silicon Sensor, DL100-7PCBA3) or a quadrant photodiode (Hamamatsu, S5981 Si-PIN). The recorded voltage signal was amplified and low-pass filtered with 100 kHz, before streamed through an acquisition card (National Instruments, PCI-6251) onto a hard drive. Our custom-made data streaming software was programmed in LABVIEW (National Instruments) and uses features of the TDMS-subpackage [15]. It allowed for acquisition with very high acquisition rates and virtually unlimited acquisition duration (tested for 1 kHz up to 2 h, and 22 min for 100 kHz). The program's error-free use has been checked up to acquisition frequencies of 1 MHz. The limitation in acquisition time was due to the increasing file size, not to the program itself.

Analysis was made on adjacent time series consisting of 2^{24} consecutive points. For an acquisition rate of $f_{\mathrm{acq}} = 22$ kHz, corresponding to time series of about 13 min. Apart from filters inherently present in the detection diodes and electronics [16], all additional filtering was applied during data analysis posterior to acquisition. In addition, a video image of the trapped sphere was recoreded by a CCD camera (Sony, XC-ES50, 25 Hz). This was to ensure that only a single sphere was in the trap both at the beginning and end of an experiment.

2.1. Calibration

An optical trap exerts a harmonic force on an trapped object, $F = -\kappa x$, where κ is denoted the trap stiffness and x is the deviation from the object's equilibrium position. The goal of

#113667 - $15.00 USD Received 1 Jul 2009; revised 15 Jul 2009; accepted 15 Jul 2009; published 17 Jul 2009

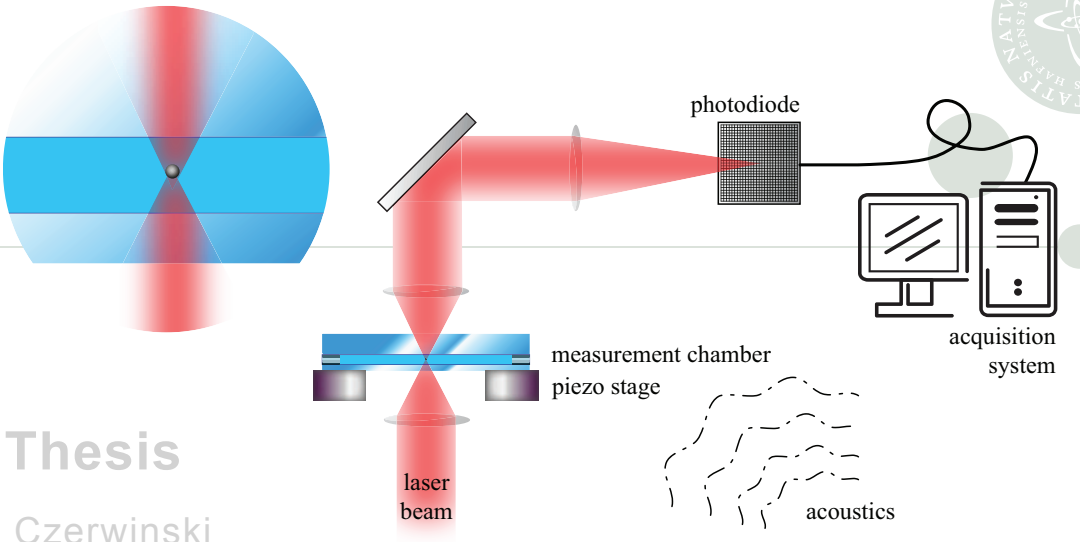

Fig. 1. Schematic drawing of the experimental setup. An infrared laser beam was focused into a sealed measurement chamber which was mounted onto a piezo stage. A polystyrene sphere was trapped in the middle of the measurement chamber which was filled with water (zoom in). The scatter light was collected onto a photodiode. The positional signal of the sphere inside the trap was streamed onto a hard drive. Acoustic noise might have interfered with the experiment.

the calibration procedure is to extract κ which completely characterizes the thermal motion of the trapped object. The equation of motion is well described by the Langevin equation, and a Fourier transformation yields the positional power spectrum, from which the ratio between the trap stiffness and the friction coefficient γ can be found [10]. This ratio is denoted the corner frequency f_c:

$$f_c = \frac{\kappa}{2\pi\gamma}. \tag{1}$$

If a sphere is trapped far away from any surfaces, γ is given by Stokes law: $\gamma = 6\pi\eta r$, where η the viscosity of water ($\eta = 8.9 \cdot 10^{-4}$ sPa), and r the radius of the sphere. The power spectral analysis also provides information regarding the conversion factor β which converts the position measured in volts by the photodiodes to position travelled in nanometers by the trapped sphere [17].

In order to find the correct time interval for the calibration time series we first calculated the Allan variance. For our measurements the absolute minimum of the Allan variance typically occurred around a measurement time in the order of a few seconds, as will be detailed around the description of Fig. 3. Thus, for an acquisition frequency of f_{acq}=22 kHz, we used 2^{16} data points for one individual calibration. Calibration was performed by the power-spectrum method as described in [18] using the program from Ref. [19]. Ten individual calibrations from a longer time series were used to calculate the corner frequency and the conversion factor.

Fourier transformation allows for a reliable, simple, and quick way of calibrating measurements in optical tweezers on-the-fly. In addition, it is particularly useful to pinpoint high-frequency noise. The clear distinct peak in the power spectrum can typically be tracked down to a noise source and eliminated directly. However, when considering only the very low frequency part, assumptions must be made about the drift [11]. Additionally, the typical frequency resolution is simply not good enough. One way to quantify accumulative noise over a broader

#113667 - $15.00 USD Received 1 Jul 2009; revised 15 Jul 2009; accepted 15 Jul 2009; published 17 Jul 2009

frequency band is to look at the integrated noise spectrum [9]. For this one has to assume for instance the boundaries of the integration interval.

2.2. Monte-Carlo Simulations

To compare the experimentally measured time series to values expected for systems that are not exposed to drift, we developed a Monte-Carlo simulation [20]. It calculated the position of micron-sized spheres in an optical trap in meters. The positions of the sphere were drawn with a spacing of numbers of $2.22 \cdot 10^{-16}$. The radius of the sphere r, the corner frequency f_c, the trapping stiffness κ, the acquisition frequency f_{acq}, and the number of sampled points N could be varied. Adjacent time series gained by simulations were treated as regular data and compared to experimental results.

2.3. Allan Variance

For purely stochastic fluctuations which are frequency independent and thus can be used for calibration in atomic clocks or optical tweezers, classical variances usually do not converge. This leads to situations where for example changes to the position due to drift are hidden inside the fluctuating signal. Allan variances have been developed as a consequence of the need of precise atomic and molecular measurements to reveal low- and very-low frequency drift phenomena [21]. It was designed to extrapolate the drift of a system at infinity from finite measurements. Allan variance converges to a finite value for all external noise classically found in nature: Drift (as accumulative noise with $1/f$-characteristics), shot noise, damped oscillations, etc.

Definition. Given a time series of N elements and a total measurement time of $t_{\mathrm{acq}} = f_{\mathrm{acq}} N$, then Allan variance is defined as:

$$\sigma_x^2(\tau) = \frac{1}{2}\left\langle (x_{i+1} - x_i)^2 \right\rangle_\tau \tag{2}$$

with x_i being the mean over a time interval of a length $\tau = f_{\mathrm{acq}} m$, m the number of elements in this particular interval. $\langle ... \rangle$ denotes the arithmetic mean. In words, the Allan variance is half the averaged squared mean of neighboring intervals. Consequently, Allan variance can only be calculated for $\tau \leq t_{\mathrm{acq}}/2$, and it is always ≥ 0. Using $\tilde{x} = \beta x$, the linearity of the Allan variance follows directly from Eq. (2):

$$\sigma_{\tilde{x}}^2(\tau) \quad = \quad \frac{1}{2}\left\langle (\tilde{x}_{i+1} - \tilde{x}_i)^2 \right\rangle = \beta^2 \sigma_x^2(\tau). \tag{3}$$

Therefore, the conversion of Allan variance from arbitrary units to e.g. meters could be done at any time, posterior to calibration for instance.

The statistical error is defined as the standard error of the mean of Eq. (2):

$$\mathrm{SE}_{\sigma(\tau)} = \frac{\sigma_x(\tau)}{\sqrt{n}} = \sqrt{\frac{m}{N}}\sigma_x(\tau) = \sqrt{\frac{\tau}{t_{\mathrm{acq}}}}\sigma_x(\tau). \tag{4}$$

This is valid for $\tau \ll t_{\mathrm{acq}}$. For $\tau < t_{\mathrm{acq}}$, $\mathrm{SE}_{\sigma(\tau)}$ can be approximated by utilizing $n \approx \lfloor N/m \rfloor = \lfloor t_{\mathrm{acq}}/\tau \rfloor$. Note, in this definition the neighboring time intervals of length τ are in principle conditionally independent. When τ is on the order of t_{acq} one faces the problem of low statistics.

Overlapping Allan Variance. To account for the huge statistical error of the Allan variance, Eq. (4), in case of large τ, one can give up the statistically independence of time intervals and use a sliding interval instead. One calculates the difference of two neighboring intervals each containing m elements. Then the intervals move one element further in time while both intervals

#113667 - $15.00 USD Received 1 Jul 2009; revised 15 Jul 2009; accepted 15 Jul 2009; published 17 Jul 2009

loose their 'oldest' element, conserving their number of elements. Consequently, the statistical error scales with $1/\sqrt{m(n-1)}$ instead of $1/\sqrt{n}$ as in Eq. (4), the conditionally independent case.

Normal variance. Often, the standard way to calculate variance as the square of the standard deviation of the mean with a sliding window averaging over τ has been used to evaluate drift in a data set with mean $\bar{x}$:

$$\sigma^2(\tau) = \frac{1}{2}\left\langle (x_i - \bar{x})^2 \right\rangle_\tau . \tag{5}$$

However, one problem of this normal variance is that it does not converge for noise regularly occuring in nature, e.g. white noise.

2.4. Thermal Limit

The standard error of an averaged position of an object can be used to access its limit for positional detection. It depends only on its diffusion $\langle x^2 \rangle = 2D\tau$ with the diffusion constant $D = k_B T/\gamma$. It can be further confined by a trapping potential characterized by a trapping constant κ. Using the same approximation as for Eq. (4), the statistical error for a trapped sphere becomes:

$$SE_{\langle x \rangle} = \frac{1}{\sqrt{n}}\sqrt{\langle x^2 \rangle} \approx \sqrt{\frac{2k_B T\gamma}{k^2\tau}}. \tag{6}$$

This limit cannot be beaten by any measurement that does not oversample a desired signal. In the following the Allan variances found are compared to this thermal limit. In the case of dual optical traps the expression is slightly changed [11].

2.5. Allan Variance for Optical Tweezers Setups

To analyze data from experiments with optical tweezers a set of requirements has to be fulfilled. To access a broad range of possible values for time intervals τ, one of the requirements is a device which allows for an acquisition of positional data at a fast and a reliable rate over a (very) long measurement time.

Allan variances of position time series of a trapped polystyrene sphere were calculated by using a custom-made MATLAB program [22]. The program calculated time-stamped as well as time varying data. In the case of time-stamped data, vectorization of the interval used for mean and difference calculations allow for very fast calculation of the Allan variance even for our longest data sets.

We tested the impact of various parameters, e.g. acoustic noise, sample stabilty, geometry, and photodiodes by doing a set of three time series (typically at $f_{\mathrm{acq}} = 22$ kHz for about 13 min, i.e. 2^{24} data points for each coordinate). Then we altered the parameters and repeated the measurements. Though the Figs. of the results section represent plots of particular datasets, all experiments have been repeated as described above and all results explicitly stated are solid and reproducible. We found it advantageous to plot Allan variances in log-log plots. In those, slopes correspond to the exponent of a proposed relation.

3. Results

Using the optical tweezers setup we measured time series of a sphere's position and using Monte-Carlo simulations we created time series of the same length using the same physical parameters. One important difference between the experimental data points and the simulation was that the experimental data were subject to various sources of noise, e.g. long term drift. There were no such noise terms in the simulated data. Figure 2(a) shows the position versus time of an optically trapped polystyrene sphere, green line shows experimental results, light grey line

#113667 - $15.00 USD Received 1 Jul 2009; revised 15 Jul 2009; accepted 15 Jul 2009; published 17 Jul 2009

simulated data. (b) shows position histograms of two complete time series $N = 262,144$ which overlap precisely. In (c) the positional power spectral density of the two data sets are plotted, the full lines show Lorentzian fits to the power spectra. These fits include the effect of aliasing and for the experimental data the filtering effect of the photodetection system and electronics as implemented in the software [19]. The full black line is a fit to experimental data, and the light grey one is fitted to simulated data. The point where the curve crosses from being horizontal to having a slope of -2 is denoted the corner frequency f_c [18]. It is directly proportional to the trap stiffness κ (Eq. (1)). At high frequencies one sees that the well understood effect of photodiode filtering [16] causes the experimental data to lie beneath the simulated data, which are 'only' subject to aliasing [18]. Drift, which is inherently present in the experimental but not in the simulated data, does not show, not even at the low frequency end.

3.1. Allan Variance for Individual Experiments

The Allan variance was calculated from the time series using Eq. (2), for the example shown in Fig. 3 where the original time series spanned about 13 min. The green curves are from an experiment where a polystyrene sphere with a diameter of 800 nm was trapped with a corner frequency of 800 Hz, hence $\kappa = 33.6$ pN/μm. The green-grey curves stem from a Monte-Carlo simulation. The orange curves are from an experiment with a stronger trap, f_c=1600 Hz, $\kappa = 67.7$ pN/μm. The orange-grey curves are from the corresponding simulation. The full lines denote the overlapping Allan variance. Due to its improved statistics, it is always inside the variation of the Allan variance. This is particularly evident for large τ.

The dashed lines with a slope of $-1/2$ are the thermal limits for those two trapping stiffnesses according to Eq. (6). For short time intervals, all Allan variances fall below the thermal limit because adjacent positions are correlated. The absolute maxima of the Allan variance can be found at $\pi\tau_c = (2f_c)^{-1}$. The inset of Fig. 3 shows the autocorrelation time, orange is for the strong trap, green for the weaker one. For $\tau > 2\pi/(2f_c) = 2\pi^2\tau_c$, Allan variances are above the respective thermal limits and decay with a characteristic slope of $-1/2$ for a wide range of measurement times. The fact that the Allan variance stays very close to the thermal limit is a benchmark of an extremely stable setup. The deviation from the thermal limit beyond 1 s is due to drift, as the comparison between simulated and experimental data illustrates. The Allan variance reaches a global minimum for measurement times in the range of seconds. This is the timespan which denotes the optimal measurement time for calibrations. Here one finds a balance between a time long enough allowing for the Gaussian distributed parameters to be accurately determined and a time short enough that drift does not yet play a significant role. This optimal measurement time depends on the trap stiffness. As expected, a stronger trap ensures a smaller Allan variance than a weaker trap, which implies a higher positional accuracy. This is particularly true for long time scales. The normal variance is also plotted in Fig. 3 using dotted lines.

3.2. Accuracy Depends on Acquisition Frequency

Another question which was addressed by Allan variance analysis was the question of optimal acquisition frequency f_{acq}. A polystyrene sphere was optically trapped and the data acquisition frequency was varied between 10 Hz and 100 kHz. The result of the corresponding overlapping Allan variance is shown in Fig. 4.

In Fig. 4(a), the graphs have the same characteristic trajectories as those shown in Fig. 3, but it is apparent that the Allan variance decreases with higher acquisition frequency up to a certain threshold. This threshold is the inverse correlation time τ_c^{-1} and depends on the trapping stiffness. It can be found in the plotted data set at $\tau_c^{-1} = 2\pi f_c \approx 10$ kHz. Above this threshold, an increase in frequency does not change the Allan variance for the majority of the measure-

#113667 - $15.00 USD Received 1 Jul 2009; revised 15 Jul 2009; accepted 15 Jul 2009; published 17 Jul 2009

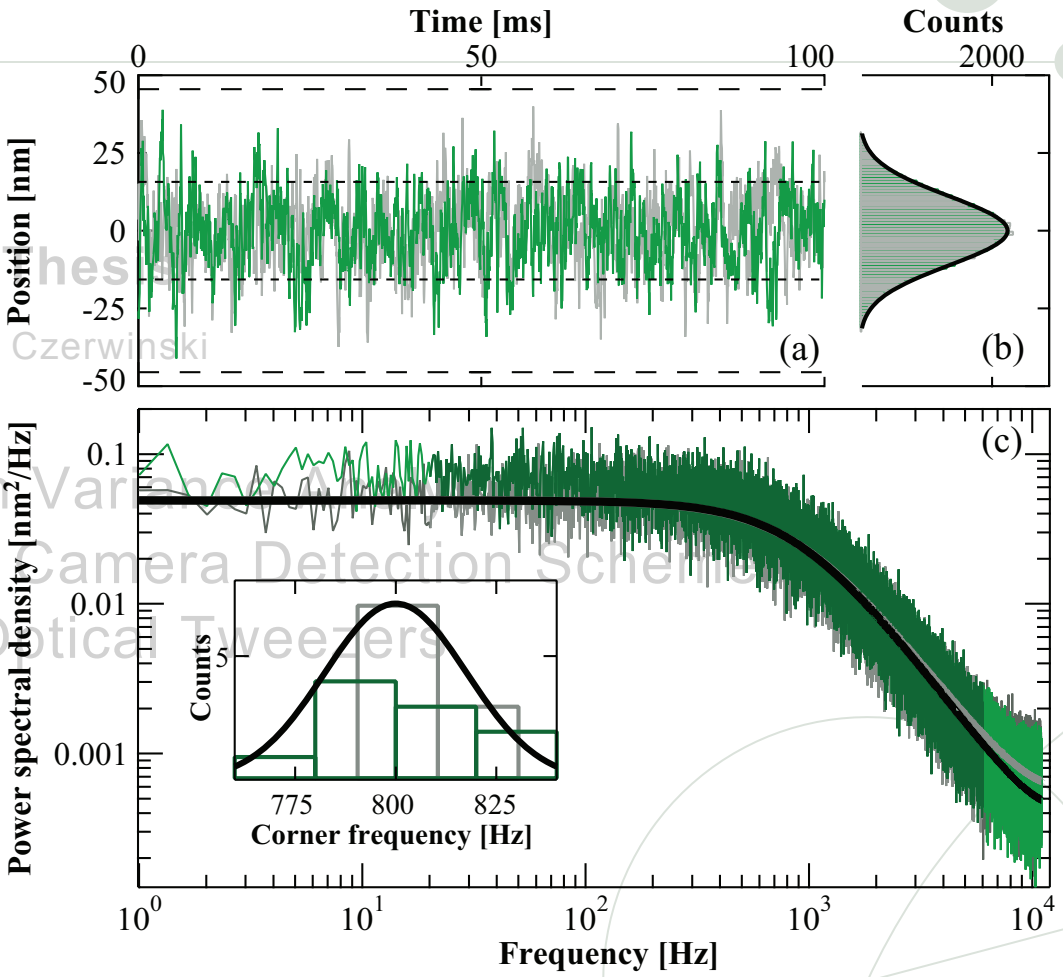

Fig. 2. (a) Experimental (green) and simulated (grey) position time series of an optically-trapped polystyrene sphere in water. The traces are centered around 0 nm, and the dashed lines indicate the interval $\pm\sigma$, respectively $\pm 3\sigma$. (b) Variance σ is obtained by fitting a Gaussian to the overlapping positional histogram. (c) The power spectral density of experimental (green) and simulated (grey) positional sequences. Each graph is the average of 10 individually calculated power spectra for traces of about 3 s. The band from 20 to 6000 Hz was used to obtain corrected Lorentzian fits (experimental: black; simulation: grey). The inset shows the spread in corner frequencies from individual calibrations. This spread follows a Gaussian distribution.

#113667 - $15.00 USD Received 1 Jul 2009; revised 15 Jul 2009; accepted 15 Jul 2009; published 17 Jul 2009

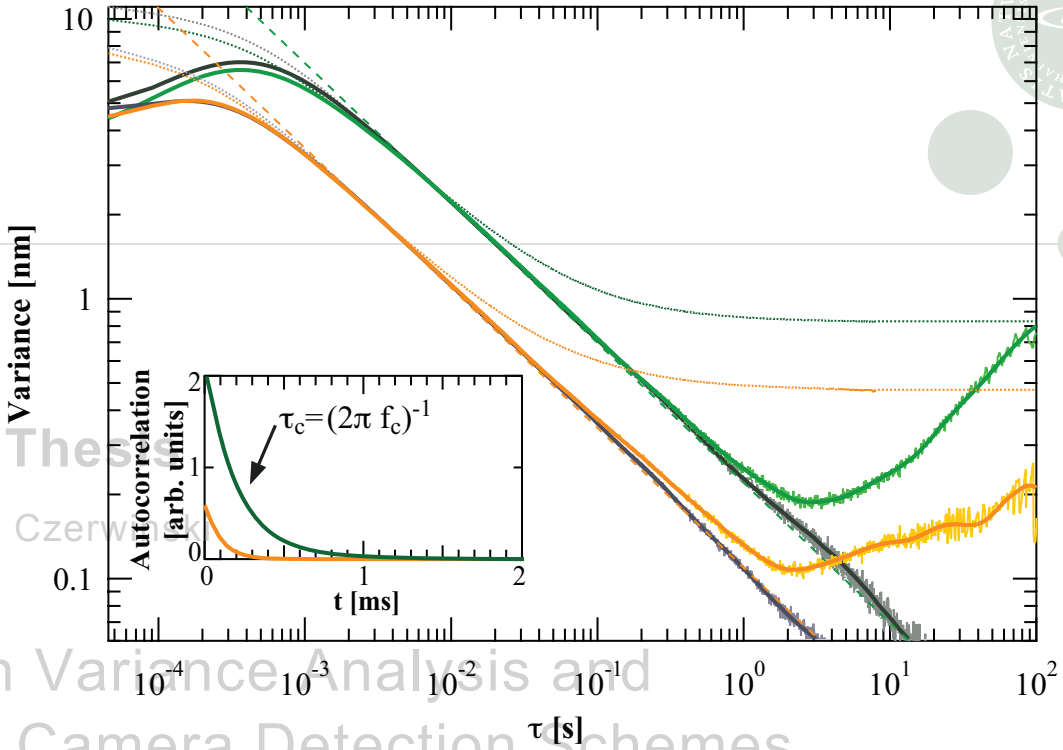

Fig. 3. Variances of individual optical tweezers experiments. The variances were calculated from the position of a polystyrene sphere trapped with κ =67.7 pN/μm (orange) or with κ =33.6 pN/μm (green). Grey graphs show results of Monte-Carlo simulations using the same physical parameters. Dashed lines are the thermal limits according to Eq. (6). The dotted lines are graphs of the normal variances using Eq. (5). Remarkably, the Allan variance provides half an order of magnitude higher sensitivity for $\tau > 1$ s.

ment times. Only above the optimal interval, around 10 s, it seems beneficial to improve the acquisition frequency above 10 kHz. However, the bandwidth of the used position-sensitive photodiode was found to lie in between 43 and 47 kHz. Hence, the apparent aliasing might be the reason for the steeper slope for measurement times $\tau > 20$ s in the plotted graphs.

Figure 4(b) shows the result of rescaling the measurement time onto the number of acquired data points. The Allan variance changes with the number of acquired data points for various sampling frequencies. Hence, for a high acquisition rate the number of data points needs to be large in order to achieve highest accuracy. In principle, this can be used to extract information regarding how much extra precision is gained by acquiring additional data points. Furthermore, the difference of the graphs from the 'line of maximum information' indicates how much information a data point at the given acquisition frequency contains. For acquisition frequencies $f_{\mathrm{acq}} < \tau_c^{-1}$ one measures thermal fluctuations of the sphere without any informational content.

3.3. *Acoustics and Chamber Geometry*

We also investigated the effect of acoustic noise in the lab. Two different situations were compared: (i) A silent lab early Saturday morning where efforts were made to shield the equipment from noise. And (ii) a lab with more acoustic noise under everyday laboratory conditions, e.g., other people working the the lab and talking, the radio on, the equipment was not covered and

#113667 - $15.00 USD Received 1 Jul 2009; revised 15 Jul 2009; accepted 15 Jul 2009; published 17 Jul 2009

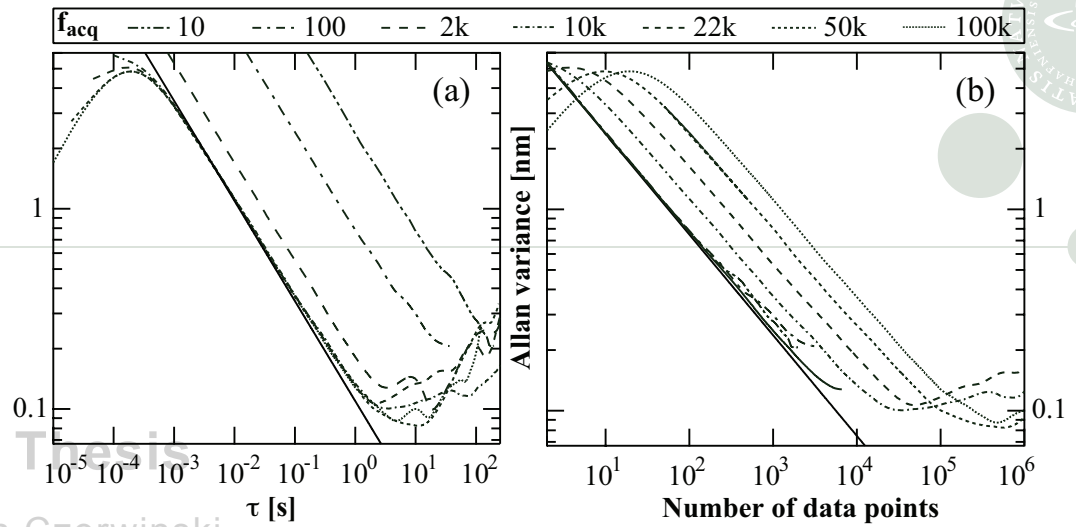

Fig. 4. Allan variance depends on the acquisition frequency (a) and on the number of data points (b). Each time series had a length of about 13 min, the acquisition frequency f_{acq} was varied, and the trap stiffness was $\kappa = 67.7$ pN/μm.

ambient light would also enter the photo detection system. Figure 5 shows the measurements of Allan variance under those two conditions. The full lines are Allan variances of experimental data from an optically trapped sphere under virtual silence (i), and the dash-dotted lines are from noisy conditions (ii).

The aqueous sample chamber was asymmetric with inner dimensions 5 cm (x), 1 cm (y), and 95 μm (z) and the sphere was trapped approximately in the center of this chamber. The green traces in Fig. 5 are Allan variances of the adjacent time series in x, the red traces those of y. The black full lines denote the thermal limit. The measurement chamber was sealed with a thin glass cover slip at the bottom towards the focusing objective and at the top either a thick cover slip (1 mm, data in Fig. 5(a)) or a thin cover slip (0.13–0.16 mm, data in Fig. 5(b)).

Figure 5 shows that the effect on the Allan variance of reducing acoustic noise is minimal on the y-direction, the smallest lateral dimension of the chamber. However, in the x-direction, the longest lateral direction of the chamber, there is a significant effect of reducing acoustic noise. To check the directional dependence of these results we rotated the chamber 90° and still saw the effect. In other words, the difference in x and y directions are due to sample geometry and not to asymmetries in the laser or detection system. All other plots of Allan variances in the present letter originate from the longest direction in an elongated chamber (corresponding to the x-direction in Fig. 5).

Making the chamber with a thick rather than a thin cover slip at the top stabilizes the chamber for all sampling times above ~ 0.3 s. This can be seen by comparing Figs. 5(a) and 5(b). To facilitate the comparison a grey horizontal line is drawn at 0.17 nm accuracy in both plots. Another effect emerging from using different upper cover slips is the different scaling properties of the Allan variance at long measurement times. Full lines with slopes of 1 in (a) and $1/2$ in (b) are drawn in the Fig. 5 to facilitate the comparison of the scaling trends of the Allan variance for $\tau > 20$ s.

#113667 - $15.00 USD Received 1 Jul 2009; revised 15 Jul 2009; accepted 15 Jul 2009; published 17 Jul 2009

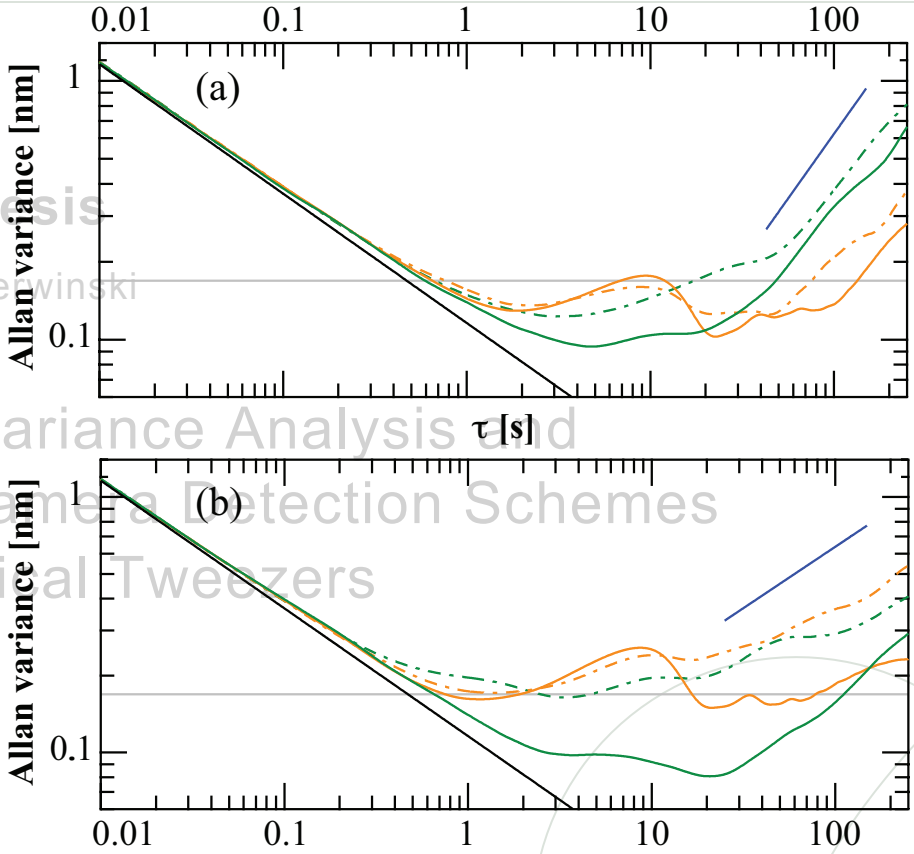

Fig. 5. Impact of measurement-chamber construction and acoustic noise in the laboratory. (a) Allan variance for the position of a trapped sphere, $\kappa = 53.4$ pN/μm. x (green) is the longest lateral dimension of the measurement chamber. Accordingly, y (orange) denotes the shortest lateral dimension. The upper cover slip has a thickness of 1 mm. Solid lines are measured in virtual silence, dash-dotted lines are measured with acoustic noise in the laboratory. (b) Same conditions as in (a), but using an upper cover slip of a thickness of 0.13–0.16 mm. The solid black curves represent the thermal limit and grey line is a guide to the eye at 0.17 nm. The blue lines indicate the slope for low-frequency drift, 1 for (a) and 1/2 for (b).

#113667 - $15.00 USD Received 1 Jul 2009; revised 15 Jul 2009; accepted 15 Jul 2009; published 17 Jul 2009

3.4. Piezo Stage

Many optical tweezers experiments involve the usage of a piezo stage. It might be possible that mounting the sample on a piezo stage induces additional noise. To investigate this we performed an experiment where a sphere was optically trapped and its Allan variance was calculated both for the situation where the piezo stage was turned on and where it was off. Figure 6 shows the Allan variance of a trapped sphere, $\kappa = 33.6$ pN/μm (violet) with the piezo on. When decreasing the trap stiffness to $\kappa = 15.3$ pN/μm (red), the loss in accuracy over measurement intervals of 0.5 s$< \tau <$110 s became even more pronounced; whereas switching off the piezo and keeping the trap stiffness constant at $\kappa = 15.3$ pN/μm (green) eliminated the effect. Hence, the piezo does add noise to the system, in particular in a measurement time interval 0.5 s$< \tau <$110 s. Furthermore, Fig. 6 confirms the findings from Fig. 3 that stronger traps can partially eliminate low-frequency noise. The black trace shown in Fig. 6 is the Allan variance of the output of the control box yielding the position of the piezo while the sample was mounted. For short measurement times, the Allan variance shows local maxima that correspond to odd-numbered divisors of the piezo's resonance frequency. The resonance of the piezo has thus not been altered significantly by mounting the stage. At measurement times within 0.5 s$< \tau <$110 s, the noise of the stage alone peaks in the same interval as the noise peak in the violet and red curves. Therefore, we propose that the piezo stage contributes to the noise as quantified by Allan variance in a frequency interval as visualized by the grey shading in Fig. 6. Those low-frequency phenomena would be challenging to identify using standard noise-detection methods.

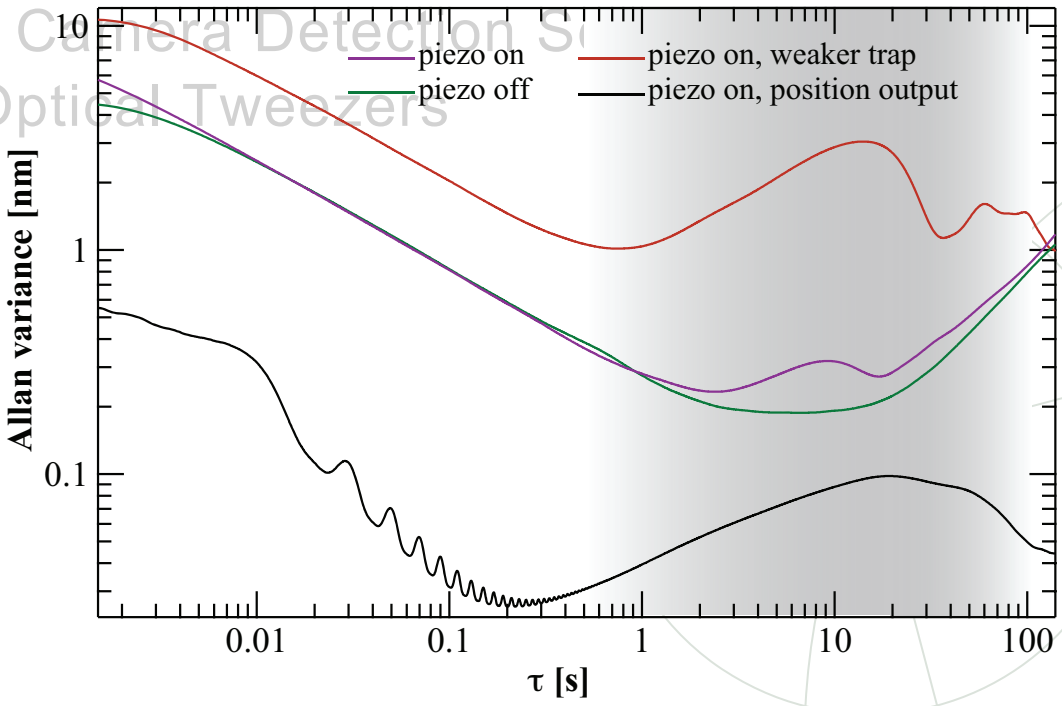

Fig. 6. Impact of piezo stage on Allan variance for a trapped sphere. When the piezo is switched on a hill in the Allan variance within the interval 0.5 s$< \tau <$110 s is observed (grey shading). It is more pronounced for a weaker trapped sphere, $\kappa = 15.3$ pN/μm (red), than for a strongly trapped sphere, $\kappa = 33.6$ pN/μm (violet). The Allan variance of the piezo itself is plotted in black. When the piezo is switched off (green), the hill disappears.

#113667 - $15.00 USD Received 1 Jul 2009; revised 15 Jul 2009; accepted 15 Jul 2009; published 17 Jul 2009

3.5. Comparison of Photodiodes

One further issue which was investigated by Allan variance analysis was the noise contribution from different types of photodiode-based detection systems, from the laser, and the data acquisition electronics. These effects are visualized in Fig. 7: The full lines show Allan variances of a trapped polystyrene sphere, $\kappa = 33.6$ pN/μm, using either the position-sensitive diode (PSD, green) or the quadrant photodiode (QPD, orange). It was the same sphere trapped in both cases. The performances of the two types of photodiodes were quite similar, but for the shortest as well as for the longest measurement times the PSD had a smaller Allan variance. Another experiment was performed where there was nothing inside the optical trap, but the laser was shining directly at the photo detection system. An optically trapped sphere has a focusing effect on the laser light, so in the absence of a trapped sphere the total signal on the detection system is significantly smaller than when a sphere is trapped using the same laser intensity. The dashed lines in Fig. 7 show the Allan variance of the laser signal as detected by the QPD (orange) and PSD (green), respectively. Generally, the noise of the PSD is lower than of the QPD. Interestingly, one sees a pronounced peak in the Allan variance of the QPD around 16 ms. This time interval corresponds exactly to the detection delay time reported for this particular diode [16]. The black dotted line is the Allan variance of the electric noise from the acquisition system, in this experiment the PSD was on, but the laser was off. The dash-dotted horizontal line in Fig. 7 denotes the resolution of the acquisition system.

4. Discussion

Allan variance is a strong tool to quantify noise in optical tweezers setups. However, it is advantageous to combine it with Fourier analysis. The Fourier transformation of a positional time series is conveniently used for calibration and is efficient to identify noise that occurs at high frequencies, typically above 1 Hz. Nonetheless, Fourier analysis lacks resolution for noise with characteristic frequencies lower than approximately 1 Hz. In particular an accumulative low-frequency noise as drift is almost impossible to identify. One should also be aware that for a method which considers the integrated noise one limitation is that it strongly depends on the choice of bandwidth. The normal variances go towards an asymptotic value which denotes the positional variance of the trap, but Allan variances can probe way below this limit. The reason can be found in the convergence of the Allan variance for most of the naturally occurring types of noise, whereas a normal variance does not converge for purely stochastic noise. Thus, a normal variance carries no information about, e.g. the optimal measurement time for calibrations.

In our experiments Allan variance analysis has revealed that, if a sampling frequency of 22 kHz and typical trap stiffnesses of 10–140 pN/μm are used, the optimal length of a time series for calibration is in the order of seconds, not e.g. tens of seconds. This time scale is on the same order as reported in [14]. Still, our Allan variance is closer to the thermal limit than those reported for a similar setup in [14]. This finding emphasizes the stability of our setup. This comparison also shows one strength of the Allan variance analysis, namely to compare different labs, different setups, or different settings with respect to noise contributions.

One should note, that when investigating other measures than just positions, one might need to construct an adapted Allan variance. An example can be found in [14] where an Allan variance for force measurements is derived. Notably, these may show the higher force accuracy and time stability for weaker traps.

Interestingly, we found a pronounced dependence of the Allan variance on chamber geometry and on whether the measurement chamber had been stabilized with a thicker cover slip. Thicker cover slips decrease the Allan variance, up to measurement times in the order of hundreds of seconds. However, beyond those we found steeper slopes for thick cover slips. As thick cover slips were meant to stabilize measurements made in microscopes over all timespans, this

#113667 - $15.00 USD Received 1 Jul 2009; revised 15 Jul 2009; accepted 15 Jul 2009; published 17 Jul 2009

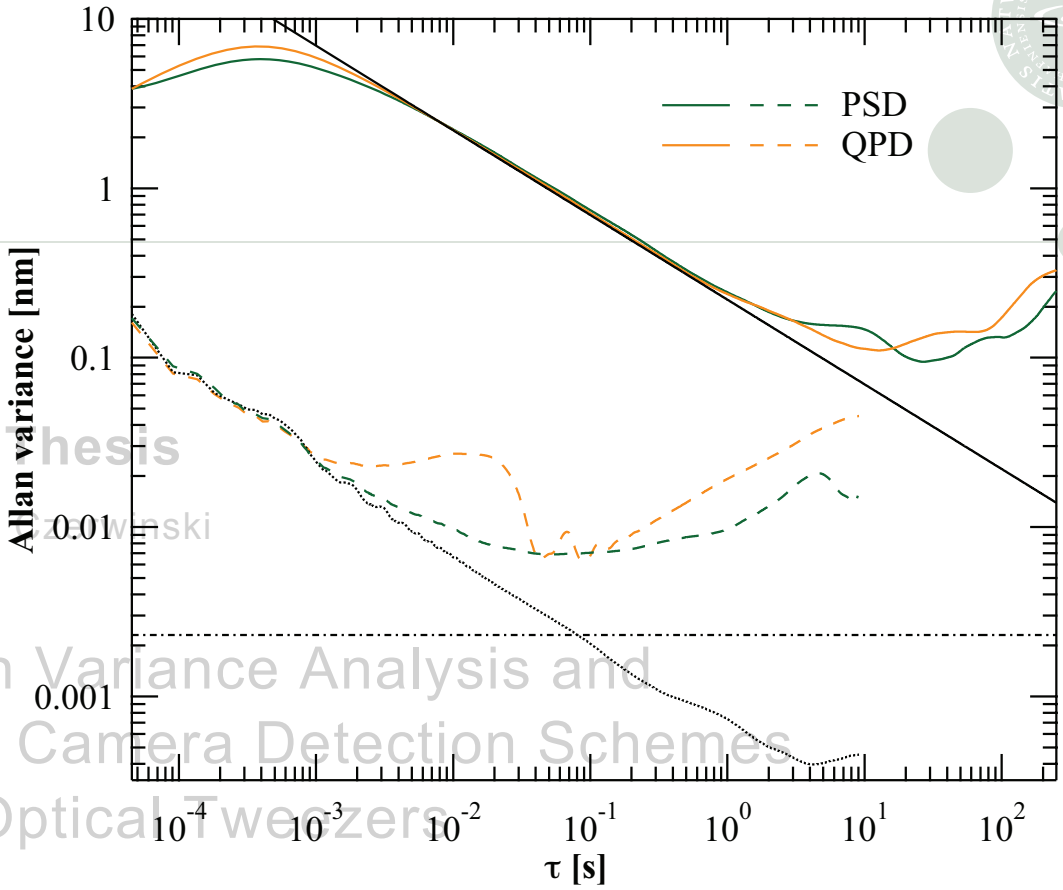

Fig. 7. Effect of photodiodes on Allan variance, PSD (green) and QPD (orange), $\kappa = 33.6$ pN/μm. The solid black line gives the thermal limit. The dashed lines mark the Allan variance when the diodes are shined on by the laser with nothing trapped. The dotted line marks the purely electronic noise when every illumination was blocked. It drops below the best resolution possible for the given photodiode-based detection system with the used acquisition settings (dash-dotted line).

was unexpected. Here again, Allan variance analysis revealed and quantified a low-frequency drift phenomena which would not have been visible by the normal variance. For the chamber geometry, the shortest direction of the chamber was subject to significantly more noise than the longer direction. The origin of this geometry dependence is subject to future investigations. Elimination of acoustic noise does not significantly decrease the Allan variance, in particular not along the shortest direction of the sample chamber. Hence, one can safely tune into one's favorite radio station and operate experiments during regular working hours.

Optical tweezers setups are often equipped with photodiode detection systems and the chamber often mounted on a piezo stage. Both the photodiode and the piezo stage contribute to the total noise spectrum of the system, so if the piezo stage is not necessarily needed for a particular experiment, it would be advantageous to switch it off. Allan variance is not a measure of resolution, but rather of accuracy. One would have to put a signal of a known input into the system and monitor its output to obtain a measure of the resolution. For such experiments one typically uses a piezo stage to move a stuck sphere in a controlled fashion. But, as piezo systems are exposed to fluctuations and drift, resolution inputs should therefore be chosen where

#113667 - $15.00 USD Received 1 Jul 2009; revised 15 Jul 2009; accepted 15 Jul 2009; published 17 Jul 2009

the fluctuations of the piezo stage have the smallest Allan variance.

A comparison of the performance of a quadrant photodiode to the performance of a position sensitive diode showed that they were nearly performing identically. Nevertheless, both for very short and very long measurement times the position sensitive diode was performing slightly better. Moreover, we saw the footprint of the 3 dB filtering frequency of the quadrant photodiode around 16 ms as expected [16].

Allan variance seems to be a straight forward method to quantify noise in optical trapping assays. One reason why it has not been established before could be the necessary software implementations because one has to work with very large datasets. To our knowledge, only one publication [14] previously took advantage of this method, even though they limited their analysis to data sets of 300,000 points taken over 5 min. Our software solutions capable of handling significantly larger datasets are freely available through the MATLABCentral.

Our results showed that optical tweezers have a resolution close to the thermal limit for measurement times between 100 ms and 100 s. This is precisely the interval where most of the biological processes like molecular motors typically have been tested with optical tweezers. Thus, Allan variance analysis might strengthen these experiments against criticism regarding drift sensitivity. With the tools described in this letter this type of analysis can be done on-the-fly along with regular experiments.

5. Conclusions

We have used Allan variance as a method to quantity noise in a force-measuring optical tweezers setup over more than 6 decades in time. The noise which is pinpointed by this method is difficult or impossible to quantify by other methods such as power spectral analysis or normal variance analysis. Through Allan variance analysis we determined the optimal measurement time to achieve a calibration with highest accuracy, as well as the optimal sampling frequency. Allan variance analysis has also shown that the measurement chamber stability as well as its geometry influences the noise spectrum. Typically, chambers for optical trapping experiments are mounted on a piezo stage and data are acquired by photodiodes. We quantified the magnitude and typical interval of noise contribution from these pieces of equipment, thus making it possible for example to perform a qualified choice between which type of diode to use for a particular experiment. In principle, this type of analysis can be used in any kind of single-molecule technique where it is advantageous to quantify and possibly eliminate or minimize noise sources. It can easily be used as a complimentary technique, in addition to Fourier analysis, as a standard method of comparing different laboratories and their performance.

Acknowledgements

We acknowledge discussions with and inputs from M. Andersson, P. M. Bendix, K. Berg-Sørensen, P. Gerlee, U. F. Keyser, M. Mahamdeh, S. A. Mir, R. Seidel, and D. Stein. The project was financially supported by the Excellence program of the University of Copenhagen, and the Marie Curie Grant MP6-MEST-2004-504465.

#113667 - $15.00 USD Received 1 Jul 2009; revised 15 Jul 2009; accepted 15 Jul 2009; published 17 Jul 2009

FACULTY OF SCIENCE
UNIVERSITY OF COPENHAGEN

PhD Thesis

Fabian Czerwinski

Allan Variance Analysis and Fast Camera Detection Schemes for Optical Tweezers

Academic Advisor: Lene B. Oddershede

Submitted: September 27, 2010

Quantifying and pinpointing sources of noise in optical tweezers experiments

Fabian Czerwinski, Andrew C. Richardson,
Christine Selhuber-Unkel, and Lene B. Oddershede

Niels Bohr Institute, University of Copenhagen,
Blegdamsvej 17, DK-2100 Copenhagen, Denmark

ABSTRACT

One limitation on the performance of optical traps is the noise inherently present in every setup. Therefore, it is the desire of most experimentalists to minimize and possibly eliminate noise from their optical trapping experiments. A step in this direction is to quantify the actual noise in the system and to evaluate how much each particular component contributes to the overall noise. For this purpose we present Allan variance analysis as a straightforward method. In particular, it allows for judging the impact of drift which gives rise to low-frequency noise, which is extremely difficult to pinpoint by other methods. We show how to determine the optimal sampling time for calibration, the optimal number of data points for a desired experiment, and we provide measurements of how much accuracy is gained by acquiring additional data points. Allan variances of both micrometer-sized spheres and asymmetric nanometer-sized rods are considered.

Keywords: optical tweezers, optical trapping, noise, drift, calibration, Allan variance, piezo stage, nanorods

INTRODUCTION

Optical tweezers are the perfect nano-tool for single-molecule manipulation and investigations.[1] With a correctly chosen wavelength they are nearly non-invasive and can be used to manipulate entire living microorganisms[2,3] or track organelles inside a cell.[4] For single-molecule investigations, often a handle, for example in the form of a dielectric micron-sized object, is attached to the molecule of interest. Optical tweezers can then follow the motion of the handle and calculate the forces exerted on the handle with sub-piconewton resolution. The handle is often a polystyrene sphere with a diameter of a couple of micrometers, but even nanoparticles such as gold spheres,[5] gold nanorods,[6] spherical silver nanoparticles,[7] or even individual quantum dots[8] can be individually trapped and used as force transducers.

For single-molecule experiments it is extremely important to measure the distances moved and forces exerted by the single molecule as accurately as possible.[9] Therefore, it is crucial to minimize or eliminate noise and drift and to perform force calibration as accurately as possible. Much effort has been put into minimizing noise, for instance entire setups have been covered to eliminate pressure fluctuations; the equipment is most often placed on an optical table and sometimes even on a foundation which is separated from the rest of the building. A successful way to eliminate drift is by using a laser beam parallel to the trapping laser to track the motion of a feducial marker which is attached in proximity to the handle of interest and thus subject to a similar drift.[10] This setup, however, requires the use of at least two laser beams and two independent detection systems. Another way to reduce drift that is often employed in optical trapping setups is to move the system of interest away from any surface subject to significant drift. This could be done by using a dual-trap setup and suspending the molecule of interest between two individual handles. But how efficient are these methods? And which types of noise should one really worry about in optical trapping experiments? To answer these questions it is essential to be able to quantify the noise introduced by each part of the equipment or surroundings.

Further author information:
F.C.: E-mail: czerwinski@nbi.dk
A.C.R.: E-mail: richards@nbi.dk
C.S.U.: E-mail: selhuber@nbi.dk
L.B.O.: E-mail: oddershede@nbi.dk

Optical Trapping and Optical Micromanipulation VI, edited by Kishan Dholakia, Gabriel C. Spalding, Proc. of SPIE
Vol. 7400, 740004 · © 2009 SPIE · CCC code: 0277-786X/09/$18 · doi: 10.1117/12.827975

Submitted: September 27, 2010

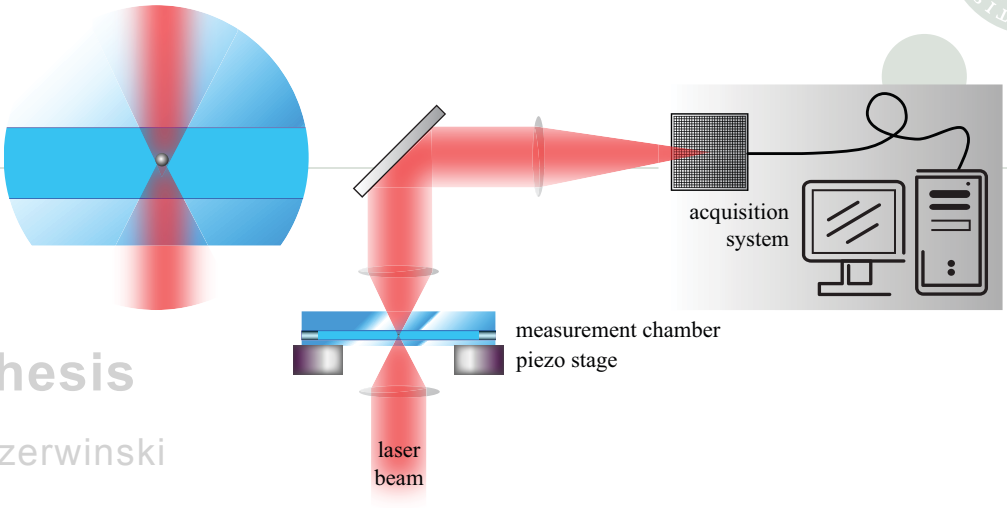

Figure 1. Schematic drawing of experiments. A highly focused infrared laser beam traps a polystyrene sphere inside a custom-made measurement chamber that is mounted on a piezo stage. The forward scattered light is collected onto a photodiode that transmits the sphere's position into an acquisition system.

Fourier analysis is an excellent tool to calibrate optical tweezers on-the-fly. Furthermore, peaks occuring in the high frequency part of the power spectrum can often easily be traced backwards to a particular noise contribution. However, Fourier analysis is not optimal for identifying and quantifying low-frequency noise, which drift, as inherently present in experiments, produces. However, Fourier analysis has been used to judge the noise stemming from particular experimental settings,[11,12] but for such an analysis various assumptions have to be made about the bandwidth of the integration. Also, the regular positional variance is often used as a measure for noise. However, the normal variance does not converge for purely stochastic types of noise, such as white noise.

In this Proceeding, we propose Allan variance analysis as a simple and efficient tool to pinpoint and quantify noise in optical trapping facilities. The Allan variance of the positions visited by an optically trapped particle can be calculated on-the-fly during an experiment and used, e.g., to determine the optimal length of a time series for accurate calibration.[13,14] By comparison to simulated data with no drift present it has been explicitly shown that Allan variance is an excellent tool to pinpoint and quantify low-frequency drift.[14,15] Allan variance analysis has been specifically used to verify that a CMOS camera had sufficient time resolution to track an optically trapped particle.[13] In addition, Allan variance analysis is able to reveal noise contributions from commonly used photodiode-based detection systems in optical trapping experiments,[14] thus providing a platform for a qualified choice between, for example, a position-sensitive rather than a conventional quadrant photodiode for certain sets of experiments. Moreover, Allan variance has revealed the impact of the piezo stage, the acoustic noise in the laboratory, and the geometry and stability of the sample chamber on the noise spectrum. Complementary and additional to Fourier analysis, Allan variance analysis provides a basis for an optimal setup design.[14] In this Proceeding, we review some of these results. In addition, we provide information about how the Allan variance of a measurement can be improved by acquiring additional data points and about the Allan variance of an asymmetric gold nanorod.

METHODS

By focusing a laser beam into a measurement chamber that is mounted onto a piezo stage inside an inverted microscope (Leica DMIRBE), the optical trap is created. For trapping polystyrene speres (Bangs Laboratories, diameter (800 ± 10) nm) we used a water immersion objective (Leica, HCX, 63x, NA=1.20) at a color correction at its lowest setting (0.13 mm) and a measurement chamber of two cover slips (bottom: thickness 0.13–0.16 mm, top: 1 mm) sandwiched together by double sticky tape. The actual trap was formed in the middle of the

Submitted: September 27, 2010 Proc. of SPIE Vol. 7400 740004-2

chamber (total height (95 ± 5) μm). For trapping gold nanorods,[6] an oil immersion objective (Leica, HCX PL Apo, 63?, NA =1.32) was used and the immersion oil was chosen to compensate spherical abberations.[16] Here, the measurement chamber was custom-made from two cover slips (bottom: thickness 0.16–0.19 mm, top: 1 mm) held together by parafilm. The nanorods were trapped 5 μm above the bottom. Their dimensions were for the longer axis $x = (63.8 \pm 7.4)$ nm and for the shorter axis $y = (37.3 \pm 5.0)$ nm (verified by transmission electron microscopy prior to measurements). In all cases, measurement chambers were sealed with vacuum grease to prevent evaporation. To ensure the optimal pointing stability of the laser beam, we switched on the laser at least one hour prior to experiments. All measurements were done at room temperature.

A schematic drawing of the essential parts of the experiment is shown in Figure 1. The forward scattered light is focused onto a position-sensitive photodiode (Pacific Silicon Sensor, DL100-7PCBA3) or onto a quadrant photodiode (Hamamatsu, S5981). Its output in voltage is connected through an amplifier, a low-pass filter of 100 kHz, and an acquisition card (National Instruments, PCI-6251) to a computer. By utilizing our data-streaming software that was custom-made in LABVIEW,[17] we were not limited by the amount of acquired data (tested 2 h at 1 kHz, and 22 min at 100 kHz).

Typically, for trapped spheres, the analysis was applied to adjacent time series of 2^{24} positions acquired at various acquisition frequencies. For nanorods, the time series consisted of 2^{21} positions acquired at 22 kHz. All additional filtering was carried out posterior to acquisition. For visual observation of the spheres right before and after experiments, a CCD camera (Sony, XC-ES50, 25 Hz) was used, whereas the nanorods could not be visualized optically.

Calibration. An optically trapped object experiences a harmonic force $F = -\kappa x$ with the trap stiffness κ and the distance x from the equilibrium position. Thus, κ characterizes the thermal motion of the trapped object. For the analysis, the Langevin equation is typically solved and Fourier transformed. The result is a positional power spectrum that allows for finding the ratio between κ and the friction coefficient γ, i.e. the corner frequency f_c:

$$f_c = \frac{\kappa}{2\pi\gamma}. \tag{1}$$

In case a sphere is trapped far away from any surface, the Stokes law gives: $\gamma = 6\pi r\eta$, where r is the radius of the sphere and η the viscosity of the surrounding medium; here, in all experiments, deionized water, $\eta = 8.9 \cdot 10^{-4}$. The nanorods have the shape of sphero-cylinders. We approximated their shape as cylinders in order to calculate their drag coefficients accordingly.[6] The conversion factor β, which relates the distance measured in volts to the distance travelled in meters by the trapped object, was found by comparing theoretical and experimental diffusion constants.[18]

In a first step, we calculated the Allan variance to obtain the optimal measurement time for calibration. Secondly, we calibrated conditionally independent intervals of the time series with that particular length. We used the power-spectrum method as described previously[19] with the freely available program.[20] Finally, we calculated various types of variances.

For typical noise phenomena found in nature, classical variances do not converge. For example, purely stochastic noise does not converge for the **normal variance**:

$$\sigma^2(\tau) = \frac{1}{2}\left\langle (x_i - \bar{x})^2 \right\rangle_\tau, \tag{2}$$

where $\bar{x}$ denotes the mean of the time series and x_i the mean of positions within the interval of length τ.

The **Allan variance** is designed to converge for most naturally occuring noise.[21] Given a time series consisting of N elements and a total measurement time of $t_{\mathrm{acq}} = f_{\mathrm{acq}}N$, the Allan variance is defined as:

$$\sigma_x^2(\tau) = \frac{1}{2}\left\langle (x_{i+1} - x_i)^2 \right\rangle_\tau, \tag{3}$$

where x_i is the mean of the measurement interval τ. In words, the Allan variance is half of the mean of the squared differences of neighboring intervals of a given length.

Submitted: September 27, 2010 Proc. of SPIE Vol. 7400 740004-3

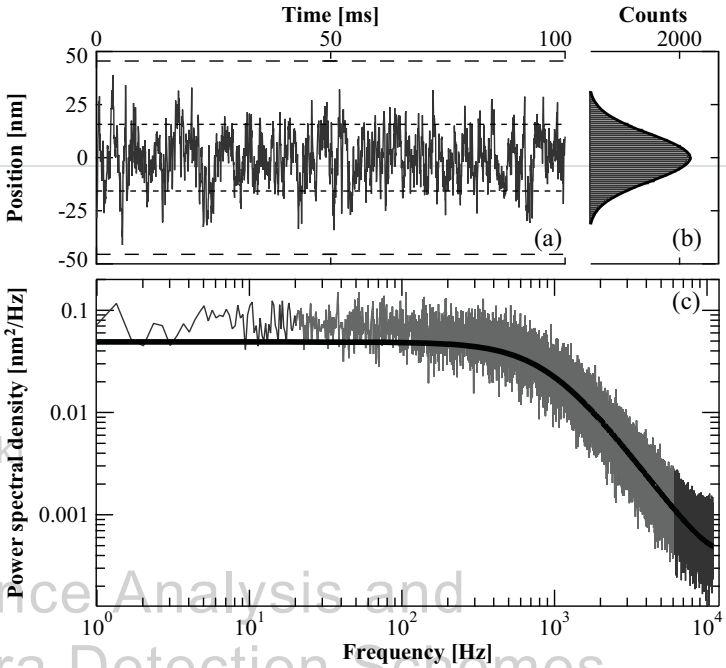

Figure 2. Time series analysis of an optically trapped polystyrene sphere, $\kappa = 67.7$ μm/pN. (a) Position as a function of time. (b) Histogram of positions, fitted by a Gaussian distribution. (c) Power spectrum of positions. The full line is a fit to the grey region which incorporated aliasing and filtering effects.

One can trade the Allan variance's conditional independence of neighboring intervals to gain a much smaller statistical error. For the **overlapping Allan variance**, one simply calculates all possible differences of neighboring intervals in a given time series. For a more comprehensive discussion we refer elsewhere.[14]

As **thermal limit** for an object in an spatially confined trap, the standard error of an object's position averaged over the time interval τ is:[14]

$$SE_{\langle x \rangle} = \frac{1}{\sqrt{n}} \sqrt{\langle x^2 \rangle} \approx \sqrt{\frac{2 k_B T \gamma}{\kappa^2 \tau}}, \tag{4}$$

with $k_B T$ being the thermal energy. This limit cannot be bettered by any measurement of an object trapped by a single beam. Nevertheless, for so-called dual-beam traps this limit is about a factor 1.19 smaller.[13]

Allan variances were calculated with a custom-made MATLAB program.[22] We measured Allan variances for various objects and parameters (trap stiffness, acquisition frequency, piezo) by acquiring three time series. Then the parameter was altered and we repeated the measurements. If not stated otherwise, we plotted the overlapping Allan variance in a log-log plot. All results stated in the following section are explicit and reproducible, although we chose to plot only particular data sets in order to keep a clear representation.

RESULTS AND DISCUSSION

In the majority of the experiments a polystyrene sphere was trapped in an aqueous environment in the center of the measurement chamber such that the distance to any surface was significantly larger than the diameter of the sphere. Using the position sensitive diode the time series of the sphere was recorded and used for a calibration routine which returned the corner frequency f_c, the trap stiffness κ, and the conversion factor β. Figure 2 (a) shows the time series of the positions visited by a trapped particle. The histogram of all positions visited is plotted in (b), and is very well-fitted by a Gaussian distribution. Figure 2 (c) shows the corresponding power spectrum. Here, the light grey part is fitted by a Lorentzian function (black full line) which takes into account

Submitted: September 27, 2010 Proc. of SPIE Vol. 7400 740004-4

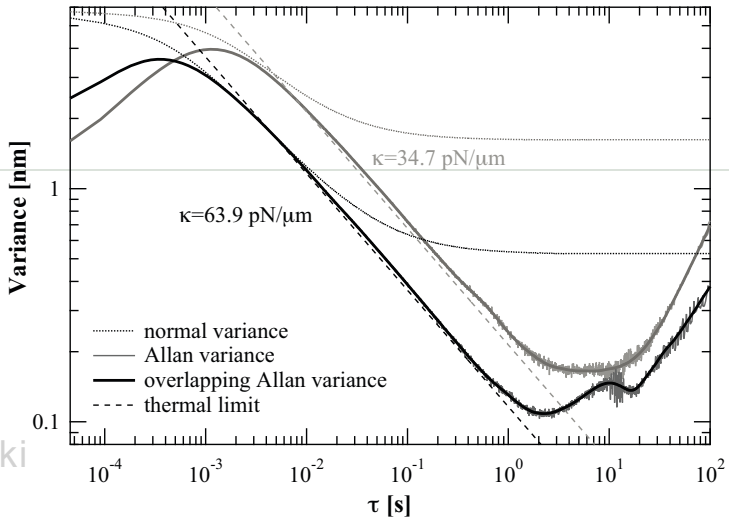

Figure 3. Variances of a polystyrene sphere trapped strongly, κ=63.9 pN/μm (black), or weakly, κ=34.7 pN/μm (grey). The lighter graphs denote the Allan variances, the thicker ones the overlapping Allan variances. Dashed lines are the thermal limits, dotted lines the normal variances.

the filtering effect of the photodiode[23] and aliasing[19] using programs described above.[20] Though the system is subject to low-frequency drift, this does not show neither in the time series, nor in the histogram, nor in the power spectrum, not even when compared to a simulation of the situation without drift using similar physical parameters.[14]

From time series as in Figure 2 the Allan variance can be calculated using Equation (3).[22] A typical result is shown in Figure 3 where the Allan variance is plotted as a function of data acquisition time for a strong, κ=63.9 pN/μm (black), and a weak, κ=34.7 pN/μm (grey), optical trap. The thicker lines denote the overlapping Allan variance for the same time series. The two dashed lines with slopes of $-1/2$ correspond to the thermal limits (Equation 4). For short measurement intervals the Allan variance is smaller than the thermal limit, this is due to the correlation of the data points. The maximum of the Allan variance is at $\pi\tau_c$ where

$$\pi\tau_c = \frac{1}{2f_c}. \tag{5}$$

For measurement intervals where the Allan variance is larger than the thermal limit, the data points are not correlated. The observation that the Allan variance is very close to the thermal limit in the measurement time span between 100 ms and 1 s is evidence of an extremely stable setup. The Allan variance has a global minimum at around 1–10 s, the exact postion of this minimum is dependent on the trap stiffness. This global minimum denotes the optimal measurement time for calibrations. This minimum is the time where the Gaussian distributed parameters have been measured for a time long enough to allow for their fairly precise determination while the time interval is still short enough that drift is not yet a significant problem. Noticeable also, is the fact that the stronger trap has a lower Allan variance, hence, a better accuracy than the weaker trap. The dotted lines in Figure 3 denote the normal variance (Equation 2). The normal variance does not converge and consequently does not provide the necessary resolution to determine the optimal measurement time.

Figure 4 (a) shows the Allan variances as a function of the number of acquired data points. A polystyrene sphere is trapped with κ=67.7 pN/μm while the acquisition frequency is parameterized. The tested frequencies range from 10 Hz to 100 kHz. For all frequencies, the acquisition of additional data points does not increase the accuracy above a certain threshold, for instance at 2^{15} for 10 kHz, because the Allan variance shows an absolute minimum. Furthermore, the closer a graph stays to limit of maximum information per individual data point, i.e. quasi the 'thermal limit' in this way of representation, the more valuable is the acquisition of an additional data point. Figure 4 (b) shows the negative values of the derivatives of the Allan variances with respect to the

Submitted: September 27, 2010 Proc. of SPIE Vol. 7400 740004-5

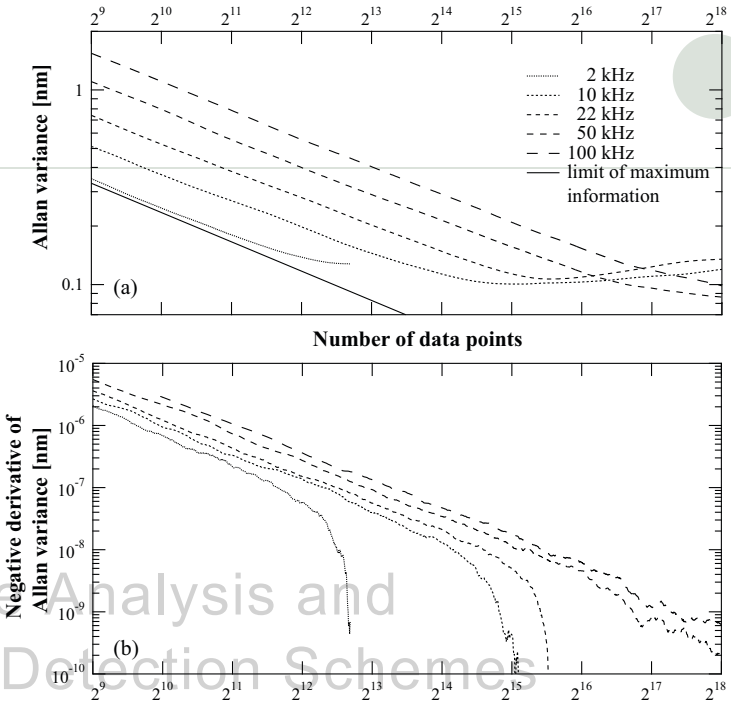

Figure 4. Frequency dependence of Allan variance and its negative derivative for a sphere trapped with κ=67.7 pN/μm. (a) Allan variance as a function of number of acquired data points. The full line denotes the limit of how much positional information a single data point could possibly hold. (b) Negative derivative of Allan variance with respect to the number of data points.

number of data points – it gives the increase in accuracy by acquiring more data points. For a specific acquisition frequency, it passes through zero when its sampling has been optimal and for more points drift would start to dominate. Consistently, these graphs show that if the sampling frequency is 10 kHz, essentially nothing is gained by acquiring more than 2^{15} data points.

Often, the measurement chamber of an optical trapping experiment is mounted on a piezo-electric stage. To investigate the possible contribution from the piezo stage to the noise spectrum we measured the Allan variance for two similar trapping experiments. In Figure 5 one sees the first case with the piezo switched off (full black line), and the second case with the piezo switched on (dashed line). There is a distinct peak in the Allan variance at around 10 s which seems to originate from the piezo stage. The lower dotted line in Figure 5 is the Allan variance of the position of the piezo stage as given by the piezo control box. This noise spectrum also peaks at around 10 s and hence supports the conclusion that the piezo stage itself contributes to the noise spectrum over a broader low-frequency band as indicated by the grey shading. At short measurement times the Allan variance of the piezo output has some oscillations which correspond to the odd-numbered divisors of the piezo's resonance frequency of 100 Hz. The fact that the piezo contributes to the noise spectrum implies that if it is not strictly needed for a particular experiment, it should be switched off.

So far, all figures and results presented both in the present Proceeding and in literature [13, 14] have addressed optical tweezing of micrometer-sized spherical objects. It is, however, also possible to trap significantly smaller and non-spherical objects, such as gold nanorods. Gold nanorods as thin as 8 nm and with aspect ratios up to 5.6 have been optically trapped.[6] These asymmetric nanorods align inside the trap with their longest direction along the electrical field vector of the trapping laser and the spring constant correlates directly with the polarizability of the rod. Figure 6 shows the Allan variance calculated from an experiment where an individual gold nanorod (long axis (63.8 ± 7.4) nm, short axis (37.3 ± 5.0) nm) was optically trapped. The black trace is the Allan variance along the longest dimension of the rod, the grey trace along the shortest dimension of the rod. The

Submitted: September 27, 2010 Proc. of SPIE Vol. 7400 740004-6

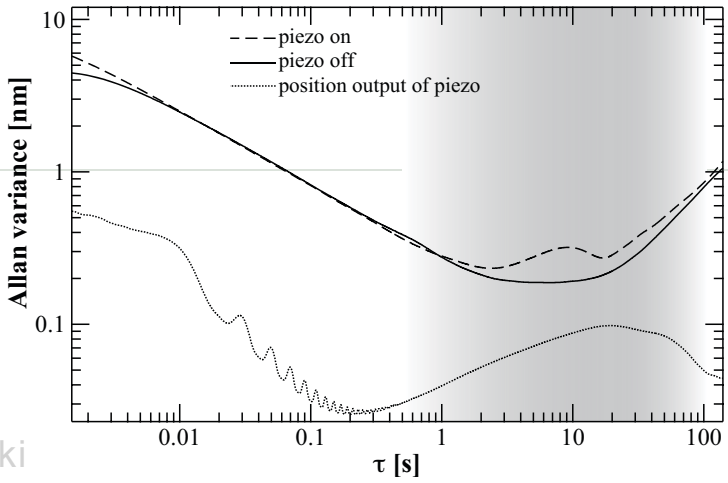

Figure 5. Contribution from the piezo stage to the Allan variance. The full line shows the Allan variance of a trapped sphere when the piezo stage is off, the dashed line is the Allan variance when the piezo is switched on. The dotted line is the Allan variance of the position output from the piezo control box with a significant noise contribution over a broad frequency band indicated by grey shading.

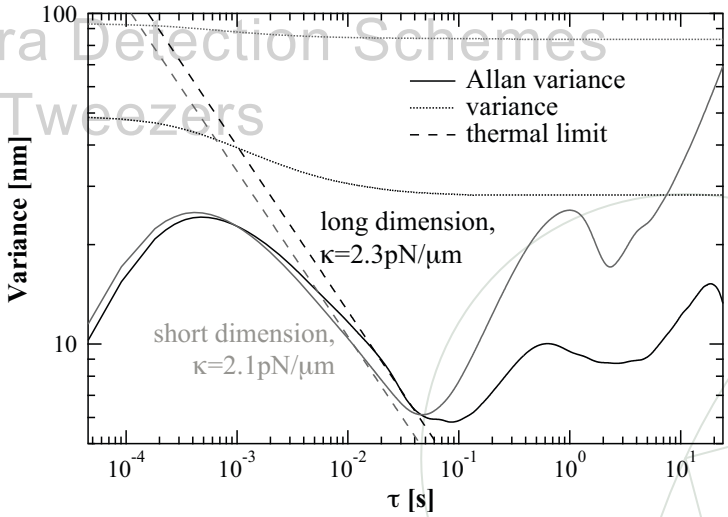

Figure 6. Variances of optically trapped gold nanorods. The black curve is along the longest direction of the rod, $\kappa = 2.3$ pN/μm, the grey curve along the shortest direction of the rod, $\kappa = 2.1$ pN/μm. The dotted lines are the corresponding normal variances, the dashed lines the thermal limits.

thermal limit for the shortest dimension is lower as we consider here r to be the short axis (Equation (4). Figure 6 also points out that for long measurement times, the Allan variance is smaller for a stronger trapping stiffness. Moreover, it shows that the optimal measurement interval is shorter for lower thermal limits rather than for the trap stiffness. The optimal measurement intervals are on the order of a tenth part of a second, which is significantly shorter than the optimal measurement times for the much larger polystyrene spheres, typically on the order of seconds (Figure 3). At measurement times longer than the absolute minimum, there are distinct peaks in the Allan variances of both directions. As the measurement chamber was as narrow as 30 mm × 5 mm, it might be possible that those peaks originate from the geometry of the chamber.[14] The dotted lines denote the normal variances of the plots, which, also here, do not reveal any information about, e.g., optimal measurement time or the impact of drift.

Submitted: September 27, 2010 Proc. of SPIE Vol. 7400 740004-7

CONCLUSION

We presented Allan variance analysis as an excellent tool to quantify noise in experiments where micro- and nanometer-sized particles were optically trapped. Furthermore, we pointed at our proper software solutions that can easily be used for on-the-fly analyses to determine important measurement parameters, as for instance the optimal measurement time for calibrations, or the optimal number of acquired data points for a particular experimental setting.

Fourier analysis can conveniently be used to perform calibration procedures. Furthermore, its use to pinpoint high-frequency noise is excellent. However, for low-frequency noise which is inherently present in every experiment, Allan variance analysis is superior. This method has been used to quantify the noise contribution from photodiode-based detection systems, the influence of the noise on chamber stability and geometry,[14] and, as reviewed here, the noise contribution from the piezo stage. Allan variance analysis was mostly used on positional time series from spherical, micron-sized polystyrene spheres, but it can be utilized even for nanometer-sized gold rods. Here, the overall noise contribution was asymmetric, strongly correlated to the alignment of the nanorods inside the trap.

We think that Allan variance analysis, complementary and additional to Fourier analysis, allows for the development of a common standard in research that accesses optical tweezers, as it contains the possibility to compare noise and drift in different experiments, settings, setups, and even laboratories.

ACKNOWLEDGMENTS

We acknowledge discussions with M. Andersson, P. M. Bendix, and K. Berg-Sørensen. We thank C. Sönnichsen and I. Zins for providing the gold nanorods. The study was financially supported by a University of Copenhagen Excellence Grant. C.S.U. is supported by the German Academy of Sciences Leopoldina through grant BMBF-LPD 9901/8-164.

REFERENCES

1. J. Moffitt, Y. Chemla, S. Smith, and C. Bustamante, "Recent advances in optical tweezers," *Ann. Rev. Biochem.* **77**, pp. 205–228, 2008.
2. A. Ashkin, J. Dziedzic, and T. Yamane, "Optical trapping and manipulation of single cells using infrared laser beams," *Nature* **330**, pp. 769–771, 1987.
3. M. Rasmussen, L. B. Oddershede, and H. Siegumfeldt, "Optical tweezers cause physiological damage to E. coli and listeria bacteria," *Appl. Environ. Microbiol.* **74**, pp. 2441–2446, 2008.
4. I. M. Toliç-Nørrelykke, E.-L. Munteanu, G. Thon, L. B. Oddershede, and K. Berg-Sørensen, "Anomalous diffusion in living yeast cells," *Phys. Rev. Lett.* **93**, p. 078102-, 2004.
5. P. M. Hansen, V. Bhatia, N. Harrit, and L. B. Oddershede, "Expanding the optical trapping range of gold nanoparticles," *Nano Lett.* **5**, pp. 1937–1942, 2005.
6. C. Selhuber-Unkel, I. Zins, O. Schubert, C. Sönnichsen, and L. B. Oddershede, "Quantitative optical trapping of single gold nanorods," *Nano Lett.* **8**, pp. 2998–3003, 2008.
7. L. Bosanac, T. Aabo, P. M. Bendix, and L. B. Oddershede, "Efficient optical trapping and visualization of silver nanoparticles," *Nano Lett.* **8**, pp. 1486–1491, 2008.
8. L. Jauffred, A. C. Richardson, and L. B. Oddershede, "Three-dimensional optical control of individual quantum dots," *Nano Lett.* **8**, pp. 3376–3380, 2008.
9. E. Abbondanzieri, W. Greenleaf, J. Shaevitz, R. Landick, and S. Block, "Direct observation of base-pair stepping by RNA polymerase," *Nature* **438**, pp. 460–465, 2005.
10. A. R. Carter, Y. Seol, and T. T. Perkins, "Precision surface-coupled optical-trapping assay with one-basepair resolution," *Biophys. J.* **96**, pp. 2926–2934, 2009.
11. F. Gittes and C. Schmidt, "Signals and noise in micromechanical measurements," *Methods Cell. Biol.* **55**, pp. 129–156, 1998.
12. M. Klein, M. Andersson, O. Axner, and E. Fallman, "Dual-trap technique for reduction of low-frequency noise in force measuring optical tweezers," *Appl. Opt.* **46**, pp. 405–412, 2007.

13. G. M. Gibson, J. Leach, S. Keen, A. J. Wright, and M. J. Padgett, "Measuring the accuracy of particle position and force in optical tweezers using high-speed video microscopy," *Opt. Express* **16**, pp. 14561–14570, 2008.
14. F. Czerwinski, A. C. Richardson, and L. B. Oddershede, "Quantifying noise in optical tweezers by Allan variance," *submitted* , 2009.
15. F. Czerwinski, "BeadFluct v1.0," MATLAB*Central* **24196**, 2009, *http://www.mathworks.com/matlabcentral/fileexchange/24196*.
16. S. N. S. Reihani and L. B. Oddershede, "Optimizing immersion media refractive index improves optical trapping by compensating spherical aberrations," *Opt. Lett.* **32**, pp. 1998–2000, 2007.
17. F. Czerwinski and L. B. Oddershede, "Reliable data-streaming software for photodiode readout in LABVIEW," *in prep.* , 2009.
18. L. B. Oddershede, S. Grego, S. Nørrelykke, and K. Berg-Sørensen, "Optical tweezers: probing biological surfaces," *Probe Microsc.* **2**, pp. 129–137, 2001.
19. K. Berg-Sørensen and H. Flyvbjerg, "Power spectrum analysis for optical tweezers," *Rev. Sci. Instrum.* **75**, pp. 594–612, 2004.
20. P. M. Hansen, I. Toliç-Nørrelykke, H. Flyvbjerg, and K. Berg-Sørensen, "tweezercalib 2.1: Faster version of MATLAB package for precise calibration of optical tweezers" *Comput. Phys. Commun.* **175**, pp. 572–573, 2006.
21. D. W. Allan, "Statistics of atomic frequency standards," *Proc. IEEE* **54**, 221–230, 1966.
22. F. Czerwinski, "allan v1.71," MATLAB*Central* **21727**, 2008, *http://www.mathworks.com/matlabcentral/fileexchange/21727*.
23. K. Berg-Sørensen, L. B. Oddershede, E. Florin, and H. Flyvbjerg, "Unintended filtering in a typical photodiode detection system for optical tweezers," *J. Appl. Phys.* **93**, pp. 3167–3176, 2003.

FACULTY OF SCIENCE
UNIVERSITY OF COPENHAGEN

PhD Thesis

Fabian Czerwinski

Allan Variance Analysis and Fast Camera Detection Schemes for Optical Tweezers

Academic Advisor: Lene B. Oddershede

Submitted: September 27, 2010

Quantum dots as handles for optical manipulation

Liselotte Jauffred[1], Marit Sletmoen[2], Fabian Czerwinski[1], and Lene Oddershede[1]

[1]The Niels Bohr Institute, University of Copenhagen, Denmark

[2]NTNU, Trondheim, Norway

ABSTRACT

Individual colloidal quantum dots can be optically trapped and manipulated by a single infrared laser beam operated at low laser powers.[1,2] If the absorption spectrum and the emission wavelength of the trapping laser are appropriately chosen, the trapping laser light can act as a source for two-photon excitation of the trapped quantum dot. This eliminates the need for an additional excitation laser in experiments where individual quantum dots are used both as force transducers and for visualization of the system. To use quantum dots as handles for quantitative optical force transduction, it is crucial to perform a precise force calibration. Here, we present an Allan variance analysis[3] of individual optically trapped quantum dots and show that the optimal measurement time for experiments involving individual quantum dots is on the order of 0.3 seconds. Due to their small size and strong illumination, quantum dots are optimal for single molecule assays where, optimally, the presence of the tracer particle should not dominate the dynamics of the system. As an example, we investigated the thermal fluctuations of a DNA tether using an individual colloidal quantum dot as marker, this being the smallest tracer for tethered particle method reported.

Keywords: Quantum dots, optical trapping, tethered particle motion, Allan variance

1. INTRODUCTION

Colloidal quantum dots (QDs) are semiconducting crystals with sizes in the range from a few to hundred of nanometers.[4,5] They are bright and photo-stable with a broad excitation spectrum and a narrow emission spectrum, normally distributed around a specific wavelength λ. Because of the high quantum yield and low bleaching, QDs have a broad range of applications in the investigation of biological systems,[4,6–8] e.g, single-particle tracking of individual receptors in a cell membrane[9] and in vivo imaging.[10]

Optical tweezers are often used to trap and manipulate nanometer-sized particles, the interest arises from the fact that the nanoparticles serve as excellent handles for investigations of individual biomolecules. Within the recent years there have been several reports on optical trapping of metallic nano-particles[11–15] with dimensions down to 8 nm. QD are among the nanoparticles with inducible dipole moments which can be optically trapped by an individual infrared relatively weak laserbeam.[1,2] From knowledge of the thermal fluctuations of the nanoparticle within the trap, one can deduce the trapping force acting on the quantum dot and the polarization of the particle.[1]

QDs can be exited by two-photon absorption of infrared laser light which simultaneously traps the QDs. The absorption does not alter the trapping properties, e.g., the spring constant, in any pronounced way.[2] Two-photon absorption of the trapping laser light does give rise to bleaching of QDs. However, bleaching is more rapid if the QDs in addition to the trapping laser are illuminated by a Hg lamp.[2] Hence, it is beneficial to only use a single light source for both trapping and excitation.

It is custom to perform force calibrations in order to quantitatively measure forces present in trapping assays. One common way to do this is through power spectral analysis.[16] This can be combined with Allan variance

Further author information:
L.J.: E-mail: jauffred@nbi.dk
M.S.: E-mail: marit.sletmoen@ntnu.no
F.C.: E-mail: czerwinski@nbi.dk
L.O.: E-mail: odder@nbi.dk

Submitted: September 27, 2010

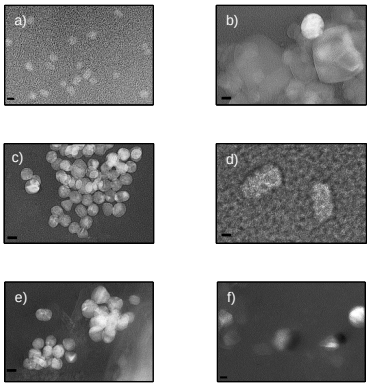

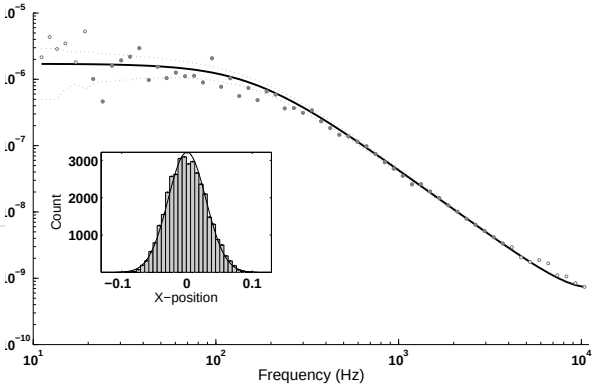

(a) TEM pictures of a) 525 nm QDs, b) 585 nm QDs, c) 605 nm QDs, d) 655 nm QDs (note the elongated shape), e) 705 nm QDs, f) 800 nm QDs. The scale bars corresponds to 10 nm.

(b) Power spectrum of the lateral positions visited by an optically trapped QD (wavelength of 585 nm). Full line is a Lorentzian fit to the data,[17] punctuated lines represents STD. The corner frequency f_c of the Lorentzian fit is (159.3 ± 6.5) Hz. The inset shows the distribution of positions visited by the QD in the optical trap for the same time series, full line is a Gaussian fit.

Figure 1.

analysis which provides information concerning the optimal time window to perform force calibrations and system measurements, and which also serves as a method to minimize force contributions in the experimental setting.[3]

Here, we show how the optical trapping properties of individual QDs vary as a function of QD emission wavelength, the emission wavelength being closely related to the physical size of the QD. Also, we perform an Allan variance analysis of the time series originating from the optical trapping experiment, this analysis revealing the optimal calibration window and quality of the experimental setting. Finally, we present an example of how to use individual QDs as markers of single molecule systems. We used QDs were as tracer particles of DNA tethered particle method (TPM) and the analysis revealed that this small tracer particle had a minimum of influence on the dynamics of the DNA tether.

2. DEPENDENCE OF TRAPPING STRENGTH ON QUANTUM DOT SIZE

It is important to correctly choose the QD such that it matches the given experimental goals and conditions, e.g., available excitation lasers and filter cubes. Therefore, the optical trapping properties of QDs were determined as a function of emission wavelength or size. The optical trap was based on a 1064 CW laser implemented in an inverted Leica SP5 microscope, details regarding the experimental settings are given in References.[1,2] Figure 1(a) shows TEM images of the QDs investigated in the present study.

It is well established that the optical tweezers exert a harmonic force on the trapped particle: $\mathbf{F} = -\kappa\mathbf{x}$, where κ denotes the trap stiffness and $\mathbf{x}$ is the position of the particle with respect to the center of the trap. To quantify κ and hence find the range of optical forces exertable on a QD we performed a power spectral analysis of the time series using the routines described in Reference.[17] The distance between the QD and the cover slide surface was very large in comparison to the radius of the QD, and we approximated the overall shape of the QD as a sphere. Hence, the drag coefficient, γ, can be found by Stoke's Law, $\gamma = 6\pi\eta d$, where d is the effective diameter of the QD. The equation of motion of a particle performing Brownian fluctuations inside an optical trap at low Reynolds number in one direction is:

$$\mathbf{F}(t) = \gamma\frac{d\mathbf{x}}{dt} + \kappa\mathbf{x}, \tag{1}$$

λ	core (nm)	composition	d (nm)
525 nm	3-4	CdSe/ZnS	10 ± 2
585 nm	5.3	CdSe/ZnS	26 ± 12
605 nm	(4×9.4)	CdSe/ZnS	13 ± 1
655 nm	(6×12)	CdSe/ZnS	$(40 \pm 5) \times (24 \pm 3)$
705 nm	ND	CdSeTe/ZnS	16 ± 3
800 nm	ND	CdSeTe/ZnS	21 ± 3

Table 1. Physical characteristics of investigated QDs. First column gives emission wavelength λ, second column the size of the core which is given by the diameter if the QDs are spherical or by the semi-major and semi-minor axes where the QDs are more ellipsoidal, third column states the material composition.[19] The last column gives the outer diameter d as measured by TEM.

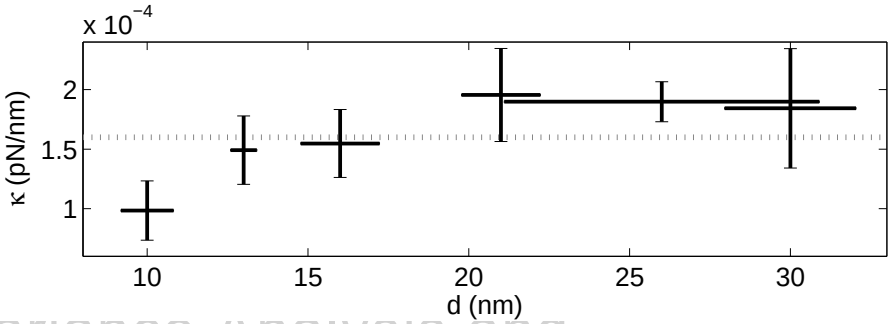

Figure 2. Trapping strength κ dependence on diameter d for laser power of 0.4 W. The points denotes the mean of the data points calculated using the d and f_c. In the case of the elongated 655 nm QD, $d \sim 30$ nm. The dotted line corresponds to the mean value of κ. All error bars denote one SEM.

where $\mathbf{F}(t)$ is a stochastic force resulting from the thermal motion of the media surrounding the trapped particle. Fourier transformation of the equation of motion gives the positional power spectrum which follows a Lorentzian function:

$$P(f) = \frac{k_B T}{\gamma \pi^2 (f^2 + f_c^2)}, \tag{2}$$

where γ is the drag coefficient and the corner frequency is denoted f_c. The corner frequency distinguishes the plateau region of slow fluctuations and the region with a scaling exponent of -2. This is the characteristic of Brownian motion for rapid fluctuations. f_c is related to κ and to γ of the QD: $f_c = \frac{\kappa}{2\pi\gamma}$. Fig. 1(b) shows an example of the power spectrum of positions visited by a 585 nm QD in a direction orthogonal to the propagating laser light. The full line is a fit by a Lorentzian function taking into account aliasing and the filtering effects of the quadrant photo-diode system.[17,18] The inset in Fig. 1(b) shows that positions visited by the QD inside the optical trap follow a Gaussian distribution (full line).

Table 1 gives an overview of the physical characteristics of the QDs used in the present study. The QDs consist of a CdSe or CdSeTe core surrounded by a ZnS shell. All QDs were bought from Invitrogen who also provided the informations shown in the 3 first rows in Table 1. We made transmission electron microscopy (TEM) pictures of the QDs, examples are shown in Fig. 1(a), to determine the sizes.

Fig. 2 shows the trap stiffness, κ, as a function of QD diameter d as determined by the TEM pictures. The value of κ is calculated from the experimentally found f_c's and the diameter, d. The dotted line shows the average value: $\kappa = (1.6 \pm 0.4) \times 10^{-4}$ pN/nm (mean ± STD). For the investigated QDs, the trap stiffness appears constant, independent of emission wavelength, λ, or physical size, d. However, a close inspection of Fig. 2 indicates that κ could be increasing as a function of QD size. This is supported by a Students t-test, which shows that κ for the 525 QD is significantly smaller than κ for the 800 nm QD ($p = 0.6981$).

3. ALLAN VARIANCE ANALYSIS FOR QUANTUM DOTS

Allan variance analysis is a method to quantify noise. In comparison to power spectral analysis it is in particular well suited to pinpoint low-frequency noise. In contrast to the normal variance, Allan variance converges for

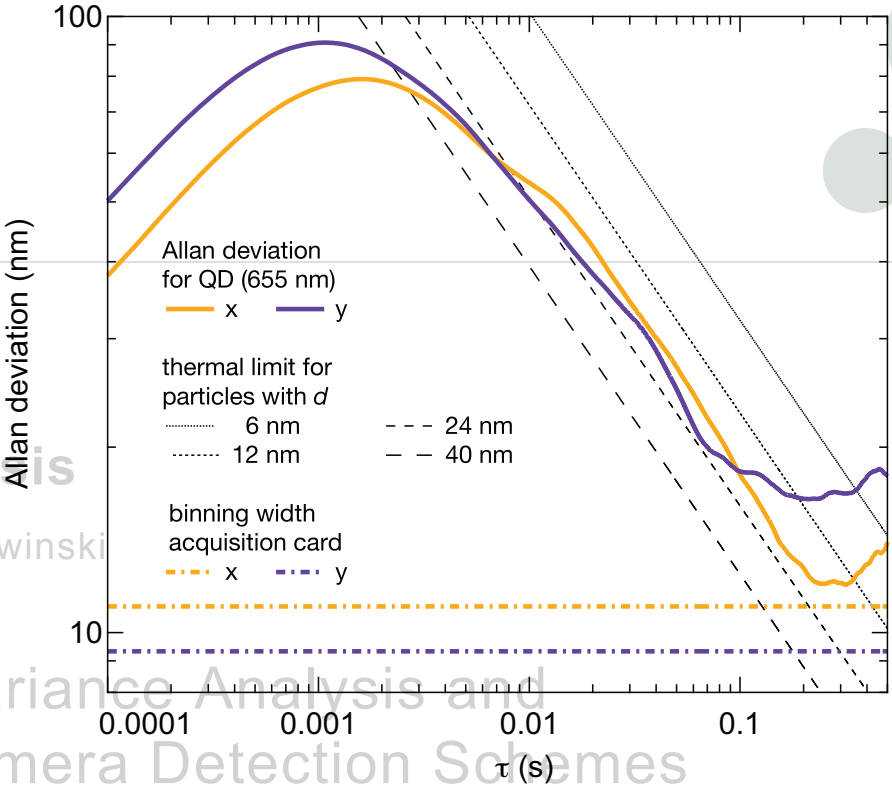

Figure 3. Allan deviation of a 655 nm QD as a function of measurement time τ for the two lateral directions x (orange) and y (purple). The thermal limit is plotted for spherical particles with diameters $d = 6$, 12, 24, and 40 nm, respectively. The optimal measurement time is at the global minimum for the Allan deviation, $\tau \sim 0.3$ seconds. The noise inherently present in the acquisition card sets a technical limit.

most of the naturally occuring types of noise. Through Allan variance analysis one can determine the optimal time for a measurement or calibraion, this is the time where the advantage of drawing additional points from a Gaussian position distribution is overcome by the drift inherently present in a real experiment. For a timeseries of N elements and a total measurement time of $t_{\mathrm{acq}} = f_{\mathrm{acq}}^{-1} N$ the Allan variance, $\sigma_x^2(\tau)$, is defined as follows:[3,20]

$$\sigma_x^2(\tau) = \frac{1}{2}\left\langle (x_{i+1} - x_i)^2 \right\rangle_\tau . \tag{3}$$

Here, x_i is the mean of a time interval of length $\tau = f_{\mathrm{acq}}^{-1} m$, m being the number of elements in this particular interval. In words, the Allan variance is half the averaged squared mean of neighboring intervals each of length τ.

The Allan deviation, $\sigma_x(\tau)$, of an optically trapped 655 nm QD w is plotted in Fig. 3. At measurement times below $\tau = 0.03$ s the positions are oversampled. In the interval $\tau = 0.03$ s to $\tau = 0.3$ s the Allan deviation steadily decreases, thus showing that additional data acquisition reduces the overall measurement noise, consistent with the positions being drawn from a Gaussian distribution. Around $\tau = 0.3$ s the Allan deviation reaches a minimum, this is the optimal measurement and calibration time for an individual quantum dot in the optical trap. At larger τ noise originating from low-frequency drift in the equipment kicks in and increases the Allan deviation.

From knowledge of the physical size of a particle the thermal limit for position determination can be calculated.[3] This limit cannot be beaten by any measurement that does not oversample the signal. The 655 QD depicted in Fig. 3 is elongated (~ 24 x 40 nm^2), and the straight lines on the figure denote the thermal limits of particles with sizes of 6 nm, 12 nm, 24 nm, and 40 nm, respectively. The larger the particle, the less its thermal diffusion, the lower the thermal limit. Also shown in the figure is the limitation originating from the binning of

data on the acquisition card (PCI M-6251, National Instruments). This sets a technical limit to a measurable accuracy. The Allan variance of the 655 QD in both lateral directions fall just above the thermal limit for a 24 nm particle, hence, not much noise is present, the equipment is performing very well. At present we do not know the orientation of an elongated QD within the optical trap. It is possible that it orients along the electrical field of the trap as is the case for an optically trapped gold nanorod.[14]

The optimal measurement time ($\tau = 0.3$ seconds) for a trapped colloidal QD is fairly short in comparison to, e.g., the optimal measurement time for a micron-sized polystyrene bead ($\tau \sim$ 2-5 seconds).[3] However, it is significantly longer than the optimal measurement time for a gold nanorod ($\tau \sim 0.05$ seconds),[21] despite the fact that the trap stiffness for a gold nanorod is essentially identical to the trap stiffness for a colloidal QD.[1,14]

4. TETHERED PARTICLE MOTION WITH QUANTUM DOTS

Their small size, low bleaching, and high quantum yield make QDs ideal tracker particles for assays that rely on the tethered particle method (TPM). We investigated the thermal fluctuation of a QD attached to a 1.36 μm dsDNA tether. The equation of motion of a particle (with low Reynolds number) tethered to a surface and performing Brownian fluctuations is (in one dimension):

$$\mathbf{F}(t) = \gamma \frac{d\mathbf{x}}{dt} + \mathbf{F}_{DNA}, \tag{4}$$

where $\mathbf{F}_{DNA}$ is the force exerted by the DNA tether on the particle. The first term on the right hand side depends linearly on the radius, R, of the tethered particle. Hence, for small particles the Brownian motion is dominated by the macromolecule and not by the tracer particle. The proximity of the tethered particle to the anchoring surface affects both the interpretation of the tethered particle's motion and the possible conformations of the tethering macromolecule.[22] The dynamics of the tracer particle does not dominate the dynamics of the tethering macromolecule when its radius, R_{QD}, fulfills

$$R_{QD} < \sqrt{2/3\, N \cdot l_k^2}, \tag{5}$$

where l_k is the Kuhn length and N the number of segments. The right hand term is derived as the theoretical root-mean-square displacement (RMS) of the 2D projection.[23] It has a value 294 nm for the 605 nm QD. Hence, with a QD tracer particle we are in the limit where movements of the tracer is dominated by the tethering DNA.

4.1 Methods

The double stranded DNA tether had a length of 1.36 μm, biotin was specifically attached to one end and digoxygenin to the other end. Complete information regarding the preparation of the DNA is found in Reference.[24] Sample chambers were prepared with an anti-digoxygenin-coating which would bind to the digoxygenin end of the DNA tether. After incubation with 0.1 nM DNA in TE (10 mM Tris-HCl and 1 mM EDTA) buffer the samples were incubated with streptavidin-coated QDs (Invitrogen) in TE buffer that would bind to the biotin-end of the DNA. The solution was then interchanged with TE buffer containing 2 mg/ml α-casein and the samples were sealed with vacuum grease.

The QDs were excited using a Hg lamp. Images of the samples were collected with a cooled electron-multiplying CCD (Andor Ixon) with a rate of 10/s. The image sequences were analyzed with the particle tracker routine Spottracker2D,[25] available as plug-in for ImageJ. The coordinates of the QD were extracted through a tiff-stack. To discriminate multi-tether events only symmetric in-plane motion about the anchor point were regarded. The second moments of the positions give the co-variance matrix:

$$c_{x,y} = N^{-1} \Sigma_1^N x_k y_k - \overline{x}\,\overline{y}, \tag{6}$$

where x and y are the positions in the two directions in the projected plane, $\overline{x}$ and $\overline{y}$ are average displacements around the anchor point, and N is the total number of frames. If the dynamics of the tracer particle were perfectly symmetric, the eigenvalues of this matrix (λ_1, λ_2) would be equal. Our criterion for symmetry was $\sqrt{\lambda_{max}/\lambda_{min}} \leq 1.1$.[26]

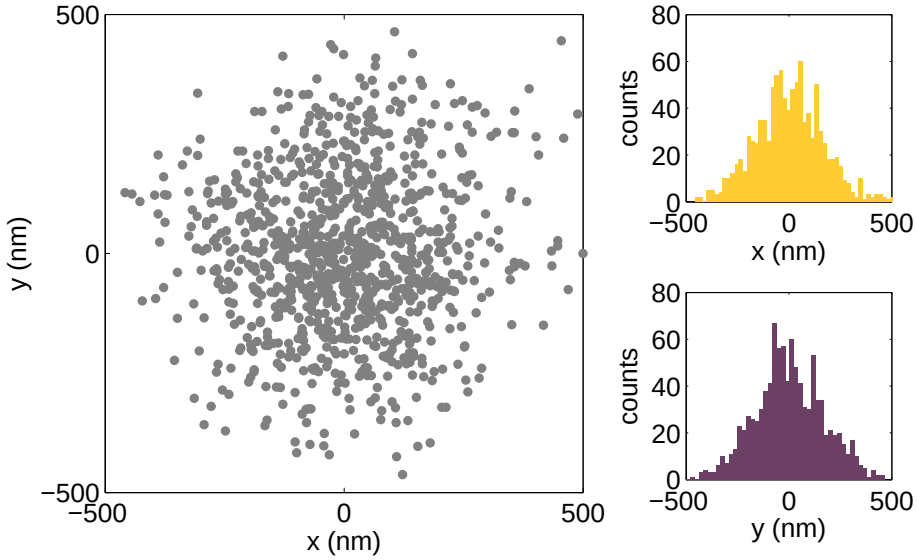

Figure 4. Positions visited by a QD tethered to a surface with DNA (L $\sim$ 1.36 μm). The 2D projected positions visited are plotted to the left. The position distributions of the two lateral directions are shown to the right.

The experimental RMS is a function of the total sampling time or time lag τ:

$$\mathrm{RMS}_\tau = \sqrt{\langle (x-\overline{x})^2 + (y-\overline{y})^2 \rangle_\tau}. \tag{7}$$

For tethered Brownian motion around an anchor point RMS approaches a constant value. In addition to the symmetry criterion we had a lower limit on the RMS displacement, this is in order to remove those data sets where multiple (more than two) tethers attach to an individual QD, or the QD is unspecifically bound to the lower cover slide. In conclusion, we only consider those datasets for which RMS $\in \{100\text{ nm} : L\}$, L being the contour length of the tether.

4.2 Results

One example of a TPM data is shown in Fig. 4. This figure shows a scatter plot of the positions visited by the tracer QD. The dynamics appears symmetric and indeed fulfills the symmetry criteria. Also shown are histograms for the positions visited in the two lateral directions.

Fig. 5 shows $\langle \mathrm{RMS}_\tau \rangle$ as a function of time, data originates from 18 individual DNA tethered QDs, all fulfilling the symmetri criteria. $\langle \mathrm{RMS}_\tau \rangle$ reaches the expected plateau at 238 nm for $\tau > 15$ s. The QDs used in the present study are the smallest particles every reported as tracer particles for TPM. Their presence has only a small influence on the dynamics of the DNA tether and hence, they are optimal to use for TPM studies. Also, their large photo-stability ensures that they are traceable for a long time. The fluorescence intermittencies of QDs is an issue to consider. However, existing software compensates for the blinking thus that it becomes unimportant for dynamics on the time-scale of seconds.[9]

In principle, Allan variance analysis can be performed on any type of time series. Hence, we also performed it on the time series of positions visited by the DNA tethered QD. The result is also shown (in yellow) in Fig. 5. Notice that the axes in this figure are linear (axes were logarithmic in Fig. 3). The Allan variance decreases with increasing τ and within our measurement time it never reaches a global minimum. Hence, with the drift present in this experiment, the system is stable for tens of seconds.

5. CONCLUSION

Quantum dots are optimal handles to use for manipulation and visualization of nano-scale systems. With a single infrared tightly focused laser beam one can both optically trap and perform two-photon excitation of individual

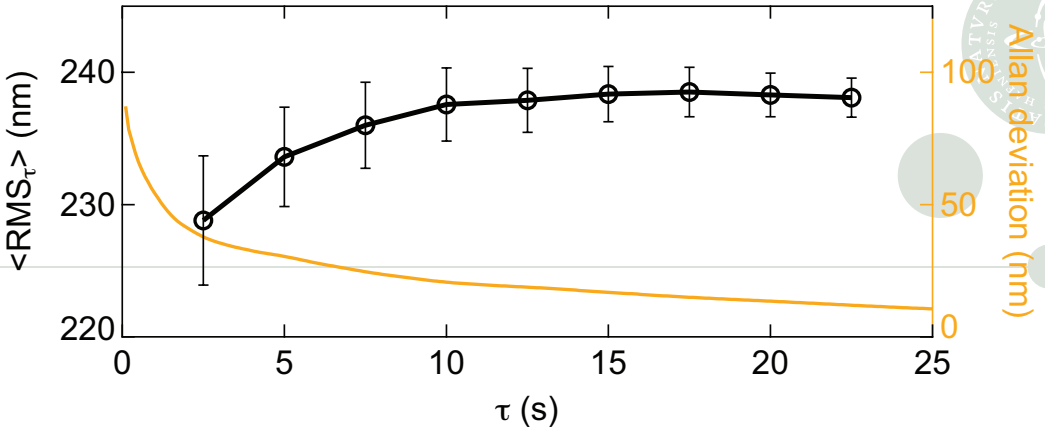

Figure 5. The black circles (left ordinate axis) show $\langle \mathrm{RMS}_\tau \rangle$ as a function of τ for TPM of a QD attached to a DNA tether. Error bars denote one SEM. $\langle \mathrm{RMS}_\tau \rangle$ approaches a constant value of 238 nm. The averaged Allan deviation for the same data is plotted on the same graph (yellow curve, right ordinate axis). The Allan deviation constantly decreases, no global minimum is obtained within this measurement. After 10 seconds, the noise is smaller than 10 % of $\langle \mathrm{RMS}_\tau \rangle$.

colloidal quantum dots. The trapping strength is nearly independent of quantum dot emission wavelength or its physical size in the range investigated here. Allan variance analysis revealed that the optimal trapping time of an individual colloidal quantum dot is on the order of 0.3 seconds, which is longer than the optimal trapping time for a gold nanorod, but shorter than for a μm sized polystyrene bead trapped with the same equipment. Individual quantum dots were specifically attached to a DNA tether, which is the other end was attached to a cover slide, these quantum dots were used to investigate the tethered particle motion of the combined DNA-quantum dot complex. Due to the small size of the quantum dot, the systems dynamics was dominated by the DNA tether rather than by the tracer particle. It is, therefore, an ideal system to investigate dynamics of macromolecules.

6. ACKNOWLEDGEMENTS

We are grateful to Szabolcs Semsey, ELTE, Budapest, who has prepared the DNA tethers for these experiments. Also, LBO acknowledges financial support from a University of Copenhagen excellence grant.

REFERENCES

[1] Jauffred, L., Richardson, A. C., and Oddershede, L. B., "Three-dimensional optical control of individual quantum dots," *Nano Lett.* **8**(10), 3376 – 3380 (2008).

[2] Jauffred, L. and Oddershede, L., "Two-photon quantum dot excitation during optical trapping," *Nano Lett.* **10**, 19271930 (2010).

[3] Czerwinski, F., Richardson, A. C., and Oddershede, L. B., "Quantifying noise in optical tweezers by Allan variance," *Opt. Express* **17**, 13255–13269 (2009).

[4] Michalet, X., Pinaud, F., Lacoste, T. D., Dahan, M., Bruchez, M. P., Alivisatos, A. P., and Weiss, S., "Properties of fluorescent semiconductor nanocrystals and their application to biological labeling," *Single mol.* **2**, 261–276 (2001).

[5] Dubertret, B., Skourides, P., Norris, D. J., Noireaux, V., Brivanlou, A. H., and Libchaber, A., "In vivo imaging of quantum dots encapsulated in phospholipid micelles," *Science* **298**(5599), 1759–1762 (2002).

[6] Chan, W. C. W. and Nie, S. M., "Quantum dot bioconjugates for ultrasensitive nonisotopic detection," *Science* **281**(5385), 2016–2018 (1998).

[7] Michalet, X., Pinaud, F., Bentolila, L., Tsay, J., Doose, S., Li, J., Sundaresan, G., Wu, A., Gambhir, S., and Weiss, S., "Quantum dots for live cells, in vivo imaging, and diagnostics," *Science* **307**, 538–544 (2005).

[8] Larson, D., Zipfel, W., Williams, R., Clark, S., Bruchez, M., Wise, F., and Webb, W., "Water-soluble quantum dots for multiphoton fluorescence imaging in vivo," *Science* **300**, 1434–1436 (2003).

[9] Dahan, M., Levi, S., Luccardini, C., Rostaing, P., Riveau, B., and Triller, A., "Diffusion dynamics of glycine receptors revealed by single quantum dot tracking," *Science* **302**, 442–445 (2003).

[10] Ballou, B., Lagerholm, B., Ernst, L., Bruchez, M., and Waggoner, A., "Noninvasive imaging of quantum dots in mice," *Bioconjugate Chem.* **15**, 79–86 (2004).

[11] Svoboda, K. and Block, S. M., "Biological applications of optical forces," *Ann. Rev.* **23** (1994).

[12] Bosanac, L., Aabo, T., Bendix, P. M., and Oddershede, L. B., "Efficient optical trapping and visualization of silver nanoparticles," *Nano Lett.* **8**, 1486–1491 (2008).

[13] Hansen, P. M., Bhatia, V. K., Harrit, N., and Oddershede, L., "Expanding the optical trapping range of gold nanoparticles," *Nano Lett.* **5**(10), 1937–42 (2005).

[14] Selhuber-Unkel, C., Schubert, I. Z. O., Sönnichsen, C., and Oddershede, L. B., "Quantitative optical trapping of single gold nanorods," *Nano Lett.* **8**(9), 2998–3003 (2008).

[15] Hajizadeh, F. and Reihani, S. N. S., "Optimized optical trapping of gold nanoparticles," *Opt. Express* **18**, 551–559 (2010).

[16] Berg-Sørensen, K. and Flyvbjerg, H., "Power spectrum analysis for optical tweezers," *Rev. Sci. Instrum.* **75**(3) (2004).

[17] Hansen, P. M., Tolic-Nørrelykke, I. M., Flyvbjerg, H., and Berg-Sørensen, K., "tweezercalib 2.0: Faster version of matlab package for precise calibration of optical tweezers," *Comp. Phys. Commun.* **174**(6), 518–520 (2006).

[18] Berg-Sørensen, K., Oddershede, L., Florin, E.-L., and Flyvbjerg, H., "Unintended filtering in a photodiode detection system for optical tweezers," *J. Appl. Phys.* **96**(6), 3167–3176 (2003).

[19] Kraus, M., "Personal communication about quantum dot sizes," tech. rep., Invitrogen (2008).

[20] Allan, D. W., "Statistics of atomic frequency standards," *Proc. IEEE* **54**, 221230 (1966).

[21] Czerwinski, F., Richardson, A. C., Selhuber-Unkel, C., and Oddershede, L. B., "Allan variance analysis as useful tool to determine noise in various single-molecule setups," *Allan Variance Analysis as Useful Tool to Determine Noise in Various Single-Molecule Setups* **7400**, 740004 (2009).

[22] Segall, D., Nelson, P., and Phillips, R., "Volume-exclusion effects in tethered-particle experiments: Bead size matters," *Phys. Rev. Lett.* **96** (2006).

[23] Boal, D., [*Mechanics of the Cell*], Cambridge University Press, 1 ed. (2002).

[24] Jauffred, L., *Optical manipulation and biological applications of quantum dots*, PhD thesis, The Niels Bohr Institute, University of Copenhagen (2010), *http://www.nbi.dk/odder/Theses/JauffredPhD.pdf*.

[25] Sage, D., Neumann, F., Hediger, F., Gasser, S., and Unser, M., "Automatic tracking of individual fluorescence particles: Application to the study of chromosome dynamics," *IEEE Transac. Image Proc.* **14**, 1372–1383 (2005).

[26] Han, L., Lui, B. H., Blumberg, S., Beausang, J. F., Nelson, P. C., and Phillips, R., [*Mathematics of DNA Structure, Function and Interactions, Chapter: Calibration of Tethered Particle Motion Experiments*], Springer New York (2009).

High-Speed Video-Based Tracking of Optically Trapped Colloids

O Otto[1], J L Gornall[1], G Stober[2], F Czerwinski[3], R Seidel[4] and U F Keyser[1]

[1] Cavendish Laboratory, University of Cambridge, J. J. Thomson Avenue, Cambridge CB3 0HE, UK.
[2] University of Rostock, Leibniz-Institute of Atmospheric Physics, Schlossstr. 6, 18225 Kuehlungsborn, Germany.
[3] Niels Bohr Institute, Blegdamsvej 17, 2100 Copenhagen, Denmark.
[4] Biotechnological Center, TU Dresden, Tatzberg 47-51, 01307 Dresden, Germany.

E-mail: ufk20@cam.ac.uk

Abstract. We have developed an optical tweezers setup with high-speed and real-time position tracking based on a CMOS camera technology. Our software encoded algorithm is cross-correlation based and implemented on a standard computer. By measuring the fluctuations of a confined colloid at 6,000 frames per second, without any limitations in acquisition time, we demonstrate an alternative to quadrant photodiodes. The optical trap is calibrated by using power spectrum analysis and Stokes method. We show that the trap stiffness is independent of the selected camera frame rate. Analysis of our data by Allan variance demonstrates conclusively that we can measure close to the thermal limit of our system while obtaining a spatial resolution of approximately 1 nm.

Submitted: September 27, 2010

1. Introduction

The ability to manipulate single particles without any mechanical contact makes optical tweezers a unique tool in biology, physics and material sciences [1, 2, 3]. Following the pioneering work of Ashkin in the 70s [4], optical trapping is now routinely used to study the mechanical properties of polymers, the physics of colloids and proteins, including molecular motors on a single molecule level [5]. Optical tweezers can exert piconewton forces on micrometer-sized objects while measuring the resulting displacements with nanometer resolution [5, 6, 7, 8].

The position of a trapped particle must be determined with high temporal and spatial resolution if piconewton scale forces are to be measured [6]. Traditionally this is done using a quadrant photo diode (QPD) detector [5, 6, 9]. QPD detectors can readily achieve nanometer spatial and microsecond temporal resolution, and therefore, they are a common choice for force measuremnts [10]. The position of a particle can also be tracked with video-based position detection. CCD cameras are capable of position determination with sub-pixel accuracy [11] but lack temporal resolution, typically $\sim$ 25-120 Hz [10]. Compared to CCDs, complementary metal oxide semiconductor (CMOS) imaging senors have all the conversion electronics required built into each pixel. Each pixel provides a complete binary value within microseconds, resulting in frame rates up to 100 kHz [7, 8, 10, 12, 13]. The position of a trapped particle can be determined using several different algorithms, each of which have various advantages and disadvantages depending on the application [11]. Direct fit of a Gaussian curve to the particle intensity profile is highly accurate for small particles, but cannot be used for large objects. Centroid based algorithms calculate the center of mass of two successive images and are easy to implement, however their results depend strongly on the image background. In our work, we use a cross-correlation algorithm for position calculation which is almost as precise as a direct Gaussian fit, but can be applied to particles several micrometers in size [11].

In this paper, we describe an optical tweezers setup with CMOS camera based position detection. Images are streamed to a standard personal computer and our custom software analyzes the images and calculates particle positions, in real-time, using cross-correlation. We show our system is capable of video-based tracking of optically trapped colloids at 6,000 frames per second (fps) with a resulting temporal bandwidth of 3 kHz. Data acquisition and position determination can be performed over an indefinite period of time. Standard techniques such as power spectrum analysis and Stokes drag are used to calibrate the optical traps. The Allan variance is used to characterize the stability of our system, from which we obtain the optimal time for calibration measurements and proof that we can determine the position of a colloid with an accuracy of $\sim$1 nm over several seconds.

2. Experimental setup

The optical setup is based around an inverted microscope, as shown in Fig. 1. A Ytterbium fiber laser (YLM-5-LP, IPG Laser, Germany, maximum output 5 W) is used for optical trapping, which operates at a wavelength of 1064 nm. At the chosen wavelength, the absorption coefficient of water is small, reducing laser induced heating of the sample [14]. The laser beam is expanded to $\sim$ 7.2 mm and coupled into the back aperture of a water-immersion microscope objective (Olympus UPlanSApo/IR, 60×, NA=1.20) in order to focus the laser beam to a diffraction limited spot within the sample cell. The sample cell consists of a 100 μm thick cover slip and a PMMA block, separated by a PDMS spacer. It is mounted on an XYZ piezo nanopositioning stage (P-517.3, Physik Instrumente, Karlsruhe, Germany), which allows multi-axis motion with a resolution of 1 nm and a range of 100 μm in the x - and y-directions and 20 μm in the z-direction. The stage is controlled using a multi-channel digital piezo controller (E-710.3, Physik Instrumente, Karlsruhe, Germany) connected to a PC via a GPIB interface. The colloid within the sample cell is illuminated by a cold-light source (150 W) (Fiber Lite DC-950) in transmission mode. Light diffracted from the particle and leaving the rear focal plane of the objective is imaged by a f=20 cm tube lens (not shown) onto the camera (Fig. 1). All our calibration experiments are carried out with polystyrene colloids (diameter $d = 3.27\,\mu$m, Kisker, Germany) in deionized water. The position of a colloid in the optical trap is determined by high-speed video position detection using a CMOS camera (MC1362, Mikrotron, Germany) and high performance NI PCIe-1429 camera-link frame-grabber card (National Instruments, UK) [5, 8, 12]. This allows us to analyze the dynamics of an optically trapped colloid on microsecond timescales in real-time.

3. Position tracking software

The position tracking software must be capable of simultaneous image acquisition and position tracking, in real-time, with high temporal bandwidth. In addition, it is required to track one or more particle positions with sub-pixel accuracy. At full resolution (1280×1024), our CMOS camera is capable of frame rates up to 500 fps. The frame rate can be increased by restricting the field of view to a region of interest (ROI) significantly smaller than the full resolution of the camera. The typical amplitude of the motion of a trapped colloid is of the order of tens of nanometers. Considering that the colloids used are a few micrometers in diameter, and the camera has a resolution of 214 nm/pixel, the ROI can safely be reduced to a frame size of 100×100 pixels (px), allowing images to be taken at 6,000 fps with a corresponding shutter time of 162 μs.

The tracking algorithm itself is cross-correlation based. The initial colloid position is calculated in a sub-ROI of e.g. 30×30 px in size, which closely fits the outline of the trapped colloid, as shown in Fig. 2(a). A rectangular array of pixels, 4×30 px in size, passing through the center of the sub-ROI, is binned and then normalized to give the

Submitted: September 27, 2010

mean intensity profiles for the x- and y-axes. To obtain sub-pixel accuracy, the cross-correlation of the mean intensity distribution with its reverse is calculated by applying the convolution theorem. A typical result is shown in Fig. 2(b). The peak in the cross correlation is then fit with a second-order polynomial using seven points around the maximum value to determine the particle position. The displacement of the colloid is calculated by comparing two subsequent images. We chose the graphical programming language LabView (National Instruments) as a basis for our acquisition software. Image recording, tracking and streaming are done in a highly parallelized manner, directly assigned on different cores. Communication between timed loops is achieved by queues. Streaming of the tracked position is done into the RAM and subsequently onto the hard disc. In practice, acquisition was performed continuously for one hour at 6,000 fps.

4. Position measurements and calibration

The optical trap was characterized by analyzing the Brownian fluctuations of a confined polystyrene bead in deionized water. Figure 3 shows the calculated power spectral density (PSD) at laser powers of $P_L = 25\,\mathrm{mW}, 100\,\mathrm{mW}$ and $200\,\mathrm{mW}$. The fluctuations of the colloid were recorded for 14 s with a temporal bandwidth set at 3 kHz, in real-time and using video tracking, as described above. The PSD reveals the typical Lorentzian profile of a trapped object described by:

$$S(f) = \frac{k_B T}{\gamma \pi^2 (f_c^2 + f^2)} \quad , \tag{1}$$

where k_B is the Boltzmann constant, T the temperature and γ is the drag coefficient for a bead with radius r moving in a fluid with viscosity η:

$$\gamma = 6\pi\eta r \quad . \tag{2}$$

The corner frequency f_c is given by:

$$f_c = \frac{k_{trap}}{2\pi\gamma} \tag{3}$$

and separates the power spectrum into two parts. For $f << f_c$ the colloid is confined in the optical trap and the PSD remains constant. At higher frequencies $f >> f_c$ the power spectrum decays as $1/f^2$, which is characteristic of free diffusion [6]. To determine the corner frequency f_c, and consequently the trap stiffness k_{trap}, the power spectrum is integrated numerically and the resulting arctangent function is fit using the method of least squares. An example of this is given in the inset of Fig. 3 for a laser power of 100 mW. For all calculations, lower and upper limits are set on the corner frequency of $f_{c,min} = 10\,\mathrm{Hz}$ and $f_{c,max} = 500\,\mathrm{Hz}$, respectively. This reduces the influence of low frequency drift and aliasing on the calculations of the corner frequency.

Figure 4 summaries measurements of the corner frequency for various laser powers and camera frame rates. Each data point in Fig. 4 a) is calculated from a data set of 80,000 images and analyzed as described above. The shutter time of the camera was kept constant at $W = 162\,\mu\mathrm{s}$ to ensure the background noise due to illumination was

independent of frame rate. At a given laser power, the corner frequency is independent of the camera frame rate, as expected. For high laser powers and frame rates below 1 kHz, we see a deviation of f_c towards larger values. This effect can be explained by aliasing. If the sampling rate approaches the corner frequency of the trapped colloid (under-sampling) high-frequency contributions of the power spectrum are folded back into low-frequency parts. This causes a shift of the PSD towards higher frequencies and results in an artificially larger corner frequency. Figure 4 b) shows the corresponding trap stiffness (k_{trap}), calculated using Eq. 3, as a function of the applied laser power. At a sufficiently high sampling rate of 4,000 fps the trap stiffness as a function of the applied laser power shows the expected linear dependency. Data recorded at a lower camera frame rate of 500 fps reveals a clear deviation from the linear behavior because of aliasing effects [15].

To verify the accuracy of the f_c values obtained by power spectrum analysis, we applied a second calibration method. The drag force method is based on Stokes law:

$$F_S = 6\pi\eta r v \quad , \tag{4}$$

where F_S is the viscous force and v the velocity of the bead relative to its surrounding solution. When the medium containing fluidic cell is moved a trapped colloid experiences a Stokes force and is displaced out of its equilibrium position. The harmonic potential of the optical tweezers [5, 16] leads to a counteracting linear force F_H following Hooke's law:

$$F_H = -k_{trap}\Delta x \quad , \tag{5}$$

where Δx is the measured displacement of the bead. Balancing Eq. 4 and Eq. 5 leads to an expression which allows for easy calculation of k_{trap}. The inset of Fig. 5 illustrates how this is done in practice. We use the piezoelectric stage to exert a force on a confined bead and measure the displacement from the trap center. The corner frequency is then calculated using Eq. 3. Figure 5 shows a comparison of calibration by power spectrum analysis and Stokes calibration for a polystyrene colloid at a fixed camera frame rate of 3,000 fps. Both methods reveal the expected linear relationship and give identical results for f_c as a function of the applied laser power. These results demonstrate that our optical tweezers setup and video tracking algorithm are capable of real-time position tracking with a temporal bandwidth up to 3 kHz.

5. Allan variance of position data

In addition to calibration by power spectrum analysis, Allan variance is a powerful method to determine the spacial resolution of an optical tweezers setup [7]. It allows for precise and assumption-free quantification of noise and drift sources like white noise, shot noise and damped oscillations [17]. In contrast to classical variances the Allan variance converges to finite values. It enables the user to calculate the optimal measurement time and frequency for calibration of an existing setup [17, 18].

The Allan variance of position data is given by:

$$\sigma^2_{Allan}(\tau) = \frac{1}{2}\left\langle (x_{i+1} - x_i)^2 \right\rangle_\tau \quad , \tag{6}$$

where x_i is the mean over a time interval of a length τ. In contrast the normal variance $\sigma^2(\tau)$ is given by:

$$\sigma^2_{normal}(\tau) = \frac{1}{2}\left\langle (x_i - \bar{x})^2 \right\rangle_\tau \quad . \tag{7}$$

Here, we apply the Allan variance to analyze the fluctuations of an optically trapped polystyrene colloid. Using the video tracking method described above, the position of the colloid was determined at a frame rate of 6 kHz for 120 s, giving a total of 720,000 data points. The minimum in the Allan deviation plot in Fig. 6 reveals an optimal acquisition time of a few seconds which gives maximal accuracy in the position determination. This means that, for acquisition times exceeding this value, low-frequency drift becomes dominant decreasing the accuracy of the measurement. In contrast, calculation of the standard deviation does not allow one to draw such a conclusion (Fig. 6).

It is useful to compare the obtained Allan deviation values to the standard error (SE) of the averaged position of an optically trapped colloid. This can be used to place a limit on the overall accuracy of the position detection [17]:

$$SE_{\langle x \rangle} = \frac{1}{\sqrt{n}}\sqrt{\langle x^2 \rangle} \approx \sqrt{\frac{2k_B T\gamma}{k^2\tau}} \quad , \tag{8}$$

This limit cannot be beaten by any measurement that does not over-sample a desired signal, it is inherent in the random nature of the Brownian motion. As shown in Fig. 6, the position of the colloid can be measured within 1 nm of the thermal limit for several seconds, which is remarkably close to that achieved for photodiode-based detection systems [17, 19, 20].

6. Discussion

Precise position tracking of an optically trapped colloid requires that the detection system has high spatial resolution and high temporal bandwidth. Classically, this can be achieved using quadrant photo diodes [5, 6]. CMOS cameras offer an easy to handle alternative [8, 12] but are traditionally restricted to acquisition rates < 1 kHz and finite acquisition times [7, 13, 15]. One reason for this is the ultimate limit set by illumination and the number of photons reaching the camera sensor. To overcome this problem Biancaniello and Crocker describe an optical tweezers setup based on laser illumination [10]. This procedure allows for video-based offline position tracking with 10 kHz bandwidth but require great deal of experimental skill because of interferences due to coherent laser illumination. Gibson *et. al* have also performed measurements with optical tweezers to determine the accuracy of particle position tracking and force determination [7]. Using a CMOS camera and standard equipment for illumination they achieve 0.5 kHz temporal bandwidth and a positional accuracy of 1 nm.

Here, we overcome these limitations by demonstrating position tracking of a single colloid with frame rates up to 6 kHz in real-time. We introduce an optical tweezers setup based on standard components for illumination, optics and trapping. Position tracking is done by a software implemented cross-correlation algorithm following data acquisition from a CMOS camera. We calibrate our optical trap by power spectrum analysis. The corner frequency depends linearly on the applied laser power, as expected. We perform these measurements for acquisition rates between 500 fps and 6,000 fps and reveal that the acquisition rate of the camera does not influence the tracking algorithm. Indeed, we show that we can perform video position tracking at a temporal bandwidth of 3 kHz, in real-time, without any restrictions in acquisition time. Consequently, we are able to calibrate stiff optical traps with corner frequencies exceeding 100 Hz by performing power spectrum analysis on position data obtained from video tracking.

We confirm our results from power spectrum analysis with data obtained from Stokes calibration and show that both methods give the same results. For further characterization of our optical tweezers system, we measure the Allan variance for a 120 s time trace recorded at 6,000 fps. From the results we obtain an optimal acquisition time for calibration of several seconds and proof that our system can measure particle positions with an accuracy of 1 nm. In summary, the high acquisition frequencies of our CMOS-based system in combination with the high level of position accuracy of our setup allows us to use calibration techniques like power spectrum analysis and Allan variance that had originally been designed for photodiode-based systems only [19, 20].

7. Conclusions

We have demonstrated a high-speed and real-time position tracking system for optical tweezers which is based on a CMOS camera technology. The algorithm is entirely software encoded and implemented on a standard PC. It allows us to measure colloidal fluctuations with 3 kHz temporal bandwidth for hours. We show that trap stiffness is essentially independent from the selected camera frame rate. Deviations from this behavior for low acquisition rates are explained by aliasing effects. By calculating the Allan variance for our data we are able to show conclusively that we can measure at the thermal limit of our system while measuring particle positions with an accuracy of 1 nm. In summary, we demonstrate a very accurate, reliable and time-stable camera based tracking system which offers a powerful alternative to classical systems such as quadrant photo diodes.

Acknowledgments

U. F. Keyser acknowledges funding by the Emmy Noether-Program of the DFG. O. Otto thanks for the PhD fellowship and support provided by the Boehringer Ingelheim Fonds. J. Gornall is supported by a Nanoscience E+ grant.

Submitted: September 27, 2010

References

[1] A. Askin. Optical trapping and manipulation of neutral particles using lasers. *PNAS*, 94(10):4853–4860, 1997.

[2] U. F. Keyser, J. van der Does, C. Dekker, and N. H. Dekker. Optical tweezers for force measurements on DNA in nanopores. *Rev. Sci. Instrum.*, 77(10):105105, 2006.

[3] H. Salman, D. Zbaida, Y. Rabin, D. Chatenay, and M. Elbaum. Kinetics and mechanism of DNA uptake into the cell nucleus. *PNAS*, 98(13):7247–7252, 2001.

[4] A. Askin. Acceleration And Trapping Of Particles By Radiation Pressure. *Phys. Rev. Lett.*, 24(4):156–159, 1970.

[5] K. C. Neuman and S. M. Block. Optical trapping. *Rev. Sci. Intrum.*, 75(9):2787–2809, 2004.

[6] K. Berg-Sorensen and H. Flyvbjerg. Power spectrum analysis for optical tweezers. *Rev. Sci. Instrum.*, 75(3):594–612, 2004.

[7] G. M. Gibson, J. Leach, S. Keen, A. J. Wright, and M. J. Padgett. Measuring the accuracy of particle position and force in optical tweezers using high-speed video microscopy. *Opt. Express*, 16(19):14561–14570, 2008.

[8] O. Oliver, C. Gutsche, F. Kremer, and U. F. Keyser. Optical tweezers with 2.5 kHz bandwidth video detection for single-colloid electrophoresis. *Rev. Sci. Instr.*, 79(2):023710, 2008.

[9] R. Galneder, V. Kahl, A. Arbuzova, M. Rebecchi, J. O. Radler, and S. McLaughlin. Microelectrophoresis of a bilayer-coated silica bead in an optical trap: Application to enzymology. *Biophys. J.*, 80(5):2298–2309, 2001.

[10] P. L. Biancaniello and J. C. Crocker. Line optical tweezers instrument for measuring nanoscale interactions and kinetics. *Rev. Sci. Instrum.*, 77(11):113702, 2006.

[11] M. K. Cheezum, W. F. Walker, and W. H. Guilford. Quantitative comparison of algorithms for tracking single fluorescent particles. *Biophys. J.*, 81(4):2378–2388, 2001.

[12] I. Semenov, O. Otto, G. Stober, P. Papadopoulos, U. F. Keyser, and F. Kremer. Single colloid electrophoresis. *J. Colloid Interface Sci.*, 337(1):260–264, 2009.

[13] M. Towrie, S. W. Botchway, A. Clark, E. Freeman, R. Halsall, A. W. Parker, M. Prydderch, R. Turchetta, A. D. Ward, and M. R. Pollard. Dynamic position and force measurement for multiple optically trapped particles using a high-speed active pixel sensor. *Rev. Sci. Instrum.*, 80(10):103704, 2009.

[14] G. M. Hale and M. R. Querry. Optical constants of water in the 200 nm to 200 μm wavelength region. *Appl. Opt.*, 12:555–563, 1973.

[15] W. P. Wong and K. Halvorsen. The effect of integration time on fluctuation measurements: calibrating an optical trap in the presence of motion blur. *Opt. Express*, 14(25):12517–12531, 2006.

[16] T. T. Perkins. Optical traps for single molecule biophysics: a primer. *Laser Photon. Rev.*, 3(1-2):203–220, 2009.

[17] F. Czerwinski, A. C. Richardson, and L. B. Oddershede. Quantifying Noise in Optical Tweezers by Allan Variance. *Opt. Express*, 75(15):2787 – 2809, 2009.

[18] F. Czerwinski, A. C. Richardson, C. Selhuber-Unkel, and L. B. Oddershede. Quantifying and pinpointing sources of noise in optical tweezers experiments. *Proc. SPIE*, 7400:740004, 2009.

[19] P. M. Hansen, I. M. Tolic-Nørrelykke, H. Flyvbjerg, and K. Berg-Sørensen. Tweezercalib 2.1: Faster version of MatLab package for precise calibration of optical tweezers. *Comput. Phys. Commun.*, 175:572 – 573, 2006.

[20] S. F. Tolić-Nørrelykke, E. Schäfferb, J. Howard, F. S. Pavone, F. Jülicher, and H. Flyvbjerg. Calibration of optical tweezers with positional detection in the back focal plane. *Rev. Sci. Instrum.*, 77:103101, 2006.

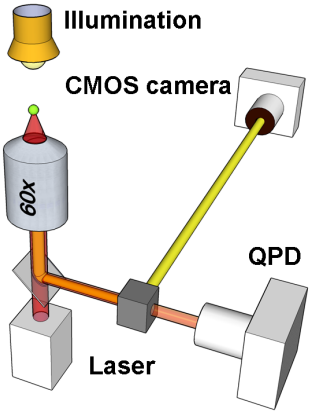

Figure 1. Schematic drawing of the custom built optical tweezers setup showing the 1064 nm Ytterbium Fiber laser and detection system consisting of a quadrant photo diode (QPD) and a high-speed video camera (CMOS). The optically trapped colloid within the sample cell (not shown) is illuminated by a 150 W cold-light source.

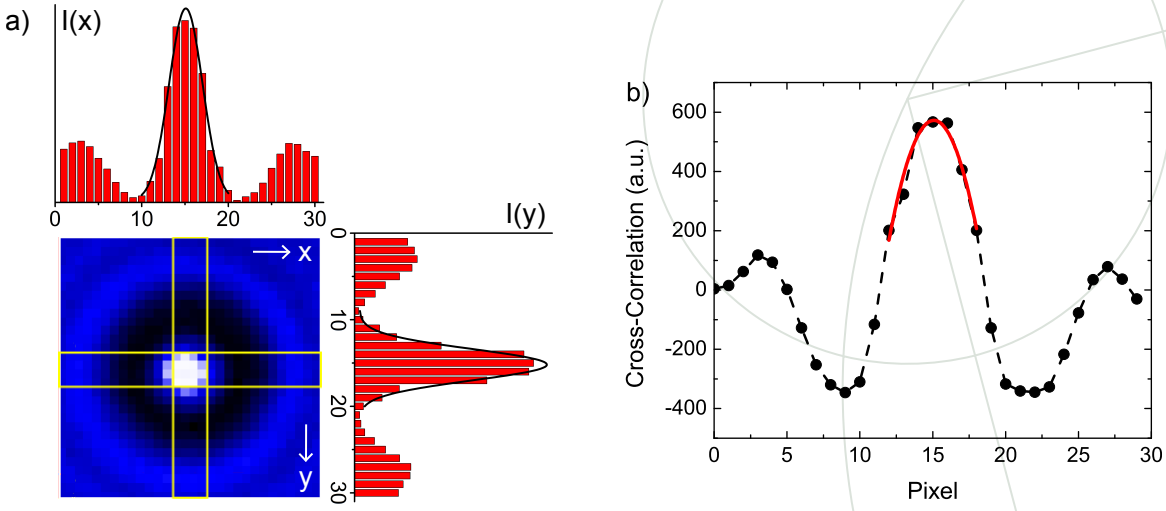

Figure 2. Implementation of the cross-correlation based position tracking algorithm. a) Image of an optically trapped colloid within a 30x30 pixel sized sub-ROI used for position calculation. This algorithm is based on deriving the position in x- and y-direction independently. b) Cross-correlation function and 2^{nd} order polynomial fit.

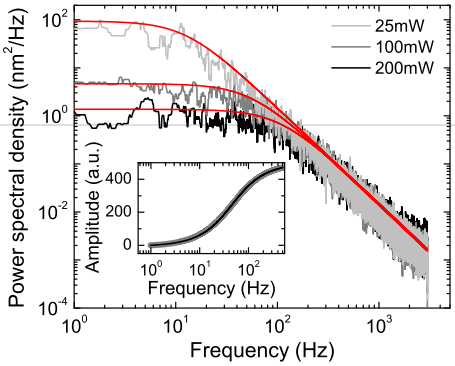

Figure 3. Power spectral density (PSD) of the Brownian motion of a confined colloid as a function of frequency. The corner frequency is calculated by numerically integrating the PSD and of fitting the resulting arctangent function (inset). The PSD was filtered using a Hamming filter.

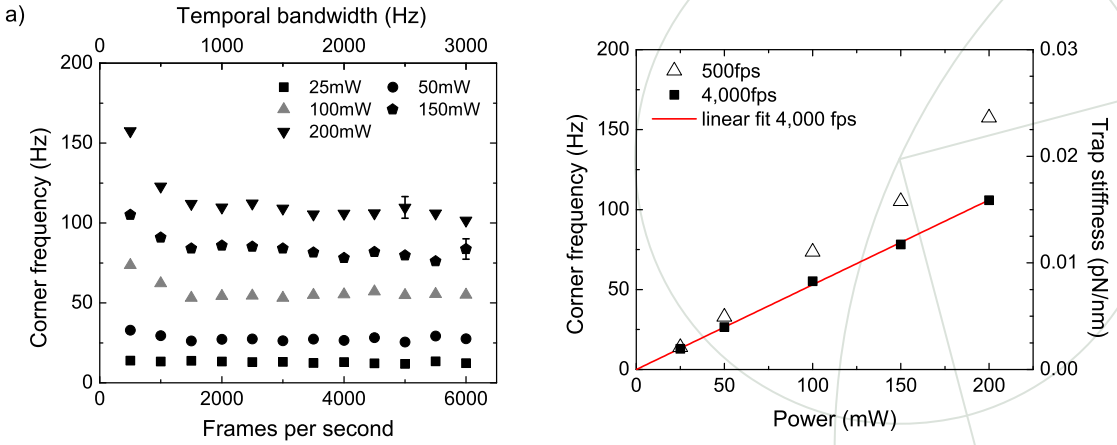

Figure 4. Calibration of optical tweezers at different camera frame rates. Corner frequency f_c was obtained by power spectrum analysis of a confined colloid. a) Dependency of f_c on camera bandwidth for different laser power P_L. At given P_L the corner frequency stays constant with increasing camera frame rate. The deviation at low frame rates can be explained by aliasing effects of the recording. The shutter time of the CMOS camera was 162 μs to ensure constant light levels. b) Trap stiffness k_{trap} as a function of laser power. The data was extracted from a) for different camera frame rates.

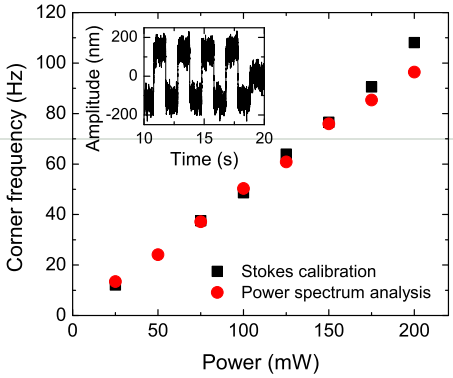

Figure 5. Corner frequency f_c as a function of laser power P_L. Calibration was performed by power spectral analysis and confirmed by the Stokes method for a colloid in deionized water. The error is given by the symbol size. Both calibration methods show the same results within the experimental deviations. The inset shows a time trace of the viscous drag on the colloid induced from a piezo stage.

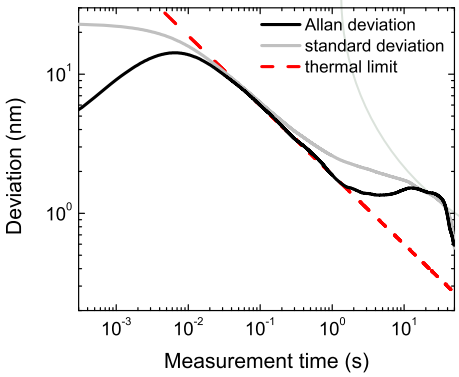

Figure 6. Statistical analysis of a time trace for an optically trapped colloid. The overall measurement time was 120 s with a sampling rate of 6,000 fps. The Allan variance plot shows a minimum around several seconds of measurement time giving an optimum measurement time for calibration.

FACULTY OF SCIENCE
UNIVERSITY OF COPENHAGEN

PhD Thesis

Fabian Czerwinski

Allan Variance Analysis and Fast Camera Detection Schemes for Optical Tweezers

Academic Advisor: Lene B. Oddershede

Submitted: September 27, 2010

TimeSeriesStreaming.vi: LabVIEW program for reliable data streaming of large analog time series

Fabian Czerwinski, Lene B. Oddershede

Niels Bohr Institute, Blegdamsvej 17, 2100 Copenhagen, Denmark

Abstract

With modern data acquisition devices that work fast and very precise, scientists often face the task of dealing with huge amounts of data. These need to be rapidly processed and stored onto a hard disk. We present a LabVIEW program which reliably streams analog time series of MHz sampling. Its run time has virtually no limitation. We explicitly show how to use the program to extract time series from two experiments: For a photodiode detection system that tracks the position of an optically trapped particle and for a measurement of ionic current through a glass capillary. The program is easy to use and versatile as the input can be any type of analog signal. Also, the data streaming software is simple, highly reliable, and can be easily customized to include, e.g., real-time power spectral analysis and Allan variance noise quantification.

Program summary

Program title: TimeSeriesStreaming.vi
Catalogue identifier: TimeSeriesStreaming_v1_0
Program summary URL: http://www.nbi.dk/~czerwin/TimeSeriesStreaming.html
Licensing provisions: Standard CPC licence, http://cpc.cs.qub.ac.uk/licence/licence.html
Distribution format: .zip / .vi
Programming language: LabVIEW
Computer: Any machine running LabVIEW 8.6 or higher
Operating system: Windows XP and Windows 7
RAM: 60 – 360 Mbyte
Memory usage: Code 40.5 Kbyte, front panel 50.7 Kbyte, block diagram 444.1 Kbyte; total VI file size 77.7 Kbyte
Classification: Data acquisition program
Nature of problem: For numerous scientific and engineering applications, it is highly desirable to have an efficient, reliable, and flexible program to perform data streaming of time series sampled with high frequencies and possibly for long time intervals. This type of data acquisition often produces very large amounts of data not easily streamed onto a computer hard disk using standard methods.
Solution: This LabVIEW program is developed to directly stream any kind of time series onto a hard disk. Due to optimized timing and usage of computational resources, such as multicores and protocols for memory usage, this program provides extremely reliable data acquisition. In particular, the program is optimized to deal with large amounts of data, e.g., taken with high sampling frequencies and over long time intervals. The program can be easily customized for time series analyses.
Restrictions: Only tested in Windows-operating LabVIEW environments, must use TDMS format, acquisition cards must be LabVIEW compatible, driver DAQmx installed.
Running time: as desirable: microseconds to hours

Key words: data acquisition, data streaming, LabVIEW, TDMS, optical tweezers
PACS: 87.80.Cc, 87.80.Ek, 07.05.Hd, 07.90.+c

1. Introduction

Precision experiments where data is acquired with high temporal resolution pose a challenge with respect to streaming and saving the data correctly onto a computer hard disk for further

Email address: czerwinski@nbi.dk (Fabian Czerwinski)
URL: www.nbi.dk/~czerwin (Fabian Czerwinski)

processing [1]. Within the nanoscience and biophysical communities, LabVIEW is often the program of choice for control of data acquisition and streaming [2, 3, 4]. Here, we present a highly reliable and efficient data streaming program in LabVIEW. The program is built into modular blocks with the goal of making the design comprehensible and easily compatible for further customization. Also, user-friendliness has been highly valued and we show how to use the program to stream time series data from two typical nanoscale experiments: One involving optical trapping assays [5], the other ionic current measurements through glass capillaries [6].

2. Program Overview

2.1. Requirements

A time series can originate from a wide range of physical signals, such as temperature, voltage, current etc. The time series, most often in the form of parallel voltage signals, enter the program through a number of channels of an acquisition card, building the interface between computers and experimental setups. Acquisition cards are available in a broad range for various tasks and quality requirements. We used National Instruments cards NI PCI-6251, NI PCIe-M6251, and NI PCI-M6040 [7]. They are coupled into TimeSeriesStreaming.vi by DAQmx, a LabVIEW-internal driver. As precondition, the acquisition card must be compatible with LabVIEW. This holds either for those that can be installed by National Instrument's *Measurement and Automation Explorer*, or for those supplied with a LabVIEW-compatible driver.

2.2. Main Program

The main program is designed in a modular fashion to offer independent as well as interconnected control of different sources of analog signals. Further, it contains support for data-streaming protocols. The programming architecture combines horizontal modules (acquisition, queuing, streaming) with vertical programming patterns (sequential structure, parallel while loops, multicore processing) in order to assure negligible error rates and optional customization.

The different modules of the program are highlighted each by their background color in Figures 1 and 2. The four modules deal with elements that concern **computer specifications** (yellow), **acquisition** (blue), **queuing** (red), and **streaming** (green). Each of the modules functions independently from the others as it communicates through well-defined programming patterns.

The usage of the program will be explained in Section 3.

Programming Patterns. Multicore processing is the ability to distribute computational jobs over more than one core, i.e. one CPU. This feature has become available in recent versions of LabVIEW. In TimeSeriesStreaming.vi multicore processing is implemented by assigning each timed loop to a specific core. On the tested systems, the CPU load of an individual core never exceeded 20%. Optimal multicoring was ensured by core assignments (highlighted yellow in Figure 2). It could also compensate for occasional interruptions by the Windows XP operating system.

Data acquisition must not be interrupted by waiting times during the streaming process. LabVIEW is optimized for *data flow control*. In TimeSeriesStreaming.vi this is achieved by transporting data packages between different loops exclusively through built-in queues (highlighted red in Figure 2). The streaming loop is not executed when the queue is empty. This strategy has proven very powerful, as it allows both loops to run as quickly as possible without potential disturbance by waiting times.

Parallelizing allows for parallel execution of computational jobs. Data acquisition is done in one while loop, data streaming in a parallel loop. Very reliable *streaming* is achieved by the powerful data format TDMS (Technical Data Management Streaming, National Instruments). Using the primitive TDMS VIs allows for high performance streaming virtually with no limitation.

3. How to use the program

A hands-on introduction to TimeSeriesStreaming.vi is given in this section. The perspective user is guided through the modules in the program's front panel (Figure 1). An experienced user could adjust the programming architecture in the block diagram at will (Figure 2).

The only **computer specification** that must be set is the processor assignment (highlighted yellow). The user can choose to perform processor assignment on quad-, duo-, or single-cores; or simply choose automatic in which case the program will usually assign the highest ordered cores. However, if the user is aware, e.g., that the Windows operating system is utilizing certain cores, it might be beneficial to assign the cores manually.

The **acquisition** module (highlighted blue) controls mainly the settings regarding the acquisition card for a particular measurement. The desired scan rate [Hz] must be given in units of Hertz. The physical channels must be specified. `Dev1/ai0:2` denotes the signals input from Dev1 through the channels 0, 1, and 2 (e.g., x, y, and z coordinates of a recorded movement). The internal limits of recordable voltage signal minimum [V] and maximum [V] are set in order to optimize the resolution of the recorded time series. It is advisable to have these settings as close as possible to the extrema of the input time series, though, without cutting any of the data points.

Acquisition cards are equipped with an on-board buffer of a certain size indicated by OnboardBuffer. event interval sets the number of data points in each interval. If this number does not exceed the limit given by OnboardBuffer, the data are optimally passed onto the memory. Therefore, it is recommendable to try to keep event interval smaller than OnboardBuffer.

On left side of the front panel, a graph displays the output of the acquisition card in Volts for all specified channels. The graph Readout AcqCard shows the last package passed to the memory. The values of minimum [V] and maximum [V] shall be set as vertical axis limits. At any time, the acquisition can be aborted by hitting STOP AcqCard. This will halt the execution of looped functions of the DAQmx driver. The indicators DAQ timeout and DAQ done light up, if one of these two reasons terminates loop and therewith the program.

[Czerwinski and Oddershede, 2010]

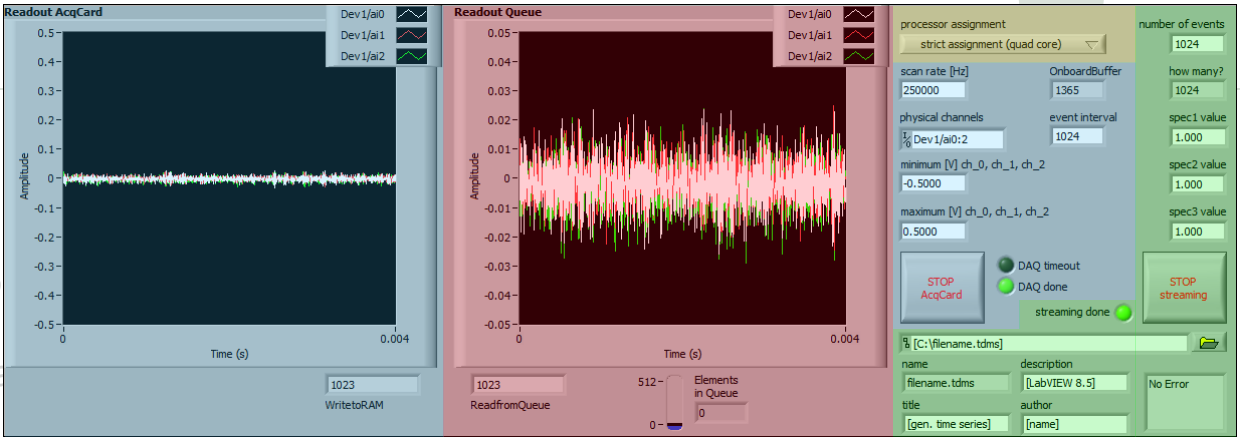

Figure 1: Front panel of TimeSeriesStreaming.vi. In- and outputs of the four programming modules are highlighted by background color: **computer specifications** (yellow), **acquisition** (blue), **queuing** (red), and **streaming** (green). Details regarding the user defined settings are given in Section 3. A high-resolution version of Figure 1 is available through http://www.nbi.dk/ czerwin/TimeSeriesStreaming.html.

Fast Camera Detection Schemes for Optical Tweezers

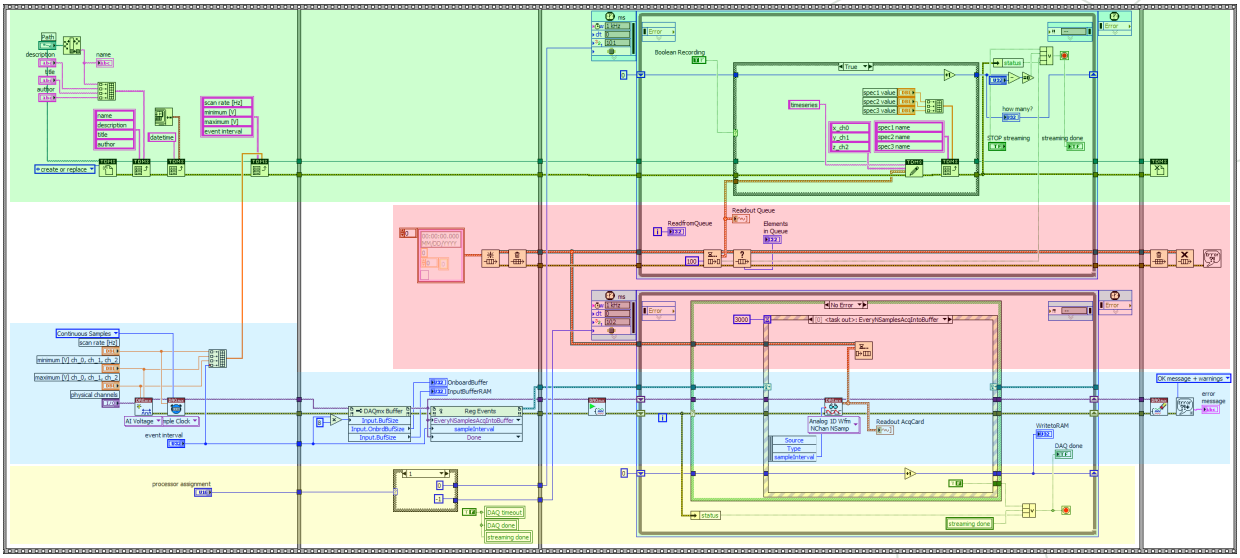

Figure 2: Block diagram of TimeSeriesStreaming.vi. The four programming modules are highlighted by background color: **computer specifications** (yellow), **acquisition** (blue), **queuing** (red), and **streaming** (green). This diagram illustrates the modular architecture of the program where horizontal modules (acquisition, queuing, streaming) can be combined with vertical programming patterns (sequential structure, parallel while loops). A high-resolution version of Figure 2 is available through http://www.nbi.dk/ czerwin/TimeSeriesStreaming.html.

The graph Readout Queue (highlighted red) displays the last package of data passed through the **queue** to the streaming module. Utilizing a user-specified voltage interval here allows for an on-screen check, e.g., for whether data could be exposed to drift. The indicator Elements in Queue reveals the queue's filling level.

Streaming and data storage are controlled by the settings highlighted in green. With number of events the user specifies the total number of event intervals to be acquired. Hence, the total number of data points will be:

$$\text{total number of points} = \text{number of events} * \text{event interval}.$$

how many? counts the processed number of events. The entries spec1 value, spec2 value, and spec3 value are numerical values. They will be stored in the resulting TDMS file in the header to the recorded data. It can regard values the user wishes to keep with the data (e.g., laser power, particle dimensions, ...).

The exact path for the TDMS file with the recorded data must be given. Therefore, replace `[C:\filename.tdms]` by an appropriate entry. Note that an already existing file will be overwritten by default. The program automatically returns the file name and stores it in the header of the TDMS file. title, description, and author can be defined by the user and are also stored in the file header.

If the total number of data points has been streamed, or if the STOP streaming button has been pressed, the program terminates and the indicator streaming done lights up. All data recorded up to that point is available in the user defined TDMS file. Also, TDMS files could be access already during streaming, e.g., from inside another VI.

Potential error messages are shown in the bottom right box.

4. Data Format and Benchmarks

Data Format. The data recorded with TimeSeriesStreaming.vi is stored in a TDMS file. TDMS is an open-source file format developed by National Instruments. It is a binary format optimized for data streaming, thus, it handles dynamically increasing files correctly. Also, one can access the file already during acquisition. There are three ways to access TDMS: Directly in LabVIEW using the primitive TDMS VIs, by third-party plug-ins, or by the program *Diadem* (National Instruments). For the latter method, it is essential to use *Diadem* version 11.1 or higher. Detailed information on how to use Diadem or how to export TDMS files into third-party products can be found under http://www.ni.com/tdms. Third-party plug-ins exist, e.g., for *Matlab*, *OpenOffice*, and *Excel*. *Origin* can open TDMS files directly.

Benchmarks. We tested the performance and stability of TimeSeriesStreaming.vi on three different computers designated for data acquisition. Their specifications are made available through the program summary URL [8]. Since LabVIEW only provides acceptable performance on machines operating Windows, we were limited by the choice of the operating system. All tested CPU architectures (quad-, duo-, and single-core) proved to yield very good acquisition. Though, the highest level of customizability applied to multicore processors. We tested the acquisition cards NI PCI-M6040, NI PCI-6521, and NI PCIe-6521. Table 1 represents the benchmarks for the NI PCI-6251 card with thermal noise as input. Scan rate, number of channels, and buffer per channel were set. Then the program ran for 4096 s and maximum filling and file size were determined. An error was counted when two consecutive 16-bit digits were exactly identical. The error rate was defined as number of errors divided by the number of data points.

In addition, we simulated basically all voltage acquisition devices with the *Measurement and Automation Explorer* and performed benchmarks with TimeSeriesStreaming.vi using the input from the simulated device.

5. Examples of Program Applications

Two brief examples of how to use TimeSeriesStreaming.vi are described here. In addition, the program has already been used to reliably stream large time series from experiments involving optical trapping of micron-sized polystyrene spheres [5], gold nanorods [9], and quantum dots [10]. Furthermore, we implemented an improved calibration protocol for optical tweezers that made use of the main programming features introduced here [11].

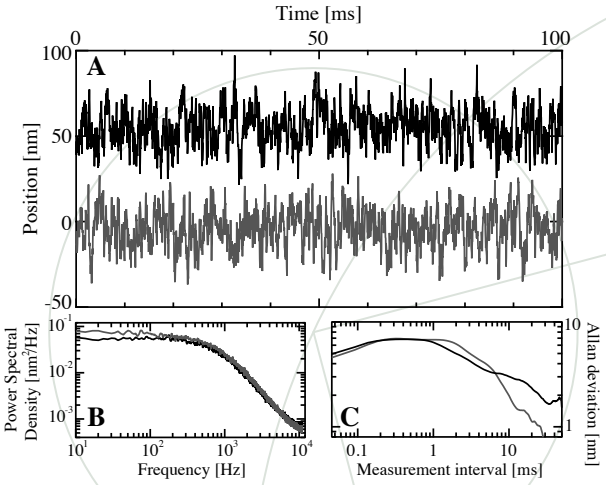

Figure 3: Example of data acquisition and time series analyses applied to an optical trapping assay. **A** Positional time series of an 800 nm polystyrene sphere which is harmonically trapped. Its lateral positions x (grey) and y (black, offset 50 nm) are recorded by a photodiode detection system. The power spectral density (**B**) and the Allan deviation (**C**) of the lateral positions visited.

5.1. Position Recording in Optical Tweezers

The development of TimeSeriesStreaming.vi was prompted by a need to stream large amounts of data from optical trapping assay to a hard disk. The goal was to analyze the noise by means of accuracy measurements [5]. Therefore, positions of a trapped microsphere were recorded at sampling frequencies

scan rate (kHz)	number of channels	buffer per channel	max filling of queue	TDMS file size (MB/s)	error rate
1,250	1	4096	0	9.6	< .000
500	2	2048	0	7.7	< .000
250	4	1024	0	15.3	.004
100	3	1366	0	2.3	.001
100	1	4096	2	2.3	.001
22	6	683	5	6.0	.003
22	3	1366	3	3.0	.001
22	1	4096	3	1.0	.001
10	1	4096	8	0.5	< .001
1	1	4096	3	0.05	< .000

Table 1: Benchmark of TimeSeriesStreaming.vi as performed on a NI PCI-6251 connected to a Windows XP computer running LabVIEW 8.6. Each individual run took 4096 s. Scan rate, number of channels, and buffer per channel were set. Maximum filling, file size, and error rate were determined.

of up to 100 kHz in the order of hours. A short time series is plotted in Figure 3A.

Experimental details are provided in Reference [5]. The positions were sampled using a photodiode detection system yielding an output in Volts, which were reformulated in terms of metric distances by a calibration factor. Figure 3B shows the positional power spectrum, which, when properly analyzed, gives information about the calibration factor as well as the strength of the optical trap [12]. A different type of time series analysis, Allan variance analysis, is excellent for quantifying noise in optical trapping assays [5, 11], in particular in the low frequency regime, which is not possible through normal variance or power spectral analysis. Figure 3C shows the Allan deviation of the same trace quantifying the exact accuracy for various measurement intervals. For this type of analysis it is crucial to have long overall measurement time series and reliable streaming of the data onto the hard disk, a requirement met by TimeSeriesStreaming.vi. The modular fashion of the program enables straight forward implementation of similar types of calibration or noise quantification routines.

5.2. *Ionic Current through Glass Capillary*

The translocation of molecules through solid-state nanopores has drawn a lot of attention in recent years due to the enormous potential they hold for parallel screening of biomolecular solutions [13]. Also, glass capillaries with a diameter of 60 nm could be used to detect DNA folding [6]. Here, we used TimeSeriesStreaming.vi to stream the the ionic current measured onto the computer hard disk. A sketch of the experiment is shown in the lower right of Figure 4. The measured current values are plotted, and in the upper left there is a zoom-in to illustrate that data acquisition was done at a very high rate (1.25 MHz). In this experiment, the error rate was zero. Hence, time series can be analyzed for events happening within sub-milliseconds, the timescale relevant for protein translocation through a nanopore [14], or for events happening on the order of minutes, a typical timescale for drift, as also visible on Figure 4.

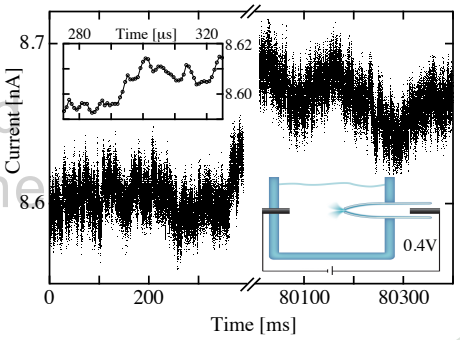

Figure 4: Time series from measurements of monovalent-ionic current through a glass capillary (diameter 60 nm), a sketch of the experiment is shown in the lower right. The inset in the upper left is a zoom-in on the time axis, showing that the acquisition card's limit of 1.25 MHz sampling can be achieved.

6. Summary

We developed a LabVIEW program that reliably streams large amounts of data correctly onto a computer hard disk. The program was checked on several individual platforms and showed to perform with a very small error rate. The program is made in a modular fashion with the aim of making it user-friendly and easily customizable. As an example, we showed how to acquire the positions of an optically trapped sphere and how this time series data can be further analyzed. We also demonstrated how the program streamed time series of ionic current measurements. As the program easily handles a broad range of analog inputs, there is a wide range of applications, particularly in biophysical nano-scale experiments as pointed out in the two examples. The source code is freely available at through the CPC Program Library and under the standard CPC license agreement [15].

Acknowledgements

We thank Lorenz Steinbock for data acquisition and help on the ionic current measurements, and Oliver Otto as well as

Jesper Tholstrup for comments on the manuscript. Also, we acknowledge financial support through the KU excellence program.

References

[1] K.C. Neuman, S.M. Block, Rev. Sci. Instrum. 75 (2004) 2787.
[2] T.M. Hansen, S.N.S. Reihani, L.B. Oddershede, M.A. Sørensen, Proc. Natl. Acad. Sci. 104 (2007) 5830.
[3] J. van Mameren, K.C. Vermeulen, F. Gittes, C.F. Schmidt, J. Phys. Chem. B 113 (2009) 3837.
[4] M. Mahamdeh, E. Schäffer, Opt. Express 17 (2009) 17190.
[5] F. Czerwinski, A.C. Richardson, L.B. Oddershede, Opt. Express 17 (2009) 13255.
[6] L.J. Steinbock, O. Otto, C. Chimerel, J.L. Gornall, U.F. Keyser, Nano Lett. 10 (2010) 2493.
[7] Specifications of National Instrument's acquistion cards are available through http://www.ni.com/dataacquisition/.
[8] Computer specifications during benchmarks are made available through the program summary URL http://www.nbi.dk/˜czerwin/TimeSeriesStreaming.html.
[9] F. Czerwinski, A.C. Richardson, C. Selhuber-Unkel, L.B. Oddershede, Proc. SPIE 7400 (2009) 740004.
[10] L. Jauffred, M. Sletmoen, F. Czerwinski, L.B. Oddershede, Proc. SPIE 7762 (2010) 776226.
[11] M. Andersson, F. Czerwinski, L.B. Oddershede, submitted (2010).
[12] K. Berg-Sørensen H. Flyvbjerg, Rev. Sci. Instrum. 75 (2004) 594.
[13] C. Dekker, Nature Nanotech. 2 (2007) 209.
[14] S.W. Kowalczyk, A.R. Hall, C. Dekker, Nano Lett. 10 (2010) 324.
[15] The standard CPC license is posted at http://cpc.cs.qub.ac.uk/licence/licence.html.

Optimizing active and passive optical tweezers calibration

M Andersson[1*†], F Czerwinski[1*], and L B Oddershede[1]

[1]The Niels Bohr Institute, University of Copenhagen, Blegdamsvej 17, 2100 Copenhagen, Denmark

[*]Authors contributed equally.
[†]Present address: Dept. of Physics, Umea University, 901 87 Umea, Sweden

E-mails: magnusan@nbi.dk, czerwinski@nbi.dk, oddershede@nbi.dk

Abstract
To obtain quantitative information from optical trapping experiments it is essential to perform a precise force calibration. Therefore, sources of noise should be pinpointed and eliminated. Fourier analysis is routinely used to calibrate optical trapping assays, this being excellent for pinpointing high frequency noise. In addition, Allan variance analysis is particularly useful for quantifying low-frequency noise and for predicting the optimal measurement time. We show how to use Allan variance in combination with Fourier analysis for optimal calibration and noise reduction in optical trapping assays. The methods are applied to passive assays, utilizing the thermal motion of a trapped particle, and to active assays where the bead is harmonically driven. The active method must be applied in assays where, e.g., the viscoelastic properties of the medium or the size or shape of the trapped object are unknown. For measurement times shorter than the optimal calibration time the noise is larger in active than in the passive assays. For times equal to or longer than the optimal measurement time though, the noise on passive and active assays are identical. As an example, we show how to quantify the influence on measurement noise of bead size and chamber geometry in active and passive assays.

Keywords: optical tweezers, active calibration, passive calibration, Allan variance, power spectrum, noise, drift, laser

1. Introduction

The possibility to perform precise micro-manipulation and measure interactions and dynamic properties of single molecules has resulted in optical tweezers being a valuable technique in the field of biophysics (1). To use optical tweezers in quantitative forces studies, a bead, typically a polystyrene bead in the micrometer regime, is used as force transducer. To calculate the exact forces exerted on the bead, it is crucial to perform force calibrations as precise as possible. Calibration protocols for precise force and position determination typically involve either passive calibration, where the Brownian motion of the trapped particle is monitored, or active calibration where the measurement chamber is oscillated with respect to the trapped bead (2-3). An active calibration has the advantage of reducing the number of variables, e.g., neither the viscosity, nor the size of the trapped object, nor its distance to nearby surfaces need to be known (2, 4-5). The number of assumptions in the final calibration step can thereby be reduced. In addition, since the range of force measured is in the sub-pN to hundreds of pN, optical trapping assays are extremely sensitive to noise picked up by the instrumentation from the surrounding environment and to drift originating, e.g., from laser instabilities and temperature gradients. Clever modifications to the classical single beam optical trapping assay have been invoked to minimize the effect of drift and noise (6-10). However, the impact of drift on active calibration protocols has not yet been systematically addressed and quantified.

Most high precision optical trapping assays routinely perform Fourier analysis of the trapped particle positions, which yield a power spectrum that can be used to deduce the spring constant, characterize the quality of the trap, and quantify high-frequency noise (11). However, Fourier analysis is not a very efficient method to pinpoint low-frequency noise and determine the optimal measurement time for calibration, e.g., for single molecule assays. For this purpose, Allan variance has proven to be a better choice (12-14). In previous studies, the effect of very-low frequency noise sources present in typical

Academic Advisor: Lene B. Oddershede

Submitted: September 27, 2010

passive assays were investigated, these include noise dependence of detection frequency, type of photo diode, presence of a passive piezo stage with capacitive feedback loop, and presence of acoustic noise (12). Here, we focus on quantification of noise in active calibration assays. Also, we show how to routinely implement Allan variance analysis alongside with power spectral analysis and provide an optimized protocol that will allow the user to improve the signal to noise ratio in both passive and active optical trapping assays. As an example of how to use this optimized method, we performed both active and passive Allan variance analysis of optically trapped beads of different sizes in different chamber geometries with the goal of quantifying the corresponding noise contribution and determine the optimal measurement time for both passive and active calibration assays.

2. Materials and methods

2.1 Sample preparation

Measurement chambers with different heights and width-to-length ratios were made by two 100 µm thick glass slides, with either a single layer of parafilm 110 ± 5 µm or a double layer of parafilm 220 ± 10 µm as spacers, that were cut into different geometries and placed between the cover slides. Cover slides were mended by heating the flow cell to 80° C. Air bubbles in the film were removed by gently applying a pressure to the top slide. Open chambers were made in a similar manner as described in (15). Phosphate buffered saline (PBS, 1x) was filtered with a 50 nm pore sized Millipore filter and degased in ultrasound for 5 min. The buffer was used to prepare dilutions of polystyrene microspheres (1:50,000 from stock) of nominal diameter 792 ± 23 nm and 2035 ± 45 nm (Polybead, Polysciences Inc.). The measurement chamber was sealed with nail polish to prevent evaporation and mounted on a piezo stage (Physics Instrument, P-517.3CL) operated in closed loop. Experiments were conducted at room temperature, 23° C.

2.2 Experimental procedures

The model system and technical approach used for studying noise in optical tweezers have been described in detail previously (12). In short, optical tweezers were implemented in an inverted microscope (Leica, DMI 6000 B). The laser was a continuous-wave Nd:YVO_4 (Spectra Physics J20I-BL-106C) operated at 800 mW, of which approximately 20 % reached the sample. The forward scattered laser light was collected on a position sensitive diode (Pacific Silicon Sensor, DL100-7PCBA3) in order to determine the position of the bead within the trap. To allow for trapping of beads deep within the chamber we used a water immersion objective (Leica, HCX, 63x, NA=1.20). The height of the chamber was measured using the characteristic laser reflection from the two surfaces and a bead was subsequently trapped at 50 µm from the bottom surface to minimize the hydrodynamic interactions with the cover slides. The bead positions were measured for 12 minutes with the position sensitive photodiode. The acquisition frequency was 22 kHz. Furthermore, acquisition card settings were chosen to ensure best possible data reliability. A schematic illustration of the experimental setting is shown in Fig. 1.

We performed both passive and active calibrations along the optimized protocol outlined in section 2.4. For the passive calibration we simply recorded the positions of the bead performing thermal motion within the trap. For the active measurements the piezo stage was driven in a sinusoidal motion at 8, 32, or 128 Hz with an amplitude of 300 nm. Piezo and bead positions were recorded for all measurements. The data was streamed to the computer utilizing a LabVIEW program optimized for reliable streaming of large time series (16). After each measurement, both active and passive, the data was scrutinized to find the trapping stiffness by the power spectrum calibration procedure (11, 17) and the noise in the experiment was quantified using the Allan variance approach (12, 18-19). The Allan variance of each data set was calculated by a custom-written Matlab program available for download (20).

2.3 Allan variance

Allan variance was designed to extrapolate the drift of a system at infinity from finite measurements (18). In contrast to the normal variance, Allan variance converges to a finite value for a broad range of typical noise sources found in biophysical experiments, such as purely stochastic white noise, shot noise, damped

oscillations etc. Therefore, Allan variance has proven itself a valuable tool to quantify the stability and noise of optical tweezers (12, 19, 21). It gives an exact quantification of the variance for neighboring measurement intervals of length τ. This allows for extrapolating the timescale at which the system is affected by high-frequency noise, e.g., originating from electronic components, as well as low-frequency noise, such as vibrations, temperature gradients, etc.

For a time series with *N* elements and a total measurement time $t_{acq} = N / f_{acq}$ the Allan variance is defined as:

$$\sigma_x^2(\tau) = \frac{1}{2}\left\langle (x_{i+1} - x_i)^2 \right\rangle_\tau \tag{1}$$

where x_i is the mean over a time interval $\tau = m / f_{acq}$, m being the number of elements in the interval. <…> denotes the average over all combinations of neighboring intervals. The convergence of the Allan variance results in a significant gain in resolution, especially for $\tau \gg \tau_c$, where τ_c is the typical correlation time of a particle undergoing Brownian motion in a harmonic trap. For measurement times significantly longer than τ_c, drift that is intrinsically present in every experimental setup becomes dominant over the fluctuations. At this transition a minimum of the Allan variance occurs, the corresponding time being the optimal measurement time for calibrations (12). Allan variance is a direct measure of the accuracy and it is assumption free. It makes possible extrapolating the impact of typical low-frequent *1/f*-noise without the need of defining bandwidth or filters. Since Fourier analysis lacks this quality, Allan variance and Fourier analysis probe complementary regimes of the frequency spectrum.

The thermal limit is given by the inherent uncertainty in determining the position of a bead with drag coefficient γ in a harmonic potential with spring constant *k* during the measurement time τ (12):

$$SE_{\langle x \rangle} = \sqrt{\frac{2k_B T\gamma}{k^2 \tau}}\,. \tag{2}$$

If not oversampled, the Allan deviation cannot overcome this standard error. The closer the Allan deviation is to the thermal limit, the less noisy the trapping facility. For $\tau > 2\pi^2\tau_c$ the Allan deviation follows the -1/2 scaling of the thermal limit with respect to τ.

2.4 Optimized protocol for calibration of optical tweezers setups

To quantitatively address and possibly minimize noise present in an optical tweezers assay, we suggest an optimized protocol for optical trapping calibration that combines power spectral and Allan variance analysis:

i) Sample position data in a passive calibration experiment for long time series with a sufficiently high acquisition frequency.
ii) Calculate Allan variance of adjacent time series for a set of measurement times τ.
iii) Determine optimal measurement time $\tau(\sigma_{x,min})$ where the Allan deviation is minimal. Use this optimal measurement time for passive and active calibrations.
iv) Calibrate over statistically independent intervals of length $\tau(\sigma_{x,min})$ using the power spectral density method (11).
v) If desirable, perform i) - iv) with active driving and fit power spectral density accordingly to Ref. (2). This is particularly useful if the drag coefficient of the trapped object or the viscoelastic properties of the surrounding media are unknown (2-3, 22)
vi) Average the fitting parameters (corner frequency f_c, conversion factors relating output voltages to distance) of consecutive, statistically independent intervals.
vii) Convert the Allan deviation from voltage units to meters, compare to thermal limit.

Academic Advisor: Lene B. Oddershede

Submitted: September 27, 2010

viii) Compare internal (e.g., active driving) and external noise (e.g., drift) levels. Quantify and possibly minimize noise sources.

This optimal protocol is not limited to optically trapped spherical particles, but is applicable to any kind of commonly used optical tweezers handles. For example, its usage on gold nanorods and quantum dots has been demonstrated (13-14).

3. Results

3.1. PSD in combination with Allan variance

Allan variance analysis can easily be performed together with the more conventional power spectral analysis, typically performed to find the force characteristics of the optical trap. To show how both power spectral density (PSD) and Allan variance can even be presented in the same plot, we used the data from a trapped 792 nm bead and sampled its position for 12 minutes. In Fig. 2, the corresponding power spectrum, averaged 4, 32, and 8192 times, respectively, is plotted together with the Allan variance of the same time sequence. To get the same physical values plotted on the ordinate axis for both the Allan variance and the PSD, the Allan variance was plotted as $2\tau\sigma_x^2$ as a function of $\pi\tau$, where $\pi\tau=f^{-1}$. The reason for the emergence of the factors π and 2 is due to the particular form of Fourier transformation used (11). Interestingly, the Allan variance (solid black line) is able to reconstruct the power spectrum and yields a high resolution analysis of the data, particularly at low frequencies. Considerable averaging is needed to make the PSD become equally precise to the Allan variance of the same dataset. The power spectrum yields noisier information regarding the low frequencies, hence, details regarding noise and drifts are lost. For high frequencies, the product of Allan variance and measurement time is slightly smaller than the power spectral density due to the fact that Allan variance only considers neighboring intervals.

3.2. Active versus passive calibration

Active calibration has the advantage of needing less pre-knowledge about the system for which, e.g., the force constant is sought. However, introducing an oscillatory motion could potentially increase the overall noise and influence the optimal measurement time. To investigate these issues we performed an experiment where a 792 nm bead was held by a stationary trap and the chamber was moved in a sinusoidal motion at 32 Hz. Also, we performed a passive calibration of the same bead. The resulting Allan deviation plots of the positions of the bead as well as the output from the piezo stage are shown in Fig. 3. The solid lines show the Allan deviation of the bead's positions, dashed lines denote the output from the piezo stage, which was turned on during both the active and passive experiments but kept stationary for the passive experiments. Green lines denote active calibration, black lines passive calibration. The dashed-dotted line denotes the thermal limit given by Eq. (2). It represents the lower limit for position detection. The trace of the passively calibrated particle (solid black line) shows that for low frequencies, noise levels are very close to the thermal limit, a benchmark of a stable setup. In accordance with previous results, the optimal measurement time is on the order of seconds, and for measurement times longer than tens of seconds the piezo stage, which was turned on but not moving, adds significant noise to the measurements (12). For the active calibration, Fig. 3 can be divided into two distinct regions, one where the driven oscillation still dominates the motion of the bead, $\tau < 6$ s, and another for longer measurement times, $\tau > 6$ s, where the Allan deviations originating from passive and active calibrations, respectively, overlap completely. In this region drift dominates the measurement. Hence, our results show that active methods have a position accuracy that is equally good as passive calibrations provided that the measurement time is long enough. The inset of Fig. 3 shows the maximum and minimum values of the positions of the bead during active calibration, when the piezo is run at 32 Hz (green symbols and lines). The maxima and minima converge and become indistinguishable for $\tau > 3$ s. Also shown are the thermal limit (dashed-dotted line) and a guide-to-the-eye of slope -1 (dashed-double-dotted line).

Academic Advisor: Lene B. Oddershede
Submitted: September 27, 2010

To zoom in on the optimal time measurement period for active calibration, we considered the divergence of the Allan deviation from the thermal limit for various driving frequencies (8, 32, and 128 Hz). Fig. 4 shows the Allan deviations of a bead undergoing active calibration subtracted the thermal limit. Fits with τ^{-1} scaling to the maximum peak values for each data set show that the deviation from the thermal limit rapidly decreases and they converge, with a deviation less than one 0.1 nm, already at approximately 1 s. The inset is a zoom-in on the interesting region where the influence of the oscillations falls below the noise present from other external sources.

3.3 Bead size and chamber geometry variations

As an example of how to go through the experimental settings with the aim of minimizing noise, we performed active and passive calibrations to pinpoint the effect of changing bead size and chamber geometry. Two different beads, with diameters 792 nm and 2035 nm, were trapped with the same laser power, the frequency of the active calibration was 32 Hz. Instead of the usual Allan variance plots, for the noise analysis we chose to use the closely related force sensitivity, $\Delta F = k(\sigma_x^2)^{1/2}$, with k being the spring constant characterizing the stiffness of the harmonic optical trapping potential. The force sensitivities as a function of τ are shown in Fig. 5a, both for the smaller bead (green lines) and for the larger bead (black lines) undergoing passive (solid lines) or active (dotted lines) calibration. The thermal limits for the two bead sizes are shown with dashed-dotted lines. As is seen in the figure, the variation in force for short time scales τ < 1 s is higher for the larger bead and the drift on the longer time scales also appear somewhat higher for the larger bead. Around the optimal measurement time (1 s < τ < 20 s) the noise contributions to the force are nearly identical for the two bead sizes.

To investigate the possibility of designing a low-noise chamber, we made systematic investigations of the force sensitivities of similar beads within a variety of chambers. In one series of experiments we systematically changed the aspect ratio in the lateral direction with respect to the trapping laser beam. Some result are shown in Fig. 5b, where the force sensitivity is plotted versus τ for a quadratic chamber with lateral dimensions 2 x 2 mm^2 (dashed-double-dotted line), a 2 x 50 mm^2 rectangular chamber (solid line), and a chamber where the circular droplet of bead solution did not touch the parafilm (dashed line), we denote this an open chamber. The height of all three chamber types was 100 μm. The thermal limit is plotted by a dashed-dotted line in Fig. 5b. Interestingly, we found that the aspect ratio of the chamber did not affect the noise level when the chamber was closed, i.e., the liquid was in contact with the parafilm. The open chamber consistently picked up more noise, approximately 50 fN, in an 1-100 s time scale. Lastly, we investigated how varying the chamber height might affect the noise; Fig. 5c shows the force sensitivity as a function of τ for trapped 792 nm beads in chambers with heights of 100 μm (solid lines) and 200 μm (dashed-double-dotted lines). The beads underwent both passive (black lines) and active (grey lines) calibration. The effect of varying chamber height, doubling the volume, was minor, both regarding the optimal measurement time and regarding the absolute force sensitivity, though with a tendency for the shallower chamber to pick up more noise.

4. Discussion and conclusion

As Fourier analysis and Allan variance analysis have different strengths, the optimal strategy encompasses the use of both methods. It is convenient to have both present in the same representation, as shown in Fig. 2. Fourier analysis is especially efficient for pinpointing high frequency noise contributions whereas Allan variance analysis elegantly quantifies low frequency contributions and provides the optimal measurement time, balancing the gain of drawing additional data points from a given distribution with the fact that inevitably for long enough timescales drift kicks in.

We systematically investigated the noise contribution from both passive and active calibrations, the latter involving a sinusoidal motion of the chamber with respect to the trapped bead. Active calibration procedures are often attractive, especially if, e.g., the friction coefficient of the trapped particle or the viscosity of the medium (2) are unknown. If active methods are used in combination with passive methods, one can even deduce trapping properties in an unknown visco-elastic environment as a living

Submitted: September 27, 2010

cell cytoplasm (3, 22). Due to the active driving, it is not surprising that at measurement times shorter than the optimal measurement time the noise on active assays is considerably larger than on passive assays. It was previously showed that the bare presence of a turned on but not actively moving piezo stage introduces significant noise to an optical trapping assay (12). Interestingly, our results showed that on timescales equal to or longer than the optimal measurement time, the active calibration does not introduce additional noise in comparison to the passive calibration. This is true for all driving frequencies tested (8-128 Hz). Therefore, the low frequency noise contribution from the peizo stage might be linked to the feedback of the controller itself. However, care should be taken since piezo stages have different inherent properties, e.g., resonance frequencies. A comparison of the maxima of the bead response in active calibration to the thermal limit in an Allan-deviation graph, allows for a good estimate of suitable driving frequencies and optimal measurement times.

The optimized active and passive calibration routine can be used to pinpoint noise in specific experimental settings. As an example, we investigated if the level of noise would be dependent on the bead size or chamber geometry. For both short and long times the smaller beads picked up less noise than the larger beads, but the noise level for large and small beads were identical in the optimal measurement time interval. These conclusions are valid both for active and passive calibration. The noise picked up by a bead in chambers where we systematically varied the lateral aspect ratio and the height of the chamber did not depend on the chamber geometry. However, a bead in an open chamber picked up significantly more noise than in a closed chamber. Hence, to minimize noise we would recommend using closed chambers.

Every experimental setup and its environmental conditions are slightly different. By employing power spectral analysis and Allan variance analysis in combination and reporting the outcomes to systematic changes, noise sources can be found, quantified and sometimes eliminated. Implementing these routines on a daily basis holds the potential to compare various setups and measurements across different laboratories with the goal of improving optical trapping standards.

Acknowledgments
We acknowledge useful discussions with Joanne L. Gornall, Liselotte Jauffred, Ulrich F. Keyser, and Oliver Otto and thank Nicola Girotti for help with Illustrator. MA acknowledges financial support from the Swedish Research Council and LBO acknowledges support from the KU excellence program.

References

1. Svoboda K, Block SM 1994 Biological applications of optical forces *Annual Review of Biophysics and Biomolecular Structure* **23** 247-85
2. Tolic-Nørrelykke SF, Schäffer E, Howard J, Pavone FS, Jülicher F, Flyvbjerg H 2006 Calibration of optical tweezers with positional detection in the back focal plane *Rev Sci Instrum* **77** 103101
3. Fischer M, Berg-Sorensen K 2007 Calibration of trapping force and response function of optical tweezers in viscoelastic media *Journal of Optics a-Pure and Applied Optics* Aug 9 S239-S50
4. Deng Y, Bechhoefer J, Forde NR 2007 Brownian motion in a modulated optical trap *Journal of Optics a-Pure and Applied Optics* **9** S256-S63
5. Schäffer E, Nørrelykke SF, Howard J 2007 Surface forces and drag coefficients of microspheres near a plane surface measured with optical tweezers *Langmuir* **23** 3654-65
6. Atakhorrami M, Addas KM, Schmidt CF 2008 Twin optical traps for two-particle cross-correlation measurements: Eliminating cross-talk *Rev Sci Instrum* **79** 043103
7. Klein M, Andersson M, Axner O, Fällman E 2007 Dual-trap technique for reduction of low-frequency noise in force measuring optical tweezers *Applied Optics* **46** 405-12
8. Abbondanzieri EA, Greenleaf WJ, Shaevitz JW, Landick R, Block SM 2005 Direct observation of base-pair stepping by RNA polymerase *Nature* **438** 460-5
9. Carter AR, Seol Y, Perkins TT 2009 Precision Surface-Coupled Optical-Trapping Assay with One-Basepair Resolution *Biophys J* **96** 2926-34
10. Wang MD, Schnitzer MJ, Yin H, Landick R, Gelles J, Block SM 1998 Force and velocity measured for single molecules of RNA polymerase *Science* **282** 902-7
11. Berg-Sørensen K, Flyvbjerg H 2004 Power spectrum analysis for optical tweezers *Rev Sci Instrum* **75** 594-612
12. Czerwinski F, Richardson AC, Oddershede LB 2009 Quantifying Noise in Optical Tweezers by Allan Variance *Opt Express* **17** 13255-69
13. Jauffred L, Sletmoen M, Czerwinski F, Oddershede LB 2010 Quantum dots as handles for optical manipulation *Proc SPIE* **7762** 77620Q
14. Czerwinski F, Richardson AC, Selhuber-Unkel C, Oddershede LB 2009 Quantifying and pinpointing sources of noise in optical tweezers experiments *Proc SPIE* **7400** 740004-1-9
15. Fällman E, Schedin S, Jass J, Andersson M, Uhlin BE, Axner O 2004 Optical tweezers based force measurement system for quantitating binding interactions: system design and application for the study of bacterial adhesion *Biosensors & Bioelectronics* **19** 1429-37
16. Czerwinski F, Oddershede L 2010 TimeSeriesStreaming.vi: LabView program for reliable data streaming of large analog time series *Computer Physics Communications* accepted, http://arxiv.org/abs/1008.1413
17. Hansen PM, Tolic-Nørrelykke IM, Flyvbjerg H, Berg-Sørensen K 2006 tweezercalib 2.1: Faster version of MatLab package for precise calibration of optical tweezers *Computer Physics Communications* **175** 572-3
18. Allan DW 1966 Statistics of atomic frequency standards *Proc IEEE* **54** 221–30
19. Gibson GM, Leach J, Keen S, Wright AJ, Padgett MJ 2008 Measuring the accuracy of particle position and force in optical tweezers using high-speed video microscopy *Opt Express* **16** 14561-70
20. Czerwinski F 2010 Allan v3.0," MatlabCentral 26659, http://www.mathworks.com/matlabcentral/fileexchange/26659-allan-v3-0
21. Mahamdeh M, Schäffer E 2009 Optical tweezers with millikelvin precision of temperature-controlled objectives and base-pair resolution *Opt Express* **17** 17190-9
22. Fischer M, Richardson AC, Reihani SNS, Oddershede LB, Berg-Sørensen K 2010 Active-passive calibration of optical tweezers in viscoelastic media *Rev Sci Instrum* **81** 015103

Academic Advisor: Lene B. Oddershede

Submitted: September 27, 2010

Figure captions

Figure 1. A schematic of the optical tweezers setup. A continuous Nd:YVO_4 laser operated at 800 mW was used to trap polystyrene beads 50 µm above the lower surface of the measurement chamber. The scattered light from the bead was imaged via the condenser onto a photodiode and digitalized with custom made LabVIEW software. The sample was mounted on a piezo stage, and during active calibration driven sinusoidally at 8, 32, and 128 Hz. Different measurement chamber geometries were tested.

Figure 2. Power spectral density plots of a trapped bead averaged over 4, 32, and 8192 time series. Overlaid is the corresponding product of the Allan variance and measurement time (solid black line). The dashed-dotted line illustrates the typical *1/f*-slope for very low frequency noise.

Figure 3. Allan deviation is plotted as a function of τ for passive (black lines) and active (32 Hz, green lines) calibrations. The solid lines show the Allan deviation of the positions of the bead, dashed lines show the Allan deviation of the output from the piezo stage. The dashed-dotted line denotes the thermal limit. The inset shows the minimum and maximum values of the bead position deviation during active calibration, shown along with the thermal limit and a guide-to-the-eye of slope -1.

Figure 4. Difference between the Allan deviation of a trapped bead's position during active calibration at 8, 32, and 128 Hz and the thermal limit. Fits to the maxima with τ^{-1}-scaling are also plotted. The inset is a zoom in onto the interesting region where the drift begins to dominate the noise induced by the active calibration procedure.

Figure 5. Application of Allan variance analysis to pinpoint noise sources in experimental settings. **A**) Comparison of force sensitivity for beads with diameters 792 nm (green lines) and 2035 nm (black lines) undergoing both passive (solid lines) and active (dotted lines) calibrations. **B**) Force sensitivity for a bead trapped in a rectangular chamber 50 x 2 mm^2 (solid line), a quadratic chamber 2 x 2 mm^2 (dashed-double-dotted line), and open chamber (dashed line). **C**) Comparison of the force sensitivity for chambers with a height 100 µm (solid lines) and 200 µm (dashed-double-dotted lines) during active calibration (32 Hz, grey) and passive calibration (black). All dashed-dotted lines denote the thermal limit.

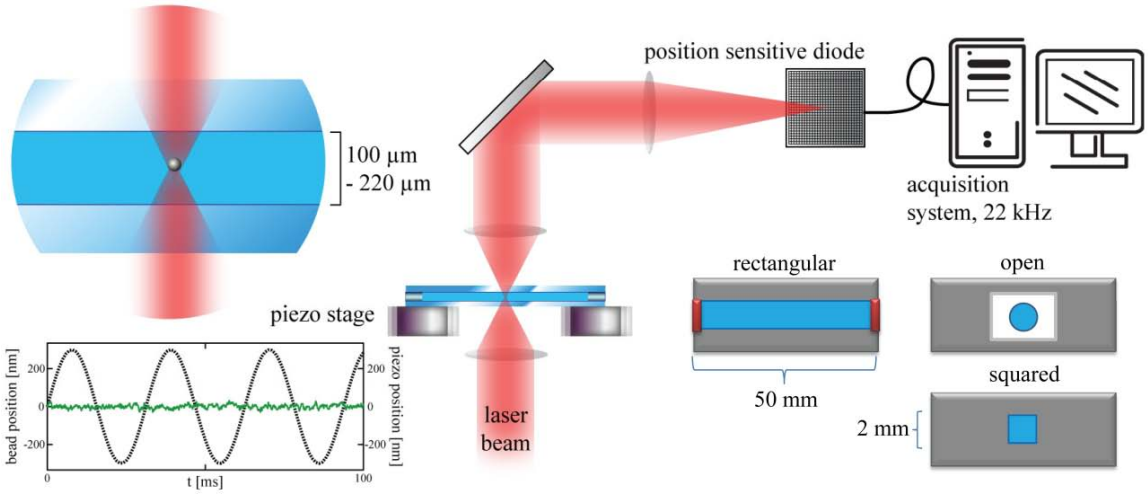

Figure 1.

Academic Advisor: Lene B. Oddershede
Submitted: September 27, 2010

[Czerwinski et al., 2011]

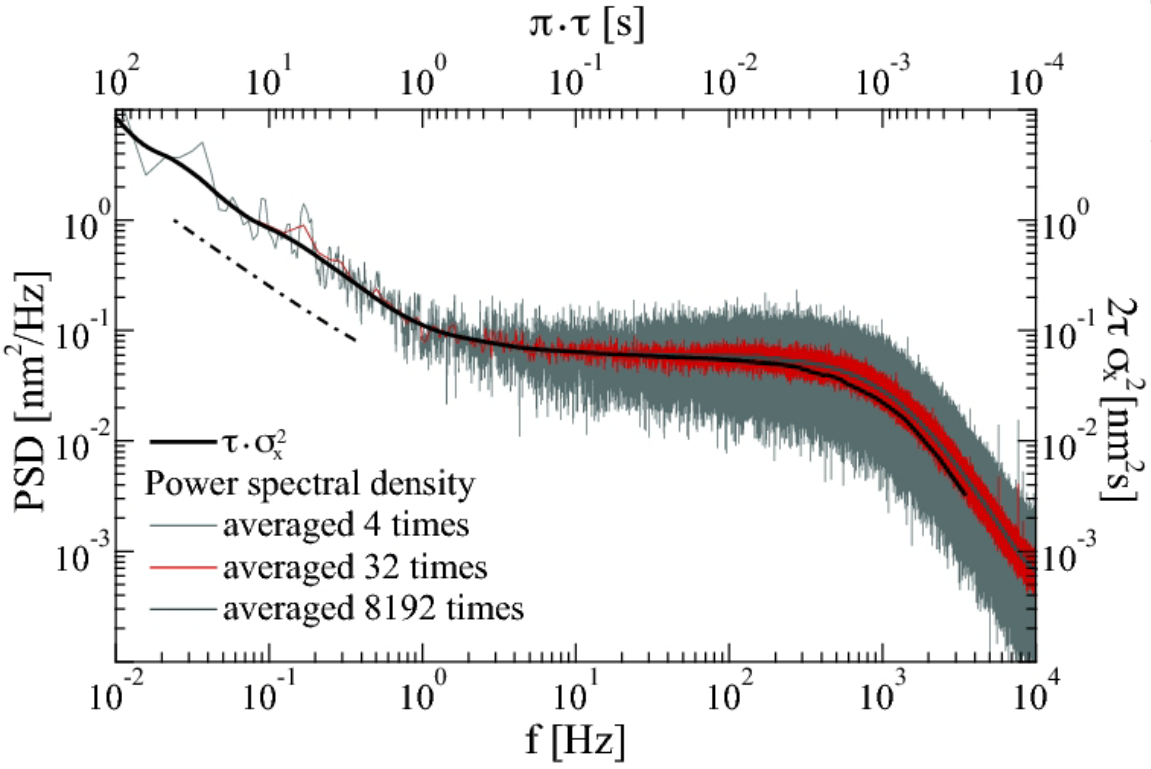

Figure 2.

Academic Advisor: Lene B. Oddershede

Submitted: September 27, 2010

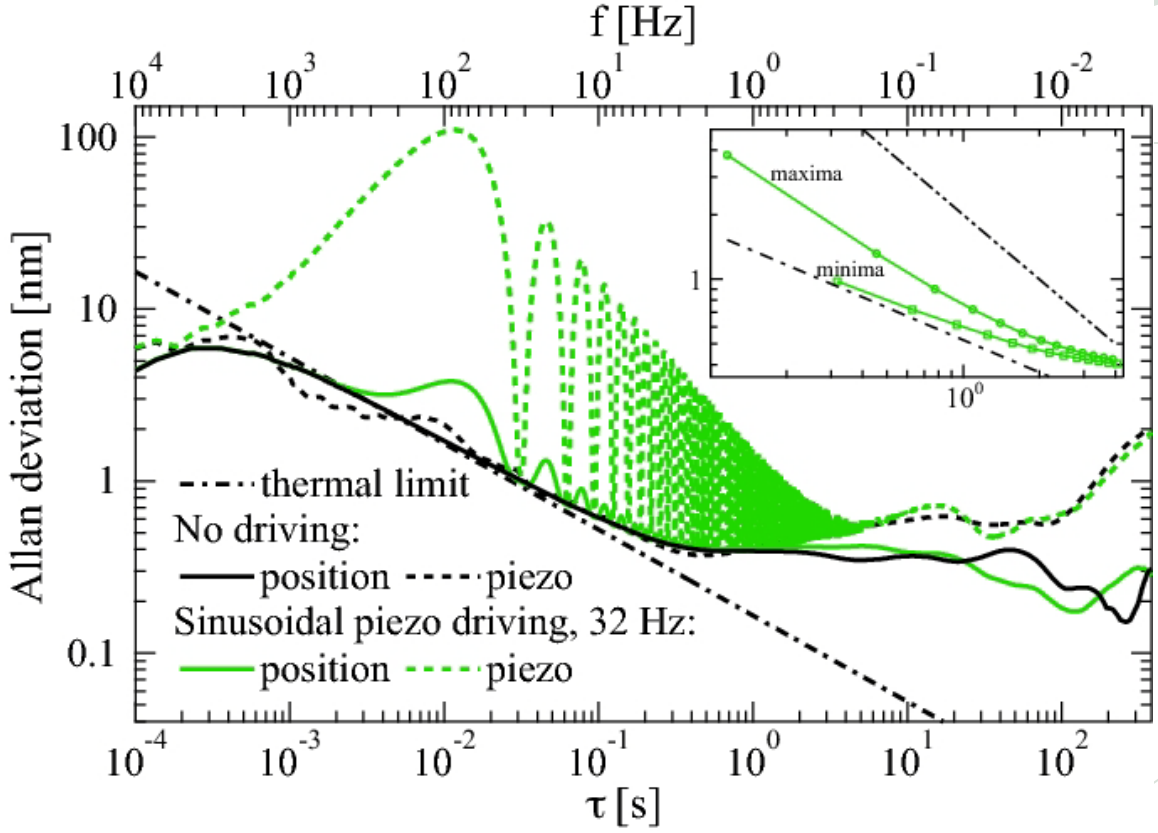

Figure 3.

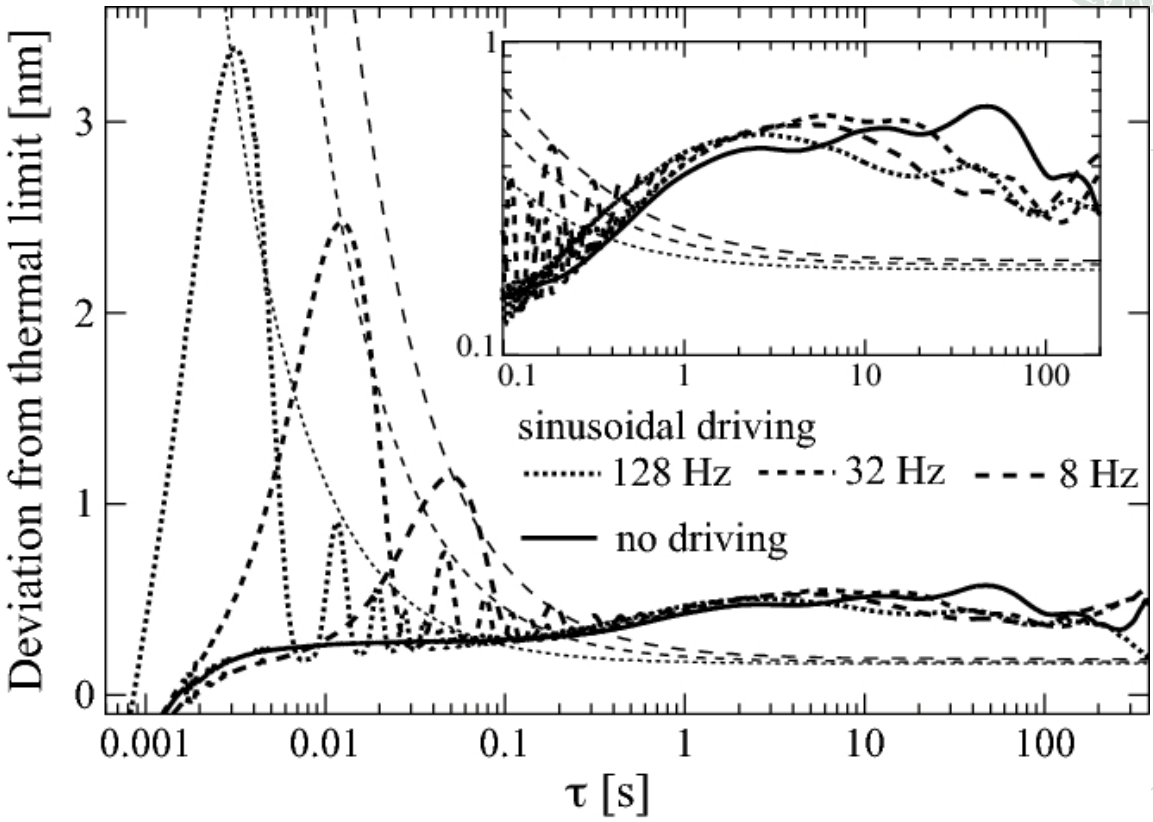

Figure 4.

Academic Advisor: Lene B. Oddershede

Submitted: September 27, 2010

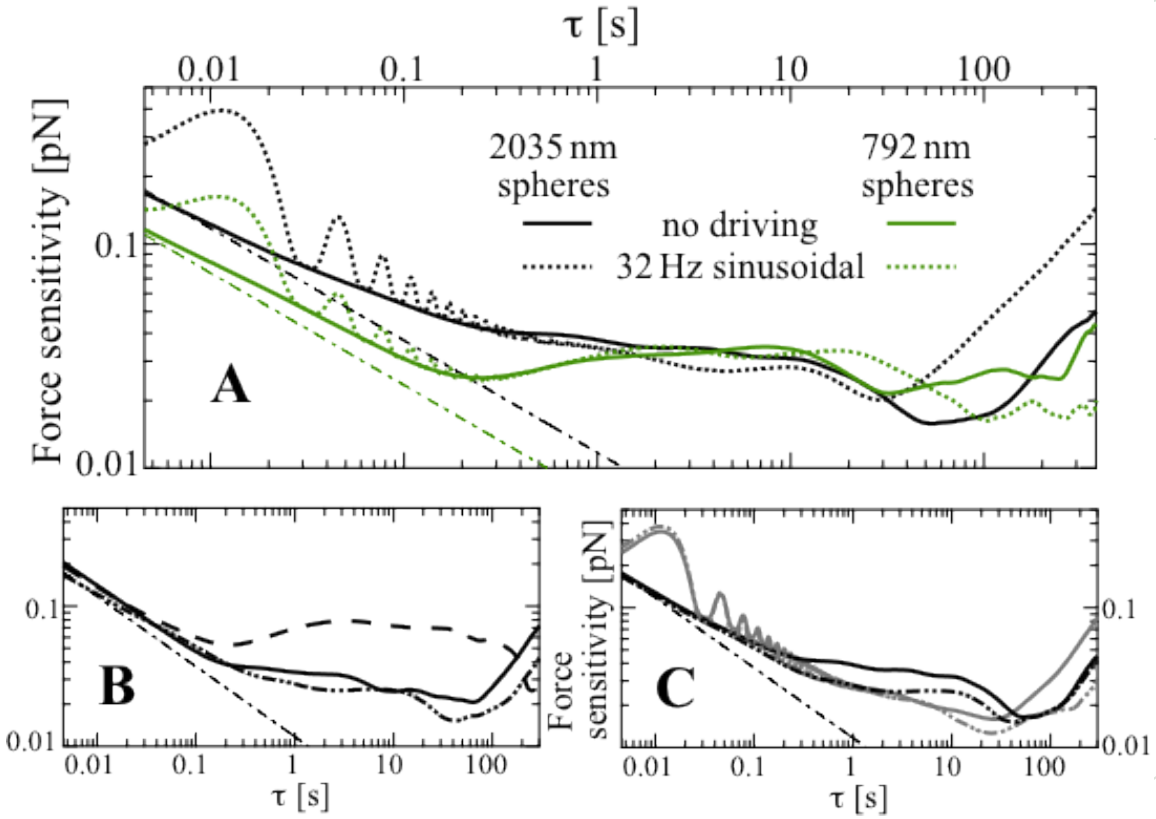

Figure 5.

Academic Advisor: Lene B. Oddershede

Submitted: September 27, 2010

Real-time Particle Tracking at 10,000 fps using Optical Fiber Illumination

Oliver Otto[1], Fabian Czerwinski[2], Joanne L. Gornall[1], Gunter Stober[3], Lene B. Oddershede[2], Ralf Seidel[4], Ulrich F. Keyser[1]

[1] *Cavendish Laboratory, University of Cambridge, J. J. Thomson Avenue, Cambridge CB3 0HE, UK.*

[2] *Niels Bohr Institute, Blegdamsvej, 2100 Copenhagen, Denmark.*

[3] *Leibniz-Institute of Atmospheric Physics, Rostock University, Schlossstr. 6, 18225 Kühlungsborn, Germany.*

[4] *Biotechnological Center, TU Dresden, Tatzberg 47-51, 01307 Dresden, Germany.*
ufk20@cam.ac.uk

Abstract: We introduce optical fiber illumination for real-time tracking of optically trapped particles with microseconds time resolution. Our light source is a high-radiance mercury arc lamp and a 600 μm optical fiber for short-distance illumination of the sample cell. Particle tracking is carried out with a software implemented cross-correlation algorithm following image acquisition from a CMOS camera. Our image data reveals that fiber illumination results in a signal-to-noise ratio usually one order of magnitude higher compared to standard Köhler illumination. We demonstrate position determination of a single optically trapped colloid with up to 10,000 frames per second over hours. We calibrate our optical tweezers and compare the results with quadrant photo diode measurements. Finally, we determine the positional accuracy of our setup to 2 nm by calculating the Allan variance. Our results show that neither illumination nor software algorithms limit the speed of real-time particle tracking with CMOS technology.

OCIS codes: (000.3110) Instruments, apparatus, and components common to the sciences; (060.2310) Fiber optics; (030.4280, 110.4280) Noise in imaging systems; (100.2960) Image analysis; (140.7010) Laser trapping; (230.5170) Photodiodes; (120.4800, 350.4800) Optical standards and testing; (350.4855) Optical tweezers or optical manipulation.

References and links

1. K. Bacia, S. A. Kim, and P. Schwille, "Fluorescence cross-correlation spectroscopy in living cells," Nat. Methods **3,** 83-89 (2006).
2. E. Betzig, G. H. Patterson, R. Sougrat, O. W. Lindwasser, S. Olenych, J. S. Bonifacino, M. W. Davidson, J. Lippincott-Schwartz, and H. F. Hess, "Imaging intracellular fluorescent proteins at nanometer resolution," Science **313,** 1642-1645 (2006).
3. M. Cheezum, W. F. Walker, and W. H. Guilford, "Quantitative Comparison of Algorithms for Tracking Single Fluorescent Particles," Biophys. J. **81,** 2378–2388 (2001).
4. U. F. Keyser, B. N. Koeleman, S. van Dorp, D. Krapf, R. M. M. Smeets, S. G. Lemay, N. H. Decker, and C. Dekker, "Direct force measurements on DNA in a solid-state nanopore," Nat. Phys. **2,** 474-477 (2006).
5. H. Salman, D. Zbaida, Y. Rabin, D. Chatenay, and M. Elbaum, "Kinetics and mechanism of DNA uptake into the cell nucleus," PNAS **98,** 7247-7252 (2001).

Submitted: September 27, 2010

6. J. Wen, L. Lancaster, C. Hodges, A. Zeri, S. H. Yoshimura, H. F. Noller, C. Bustamante, and I. Tinoco, "Following translation by single ribosomes one codon at a time," Nature **452,** 598-603 (2008).
7. A. Ashkin, "Acceleration And Trapping Of Particles By Radiation Pressure," Phys. Rev. Lett. **24,** 156-159 (1970).
8. G. M. Gibson, J. Leach, S. Keen, A. J. Wright, and M. J. Padgett, "Measuring the accuracy of particle position and force in optical tweezers using high-speed video microscopy," Opt. Express **16,** 14561-14570 (2008).
9. K. C. Neuman, and S. M. Block, "Optical trapping," Rev. Sci. Instrum. **75**(9), 2787–2809 (2004).
10. A. van der Horst, and N. R. Forde, "Power spectral analysis for optical trap stiffness calibration from high-speed camera position detection with limited bandwidth," Opt. Express **18,** 7670-7677 (2010).
11. O. Otto, C. Gutsche, F. Kremer, and U. F. Keyser, "Optical tweezers with 2.5 kHz bandwidth video detection for single-colloid electrophoresis," Rev. Sci. Instrum. **79,** 023710 (2008).
12. S. Keen, J. Leach, G. Gibson, and M. J. Padgett, "Comparison of a high-speed camera and a quadrant detector for measuring displacements in optical tweezers," J. Opt. A: Pure Appl. Opt. **9,** 264-266 (2007).
13. M. Towrie, S. W. Botchway, A. Clark, E. Freeman, R. Halsall, A. W. Parker, M. Prydderch, R. Turchetta, A. D. Ward, and M. R. Pollard, "Dynamic position and force measurement for multiple optically trapped particles using a high-speed active pixel sensor," Rev. Sci. Instrum. **80,** 103704 (2009).
14. P. L. Biancaniello, and J. C. Crocker, "Line optical tweezers instrument for measuring nanoscale interactions and kinetics," Rev. Sci. Instrum. **77,** 113702 (2006).
15. G. M. Hale, and M. R. Querry, "Optical Constants of Water in the 200-nm to 200-microm Wavelength Region," Appl. Opt. **12,** 555–563 (1973).
16. Y. Liu, D. K. Cheng, G. J. Sonek, M. W. Berns, C. F. Chapman, and B. J. Tromberg, "Evidence for localized cell heating induced by infrared optical tweezers," Biophys. J. **68,** 2137–2144 (1995).
17. U. F. Keyser, D. Krapf, B. N. Koeleman, R. M. M. Smeets, N. H. Dekker, and C. Dekker, "Nanopore tomography of a laser focus," Nano Lett. **5,** 2253–2256 (2005).
18. I. Semenov, O. Otto, G. Stober, P. Papadopoulos, U. F. Keyser, and F. Kremer "Single colloid electrophoresis," J. Colloid Interface Sci. **337,** 260–264 (2009).
19. F. Czerwinski, A. C. Richardson, and L. B. Oddershede, "Quantifying Noise in Optical Tweezers by Allan Variance," Opt. Express 17, 13255-13269 (2009).
20. F. Czerwinski, and L. B. Oddershede, "TIMESERIESSTREAMING.VI: LabVIEW program for reliable data streaming of large analog time series," Comput. Phys. Commun. accepted for publication (2010).
21. K. Berg-Sørensen, and H. Flyvbjerg, "Power spectrum analysis for optical tweezers," Rev. Sci. Instrum. **75,** 594–612 (2004).
22. C. Gosse, and V. Croquette, "Magnetic Tweezers: Micromanipulation and Force Measurement at the Molecular Level," Biophys. J. **82,** 3314–3329 (2002).
23. O. Otto, J. L. Gornall, G. Stober, F. Czerwinski, R. Seidel, and U. F. Keyser, "High-Speed Video-Based Tracking of Optically Trapped Colloids," J. Opt. A: Pure Appl. Opt. accepted for publication (2010) .
24. M. Andersson, F. Czerwinski, and L. B. Oddershede, "Allan variance for optimizing optical tweezers calibration," under review (2010).
25. F. Czerwinski, A. C. Richardson, C. Selhuber-Unkel, and L. B. Oddershede, "Allan Variance Analysis as Useful Tool to Determine Noise in Various Single-Molecule Setups," Proc. SPIE, Vol. 7400, 740004 (2009).
26. W. P. Wong, and K. Halvorsen, "The effect of integration time on fluctuation measurements: calibrating an optical trap in the presence of motion blur," Opt. Express **14,** 12517–12531 (2006).

1. Introduction

Light microscopy is one of the most versatile and successful measurement techniques providing accurate spatial and temporal information of particle movements [1]. One prominent example is the tracking of single fluorophores or whole organelles in living cells to clarify cellular processes *in vivo* [2, 3]. On the molecular level, optical tweezers offer the opportunity to characterize and monitor mechanical properties of single DNA or protein molecules in aqueous environments [4, 5, 6]. Only a few decades after their introduction, optical tweezers are now a widely used tool in physics and biology [7]. Optical tweezers can exert piconewton forces on micron-sized objects like colloidal particles while measuring the resulting displacements with sub-nanometer accuracy [8]. Two main routes are followed to measure the motion of the trapped particle, namely photo diodes and video-based particle tracking [9]. While photo diodes are suited for position detection of a single colloid, they are not ideal for applications like holographic optical tweezers because monitoring of multiple colloids is complicated. In contrast, video-based particle tracking is capable of following several colloids in the field of view at the same time [10]. The progress in the development of new cameras and illumination systems

has made it possible to extend the acquisition speed of this tracking method to the millisecond timescale [11, 12]. However, this technology is obviously limited by the number of photons that can be recorded by the CCD or CMOS camera per particle.

Recently, several groups have investigated and improved the speed and illumination techniques for single particle tracking in optical tweezers. Gibson *et al.* demonstrated video-based position determination of colloids in optical tweezers using a CMOS camera and standard desktop PC. They recorded particle positions at 1,000 frames per second (fps) in real-time and were only limited by the brightness of their tungsten-halogen lamp [8]. Using a 100 W halogen light source Keen *et al.* showed image acquisition at 2,000 fps but were restricted by the buffer size of their camera to measurement times of 4 s [12]. Van der Horst *et al.* increased the threshold in video-based position determination to 2,500 fps but were ultimately limited by the light intensity [10]. Otto *et al.* carried out experiments on single colloids in optical traps using a CMOS camera and standard software environment [11]. At acquisition rates of 5,000 fps their measurement time was limited by the size of the pre-allocated memory, only. By developing a novel pixel sensor in combination with data analysis based on field programmable gate array (FPGA) circuits Towrie *et al.* determined the position of 6 colloids simultaneously [13]. Their system allows for frame rates up to 15,000 fps but is ultimately restricted by the brightness of their standard light source. Biancaniello *et al.* overcame these limitations by introducing laser illumination into an optical tweezers setup allowing for video-based off-line position tracking with 10 kHz bandwidth [14]. Although lasers are the ultimate high brightness light source accompanying effects like coherence and collimation challenge the alignment of the optical setup.

In this paper, we describe an optical tweezers setup which is based on a novel optical fiber illumination approach and CMOS camera based particle tracking. We demonstrate that a combination of this fiber-based light-source and an entirely software implemented tracking algorithm is sufficient to follow the fluctuations of single or multiple particles at up to 10,000 fps in real-time and over the duration of hours. The quality of the optical fiber illumination is assessed by comparing the images of optically trapped colloids with those obtained in a traditional Köhler illumination alignment. We determine the signal-to-noise ratios (SNR) and show that optical fiber illumination allows for measurements at 40,000 fps with a high SNR of 10. Characterization of the optical trap and determination of the optimal measurement time is carried out using an optimized calibration protocol including Allan variance and power spectral density analysis of time series. We utilize this protocol for data obtained from CMOS measurements comparing Köhler illumination and optical fiber illumination as well as for CCD and quadrant photo diode (QPD) recordings. We show that CMOS-based position tracking allows us to measure close to the thermal limit while giving almost the same accuracy as data obtained from a QPD detector.

2. Materials and Methods

2.1. Optical Tweezers Setup

In our optical tweezers setup (Fig. 1) the beam of an Ytterbium fiber laser (YLM-5-LP, IPG Laser, Germany) is expanded to approximately 7.2 mm, and coupled into the back aperture of a water-immersion microscope objective (UPlanSApo/IR, 60×, NA=1.20, Olympus, Japan). The diffraction limited spot forms a static optical trap inside a fluidic cell. At the chosen wavelength, the absorption coefficient of water is small, reducing laser induced heating to approximately 1.5 K per 100 mW [15, 16, 17]. The fluidic cell itself consists of a 100 μm thick cover slip and a PMMA block, separated by a PDMS spacer. It is mounted onto an XYZ piezo nanopositioning stage (P-517.3, Physik Instrumente, Germany) connected to a digital piezo controller (E-710.3, Physik Instrumente, Germany). The nanopositioning stage enables multi-axis motion with a resolution of 1 nm and a range of 100 μm in the x- and y-directions and 20 μm in the z-direction.

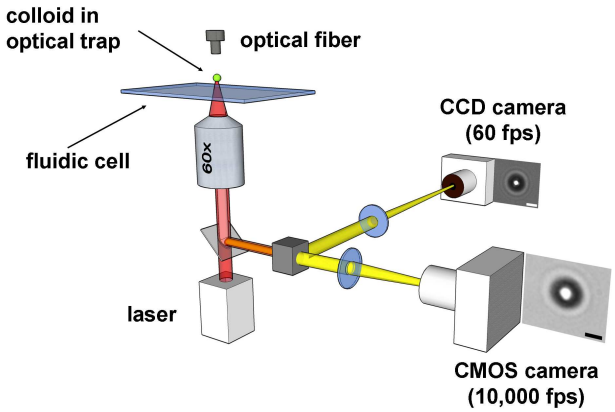

Fig. 1. Schematic drawing of the custom built optical tweezers setup. The 1064 nm laser is focused into a fluidic cell by a 60x water immersion objective. Collimated light of a mercury arc lamp (not shown) illuminates the region of interest through an optical fiber. A high-speed CMOS camera captures 10,000 frames per second and is used for position determination. A slower CCD with up to 60 frames per second is used to provide a full field of view. The length of the scale bars in the colloid images are 2 μm.

For illuminating the Region of Interest (ROI) we follow a novel approach integrating a mercury arc lamp (100 W, LOT - Oriel, UK) and an optical fiber (600 μm core diameter multimode silica fiber, NA=0.39, Thorlabs, UK) into a modular and powerful light source. Our solution has some major advantages. The lamp housing is passively cooled and does not contribute to noise in the setup. With an arc size of only 250 μm our 100 W lamp is a high-radiance source and produces very intense collimated beams. The light is focused onto the input of the optical fiber and is carried along by total internal reflection. Figure 1 shows the output of the fiber which is mounted on top of the sample cell by a custom-built adapter. The ROI is thus illuminated in transmission mode with an effective distance between light source and optically trapped colloid of less than 2 mm. Taking into account the numerical aperture of 0.39 the optical fiber illuminates an effective area of 1 mm diameter. Light diffracted by the colloid is imaged onto the camera by a tube lens with f=20 cm focal length. We estimate an effective light power over the $100 \times 100\,\text{pixels}^2 (\text{px}^2)$ ROI of approximately 1 μW.

All experiments are carried out with polystyrene colloids of diameter $(3.27 \pm 0.32)\,\mu$m (Kisker, Germany) in deionized water. The region of interest around a colloid is monitored by a CMOS camera (MC1362, Mikrotron, Germany) and a high performance frame-grabber card (NI PCIe-1429, National Instruments, UK) [9, 11, 18].

A second optical tweezers setup from Czerwinski *et al.* described in [19] is used to validate the results obtained from our CMOS-based position tracking. In contrast to our system shown in Fig. 1, Czerwinski *et al.* measure the forward scattered light from an colloid applying a quadrant photo diode (S5981, Hamamatsu, Japan) and a CCD camera (Pike-100 B, Allied Vision Technologies, USA) [20].

2.2. *Tracking Algorithm and Implementation*

We aim to perform video-based position tracking of particles at temporal bandwidths previously only accessible to photodiode detector systems [21] or FPGA controlled cameras [13]. Therefore, our technique must be capable of simultaneous high-speed image acquisition and position tracking, in real-time. At the full resolution of $1280 \times 1024\,\text{px}^2$ our camera is specified

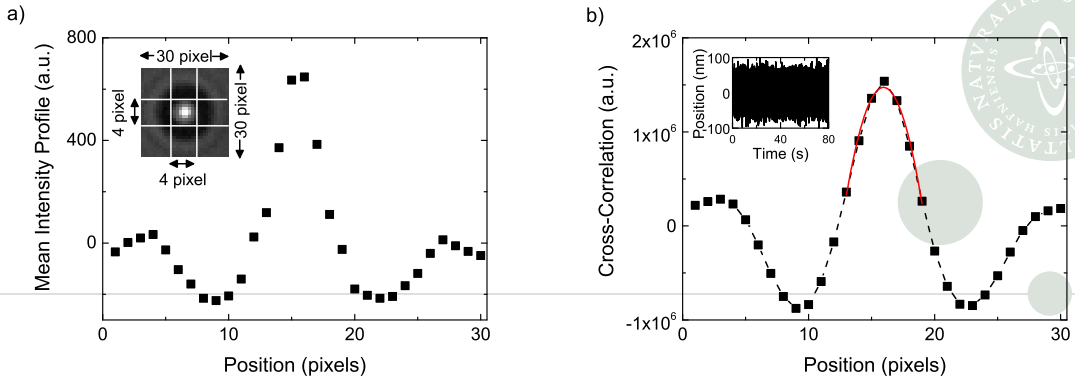

Fig. 2. Implementation of the position tracking algorithm. a) The graph shows the mean intensity profile along an $4 \times 30\,\mathrm{px}^2$ rectangular array of the $30 \times 30\,\mathrm{px}^2$ sub-ROI (inset). The intensity profile is calculated in x- and y- direction independently. b) 1-dimensional cross-correlation transformation and 2^{nd}-order polynomial fit of $\pm 3\,\mathrm{px}$ around the maxima. The inset shows a time trace for a colloid tracked for 80 s at 10,000 fps in real-time.

to 500 frames per second. Based on the CMOS chip pixel size of $14\,\mu$m we determine the resolution of our image system to 214 nm/pixel. By defining a ROI of smaller sizes ($100 \times 100\,\mathrm{px}^2$) image acquisition faster than a few thousands frames per second can be easily achieved. This leaves as limiting step the number of photons arriving at the camera within the shutter time. The shortest shutter times used in this study were $20\,\mu$s.

Since the typical amplitude of the motion of a trapped colloid is of the order of tens of nanometers, position determination must be carried out for one or more particles with sub-pixel accuracy. Our position tracking algorithm uses cross-correlation analysis, described in [22]. The initial position is defined by the user within a sub-ROI of e.g. $30 \times 30\,\mathrm{px}^2$ (inset Fig. 2a). A rectangular array of pixels, $4 \times 30\,\mathrm{px}^2$ in size, passing through the center of the sub-ROI, is binned and then normalized to give the mean intensity profiles for the x- and y-axes separately. Figure 2a shows this for the x-direction. To obtain sub-pixel accuracy, the cross-correlation of the mean intensity distribution with its reverse is calculated by applying the convolution theorem. The result is presented by the black dashed line in Fig. 2b. Subsequently, the peak in the cross-correlation is fit with a second-order polynomial using seven points around the maximum value. The difference between the peak position and the center of the sub-ROI is used to calculate the relative displacement of the colloid. In the inset of Fig. 2b we show the positions of an optically trapped colloid calculated by the above algorithm for a 80 seconds time trace tracked at 10,000 fps in real-time.

We developed our acquisition software in LabVIEW (National Instruments, Austin, TX, USA) and C/C++. Image recording, tracking and streaming are done in a highly parallelized manner, directly assigned to two different CPU cores. Communication between timed loops is achieved by queues. Streaming of the tracked positions is done into the RAM and subsequently onto the hard disk. We tested continuous acquisition over one hour at 10,000 fps. There was virtually no limitation but disk space. We also benchmarked our software implemented tracking algorithm by monitoring the lost frames in a time trace. A frame is considered to be lost if the colloid position had not been calculated before the subsequent frame was acquired. In long-term measurements at 10,000 fps we found less than 5 missing frames for every 100,000 frames recorded, i.e. 0.005 %.

2.3. Calibration and Accuracy Measurements

The optical trap was calibrated by analyzing the Brownian fluctuations of a confined polystyrene colloid in deionized water. We use the power spectral density method [21] within a recently suggested optimized calibration protocol [23, 24]. In this protocol we take a time trace and derive the Allan variance $\sigma_x^2(\tau)$ [19]:

$$\sigma_x^2(\tau) = \frac{1}{2}\left\langle (x_{i+1} - x_i)^2 \right\rangle_\tau , \tag{1}$$

where one calculates the average of the differences between the means of neighboring intervals x_i of measurement time τ. The Allan deviation is a function of time and allows the positional accuracy to be determined for any given τ. The absolute minimum denotes the optimal measurement time for calibration τ_{calib} [19].

Subsequently, we split the time trace into intervals of τ_{calib}, calculate the power spectral density (PSD) of each and derive the averaged PSD. It reveals the Lorentzian profile for the frequency spectrum of an object in an harmonic potential:

$$S(f) = \frac{k_B T}{\gamma \pi^2 (f_c^2 + f^2)} , \tag{2}$$

where k_B is the Boltzmann constant and T the temperature. For the drag coefficient γ we assume Stokes drag for a sphere with radius r moving in a fluid with viscosity η:

$$\gamma = 6\pi\eta r . \tag{3}$$

We use $\eta = 8.9 \cdot 10^{-4}\,\text{Pa}\cdot\text{s}$ for measurements in water. The trap stiffness k_{trap} is directly proportional to the corner frequency f_c:

$$k_{\text{trap}} = 2\pi\gamma f_c . \tag{4}$$

To determine the corner frequency f_c, and consequently the trap stiffness k_{trap}, the power spectrum is integrated numerically and the resulting arctangent function is fit using the least-square method. An example of this is given in the inset of Fig. 5 for a laser power of 100 mW. Only frequencies between $f_{\min} = 10\,\text{Hz}$ and $f_{\max} = 500\,\text{Hz}$, are considered. The fit is corrected for possible aliasing effects according to Ref. [21].

Knowing the trap stiffness, a thermal limit for the accuracy of the particle position averaged over the time period τ_{calib} is given by [8]:

$$SE_{\langle x \rangle} \approx \sqrt{\frac{2 k_B T \gamma}{k_{\text{trap}}^2 \tau}} . \tag{5}$$

In principle, this limit sets the positional accuracy of a Brownian particle and is proportional to $\tau^{-0.5}$. Any experimental setup though is exposed to drift that typically increases the measured deviation following τ^c with $c \leq 1$. Therefore, drift becomes dominant beyond an optimal calibration time, and additional averaging accumulates only the drift response [19].

3. Results

3.1. Illumination

Video-based position tracking is ultimately limited by the number of photons recorded by the camera [9]. A decreasing shutter time and a correspondingly increasing frame rate usually leads to an increase of noise in the image due to the lower number of photons available per time

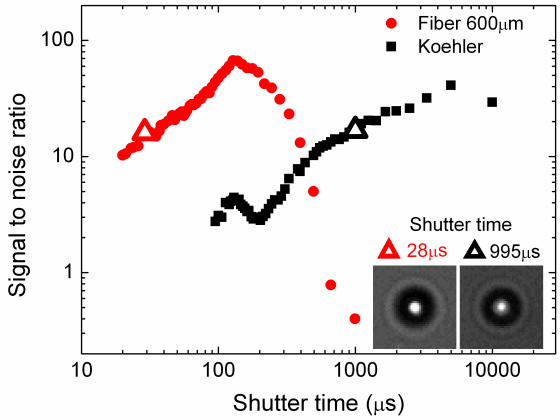

Fig. 3. Signal-to-noise ratio as a function of camera shutter time for illumination by 600 μm optical fiber (red curve) and Köhler alignment (black curve). The inset shows CMOS images of colloids yielding the same signal-to-noise ratio of 16 at very different shutter times of 28 μs (fiber illumination) and 995 μs (Köhler illumination). The intensity of each light source was kept constant during the measurement.

interval. Consequently, the spatial resolution of the optical system is reduced. Measurements at high camera frame rates require high-radiance illumination and the position tracking algorithm to be stable over a wide range of exposure times [3].

One important index to quantify the quality of an image is the signal-to-noise ratio. Generally, it is defined as the mean intensity (μ_O) of the object divided by the root mean square noise of the background (σ_B) [3]. We extend the above definition by including a correction factor μ_R that covers image artefacts at very high light levels:

$$SNR = \frac{\mu_O - \mu_R}{\sigma_B} \quad , \tag{6}$$

where σ_B is extracted from the background area not covered by an object. Diffraction of light by the optically trapped colloid creates an Airy pattern having a maximum of intensity in the center enclosed by a series of dark and bright concentric rings. Very long shutter times and overexposure of the image lead to the disappearance of the first minimum of the Airy disc and to an overestimation of the object intensity which results in an artificially high SNR. The correction factor μ_R is the mean intensity of this first concentric minimum. For short shutter times this correction factor has no effect as the area of the minimum is uniformly black and $\mu_R \to 0$. At long shutter times μ_R allows for correct consideration of effects due to overexposure and ensures that the number of pixels representing the maximum of the Airy disc remains constant.

Figure 3 compares the signal-to-noise ratio of images of optically trapped colloids illuminated by a 600 μm optical fiber and a Köhler configuration respectively. All data were analyzed for different shutter times using Eq. (6). The Köhler illumination curve yields a SNR maximum of 40 at 4,995 μs (200 fps) and decreases towards a SNR minimum of 2 at 203 μs (4,800 fps). The variations in SNR at very short shutter times originate from fluctuations in σ_B at low light levels. The maximum at 4,995 μs however is due to overexposing of the images at longer shutter times at which the signal becomes constant while the background noise is still increasing.

Submitted: September 27, 2010

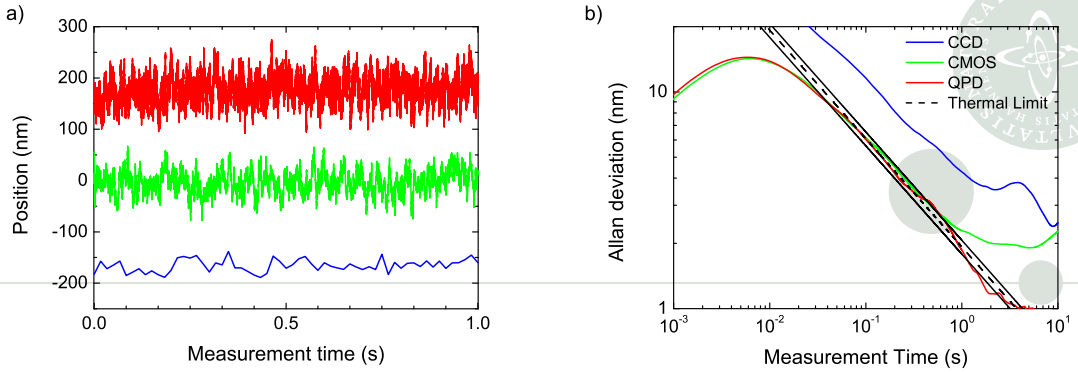

Fig. 4. a) Time traces of a polystyrene colloid optically trapped in a harmonic potential with a corner frequency of about 47 Hz. Data from a CMOS camera (green) was acquired in an experiment at 6,000 fps. Fluctuations with a quadrant photodiode at 50 kHz (red) and a CCD camera at 60 fps (blue) were recorded simultaneously at a separate setup. For visualization the data was shifted along the *y*-axis. b) Allan deviations of all time series in a) with a total length of 130 s each. The effect of aliasing causes the undersampled CCD data to be off the thermal limit by a factor of 3.

The red curve in Fig. 3 shows the SNR for fiber illumination as a function of camera shutter time. It reveals qualitative similarities with data obtained from Köhler illumination but the SNR is generally one order of magnitude higher for comparable shutter times. The signal-to-noise ratio increases to a pronounced maximum of 67 at 128 μs shutter time (7,500 fps) and decreases towards 10 at 20 μs (40,000 fps). The maximum reflects again the influence of overexposure at long shutter times where background noise dominates the image and almost all pixels are saturated to the 8-bit peak value of 255 of our CMOS sensor.

The inset in Fig. 3 shows two colloid images both having a SNR of 16. The image taken with optical fiber illumination has a 35-times reduced exposure time compared to the Köhler illuminated image. Comparing both curves underlines the power of introducing intense light sources in an optical tweezers setup.

3.2. Comparison CCD, CMOS, and QPD

After determining the optimal illumination level, we monitor the Brownian motion of optically trapped polystyrene colloids at a laser power adjusted to a trap stiffness of $k_{\mathrm{trap}} = (9.13 \pm 0.64)\,\frac{\mathrm{pN}}{\mu\mathrm{m}}$ for at least 130 s (Fig. 4a). CMOS data was acquired at a frame rate of 6,000 fps. By using a separate experimental setup time traces based on position detection via QPD and CCD were recorded simultaneously at acquisition rates f_{acq} of 50 kHz and 60 fps respectively. The shutter time of the CCD camera was adjusted to 2.56 ms and for the CMOS camera to 162 μs. Drift quantification (Fig. 4b) and calibration (Fig. 5 inset) was performed as described in Section 2.3.

In addition to determine the optimal calibration time τ_{calib} we use Allan variance to quantify the positional accuracy in an assumption-free manner. In Fig. 4b, the Allan deviation is plotted as a function of measurement time. The dashed line represents the thermal limit Eq. (5).This thermal limit depends on the drag coefficient γ and the trap stiffness k_{trap}. The largest uncertainty of γ derives from the error in the radius of the sphere. The corner frequency is determined with a relative error of $\Delta f_{\mathrm{c}}/f_{\mathrm{c}} = 2\,\%$. Using Eqs. (3), (4) and (5), the error of the thermal limit becomes:

$$\frac{\Delta SE_{\langle x\rangle}}{SE_{\langle x\rangle}} = \sqrt{\left(\frac{\Delta f_c}{f_c}\right)^2 + \frac{1}{2}\left(\frac{\Delta r}{r}\right)^2} \approx 7.35\,\% \quad . \tag{7}$$

We illustrate the impact of those uncertainties in the absolute errors of the thermal limit in Fig. 4b. Data from CMOS-based detection stays close to the thermal limit and reaches a remarkable accuracy of 2 nm when positions are averaged over 3 s to 8 s measurement time. Beyond that drift becomes dominant and the Allan deviation clearly deviates from the thermal limit. QPD and CCD measurements were done on a separate setup having the trap stiffness adjusted to the same k_{trap}. The QPD follows the thermal limit up to tens of seconds. Due to its low sampling frequency, the CCD does not allow for measuring with positional accuracies at the thermal limit. This effect has been described before [25].

3.3. Stiffness over Frame rate

Figure 5 summarizes calibration measurements with CMOS- and QPD-based particle tracking. The corner frequency was derived for various laser powers and camera frame rates. For video-based position determination two different sample illumination techniques were compared. The black data points in the lower frame rate interval between 500 fps and 6,000 fps show measurements where the colloid was illuminated with a cold-light source in Köhler alignment. Calibration between 5,000 fps and 10,000 fps was carried out based on optical fiber illumination represented by the red data points in Fig. 5. Each data point is calculated from a set of measurements of 80,000 images each and analyzed as described above. The shutter time of the camera was kept constant at 162 μs for Köhler and 95 μs for fiber illumination.

Calibration was carried out at five different laser powers: 200 mW, 150 mW, 100 mW, 50 mW and 25 mW (top to bottom in Fig. 5). At a given laser power, the corner frequency is constant over a large range of camera frame rates, as expected. The transition zone between Köhler and optical fiber illumination shows the very same results for both techniques and allows to reliably access 100 μs time resolution on a video-based tracking system. This proves that our system has sufficient bandwidth to calibrate stiff optical traps with high corner frequencies. For high laser powers and frame rates below 1,000 fps however, we see a deviation of f_c towards larger values. This effect can be explained by aliasing [26]. If the sampling rate approaches the corner frequency of the trapped colloid (under-sampling) high-frequency contributions of the power spectrum are folded back into low-frequency parts.

The stability of the optical system was confirmed by performing calibration using a quadrant photo diode at an separate optical tweezers setup. Particle tracking was done for 3.27 μm polystyrene colloids at a laser power corresponding to the 200 mW video-based measurements. The frequency regime was set between 10 kHz and 500 kHz (blue data points). The data in Fig. 5 shows that the corner frequency values are in line with data from video-based particle tracking. This covers Köhler illumination and optical fiber illumination as well. In summary, our results show that CMOS-based calibration of optical tweezers not only approaches the sampling rate of QPD systems but can give the same accuracy and stability in results.

In contrast to QPDs, cameras allow for tracking of multiple particle positions in parallel. There are only two limiting factors: The field of view of the camera sensor and the performance of the data analysis algorithm. Applying the techniques introduced in this paper we are able to synchronously track the position of two colloids at 6,000 fps in real-time (not shown).

4. Discussion

Precise position tracking of an optically trapped colloid requires high spatial and temporal accuracy to be combined in one detection system. This can be achieved by two methods. Quadrant

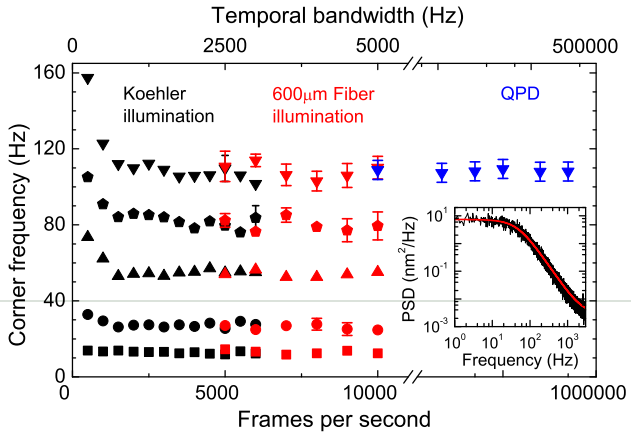

Fig. 5. Calibration of optical tweezers at different acquisition rates. Determination of corner frequency f_c was done at five different laser powers (top to bottom: 200 mW, 150 mW, 100 W, 50 mW, 25 mW) and compares results from Köhler (black) and 600 μm fiber (red) illumination respectively. At a separate setup an additional calibration with a quadrant photo diode (blue) was performed having the laser power adjusted to the video-based measurement. The error is calculated from a series of measurements and is given by the symbol size if not explicitly indicated on the graph. At given laser power the corner frequency remains constant with increasing camera frame rate. The deviation at low frame rates can be explained by aliasing effects of the recording. The shutter time of the CMOS camera was adjusted to 162 μs (Köhler illumination) and 95 μs (optical fiber illumination). The inset shows how the corner frequency f_c was obtained by power spectrum analysis of a confined colloid by numerically integrating the averaged PSD and fitting the resulting curve with an arctangent function. The corresponding time trace was recorded with the CMOS camera at 6,000 fps for 130 seconds.

photo diodes measure the particle induced deflection of laser light with a frequency of up to 500 kHz and allow for fluctuation analysis on a microseconds time scale. However, a single QPD can only monitor the position of one colloid at the same time and is therefore not directly suitable for e.g. holographic optical tweezers.

By integrating a novel optical fiber illumination technique into our optical tweezers setup we extend the effective application range of video-based particle tracking into the microseconds time scale. Light from a 100 W high-radiance mercury arc light source is coupled into a 600 μm fiber and guided directly to our sample cell. This alignment reduces the effective distance between light source and optically trapped colloid to approximately 2 mm. In contrast to laser illumination, we do not need any additional optics to correct for interference effects as the light from a mercury arc lamp is incoherent [14].

We demonstrate position tracking of a single colloid with frame rates up to 10,000 fps in real-time based on a purely software implemented cross-correlation algorithm and following image acquisition from a CMOS camera [23]. In addition, we extend our algorithm for multiple particles and demonstrate tracking of two colloids at 6,000 fps in parallel. Compared to hardware implemented algorithms our design allows for flexibility and full control by the user [13]. Our software takes advantage of multi-core programming and is implemented in a highly parallel manner. Based on these concepts we can perform high-speed video tracking for hours. In fact, the current restrictions of real-time position determination of a single colloid are only originated from the LabVIEW data processing rate. Using off-line data acquisition only, our setup

allows for position tracking at frame rates up to 40,000 fps.

We assess the quality of our novel optical fiber illumination technique by calculating the signal-to-noise ratio of a colloid image at different shutter times of our camera. We compare the results with additional measurements obtained from Köhler illumination. Cheezum *et al.* calculate the limiting SNR for cross-correlation based position detection to 6 [3]. Our data shown in Fig. 3 reveals that the signal-to-noise ratio of fiber illuminated colloids is always well above 10 for shutter times between 20 μs and 395 μs. Indeed, for measurements on the microseconds time scale corresponding to frame rates between 10,000 fps and 40,000 fps the SNR of fiber illumination is always one order of magnitude higher compared to Köhler illumination.

We characterize our optical trapping and tracking system by calculating the Allan deviation of a 6,000 fps CMOS time trace and compare our findings with 60 fps CCD and 50 kHz QPD data from a separate optical tweezers setup. Both, CMOS and QPD allow to measure close to the thermal limit for times up to several seconds. Our CMOS system reaches a remarkable positional accuracy of 2 nm even for weak traps. Allan variance analysis points out the stability of the two optical setups. Even for low trap stiffnesses, they were not significantly exposed to drift until 8 s, which was found to be the optimal calibration interval at those settings. Our tracking method assures long-term stability of positional bandwidth which to our knowledge has not been achieved by any other video-based setup so far.

We calibrate our optical trap by power spectrum analysis. The corner frequency depends linearly on the applied laser power, as expected. We perform these measurements for Köhler illumination, 600 μm fiber illumination and position detection via QPD using two different optical tweezers setups. At fixed laser power Fig. 5 shows consistent results for measurements carried out using both position detection techniques. Further, we prove that the acquisition rate of the camera does not influence the tracking algorithm and that the trap stiffness is essentially independent from the selected illumination method.

5. Conclusion

We have demonstrated the application of novel optical fiber illumination in an optical tweezers setup that allows to study colloidal fluctuations on a microsecond time scale. Particle tracking is carried out video-based in real-time using an entirely software implemented cross-correlation algorithm in a standard desktop environment. The optical fiber illumination allows for image acquisition having signal-to-noise ratios well above 10 even for 20 μs exposure times. We demonstrate CMOS-based position tracking of a single colloid with frame rates up to 10,000 fps over hours. In contrast to QPD measurements, we can straight forward study multiple particles in parallel at high bandwidth. Allan variance calculations are used to determine the positional accuracy of our setup to be about 2 nm. We use separate QPD experiments to validate our results. In summary, we demonstrate that optical fiber illumination in combination with video tracking is applicable for position determination close to sampling rates of QPD systems while yielding the same results, accuracy and stability.

Acknowledgments

U. F. Keyser and R. Seidel acknowledge funding by the Emmy Noether-Program of the DFG. O. Otto thanks for the PhD fellowship and support provided by the Boehringer Ingelheim Fonds. J. Gornall is supported by a Nanoscience E+ grant. L. B. Oddershede acknowledges support from the KU excellence program.

Submitted: September 27, 2010

FACULTY OF SCIENCE
UNIVERSITY OF COPENHAGEN

PhD Thesis

Fabian Czerwinski

Allan Variance Analysis and Fast Camera Detection Schemes for Optical Tweezers

Academic Advisor: Lene B. Oddershede

Submitted: September 27, 2010

Observing and Controlling Biomolecules with Optical Tweezers and LabVIEW

Fabian Czerwinski*, Niels Bohr Institute, University of Copenhagen, Denmark
czerwinski@nbi.dk
Oliver Otto*, Cavendish Laboratory, University of Cambridge, UK
oo226@cam.ac.uk
* Both authors contributed equally.

The Challenge: Creating optical tweezers to observe and control biomolecules at the nanometre scale, for biotechnological and applied medical research in science and industry.

The Solution: Implementing video-based and high-speed position tracking into an optical tweezers setup, using a CMOS camera in combination with NI hardware and software, allowed us to demonstrate real-time particle tracking at 10,000 frames per second for hours.

NI Products: LabVIEW 2009, PCIe-1429, PCI-6521, LabVIEW driver for Mikrotron MC1362; periphery: TDMS, Diadem 11.1, PCI-GPIB

Industries: Biotechnology, Nanotechnology, Optics; University

Abstract: Optical tweezers are an immensely versatile tool in modern biotechnology. By a highly focused laser beam only, they operate inside human cells, measure the elasticity of single DNA molecules, and probe the kinetics of various enzymes. Diverse handles such as gold nanorods or biofunctionalized microspheres are observed with sub-nanometer accuracy typically by photodiodes. Although offering high bandwidth photodiodes have major drawbacks: no long-term stability and the inability to follow more than one object at a time.
Consequently, we combined LabVIEW, NI hardware, and a CMOS camera to record optical tweezers data for hours and to track multiple particles - simultaneously and in real-time! For the first time, we overcome the temporal limitation of video-based position tracking as we reach microsecond resolution. Still, the algorithm purely remains within the LabVIEW code. Taking advantage of multicore programming, multithreading, and pipelining, our VIs analyze 10,000 frames per second. They stream particle positions onto a hard disk in the TDMS format. By applying time series analyses in real-time, the VIs enable feedback implementation and direct responses even during measurements.
In summary, innovative programming concepts and reliable hardware enhance optical tweezers to maintain sensitive control of the challenging world between biology and nanotechnology.

Submitted: September 27, 2010

Main Body:

Lasers are a fascinating and driving force in today's industry and they routinely facilitate super-precise quality control of production processes. Laser properties can be extremely well tuned; therefore, they are not harmful to tissue and ultimately used as diagnostic tools in biotechnology and medicine, making them ideal for use in bionanotechnology such as optical tweezers.

Optical tweezers are essentially a laser beam that is strongly focused by a high-numerical aperture object lens. The optical tweezers can perform very sensitive experiments inside cells, measure the elasticity of single DNA molecules, and probe the kinetics of various enzymes [1–3]. A biological sample can be finely controlled by mounting it on a piezoelectric stage. Either the sample itself or a biofunctionalised handle (an object with biomolecular coating) can be tweezed and manipulated. Often, one uses infrared lasers because of their low absorption rate in aqueous solutions in the relevant frequency band.

We project the experiment onto the back focal plane and record the resulting image using a CMOS camera. There are other detection schemes, but only CMOS cameras provide two important characteristics: visual information and long-term stability. The cameras operate in between high-bandwidth photodiodes and video-recording charge-coupled devices, combining the best of these techniques. There are, however, nontrivial challenges, such as the tracking of handle positions in real time, which is time critical and memory intensive.

We combined NI LabVIEW software, an NI PCI-6251 M Series data acquisition (DAQ) board, an NI PCIe-1429 image acquisition board, and a CMOS camera (Mikrotron MC1362) to record hours of optical tweezers data in real time. Because we wrote our code in LabVIEW, we could customise it to our needs. Using multicore programming, multithreading, and pipelining [4], the VIs analyse up to 10,000 fps of multiple regions of interest to simultaneously track and stream multiple handles into a technical data management streaming (TDMS) file. This provides the ideal interface for time-critical analysis in a VI running in parallel using the recently streamed data.

We carefully probed the fundamental limits of the optical tweezers [5 and 6]. The real-time acquisition, tracking, streaming, and analysis were excellent and had an extremely low error rate (less than 0.0001). Image recording, particle tracking, and streaming are done in parallel and directly assigned to different CPU cores.

Small polystyrene spheres (in the order of microns) exhibit Brownian motion when suspended in water within a confined harmonic potential. Careful calibration and noise characterisation is relevant for biological processes at the nanoscale. We can achieve this using the complementary approaches of Allan variance and power spectrum analysis. The accuracy corresponds to the absolute value of the Allan deviation for a given measurement time. Our setup operates at the thermal limit of Brownian motion, easily measuring nanometre displacements.

Submitted: September 27, 2010

We used the power spectral density analysis to calibrate the optical tweezers and observed two distinct regimes. At low frequencies the sphere senses the tweezers' confinement whereas at high frequencies it diffuses freely. The transition frequency between the confined flat spectrum and the diffusive one is called the corner frequency. It is linear to the harmonic trap stiffness – the most important parameter for an optical tweezers' calibration. Its derivation, especially for stronger traps, requires a high-temporal bandwidth, and consequently, fast camera frame rates. Hence, our solution can calibrate optical tweezers in real time.

Video-based particle tracking is ultimately limited by the number of photons detected. We optimised the illumination and analysed the signal-to-noise ratio (SNR) for different camera shutter times and discovered an SNR of 40 for camera acquisition rates of 10,000 fps. We can directly implement feedback control with this combination of high-speed video tracking and low-noise image analysis.

The high diversity and customisability of LabVIEW combined with video tracking makes an entirely new set of experiments possible. For example, we now have the potential to perform active tweezing of lipid granules in yeast cells. *Schizosaccharomyces pombe*, also known as "fission yeast," produces lipid granules ranging from 100 to 300 nm [1]. The cell uses these granules as transport containers, for example for ribonucleic acid (RNA) [7], and due to the larger refractive index they are good markers.

The investigation of the granules' motion on short time scales is important as it covers the typical bandwidth for active processes inside a cell. We can simultaneously observe multiple granules with the dramatically improved temporal resolution. At the same time, we can tweeze an individual granule, giving insight into transport within cells. This illustrates how optical tweezers can facilitate precise experiments for a fundamental understanding of granule transport.

Our innovative solution combines high-speed and video-based position determination with optical tweezers. Our approach directly observes and manipulates biological handles without mechanical contact. Using NI hardware and software, we can track the position of single particles at 10,000 fps in real time for hours at a time, leading to new insight into highly dynamic processes within the bio-nano world.

References:

[1] C. Selhuber-Unkel et al., Phys. Biol. 6, 25015 (2009).
[2] V. Bormuth et al., Science 325, 873 (2010).
[3] A.R. Carter et al., Biophys. J. 96, 2926 (2009).
[4] F. Czerwinski and L.B. Oddershede, Comp. Phys. Comm. accepted (2010).
[5] O. Otto et al., J. Opt. accepted (2010).
[6] F. Czerwinski et al., Opt. Express 17, 13255 (2009).
[7] P. Anderson and N. Kedersha, Trends Biochem. Sci. 33, 141 (2008).

Figures:

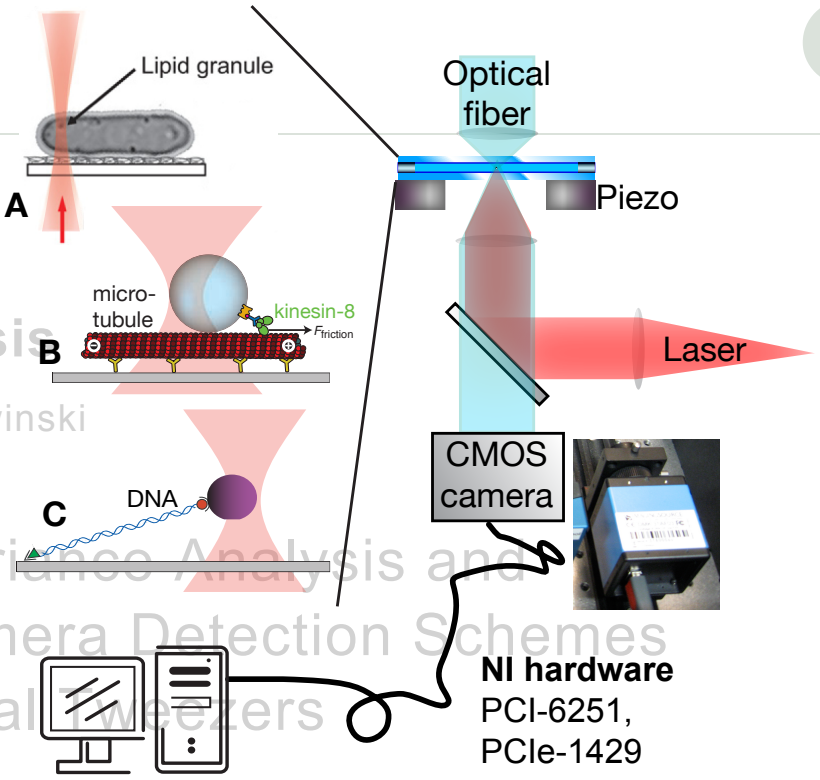

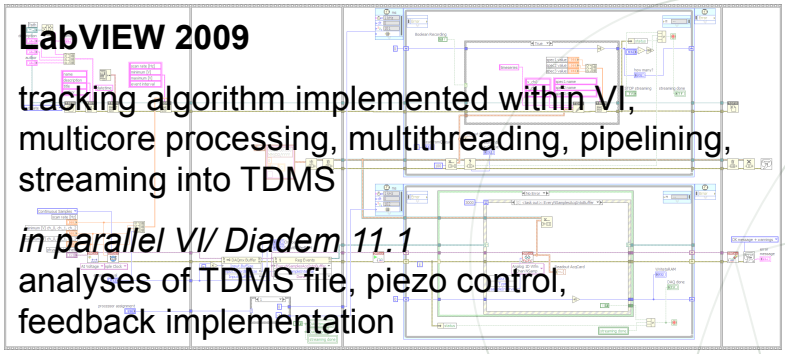

Figure 1. A sketch of optical tweezers controlled by LabVIEW. A highly focused laser beam (wavelength 1,064 nm) confines optical handles inside a microfluidic device. Possible experiments: A lipid granule inside a yeast cell can be observed (A, [1]), an individual kinesin-8 motor dragged over microtubules (B, [2]), or the elasticity of single DNA molecules measured (C, [3]). Mounting the fluidic device onto a piezoelectric stage enables accurate control. An optical fiber illuminates the sample for high signal-to-noise image acquisition. A CMOS camera records the visual information and is interfaced to the computer by an NI PCIe-1429 frame grabber. A software-based routine tracks particle positions and streams the positional information into a technical data management storage (TDMS) file in real time at 10,000 fps. In a parallel VI, the TDMS file is analyzed for time-critical information ([4], see Figure 2).

[Czerwinski and Otto, 2010]

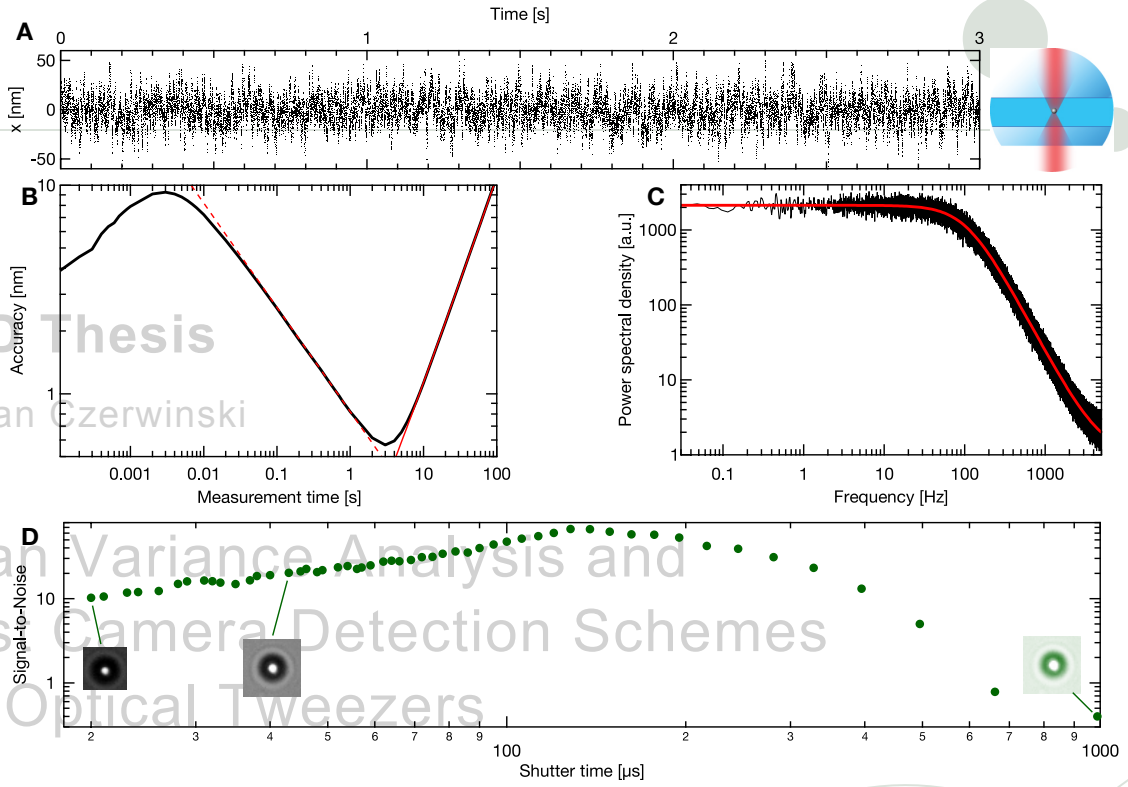

Figure 2. Time critical acquisition and analysis of an optical tweezers experiment [5 and 6]. Brownian motion of a polystyrene sphere (diameter 3.3 µm) in the harmonic potential of optical tweezers (A). The Allan variance of very long time traces is used to determine the accuracy for given measurement times (B). The positional accuracy of the sphere stays at the thermal limit (dashed red graph) and becomes in the order of a nanometer for measurement times of a few seconds. Beyond 5 s, the accuracy increases due to 1/f-noise (solid red graph). Analysis of the power spectral density allows for optical tweezers calibration and determination of high-frequency noise (C). For CMOS camera particle tracking, image quality is crucial (D). Using fiber illumination, we achieve high signal-to-noise ratios even for short shutter times of 20 µs. Three examples of regions of interests at various shutter times are given.

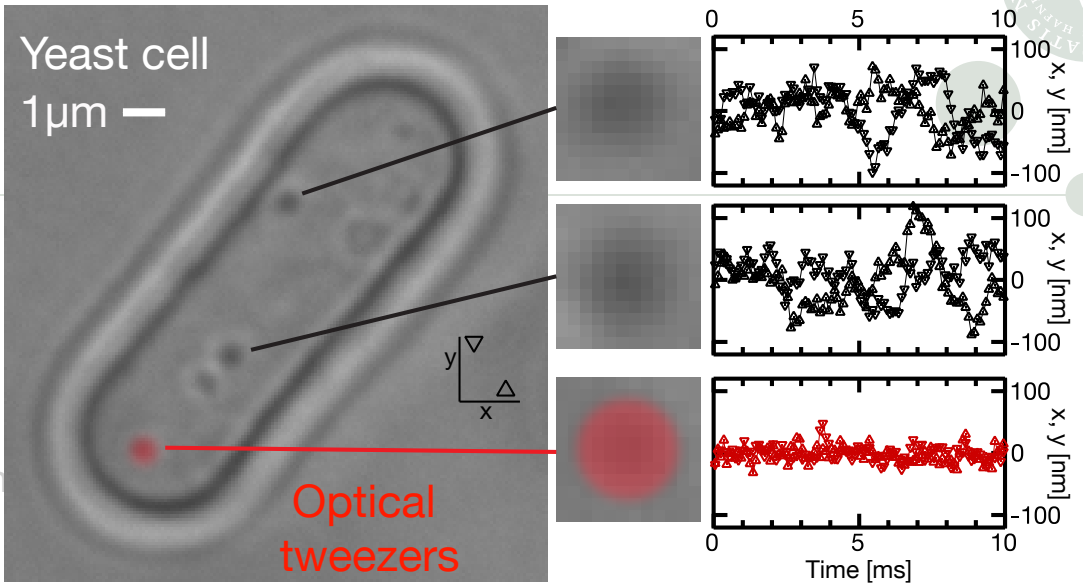

Figure 3. An illustration of possible experiments using CMOS camera tracking of lipid granules inside a yeast cell. Free granules (black time series) diffuse in the plane about 100 nm in each direction. Optical tweezers confine the Brownian motion one of a single granule (red time series). This experiment will help understanding of the complex interplay of active and passive transport processes inside the cell.